From the atmosphere to the abyss: Tracing organic carbon deposition, cadmium isotopes, and iron cycling using marine sediments

by

Logan Tegler

B.S., Arizona State University (2018)

Submitted to the Department of Earth, Atmospheric, and Planetary Sciences in partial fulfillment of the requirements for the degree of

Doctor of Philosophy

at the

MASSACHUSETTS INSTITUTE OF TECHNOLOGY

and the

WOODS HOLE OCEANOGRAPHIC INSTITUTION

February 2024

Author .....

Joint Program in Oceanography/Applied Ocean Sciences & Engineering

Massachusetts Institute of Technology & Woods Hole Oceanographic Institution

August 31, 2023

Certified by .....

Dr. Sune Nielsen, Associate Scientist with Tenure (MG&G)

Certified by .....

Dr. Tristan Horner, Associate Scientist without Tenure (MC&G)

Woods Hole Oceanographic Institution

Thesis Supervisors

Accepted by .....

Dr. Ed Boyle

Woods Hole Oceanographic Institution and Massachusetts Institute of Technology

Chair, Joint Committee for Chemical Oceanography

From the atmosphere to the abyss: Tracing organic carbon deposition, cadmium isotopes, and iron cycling using marine sediments

by

Logan Tegler

Submitted to the Department of Earth, Atmospheric, and Planetary Sciences on August 31, 2023 in Partial Fulfillment of the Requirements for the Degree of Doctor of Philosophy in Geochemistry.

Abstract

The marine biological pump refers to the formation and subsequent export of particulate organic carbon from the sunlit zone to the ocean's interior. The magnitude and attenuation of this flux exert an important control over the air–sea balance of carbon dioxide. This thesis is focused on constraining this flux, the factors that control it, and developing novel tracers for it. First, I evaluate Holocene carbon depositional fluxes in margin sediment and shed light on seafloor OC deposition. I find that margins host 19.4 T mol yr^{-1} of marine OC and, contrary to the current paradigm, less than 4 % of the OC is buried in low-oxygen environments. However, in order to understand how the efficiency of the biological pump may have changed over time, it is necessary to use proxies. In Chapter 3, I examine cadmium isotopes as a potential paleonutrient proxy. I suggest that in addition to biological uptake, Cd isotopes may be influenced by local redox conditions, remineralization, and external Cd additions. In chapter 4, I measure Cd isotopes in the Mt. McRae shale (2.5 Ga) that was deposited across a purported 'whiff' of oxygen that is believed to reflect the onset of oxygenic photosynthesis. I find that the Cd isotopes are invariant and light during the 'whiff' interval. Rather than reflecting no changes in nutrient cycling, I suggest these compositions reflect a source–sink balance between Cd-depleted surface waters and external Cd inputs. Finally, in Chapter 5, we redirect our attention to the Fe cycle. Iron is a limiting nutrient in many ocean regions, which limits the efficiency of the biological pump. We use iron isotopes and Q-mode factor analysis to identify five sources of iron to sites in the South Pacific and Southern Oceans, including: dust, a ligand-bound background source, volcanic ash, and two hydrothermal sources. Taken together, this thesis examines elemental interactions and spans temporal scales, from ancient epochs to the modern era. While we leverage trace elements as proxies of past marine biogeochemical cycles, we also stress that careful work is needed to apply and analyze them.

Thesis Supervisors: Dr. Sune Nielsen and Dr. Tristan Horner

Titles: Associate Scientist with Tenure (S.G.N.), Associate Scientist without Tenure (T.J.H)

Acknowledgments

This thesis would not be possible without the support of friends, family, and mentors. First, I would like to thank my thesis advisors, Sune Nielsen and Tristan Horner. I joined your labs as a summer student back in 2017. Then, I could have never imagined how much knowledge I would gain by working with you. I cannot express enough thanks for the time you have spent making me into a student who was ready to defend her PhD. To Ann Dunlea—you have been an inspiration to me over these last five years. You have modeled what incredible female scientists can be: wicked smart, confident, and genuinely concerned about the well-being of every member of your lab. I hope to be even a fraction of the mentor to someone one day that you have been to me. To Ariel Anbar, thank you for taking a chance on me when you saw a journalism major who wanted to try her hand at working in a chemistry lab. Your guidance led me to discover my love of isotope geochemistry.

I would like to thank my committee members (Drs. Ed Boyle, Ann Dunlea, Tristan Horner, and Sune Nielsen). I have enjoyed the opportunity to work with each of you and implement your knowledge and ideas into this thesis work. Without our many conversations about isotopes, data reduction, statistics, and scientific storytelling, there would be no thesis.

There are a number of incredible folks I have shared the lab and instrument space with over the years. Not only were you a source of ideas and scientific inspiration and a wealth of knowledge, but you are also great friends. To Jule, Chad, Yi, Andy, Margot, Iulia, Jurek, Ichiko, Gretchen, and Emily, thank you! I want to give a special shout-out to Maureen—this lab would simply *not run* without you. Our chats in and out of the lab have been a highlight of my time here. I appreciate all you do. To Peter—thank you for being an incredible office mate these last two years. I wouldn't have the thesis I do without your support, humor, and willingness to pass the 'focus rock'.

Of course, I would like to thank my family. My parents, Stephen and Kem, encouraged me from a young age to chase my passions and pursue learning opportunities. Your confidence in me has allowed me to face academic and personal challenges, and I am eternally grateful to be your daughter. To Ryley, you are the best sister I could ask for. You are always in my corner and never fail to give me words of encouragement when I most need them. To Mamma, our phone conversations remind me to zoom out on the little things and look at the big picture and appreciate everything I have been given. I love you all, always.

I was fortunate enough to be randomly assigned Nicole Collins as a roommate my freshman year of college. Nicole, you have been my fiercest ally over these last 8 years. In college, you pushed me to believe in myself and to take risks. I have grown so much as a person because I had you in my corner. I am truly grateful for the gift of your friendship.

The students and friends I met while living in Falmouth have been a source of love, support, knowledge, and inspiration over the last five years. I am so grateful to Shavonna Bent and Austen Tallman for their friendship. Our study sessions, coffee runs, TV marathons, and amazing dinners (shout out to Austen!) have defined my time in this program. During covid, the two of you keep me sane and socialized. To Kayla Gardner and Sam Clevenger—you were my first friends in the program. When only a handful of our cohort lived in Falmouth the first year, you welcomed me into your home as a pseudo-roommate. I am honored to have watched you grow from first-year grad students to incredible scientists and women. To Jule Middleton, at first, you were an excellent lab mate and an eternal source of marine chemistry knowledge! But, as we spent more time together, you grew into one of my closest friends in the Joint Program. I am honored that we got to share the grad school journey together. To my climbing crew family (Brynn, Jonas, Margot, and

Noah): thank you for keeping my sanity in check every Tuesday night for the last year. Our standing Randolph Central Rock Gym and Pho dates have meant so much to me, and I will miss our weekly antics. To my incredible friends Henry, Alta, Katie, Emman, Anna, Cory, Colin, Ichiko, and Annaliese for the long talks, excellent food, and moral support over the years. To Ashlee and Jacob, although we have been afar these last five years since college, you all have been a source of support and humor. I am grateful we have remained friends over the years!

To Hazelnut, Jovie, Fitz, Remi, Frida, Arlo, Odin, JoeJoe, Josie, Gnasher, Bailey, Cutty, Scooter, Nobska, Roux, and all the dogs and cats I've gotten to meet in Falmouth—thanks for letting me give you all the pats you deserve!

This acknowledgment would not be complete without expressing my love and gratitude to Noah Germolus. We've had quite the journey through graduate school, but my first impressions of you have been lasting: You are unique, deeply kind, and always thoughtful. Writing this dissertation would have been a vastly more stressful experience without your grounding and support. Thank you for everything. I love you.

Finally, in a program with so many students, mentors, and friends, is impossible to thank each of you by name. If you are reading this: thank you.

Financial Support

Funding for this work was provided by the National Science Foundation Graduate Research Fellowship Program (NSF Award #1122374) for providing three years of funding, the Geological Survey of America for a graduate student award in 2019, the Woods Hole Oceanographic Institution, and NSF OCE-2023456.

Table of Contents

LIST OF FIGURES

Figure 2: Panel A shows the Cd concentrations versus organic carbon concentrations. Lines on the plot indicate the range of Cd:OC expected in organic particles. Panel B is a zoomed-in version of Panel A

Figure 3: Profiles from four stations in the Ross Sea. The first column shows the O_2 composition of the water column at stations 0, 2, 24 and 14 (a-d). The second column shows the δ^{114}Cd (‰) (e-h). The third and fourth columns show the Cd concentration and P concentrations, respectively (i-p). The large-size fraction particles are shown in red diamonds with a solid line, the small-size fraction particles are shown in a blue circle with a dashed line

Figure 4: Cadmium excess accumulation in the Peru Margin is shown (diamonds). Excess Cd can come from Cd incorporation from organic matter and CdS pelagic precipitation in the bottom water. The bar represents the Cd that can come from the OC rain rate while the green fraction of the bar represents what is expected from OC that is accumulated in the sediment at 10 cm. In order of left to right, the Peru Margin stations collected along the 11˚S transect are Station 568, 449, 481, 459, 549. More information on these stations can be found in Dale et al. (2015) and Scholz et al. (2011). The station numbering scheme is from Scholz et al. (2011)

Figure 5: Data from the Peru Margin are color-coded by bottom water oxygen content (i.e., < 15µM as red diamonds and > 15 µM as blue circles). The dotted lines represent the range of expected Cd:OC via delivery with organic matter based on previous studies (e.g., Ho et al., 2003; Bourne et al., 2018). The data was collected along the 11˚S transect in the Peru Upwelling Zone. Station numbering is found in Table 1 under the sample name

Figure 6. Data from the Peru Margin. On the upper x-axis is bottom water oxygen concentration. On the lower x axis is δ^{114}Cd (‰) of the sediment sample. The y-axis is depth in the water column. The color bar indicates the Cd:OC ratio in the sediment sample. The figure illustrates that under low oxygen concentrations in the Peru Margin, the δ^{114}Cd (‰) is heavy and the Cd:OC is elevated. This suggested excess Cd pelagic precipitation in the region

Panel 7. Panel A shows the trend between OC:C ratio and δ^{114}Cd (‰) in the Peru Margin and Panel B shows fraction CdS and δ^{114}Cd (‰). The figure suggests that pelagically precipitated Cd is isotopically distinct from organically derived CdS

Figure 8: Shows the surface water Cd concentrations from Roshan et al. (2021) versus the δ^{114}Cd (‰). The correlation suggests that the isotope composition becomes heavier with increasing Cd concentrations

Figure 9: Dissolved δ^{114}Cd (‰) of seawater samples are shown alongside leachable sediment δ^{114}Cd (‰) values (highlighted in pink). The seawater δ^{114}Cd (‰) values fall off of the HNLC isotope trend at low Cd surface concentrations, likely due to inputs of aeolian sources and upward mixing of deep water. The expected range of sediment values

underlying Cd-replete regions is predicted assuming it follows the HNLC trends in the seawater with an associated fractionation factor

Figure 10: Bottom water oxygen values against the leachable δ^{114}Cd (‰). All sediments with evidence for pelagic CdS influence were removed. Only oxic and suboxic samples are included

Figure 11: Panel A shows the range of δ^{114}Cd (‰) globally using the relationships derived between Cd isotopes and Cd surface water concentrations. Panel B shows the range of δ^{114}Cd (‰) globally if the relationship between bottom water oxygen and δ^{114}Cd (‰) is used

Chapter 4

Figure 1: Stratigraphy for the Mt. McRae Shale in Western Australia. This figure is reproduced from Raiswell et al. (2011) and references therein. The associated radiometric ages are from Ono et al. (2003) and Anbar et al. (2007)

Figure 2: Panel A shows the leached concentrations of Cd, Panel B shows Cd isotope composition, Panel C shows OC (%), Panel D shows μmol Cd: mol OC, Panel E shows Cd: Mo ratios, and Panel F shows δ^{15}N (‰). Each of these values are plotted on the x-axis and height of the Mt. McRae is plotted on the y-axis. The LS1 and US1 are shaded in green and blue, respectively

Figure 3: Bulk Cd concentrations are on the x-axis and leached Cd concentrations and on the y-axis. This figure shows that the leach captured the majority of the Cd, but lithogenic material was left behind

Chapter 5

Figure 1: The VARIMAX factor scores from the Q-mode factor analysis, Elements associated with the hydrogenous fraction if the sediments produced five factors explain 97.8 % of the data (46.2%, 22.2%, 17.3%, 9.1%, and 3.1 %, respectively)

Figure 2: The first column (a-c) shows the factor loadings produced from the Q-mode factor analysis along with color-coded factor scores. The second column (d-f) shows the δ^{56}Fe measurements for each site and the last column (g-i) shows the Fe wt. % throughout each of the Sites. Age models were determined using the associated ^{187}Os/^{188}Os isotope measurements

Figure 3: The raw ^{187}Os/^{188}Os profiles for sites U1366, U1369 and U1370. The data show a smoothed Os curve relative to the reference curve. The record is unradiogenic deeper in time and becomes more radiogenic in the modern

Figure 4: Age in Myr against $^{187}Os/^{188}Os$. The red shading shows the allowable $^{187}Os/^{188}Os$ values for a given age considering bioturbation and sedimentation rates in pelagic clays. The black center line is the reference Os curve

Figure 5: The 9 panels show the work flow to date the pelagic sediments. Panels A-C show the raw $^{187}Os/^{188}Os$ values for the three sites with associated uncertainties. Panels D-F shoe the estimated age ranges given from the SOsAGES model. Panels G-I show the final age model after the SOsAGES are used in the *rBacon modeling*. The cloud around the line gives the uncertainty around the mean age estimate in Myr

Figure 6: Plots ages determined using a Co age model (Dunlea et al. 2015a) against the Os age model produced in this study for each of the three sites

Figure 7: Illustrates that the leach has an elevated Ti: Fe ratio compared to the bulk samples. This figure indicates that the leach is enhancing the hydrogenous sediment fraction relative to the lithogenic fraction.

Figure 8: This figure is broken into 5 panels, one for every factor. The $\delta^{56}Fe$ is plotted against the factor loading of the appropriate factor score relative to the sum of all the factor loadings. The plot is used to approximate what the isotope composition of each factor may be when the factor loading is contributing its maximum

Figure 9: Breaks the factor loadings into 5 panels and plots the loadings against age for each of the three sites. Shading illustrates intervals when a factor loading is of increased relative importance

Figure 10: Location and backtrack paths of Site U1366, Site U1369, and Site U1370 at 65 Ma, 34 Ma, 13 Ma, and 0 Ma. Maps were generated by Ann Dunlea using GPlates

LIST OF TABLES

Chapter 2

Chapter 3

Chapter 4

Chapter 5

Chapter 1. Elemental fluxes and isotopes in the past and present ocean

1. The importance of the biological pump

Carbon is an essential building block for creating and supporting life on Earth. Carbon forms complex molecules and is used as elemental currency in life-sustaining reactions such as photosynthesis and respiration. In addition to forming the basis of chemical exchange between organisms, atmospheric carbon dioxide is a greenhouse gas that regulates global climate and helps make Earth habitable. There are four reservoirs of carbon stored on Earth: the terrestrial biosphere, the atmosphere, the ocean (and underlying marine sediments), and the solid Earth. While the solid Earth is the largest reservoir of carbon, holding nearly 100,000 times as much carbon as the atmosphere, it only exchanges with the atmosphere slowly. In contrast, the ocean is the second largest reservoir of carbon, and it makes up ~60 times as much carbon as the atmosphere and exchanges with the atmosphere rapidly. Indeed, many researchers have turned to exploring the ability for the ocean to act as a sponge to take carbon dioxide out of the atmosphere as fossil fuels continue to be pumped in. Because of its sheer size and ability to exchange carbon with the atmosphere, quantifying the modern carbon cycle and understanding how it changes in response to perturbations in the geological past is of primary importance for climate science.

The biological carbon pump, one of the three ocean carbon pumps, refers to the processes where particulate organic matter (POC) is produced in the sunlit surface ocean and exported to depth (Volk & Hoffert, 1985). Once the POC is exported beneath the sunlit, or euphotic, zone the POC meets one of two fates. The first accounts for the vast majority of POC–it is remineralized in the ocean interior. Remineralization is carried out by heterotrophic respiration and turns complex organic molecules back into CO_2. Although most of the POC is remineralized in the ocean's interior (Dunne et al., 2007; Jahnke, 1996; Martin et al., 1987), some escapes the water column and ultimately reaches the seafloor. At the seafloor, the POC is subject to the same processes it was in the water column: organisms living in the sediment use available POC for respiration. However, a small fraction of the POC is buried under newly arriving sediment. This buried OC can be removed from the ocean/atmosphere interface for centennial-to-millions of years timescales (Berner 2003).

The vast majority of organic carbon ends up in margin sediments because these regions are associated with increased productivity in the surface waters and a shorter transit time to the seafloor. Thus, margin sediments play a profound role in the global carbon cycle, with coastal ecosystems acting as efficient carbon sequestration sites. However, the significant uncertainties

surrounding the future state of these critical coastal regions, combined with rapid anthropogenic changes, highlight the need for a better understanding of carbon deposition processes, both in the modern and in the geological past.

While oceanographers can measure sediment in the modern to put constraints on the biological pump, we cannot use carbon concentrations alone to speculate about the efficiency of the biological pump over million to billion-year intervals due to the ephemeral nature of organic carbon in the sediments and tectonic processes. To study changes in the carbon cycle on million-to-billion-year time scales, it becomes important to use other elements that are entrained within the carbon cycle as proxies for ancient biogeochemical processes. Other elements, like cadmium and iron, are entrained in the carbon cycle as these elements are incorporated into organic matter. These elements can be instructive for making inferences about productivity and nutrient utilization.

Carbon, cadmium, and iron span the periodic table and intersect different parts of the carbon cycle. However, these three elements can be appreciated together. To show that these elements are linked together, I have arranged depictions of their biogeochemical cycles in the style of a triptych. A triptych is a work of art dating back to the Middle Ages. The art is divided into three sections and displayed together. The middle panel is the most important while the flanking panels, which are still related to the central panel, are important in their own right. I place carbon in the center as it relates most directly to the biological pump. The Cd and Fe cycles flank to the left and right as they can both be used to infer changes in ancient carbon cycling, but should also be explored for their own independent, and oceanographically significant, cycles (Figure 1).

1.1 Introduction to the chapters

In the first chapter of this work, I explore the carbon cycle directly. I examine OC deposits in Holocene sediments to answer a fundamental question: just how much OC is deposited on the seafloor in the modern marine margins? In the next chapter, I explore the fidelity of cadmium isotopes as a paleonutrient proxy for ancient biogeochemical cycling. Following this, I use my results to explore Cd isotopes in a shale record from an interval in Earth's history that underwent extreme changes in ocean–atmospheric redox. Finally, I explore the sources and cycling of the element that is critical to shepherding the carbon pump in many ocean regions: the micronutrient Fe. These chapters will illuminate some of the ways in which the carbon cycle has changed over

Earth's long history. This thesis shines a light on how the community can use a trinity of elements to make inferences about ancient productivity, nutrient utilization, and nutrient supply over time.

1.2 Organic carbon fluxes on modern margins

The strength of the biological pump, or the total amount of carbon that is produced in the surface and exported to the oceans' interior, has important implications for Earth's climate. When OC leaves the surface ocean, the deficit in dissolved inorganic carbon promotes the drawdown of additional CO_2 from the atmosphere, thus influencing the Earth's climate. The recent uptick in atmospheric CO_2 has piqued scientific and political interest in processes that might accelerate CO_2 drawdown. However, there are still many questions about how the biological pump has changed over time and the processes that affect its ability to sequester carbon dioxide. For example, the burial flux of OC to the margins plays a critical role in regulating global climate and the evolution of benthic communities. Yet, the global OC burial flux and its mechanistic controls remain highly under-constrained, hampering our ability to close the long-term global C budget and predict its evolution under a range of forcing scenarios. Despite numerous efforts to constrain organic carbon (OC) fluxes to the margins, existing estimates based on top-down approaches often rely on multiple assumptions, resulting in divergent results spanning more than an order of magnitude.

In Chapter 2, I adopt a bottom-up approach by compiling measurements from sedimentary deposits to estimate regional and global fluxes of marine and terrestrial OC. This approach enables us to provide detailed constraints on global OC fluxes in margin environments, bypassing many of the assumptions made in previous estimates. Our results reveal that ~20 Tmol OC are buried annually on the margins, an amount around 40 times less than current anthropogenic CO_2 emissions.

Notably, our findings challenge the prevailing paradigm that bottom-water oxygen concentration primarily controls global OC deposition fluxes. Instead, I show that more than 50% of OC burial occurs at oxygen concentrations greater than 180 μM, while only about 4 % is buried in very low oxygen environments (< 50 μM). Water depth emerges as the major control on OC burial, serving as a proxy for exposure time. These insights carry significant implications for understanding past carbon cycle dynamics and bear relevance for future ocean-based geoengineering efforts.

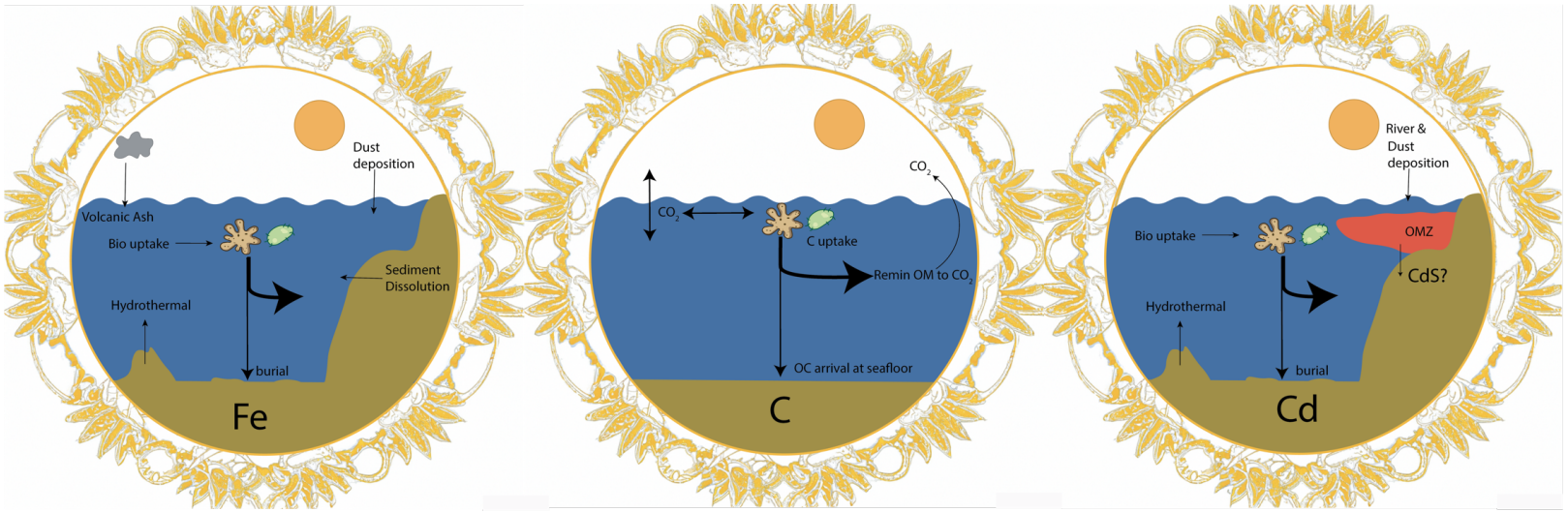

Figure 1. The left panel shows the biogeochemical cycling of Fe. The major sources include dust and ash deposition, hydrothermal, and reductive and non-reductive sediment dissolution. The sinks of Fe include burial within organic matter and scavenging onto particles. The middle panel sources the carbon cycle. Carbon exchanges between the atmosphere and ocean. Carbon dioxide is transformed into sugar molecules during photosynthesis and converted back to CO_2 during remineralization. Some carbon persists and is buried in the sediment. Finally, the Cd cycle is shown in the rightmost panel. Cd enters primarily through river and dust deposition, although some Cd also enters with hydrothermal fluids. Cadmium is lost as CdS and in burial with organic matter. In this study, I will use these cycles and isotopes of the three elements. Carbon is featured in Chapter 2, Cd is featured in Chapters 3 and 4, and Fe is featured in Chapter 5.

Another major contribution of our study is the determination of the efficiency of global OC export from the euphotic zone to the seafloor. I find that, globally, this number ranges between 2–3%, with OC attenuation showing consistency across each ocean basin, irrespective of ambient oxygen levels.

The conclusions of Chapter 2 answer an important question about the modern carbon cycle—I provide a new and robust measurement for the global OC deposition flux in marine sediments. Additionally, I suggest that OC deposition fluxes are also important to consider in high-oxygen regions, where they have often been ignored. With this answer in hand, I turn to trying to place constraints on the carbon cycle in the geological past by examining the fidelity of Cd isotopes in organic-rich sediments as a proxy for paleo nutrient use.

1.3 Cadmium and potential use as a paleonutrient proxy

Because of the ephemeral nature of carbon and the complex nature of carbon's cycling relative to other elements, it is difficult to access perturbations to the biological pump in the geological past. Therefore, scientists rely on paleoproxies to hint at changes in productivity and nutrient use. However, for a paleoproductivity proxy to be useful, the elemental patterns must either be primarily driven by phytoplankton productivity or, if not, the other processes must be readily distinguished and eliminated before analysis can take place.

Cadmium (Cd) has long been considered one of the elements that can help reconstruct changes in productivity and nutrient utilization. Cadmium is correlated with the macronutrient phosphate in the oceans. Many studies have shown that the relationship between Cd and phosphate have comparable nutrient-like properties across multiple ocean basins (Boyle et al., 1976). The uptake of Cd by microbes drives a nutrient-like concentration profile and isotopic fractionation in the surface waters (Figure 2). If this biological fractionation is preserved in the sediment, it can be used to infer something about nutrient utilization. However, while several studies have already employed Cd isotopes in ancient sediments, the paleoproxy does not consider other factors that could influence the isotope composition of the sediments. In Chapter 3, I examine the role that redox, remineralization and productivity play in setting the isotope composition of the sediments. To address this issue, I report over 100 new Cd isotope data, including scores of core-top sediments that span a spectrum of redox conditions (euxinic, anoxic, and oxic) and from four

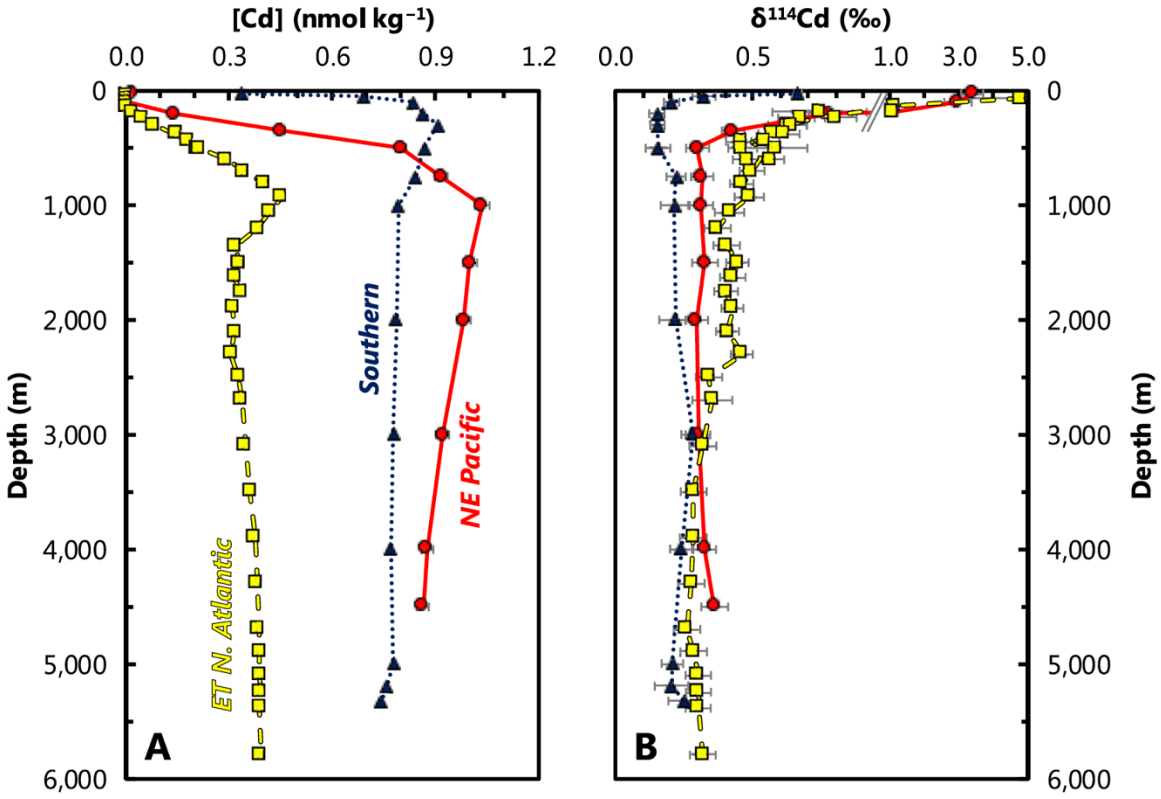

Figure 2. Figure reproduced from Horner et al. (2021). Panel A shows the Cd concentrations with depth in the North Atlantic, Southern Ocean and NE Pacific. Cadmium exhibits a nutrient-like profile: it is taken up by microbes in the surface water and remineralized with depth. Likewise, panel B shows that Cd is processed like a nutrient. The light isotope is preferred by the microbes, leaving the residual seawater heavy. During remineralization, the isotope composition becomes heavier as the organic matter is returned to the dissolved phase.

profiles of marine particulate matter from the Southern Ocean. I find that productivity in the surface water, bottom-water redox, and particle remineralization *all* likely influence the flux of isotope composition of Cd in the sediment. Additionally, I find that in Cd-depleted regions, the Cd isotope composition of sediments reflects external sources, rather than seawater itself. These findings further complicate the interpretation of sedimentary Cd isotopes; however, our results also point to several controls that may enable Cd to be used as a proxy for local redox conditions or particle remineralization.

Chapter 3 is significant because it highlights the need to explore water columns *and* sedimentary samples together when developing trace metal-based proxies. Likewise, our study contributes novel insights into the biogeochemical cycle of Cd and illustrates the importance of well-oxygenated environments to the global mass balance of Cd and its isotopes. Indeed, I close our study with a call for more measurements of Cd isotopes and concentrations in regions underlying oxic water columns with Cd-replete surface waters. With these caveats in mind, I turn to examining Cd isotopes in an ancient sedimentary record.

1.4 Cadmium isotopes in the Mt. McRae Shale at 2.5 Ga

In Chapter 4, I illustrate the complexity of using Cd isotopes as a paleonutrient proxy by measuring Cd isotopes in the Mt. McRae Shale, which was deposited at 2.5 Ga (Figure 4). The Mt. McRae Shale was deposited when Earth began to experience transient oxidation events (Anbar et al., 2007). Thus, this work can serve as a case study for applying Cd isotopes to a region that could reasonably have been expected to experience changes in nutrient utilization. However, I observe invariant isotopically light Cd signatures over the entirety of the 'whiff' interval. Our analysis, coupled with our conclusions in Chapter 3, suggests that another factor besides biological uptake is influencing the Cd isotope signature in the Mt. McRae Shale. After exploring each possibility, I determine that it is most likely that the Mt. McRae Shale was deposited under Cd-deplete surface waters. Similar to what I observe in the modern, I suggest that an external supply of Cd (likely from aeolian deposition or upward mixing of water) accounts for the observed isotopically light signature.

This chapter underscores the need to ground-truth paleo proxies in the modern before applying them in ancient environments. Indeed, the data collected for this chapter was finished

before the data acquisition for Chapter 3. At the time this study was initially completed, no study had measured Cd isotopes as light as those recorded in the Mt. McRae Shale. Therefore, without the modern measurements, I would have interpreted that the Archean Cd cycle was vastly different from today and argued the marine sediments saw a lighter sediment isotope value than had ever been measured in the modern. Such an interpretation would have clearly been erroneous. There is a clear danger in applying a theoretical framework to an ancient record. This chapter emphasizes the need to perform paired analysis in the seawater and sediment to determine how the Cd isotope sedimentary is set. Such work will be imperative to determine how and whether Cd can be used as a biogeochemical proxy.

1.5 History of the Fe Cycle

So far, the work in the thesis has attempted to explore carbon deposition in modern sediments and test the fidelity of using Cd isotopes to reconstruct nutrient utilization in modern and ancient sediments. In Chapter 5, I pivot slightly to discuss the sources of Fe over time. While I will not relate our findings directly to the biological pump in this chapter, understanding the sources of Fe is critical as Fe is often the limiting nutrient in large swaths of the ocean.

In the early days of trace metal chemistry, chemical oceanographers thought that Fe was aplenty in the surface oceans, certainly not limiting phytoplankton production. However, pervasive contamination from measuring Fe on metal ships was obfuscating the fact that Fe was sparse in many of the world's oceans, including the entirety of the Southern Ocean. Instead of solving the problem by purchasing a fleet of wooden ships, scientists developed trace metal clean sampling techniques. These techniques were paramount to allowing oceanographers to discover how important Fe cycling is in the oceans. After John Martin made his influential discovery in 1980– that the lack of Fe in areas of the surface ocean could be limiting how much carbon was exported to the ocean's interior–Fe became a beloved element for many scientists to devote their careers to.

In the early 2010's, the GEOTRACES program was launched. This program aimed to create spatial and vertical distribution maps of trace metals and their isotopes. To no one's surprise, Fe was one of the elements that would be mapped. The GEOTRACES program upended many of the traditional notions about Fe. While the paradigm at the time suggested that Fe was entirely sourced from continental dust, work from GEOTRACES showed that hydrothermal vents and

sediments were significant Fe sources (e.g., Resing et al., 2015) and that this Fe could be carried far away from the source (Fitzsimmons et al., 2017). While this news was exciting for chemical oceanographers, sediment geochemists already had clues that Fe had a source that was not dust derived. A study as far back as 1969 (before chemical oceanographers had accurately measured dissolved Fe in the surface!), a study showed elements like Fe and Mn were, at times, elevated in the sediment above what would be expected from dust (Boström et al., 1969). Of course, when that seminal paper was published, hydrothermal vents still awaited discovery (Corliss et al., 1979).

1.5.1 Unmixing Fe sources with isotopes and statistical magic

The Fe community is now well-aware that there are three major contributors to seawater-derived Fe: dust, hydrothermal vents, and sediment dissolution (Fitzsimmons & Conway 2023). In the water column, Fe isotopes have emerged as a powerful tool to trace these sources, sinks and cycling (Anderson 2020). However, understanding how these sources have changed over millions of years' time scales presents a bigger challenge. While studies by Chu et al. (2006), Horner et al. (2015) and Dunlea et al. (2021) have shown that Fe isotopes can be used to verify that dust, hydrothermal, and sediment dissolution are all important, these records were not able to tease apart how important any source was to a particular sediment sample. In Chapter 5, I unmix sources of Fe over ~90 Ma at three different pelagic clay sites in the South Pacific Gyre. Unmixing these sources will require statistical models, which will be briefly introduced here.

Factor analysis (FA) and Principal Component Analysis (PCA) are similar methods that can identify relationships between large datasets in multidimensional space. Both statistical tools are used in geological applications. However, the key difference between the two processes is that PCA will force all variables into the result, FA generates groups of factors, which will behave differently from the other factors. This is useful for unmixing sources in a geochemical application.

I will employ Q-mode FA in Chapter 5. Although two types of FA exist, the other being R-mode, Q-mode factor analysis is more useful for our purposes as it simplifies a matrix where many samples were measured at multiple temporal and spatial locations. I also perform a VARIMAX rotation after the FA to minimize the negative values that can occur in the factor scores. The VARIMAX rotation rotates the principal component axis such that the variability in the data is both orthogonal and maximized. While this rotation allows the end-member-like factor

scores to be closer to their chemical compositions (i.e., Leinen and Pisias, 1984), this method is a qualitative exercise.

The combination of Fe isotope analysis and QFA allow us to present five dominant sources of Fe in the South Pacific Gyre over the Cenozoic. This work underscores that Fe from dust is not always the most important mechanism of delivery to the open ocean. Indeed, hydrothermal Fe, volcanic ash, and even heavily processed background Fe, all contribute to Fe incorporated in the hydrogenous fraction of sediment. Interestingly, when our samples were in the Southern Ocean, hydrothermal Fe was particularly important. The findings of our study suggest that it is important for scientists to understand how much hydrothermal Fe is advected to the surface waters in HNLC regions. If the hydrothermal Fe observed in our sediment is accessible to microbes in the surface waters, this source of Fe could be important for stimulating photosynthesis, and thus carbon export, in Fe-limited regions.

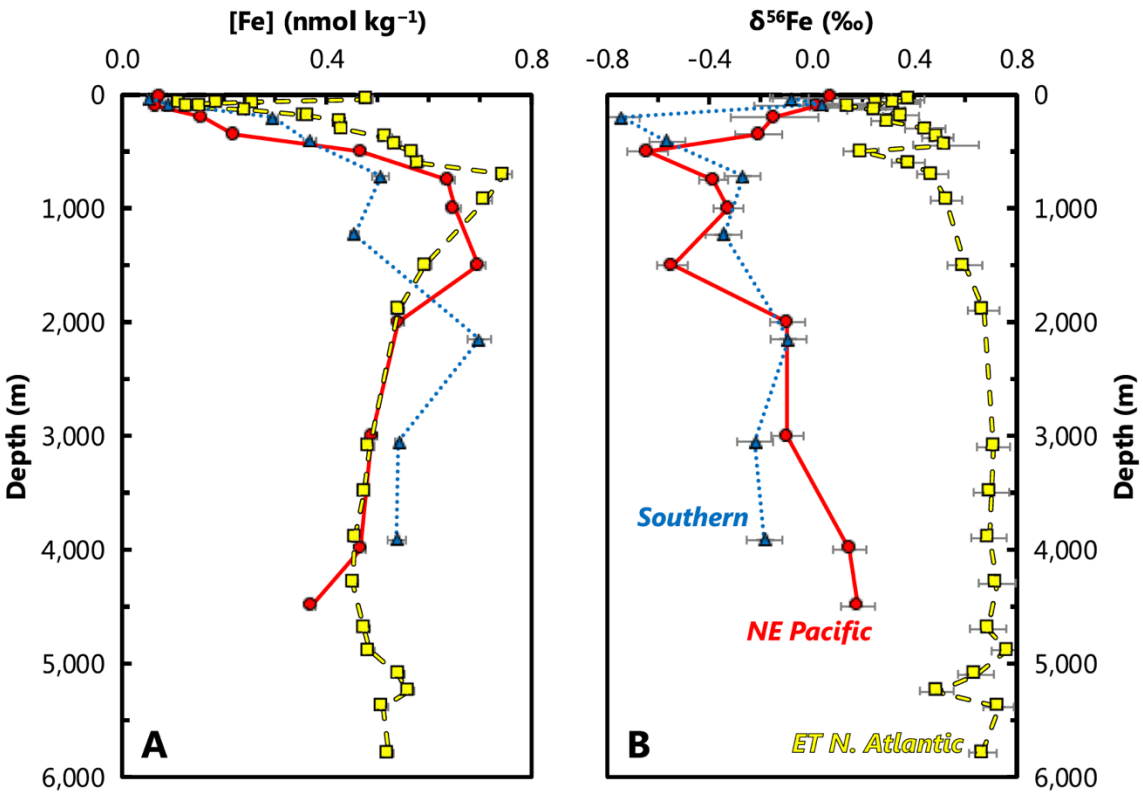

Figure 3. Figure reproduced from Horner et al. (2021). Panel A shows the Fe concentrations with depth in the North Atlantic, Southern Ocean and NE Pacific. Iron has a hybrid-type profile where it is taken up in the surface oceans by microbes and remineralized with depth. The decrease in Fe concentrations in deeper water is due to scavenging onto particles. B shows the isotope behavior between basins is markedly different, due to Fe availability and sources of Fe in each region.

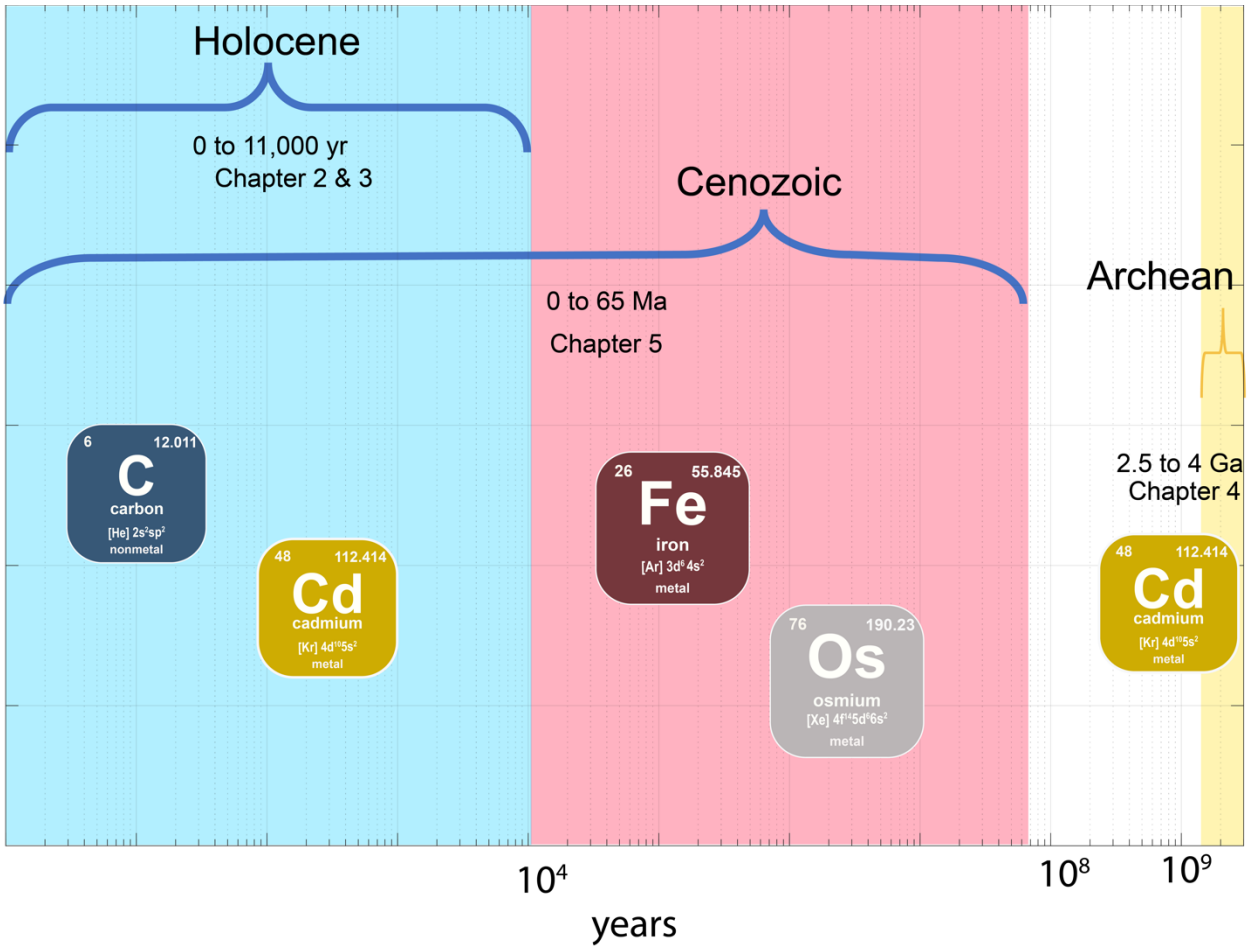

Figure 4. Geological time on a log scale. The three intervals of interest to this thesis are shown by shading (although all other geological periods are excluded). 0 to ~11,000 years include samples that were taken from Holocene sediments, the Cenozoic is covered from 0-66 (although some of our records are as old as 95 Ma), and 2.5 to 4 Ga is the Archean Eon. The major elements and isotopes I measured are broken out into these three sections.

Introduction References

Anbar, A. D., Duan, Y., Lyons, T. W., Arnold, G. L., Kendall, B., Creaser, R. A., ... & Buick, R. (2007). A whiff of oxygen before the great oxidation event?. *Science*, *317*(5846), 1903-1906.

Anderson, R. F. (2020). GEOTRACES: Accelerating research on the marine biogeochemical cycles of trace elements and their isotopes. *Annual Review of Marine Science*, *12*, 49-85.

Berner, R. A. (2003). The long-term carbon cycle, fossil fuels and atmospheric composition. *Nature*, *426*(, 323-326.

Boström, K., & Peterson, M. N. A. (1969). The origin of aluminum-poor ferromanganese sediments in areas of high heat flow on the East Pacific Rise. *Marine Geology*, *7*(5), 427-447.

Boyle, E. A., Sclater, F., & Edmond, J. M. (1976). On the marine geochemistry of cadmium. *Nature*, *263*(5572), 42-44.

Chu, N. C., Johnson, C. M., Beard, B. L., German, C. R., Nesbitt, R. W., Frank, M., ... & Graham, I. (2006). Evidence for hydrothermal venting in Fe isotope compositions of the deep Pacific Ocean through time. *Earth and Planetary Science Letters*, *245*(1-2), 202-217.

Corliss, J. B., Dymond, J., Gordon, L. I., Edmond, J. M., von Herzen, R. P., Ballard, R. D., ... & van Andel, T. H. (1979). Submarine thermal springs on the Galapagos Rift. *Science*, *203*(4385), 1073-1083.

Dunlea, A. G., Tegler, L. A., Peucker-Ehrenbrink, B., Anbar, A. D., Romaniello, S. J., & Horner, T. J. (2021). Pelagic clays as archives of marine iron isotope chemistry. *Chemical Geology*, *575*, 120201.

Dunne, J. P., Sarmiento, J. L., & Gnanadesikan, A. (2007). A synthesis of global particle export from the surface ocean and cycling through the ocean interior and on the seafloor. *Global Biogeochemical Cycles*, *21*(4).

Fitzsimmons, J. N., & Conway, T. M. (2023). Novel insights into marine iron biogeochemistry from iron isotopes. *Annual Review of Marine Science*, *15*, 383-406.

Fitzsimmons, J. N., John, S. G., Marsay, C. M., Hoffman, C. L., Nicholas, S. L., Toner, B. M., ... & Sherrell, R. M. (2017). Iron persistence in a distal hydrothermal plume supported by dissolved–particulate exchange. *Nature Geoscience*, *10*(3), 195-201.

Horner, T. J., Little, S. H., Conway, T. M., Farmer, J. R., Hertzberg, J. E., Janssen, D. J., ... & GEOTRACES–PAGES Biological Productivity Working Group Members. (2021). Bioactive trace metals and their isotopes as paleoproductivity proxies: An assessment using GEOTRACES-era data. *Global Biogeochemical Cycles*, *35*(11), e2020GB006814.

Horner, T. J., Williams, H. M., Hein, J. R., Saito, M. A., Burton, K. W., Halliday, A. N., & Nielsen, S. G. (2015). Persistence of deeply sourced iron in the Pacific Ocean. *Proceedings of the National Academy of Sciences*, *112*(5), 1292-1297.

Jahnke, R. A. (1996). The global ocean flux of particulate organic carbon: Areal distribution and magnitude. *Global Biogeochemical Cycles*, *10*(1), 71-88.

Leinen, M., & Pisias, N. (1984). An objective technique for determining end-member compositions and for partitioning sediments according to their sources. *Geochimica et Cosmochimica Acta*, *48*(1), 47-62.

Martin, J. H., Knauer, G. A., Karl, D. M., & Broenkow, W. W. (1987). VERTEX: carbon cycling in the northeast Pacific. *Deep Sea Research Part A. Oceanographic Research Papers*, *34*(2), 267-285.

Reimann, C., Filzmoser, P., & Garrett, R. G. (2002). Factor analysis applied to regional geochemical data: problems and possibilities. *Applied geochemistry*, *17*(3), 185-206.

Resing, J. A., Sedwick, P. N., German, C. R., Jenkins, W. J., Moffett, J. W., Sohst, B. M., & Tagliabue, A. (2015). Basin-scale transport of hydrothermal dissolved metals across the South Pacific Ocean. *Nature*, *523*(7559), 200-203.

Volk, T., & Hoffert, M. I. (1985). Ocean carbon pumps: Analysis of relative strengths and efficiencies in ocean-driven atmospheric CO2 changes. *The carbon cycle and atmospheric CO2: Natural variations Archean to present*, *32*, 99-110.

Chapter 2. Constraining the margin organic C flux

Abstract

Organic carbon (OC) burial in marine sediments is the largest long-term sink of atmospheric CO_2 after silicate weathering. Understanding the mechanistic and quantitative aspects of OC delivery and preservation in marine sediments is critical for predicting the role that the oceans play in modulating past and future global climate. Yet, estimates of the global OC deposition in marginal settings span an order of magnitude, and the primary controls of OC preservation remain highly debated. Here, we provide the first global margin bottom-up estimate of OC deposition to marginal settings using literature data. We quantify both terrestrial- and marine-sourced OC fluxes and explore their relationship to bottom water oxygen concentrations. We find that the margins, which we define as having a water depth of less than 1,500 m, host 23.2 ± 3.5 Tmol OC deposition per year, with 71–97 % of a marine origin. Surprisingly, more than half of the global OC deposition occurs under bottom waters with O_2 concentrations greater than 180 μM. Less than 4% of OC deposition occurs in low-oxygen environments (<50 μM O_2), at odds with the current paradigm of bottom-water O_2 being the primary control on OC preservation. Our analysis reveals that, globally, just 2–3 % of OC produced in the surface ocean escapes remineralization during transit to the seafloor. This suggests that pelagic processes, such as OC production and remineralization, exert primary control on OC deposition.

1. Introduction

Nearly 40 % of global net primary production (NPP) occurs in the ocean, equivalent to the production of about 6,500 Tmol organic carbon (OC) yr^{-1} (Falkowski et al., 1998; Jin et al., 2006). Around 1,000 Tmol (15 %) of this OC is exported below the euphotic zone and an additional ~37.5 Tmol of terrestrial OC is delivered from continental environments via rivers (Galy et al., 2015; Hedges et al., 1997). Though much of this OC will be remineralized before it reaches the seafloor (Dunne et al., 2007; Jahnke, 1996; Martin et al., 1987), OC burial is thought to be one of two long-term sinks of atmospheric carbon dioxide (CO_2), the other being silicate weathering (Urey, 1952). Despite the importance of the OC sink, the magnitude and spatial pattern of OC deposition are poorly understood, particularly along the continental margins, where most OC burial is thought to occur (Burdige, 2007). In contrast, deep-sea OC burial (i.e., below 1,500 meters, or ~85 % of the ocean floor) is more easily quantified, but constitutes a small flux relative to that buried in marginal settings (Hayes et al., 2021).

The deposition and burial of OC in margin sediments is much larger than the flux to the deep sea for two main reasons: productivity and proximity. Marginal environments are, by definition, closer to the land, which can provide essential nutrients that can stimulate plankton growth (e.g., from coastal upwelling, terrestrial run-off, and sediment dissolution). Likewise, margin environments are shallower than the deep sea, meaning that there is a shorter transit distance for OC between where it is produced and where it is buried. Despite their importance to global C budget, OC fluxes to the margins are not well constrained (Table 1). The lack of constraints reflects, in significant part, the sparsity of measurements in margin environments relative to their high degree of heterogeneity. While it is possible to measure the flux of OC accumulating in any individual sediment sample, OC fluxes can vary greatly over relatively small distances due to variations in seafloor topography, water column oxygen concentrations, rates of nutrient-rich water mass upwelling, and ecological factors that affect export and remineralization (Hedges & Keil, 1995). While it is possible to derive a first-order estimate of margin OC fluxes using global sediment averages (Gershanovich et al., 1974), such estimates cannot account for regional variations in OC fluxes. Quantifying and understanding the spatial pattern of OC deposition and burial in margin sediments, therefore, requires alternative approaches that can account for regional heterogeneity.

Almost all published estimates of margin OC burial fluxes are based on 'top-down' approaches. Top-down approaches are popular because they offer granular information on OC burial fluxes, which is necessary to account for regional heterogeneity. Top-down models achieve this by using input data with a high spatial sampling density, such as sea-surface chlorophyll concentrations or temperature, which can be determined via satellite. Global OC burial can then be modeled by considering how much OC is produced (i.e., NPP), the fraction of OC that is exported out of the euphotic zone, and how much is transferred through the water column. These latter terms have been estimated using combinations of sediment trap data and benthic O_2 fluxes (Jahnke, 2010) or through empirical relationships derived from datasets of water column POC fluxes and sedimentation rates (Dunne et al., 2005, 2007; Lutz et al., 2002). While these approaches are valuable, they require explicit parameterizations of processes that may be poorly understood. As such, top-down estimates of global margin OC burial vary by almost a factor of 40 (Table 1).

Table 1. OC Flux Estimates from Literature

Burial Rate (Tg C yr^{-1})	Burial Rate Tmol yr^{-1}	Reference	Estimate Logic
62	5.2	(Muller-Karger et al., 2005)	Used satellite data and NPP estimates. The NPP estimates were attenuated with depth to the seafloor using standard models
2218	184.7	(Archer et al., 2002)	Diagenesis model was applied to a gridded map of OC rain rates across bottom water oxygen value
561	46.7	(Middelburg et al., 1997)	Used empirical relationships between remineralization rates and water depth (geometric mean was taken)
2481	206.6	(Middelburg et al., 1997)	Used empirical relationships between remineralization rates and water depth combined with arithmetic means (arithmetic mean)
213	17.7	(Muller-Karger et al., 2005)	The OC rain rate from this work was assumed to be the rate of marine organic matter input to sediments, and burial efficiency values taken from another study (Burdige, 2007; Muller-Karger et al., 2005). These were applied to these rain rates to estimate burial rates of marine organic carbon
577	48	(Burdige, 2007)	Estimated burial efficiency based on remineralization rates. Study assumed a steady-state OC budget.
248	20.6	(Burdige, 2007)	Same as above method, but estimate assumed relict sands do not accumulate very much TOC
145	12.1	(Hedges & Keil, 1995)	Estimate was recalculated from another reference (Berner, 1989)
218	18.2	(Gershanovich et al., 1974)	Average TOC content of Holocene sediments multiplied by their areal thickness
187.08	15.6	(Jahnke, 2010)	Regionally defined fluxes from oxygen fluxes and primary productivity
290.4	24.2	(Dunne et al., 2007)	Series of algorithms starting with satellite estimate of primary productivity, converted to a sinking particle flux, estimated penetration to the sea floor, and finally accumulation in the sediments
231.6	19.4	This study	Interpolation and extrapolation of OC deposition in sediments

The wide range of top-down OC burial estimates suggests that bottom-up approaches—those that leverage measurements of the sediments themselves—may also be valuable in constraining global OC fluxes. However, bottom-up approaches for measuring OC fluxes present several of their own challenges, such as: sparse input data, the need to differentiate different types of OC, and the very definition of burial. In general, there are far fewer measurements of OC fluxes than OC concentrations. As such, there are several studies that employed machine-learning and other statistical approaches to estimate sedimentary OC stocks (Atwood et al., 2020; Lee et al., 2019), but not OC fluxes. Where bottom-up estimates of OC fluxes do exist, these studies typically focus on specific regions with high data density, rather than extrapolating to all margins (Diesing et al., 2021; Smeaton et al., 2021). Another difficulty concerns the different types of OC present in marine sediments. Marine sedimentary OC often contains a mixture of autochthonous (produced in the ocean) and allochthonous OC formed in the terrestrial environment that is transported to the seafloor. This mixing of OC types necessitates that OC from terrestrial and marine environments be tabulated separately.

A final difficulty concerns terminology: what is OC burial? True burial refers to OC that is irreversibly stored in sediments below the depth of active degradation (Keil, 2015). Ideally, we want to quantify this flux of OC because material buried to this depth is entirely removed from the surficial C cycle. However, characterizing the burial flux at this horizon is difficult, because the true depth where OC remineralization is arrested is highly variable, and may not even exist (Bradley et al., 2022). Moreover, when constructing a bottom-up estimate using literature data without sediment or pore water information to assess the degradation of OC in the core, it is impossible to ensure that every datum is below the zone of active degradation. Given these limitations, we focus our study on OC deposition, which falls between the OC rain rate and the OC flux at the depth of irreversible burial. Thus, any bottom-up estimate of global OC deposition is likely to represent an upper limit of the true OC burial flux.

Here, we estimate margin OC deposition fluxes using a bottom-up, data-driven approach that leverages hundreds of sedimentary OC deposition fluxes from recent environments (i.e., Holocene; younger than 11,000 years before the present). Our estimate accounts for vertical and spatial variability in OC deposition along continental margins and takes advantage of geospatial interpolation methods. We interpolate and extrapolate over 700 OC deposition flux measurements for sediments deposited at water depths shallower than 1,500 meters and use these to construct a

global margin OC deposition flux. We combine our bottom-up estimate for the margins with existing OC burial flux compilations from the deep sea below 1,500 m to calculate a global sedimentary OC deposition flux for marine and terrestrial OC. Our marine flux offers a new means to calculate the efficiency of the biological carbon pump and has implications for the deposition of other biologically cycled elements. If additional data become available, especially around Australia, the Southeastern Atlantic, and the South China Sea, these can be incorporated into our calculations to improve the accuracy of our OC deposition flux estimate.

2. Materials and Methods

The workflow to estimate OC deposition flux included (i) compiling the data, (ii) categorizing the data based on type of OC (e.g., terrestrial or marine) and water depth overlying the sample, (iii) interpolating between points, (iv) extrapolating to cover each region, and (v) conducting regional specific analysis. These steps are described in detail below.

Sedimentary OC deposition flux data were compiled from the PANGEA database, Integrated Ocean Discovery Program (IODP) proceedings, and through literature searches (Table S1). Many of the compiled data possessed a mass accumulation rate (MAR); however, for samples without an associated MAR, we assumed a linear sedimentation rate between sediment data points in a core that had age and depth constraints and multiplied by the dry bulk density:

$$MAR = Sedimentation\ Rate\ (cm\ yr^{-1}) \times dry\ bulk\ density\ \left(\frac{g}{cm^3}\right) \quad (1)$$

This process resulted in a MAR for every sample. An OC deposition flux was obtained by multiplying by the OC content of each sample:

$$OC\ deposition\ flux = MAR\ (cm\ yr^{-1}) \times \frac{OC\ (wt.\%)}{100} \quad (2)$$

While total OC deposition fluxes are useful, they combine autochthonous OC produced in the ocean with allochthonous OC formed in the terrestrial environment and deposited in the ocean. Since the former is useful for assessing marine CO_2 removal, we split the data into two datasets to isolate samples that may have significant terrestrial OC influence. The first dataset included sediment samples with marine and terrestrial influence (Figure 1A; *n*=804), whereas samples that were strongly influenced by terrestrially sourced OC were removed from the second dataset

(Figure 1B; *n*=691). The terrestrial influence was assessed based on C/N ratios and $\delta^{13}C$ values. In general, terrestrial OC exhibits lower $\delta^{13}C$ compared to marine OC and has a higher C/N ratio. Terrestrial $\delta^{13}C$ generally ranges from −21 to −32 ‰ (Lamb et al., 2006). Similarly, the C/N values of terrestrial matter are typically greater than 10 (Lamb et al., 2006). To ensure the removal of terrestrial matter, data points with published C/N ratios higher than 8 or $\delta^{13}C < -23$ ‰ were eliminated from the "predominantly marine" dataset (Figure 1B). While this screening does not preclude all terrestrial organic matter from influencing our marine-dominated budget (e.g., terrestrial OC dominated by C4 plants), we argue that samples used in marine estimates and that fall outside all the terrestrial screening values (C/N<8 or $\delta^{13}C>-23$ ‰) likely have relatively minor terrestrial components. If a value was previously used in a marine estimate, it was left in the marine compilation regardless of whether it had published C/N or $\delta^{13}C$ values (Cartapanis et al., 2016; Hayes et al., 2021). While this method may have allowed some terrestrial influence, having more data with minimal terrestrial material (e.g., values that have been used in other marine compilations) will provide a more robust marine estimate than having fewer data.

After the initial data compilation, a map of seafloor topography (Smith & Sandwell, 1997) was loaded into ArcMap (Esri, Redlands CA) and projected so that each pixel had an equal area (1 km^2 pixel size; Figure 1A). The distinction between the continental margins and the deep sea was challenging to define due to the unique hydrography of each region. Previous studies have placed the boundary between the margins and the deep sea between 1,000 to 2,000 meters of water depth (Burdige, 2007; Hayes et al., 2021). Here, we defined the margin as having between 0 and 1,500 meters of overlying water depth. We chose not to include deeper depths because robust OC flux estimates for the deep ocean already exist (Hayes et al., 2021). Likewise, the deep-sea OC flux is small relative to the margins. Subsequently, we created two bathymetry bins (0-1,000 m and 1,000-1,500 m water depth) and the compiled sediment OC deposition flux data were loaded into ArcMap. Within each bin, the data were interpolated and extrapolated using inverse distance weighting (IDW), which produced a specific OC deposition flux for each pixel along the continental margins. This flux calculation method estimated individual cell values by averaging the sample points near the processing cell. The closer the point is to the processing cell, the more weight that point had in the averaging process. The significance that the nearest point has relative

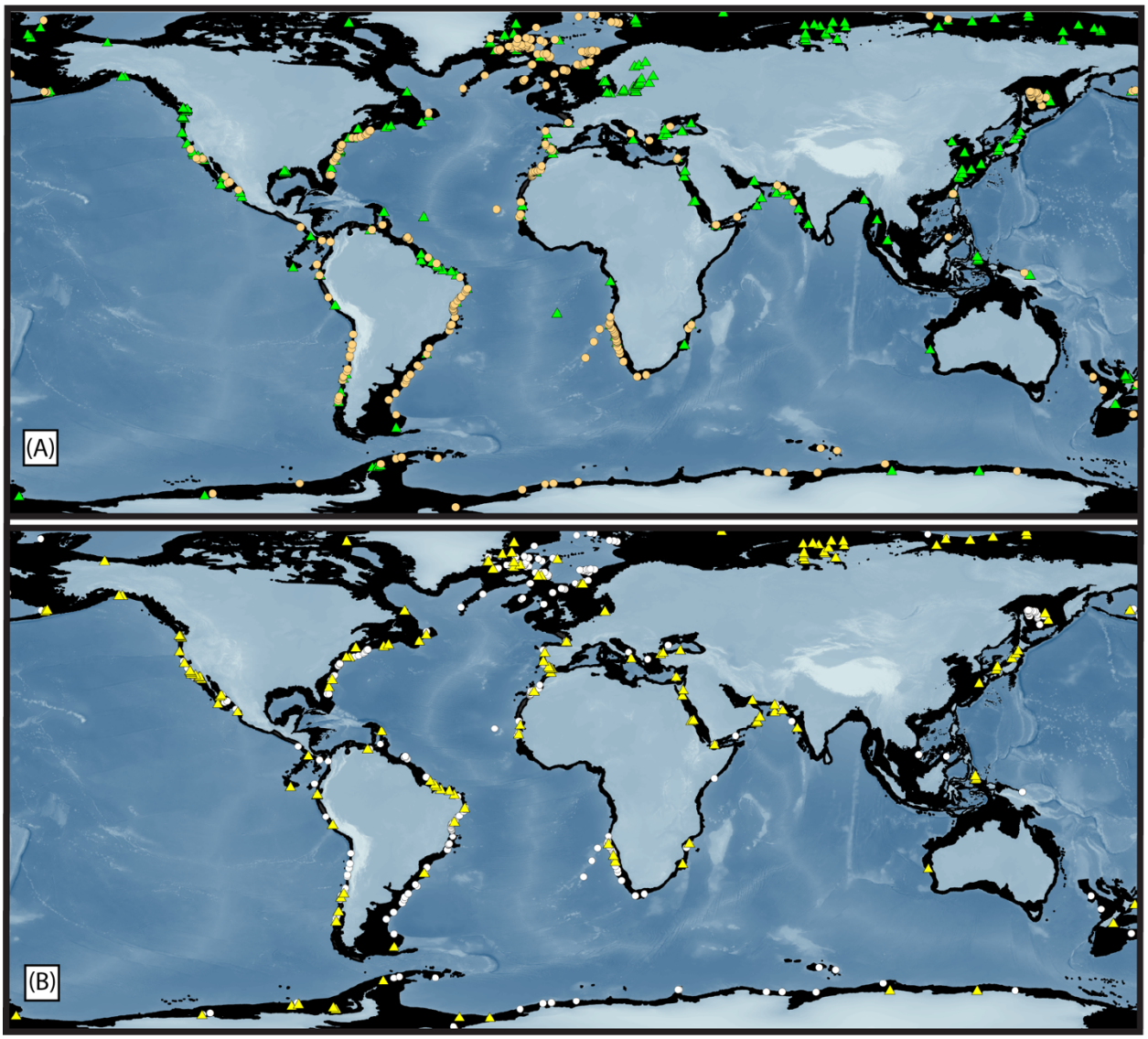

Figure 1. Global map of compiled sediments with OC deposition fluxes. Black regions show continental margins with bathymetry <1,500 meters. (A) shows samples that include both terrestrial and marine OC deposition fluxes. The triangles are data between 0-1000 meters and the circles are data between 1000-1500 meters. (B) Includes only sediments with marine-dominated OC. The triangles are data from 0-1000 meters and the circles are data from 1000-1500 meters.

Table 2. Combined marine and terrestrial OC fluxes

General Region	Figure Code	Area in km^2 (0-1000 meters)	Area in km^2 (1000-1500 meters)	Total area km^2	OC Flux (mol m^{-2} yr^{-1})	OC Flux Tmol yr^{-1}	Source
Northeast Pacific	a	5.74E+05	3.08E+04	6.05E+05	2.09	1.26	This study
Northeast Pacific	b	3.32E+05	6.96E+04	4.02E+05	2.04	0.86	This study
Northeast Pacific	c	2.16E+05	5.28E+04	2.69E+05	0.65	0.18	This study
Equatorial Pacific	d	3.43E+04	4.53E+04	7.96E+04	0.25	0.02	This study
Southeast Pacific	e	2.27E+05	6.63E+04	2.93E+05	0.86	0.25	This study
Southeast Pacific	f	2.66E+05	3.37E+04	3.00E+05	0.76	0.23	This study
Southwest Atlantic	g	1.79E+06	1.69E+05	1.96E+06	0.12	0.23	This study
Southwest Atlantic	h	6.50E+05	8.43E+04	7.34E+05	1.91	1.4	This study
West Equatorial Atlantic	i	2.94E+05	1.01E+05	3.95E+05	0.75	0.37	This study
Gulf of Mexico	j	1.02E+06	2.17E+05	1.24E+06	0.17	0.21	This study
Northwest Atlantic	k	1.79E+06	1.21E+05	1.91E+06	0.05	0.1	This study
Arctic	l	7.48E+05	2.36E+05	9.84E+05	0.62	0.61	This study
Northeast Atlantic	m	1.81E+06	3.52E+05	2.16E+06	0.55	1.2	This study
Northeast Atlantic	n	4.23E+05	8.50E+04	5.08E+05	0.72	0.37	This study
Southeast Atlantic	o	4.83E+05	9.44E+04	5.77E+05	0.21	0.12	This study
Southeast Atlantic	p	3.98E+05	5.98E+04	4.58E+05	0.16	0.07	This study
West Indian	q	4.82E+05	1.75E+05	6.57E+05	0.19	0.12	This study
Red Sea	r	3.99E+05	5.59E+04	4.55E+05	0.02	0.01	This study
Black Sea	s	2.08E+05	3.39E+04	2.42E+05	0.2	0.05	This study
West Arabian Sea	t	3.61E+05	2.65E+04	3.88E+05	0.46	0.18	This study
East Arabian Sea	u	4.47E+05	7.36E+04	5.21E+05	0.16	0.08	This study
Bay of Bengal	v	1.29E+06	2.31E+05	1.52E+06	0.59	0.90	This study
Australia (West)	w	5.81E+05	1.79E+05	7.60E+05	0.12	0.09	Jahnke
Australia (South)	x	5.75E+05	5.69E+04	6.32E+05	0.21	0.13	Jahnke
Australia (East)	y	7.20E+05	1.40E+05	8.60E+05	0.23	0.20	Jahnke
Australia (Tropical)	z	1.33E+06	2.49E+04	1.35E+06	0.25	0.34	Jahnke
West Equatorial Pacific	α	4.50E+06	5.07E+05	5.01E+06	1.05	5.24	This study
Northwest Pacific	β	2.03E+06	4.83E+05	2.51E+06	0.16	0.39	This study
Antarctic	δ	1.03E+06	5.81E+05	1.61E+06	0.54	2.35	This study
South Pacific	γ	4.03E+06	3.40E+05	4.37E+06	0.22	0.36	This study
Arctic	ε	8.11E+06	2.98E+05	8.41E+06	0.62	5.21	This study
Northeast Pacific	ζ	2.65E+04	2.78E+04	5.43E+04	0.06	0.02	This study
Mediterranean Sea	ϑ	1.07E+06	2.27E+05	1.30E+06	0.02	0.03	This study
Sum		3.82E+07	5.3E+06	4.35E+07		23.2	

to further ones is controlled by defining the "power". A higher power placed an additional emphasis on the nearest points and a lower power placed less emphasis on these points. We used a power of two (i.e., 1/distance^2) in ArcMap to process our data, meaning that a sample twice as far away from the target pixel than another sample would be weighted 4 times less. By default, ArcMap interpolates over the data within a minimum spatial bounding box that encompasses all the data. However, this does not allow ArcMap to produce a map that covers the entire region of interest. Thus, we created a bounding box using extrapolation that is larger than the minimum spatial bounding box and covered the entire region. To do this, the processing extent box was set to the size of each region of interest (Table 2). Extrapolated OC fluxes were bounded by the values encountered in that region; extrapolations could not yield OC deposition fluxes that were more (or less) than the largest (or smallest) observed OC deposition fluxes within the bounding box. Once every pixel had a defined flux, the pixels were then summed to produce a total OC deposition flux for the defined area.

The spatial binning reveals sampling biases. Some regions are data-dense and are presumed to give the most accurate interpolations. Conversely, some areas have too little data to interpolate. Therefore, we divided the margin into 30 distinct regions, which constrained the distance over which any individual datum can be interpolated within that region. For each region, we assessed if alternative methods were required to obtain the most robust OC burial flux. These methods either used the higher-density data within one bathymetric bin to extrapolate a flux to the other bin or, in a few cases with particularly poor data coverage, adopted previous estimates from the literature. These details are included in the results and discussion. A complete ArcMap workflow can be found within the supplementary information.

3 Results and Discussion

Here we explore the results of four flux calculation methods to estimate OC deposition from global sedimentary samples (Figure 1). In order of increasing robustness, we refer to these four OC deposition flux estimates as: unconstrained (3.1.1.); bathymetrically-constrained (3.1.2.); regionally- and bathymetrically-constrained (3.1.3.); and regionally-, bathymetrically-, and genetically-constrained (3.1.4.; i.e., whether OC is of terrestrial or marine origin).

3.1. Organic carbon deposition along the continental margins

3.1.1. Unconstrained flux estimate

Our most straightforward flux calculation considered all data between 0 and 1,500 meters and interpolated and extrapolated globally to all margins. This flux calculation method yielded a flux of 38.9 Tmol OC yr^{-1}. However, the unconstrained method revealed a fundamental limitation. Depending on data density in a region, unrepresentative OC deposition fluxes may be vertically extrapolated over the entire slope. Since OC arriving to the seafloor strongly attenuates with depth, vertical extrapolation too far from the original sample may yield unreasonably high (or low) deposition fluxes for the margin. This effect is particularly problematic if most of the data from a region used in flux calculation are from a single shallow (or deep) water depth. Therefore, it was necessary to add a bathymetric constraint to our calculation.

3.1.2. Bathymetrically constrained flux estimate

We employed a second interpolation method to account for the depth dependence of marine OC burial flux attenuation. We created the bathymetry bins by clipping based on the bathymetry from Smith & Sandwell (1997). This method divided the data into two bins: 0–1,000 meters and 1,000–1,500 meters. This grouping limited the effects of the deepest points from being extrapolated up the margins and artificially depressing the margin flux. Similarly, it prevented the shallow points from being extrapolated far down slope, which would artificially inflate the margin fluxes. By increasing the number of depth bins, we reduced vertical extrapolation, though this came at the cost of diminishing data density in certain bins in several regions. We recognize that more bins would be preferable, but this would only be possible if more data were available. Two depth bins optimized this tradeoff between bathymetry and data density. Using these two bins, the estimated OC depositional flux significantly increases relative to the flux calculation without bins. In the 0–1000-meter bin, our flux calculation yielded an OC deposition flux of 41.7 Tmol C $yr^{-1,}$ and in the 1000–1500-meter bin 0.6 T mol C yr^{-1}. Thus, the total OC deposition flux with this method is 42.3 Tmol C yr^{-1}. The overall increase in OC deposition flux suggests that the unconstrained flux estimate tended to extrapolate upslope more often than downslope, thus artificially depressing the OC deposition flux. However, this method still has several limitations that impact the accuracy of the results. As with the unconstrained method, this approach cannot differentiate OC deposition fluxes by region. Therefore, regions with low data density will include extrapolated flux values from hydrographically unrelated environments. For example, in this method, the Gulf of Mexico is significantly influenced by the California margin due to their

geographic proximity, even though they are hydrographically dissimilar. This effect is most pronounced if the nearest data exhibit extremely high or low flux estimates, or if few data points define a region with a large areal extent, or if there is a thin land barrier separating ocean basins. For example, high terrestrial fluxes from the Arctic may be interpolated far away from the terrestrial inputs and thus artificially increase the OC global estimate. Therefore, while this binning approach does address the role of OC depositional flux attenuation, additional samples are required to account for regional variability.

3.1.3. Regionally and bathymetrically constrained flux estimate

To mitigate any interpolation or extrapolation in between hydrographically distinct regions, we performed a third flux calculation whereby we divided the global margins into 30 regions based on geography, hydrography, and data density for a total of 60 bins (Figure 2). We suggest this method best reflects OC deposition across the margins. Regions were defined as close as possible to those defined in a previous study (Jahnke, 2010), where the margins were separated into five categories: polar, subpolar, monsoonal, tropical, eastern boundary current, and western boundary current. The polar regions, which include the Arctic and the region near Antarctica, were defined by ecosystems that have extreme seasonality (e.g., light limitation and have ice-cover for a significant part of the year). The sub-polar margins are in the high-latitude regions, which lie between the polar regions and the east and western-boundary current regions. The Western and Eastern Boundary currents are regions where water flows parallel to the margins, where west coast margins are characterized by upwelling and oxygen minima. Both have strong boundary currents. The monsoonal margins are regions that are affected by monsoonal wind patterns. Here, and in (Jahnke, 2010), the monsoonal margins are only based in the Northern Indian Ocean. Finally, the tropical margins are simply located at the low latitudes, and are found roughly between 15˚ S and 15˚ N. For a detailed breakdown of these regions, the reader is referred to Jahnke (2010).

After breaking our margin area into these five categories, we considered data density in defining our regions. For example, instead of grouping the coast of western North America as the same eastern boundary current area, we split our dataset into three regions—the Gulf of Alaska, California margin to Canada, and Mexico to Panama. These splits are possible because of the higher data density in these regions. Additionally, regions with low data density were necessarily defined by the location of samples. Once the region and bins were defined, we interpolated OC

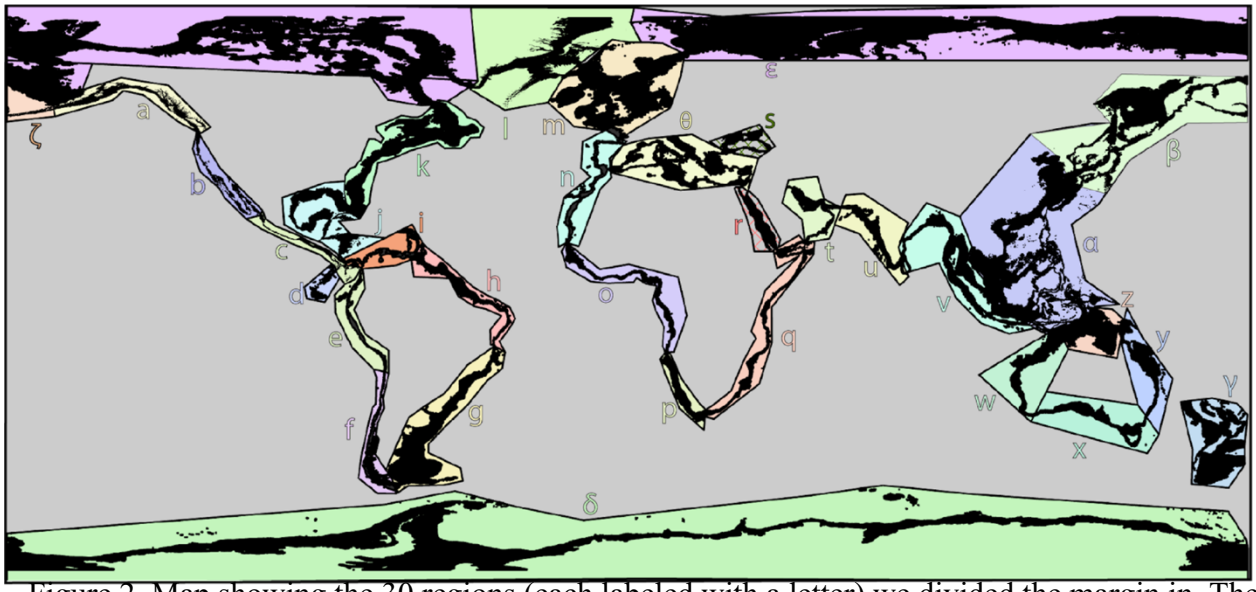

Figure 2. Map showing the 30 regions (each labeled with a letter) we divided the margin in. The black area is the seafloor from 0–1500 meter water depth. The colored part around each region illustrates where the boundaries of the regions are. Each region is given a letter so that it can be referred to more easily without depending on the names of landmass.

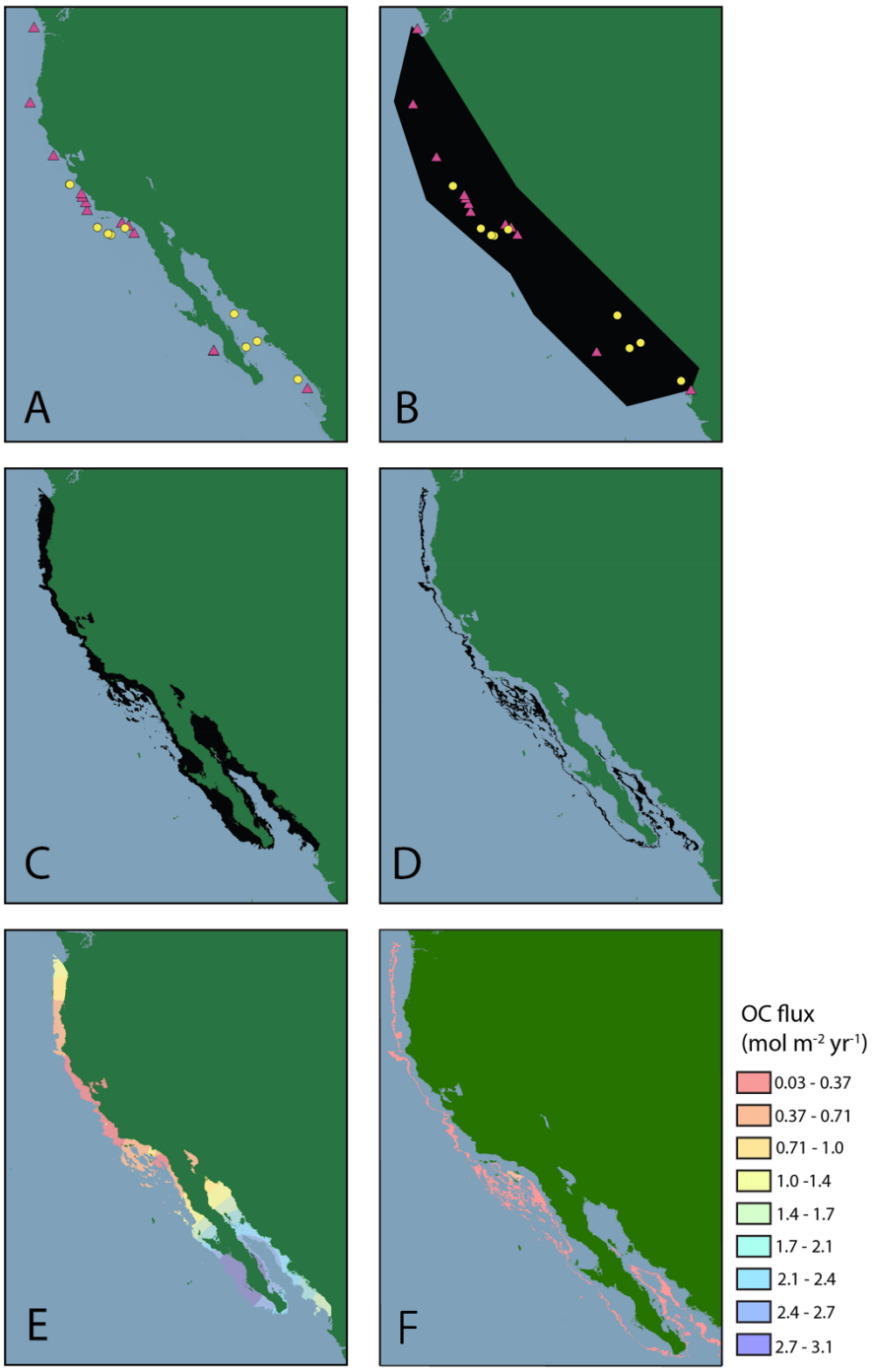

Figure 3. Maps of the California Margin (region b) illustrating the workflow of creating depth bins and the result of interpolating between data points. (a) Pink triangles indicate data between 0-1000 m water depth and yellow circles are between 1000-1500 m. (b) Regions of interest clipped around the data (c) Seafloor area from 0-1000m water depth within the regionally clipped area (d) Seafloor area from 1000-1500m water depth within the regionally clipped area (e) Interpolated OC fluxes within the 0–1000-meter depth bin (f) Interpolated OC fluxes within the 1000–1500-meter depth bin. Final values were ascertained by summing the fluxes in each region. This process was repeated for each region of interest.

deposition fluxes separately within the two bins in each region (e.g, 0-1,000 meters and 1,000-1,500 meters). We summed these values for the final OC deposition flux and repeated the steps for each of the 30 regions. The steps from defining regions, bathymetry, and interpolation are shown in Figure 3 (A-F). Thus, we achieve a regional and margin-wide flux (Table 2). This regionally and bathymetrically constrained flux method is our preferred approach as it accounts both for bathymetry and ensures that extrapolations do not occur across dissimilar regions. This method yields a global OC deposition of 23.2 ± 3.5 Tmol yr^{-1}.

3.1.4. Regionally and bathymetrically constrained flux estimate for marine OC

Our bottom-up approach considers the OC that is incorporated into seafloor sediments, not what is predicted to arrive from top-down estimates of OC produced in surface marine environments. However, this includes OC produced autochthonously and OC formed on land that is ultimately buried in the ocean . The autochthonous fraction is the fraction that matters for constraining the magnitude and efficiency of the ocean's biological pump, whereas the allochthonous fraction does not. In this fourth method, we separated the fraction of OC deposition due solely to marine production from the terrestrial inputs, thus allowing us to estimate the carbon flux associated with the marine biological pump. As described in detail in the methods section, we filtered out sediments with a measured C/N ratio above 8 or a value of $\delta^{13}C$ that implies a significant component of terrestrial material (i.e., $\delta^{13}C < -23$ ‰). While this method allowed for a more accurate estimation of marine OC deposition fluxes, the screening removed around 15 % of the data, thus leading to regions with insufficient data in either the deep (1,000-1,500 m) or shallow (0-1,000 m) bins to interpolate within each region. We leveraged the patterns observed in high-data-density regions to make a marine OC deposition flux estimation in these low-data-density bins. We selected six regions with high density data coverage, contrasting hydrography, and water column OC flux attenuation and evaluated how the deep and shallow bins were compared. The six regions we examined in detail were located in the Northeast Pacific (Region b), the Southeast Pacific (Region f), the Northwest Atlantic (Region k), the Northeast Atlantic (Region n), and the Arctic (Regions ε and l; e.g., Table 3).

We observe that the ratios of deposition flux between the shallow and the deep bin in all our test sites are similar and have values of 7.8 to 16.4 (Table 3) regardless of the substantial differences in NPP, and potential remineralization rates and OC preservation between low- and well-

oxygenated regions. We can use the systematic differences in OC deposition rates with water depth to estimate OC deposition fluxes in regions where only one of our two bins has sufficiently dense data coverage to allow for a robust estimation. We achieved this by using a Monte Carlo method to determine the relationship between the shallow and deep bins within data-dense regions. First, we randomly delete two data points from the shallow depth bin, while leaving all of the deep depth fluxes undisturbed. Then to account for uncertainty in the deposition fluxes in the remaining shallow values, we randomly assign a new deposition flux estimate that is within 15 % of the reported deposition flux. We choose 15 % to account for uncertainties in the MAR and OC (%) measurements in the data, which we used to estimate OC deposition fluxes. It is challenging to predict the uncertainty in the MAR and OC (%) values from the literature. Many of the studies used in this data compilation reported estimated MAR uncertainties of around 15 %. Once we assign uncertainties to the remaining four shallow values, we use the data points to estimate the two missing shallow bin values. This process is repeated 500,000 times for the shallow bin. Then, the entire process is completed for a scenario that removes data from the deep bin. Finally, we plot the average predictions and their uncertainties against the known values (Figure 4). We find that our predicted values reproduce the true values within uncertainty and the bootstrapped data consistently predicts that the average ratio of shallow-to-deep fluxes is 12.7 ± 1.1 (1SD, Figure 4). Finally, because these regions cover a broad range of depositional environments, we infer that this method allows us to estimate the OC deposition fluxes to the first order with associated uncertainties. To check that this estimated ratio and associated uncertainty was not simply reflecting the prescribed 15 % uncertainty, we bootstrapped the raw data for the six test sites without assigning uncertainties. Here, we found that the average ratio was 12.6 ± 1.2 (1SD), which is identical, within uncertainty, of the Monte Carlo method.

Finally, to account for uncertainties in high-density data areas where applying a ratio is not needed, we apply a 15 % uncertainty on each deposition flux estimate. To estimate the uncertainties in the fluxes ascertained by the ratio method, we estimate a minimum and maximum flux with a ratio of 12.7 ± 1.1 (1SD). Thus, using our ratio approach, the regional, binned interpolation considering only marine-dominated samples gives an OC deposition flux between 16.4 and 22.5 Tmol yr^{-1}. Our average value, which uses a ratio of 12.7 and the measured flux estimates without the associated 15 % uncertainty is 19.4 T mol yr^{-1}. Thus, the marine flux

Table 3. Regions with high marine data density

Coastal Region	Basin	Total Area (km^2)	Total area (km^2) 0-1000 meters	Total Area (km^2) 1000-1500 meters	Deposition Rate (mol m^{-2} yr^{-1}) 0-1000 meters	Deposition Rate (mol m^{-2} yr^{-1}) 1000-1500 meters	Total Deposition Tmol OC yr^{-1}	Ratio
b	NW Pacific	4.20E+05	3.32E+05	8.90E+04	1.51	0.13	0.51	11.44
f	SW Pacific	3.10E+05	2.66E+05	3.37E+04	0.85	0.06	0.23	13.60
k	NW Atlantic	1.70E+06	1.79E+06	1.21E+05	0.08	0.01	0.14	7.80
ε	Arctic	8.41E+06	8.11E+06	2.98E+05	0.39	0.03	3.16	14.09
l	Arctic	9.84E+05	7.48E+05	2.36E+05	1.19	0.10	0.91	11.34
n	NE Atlantic	5.08E+05	4.23E+05	8.50E+04	0.86	0.05	0.37	16.44

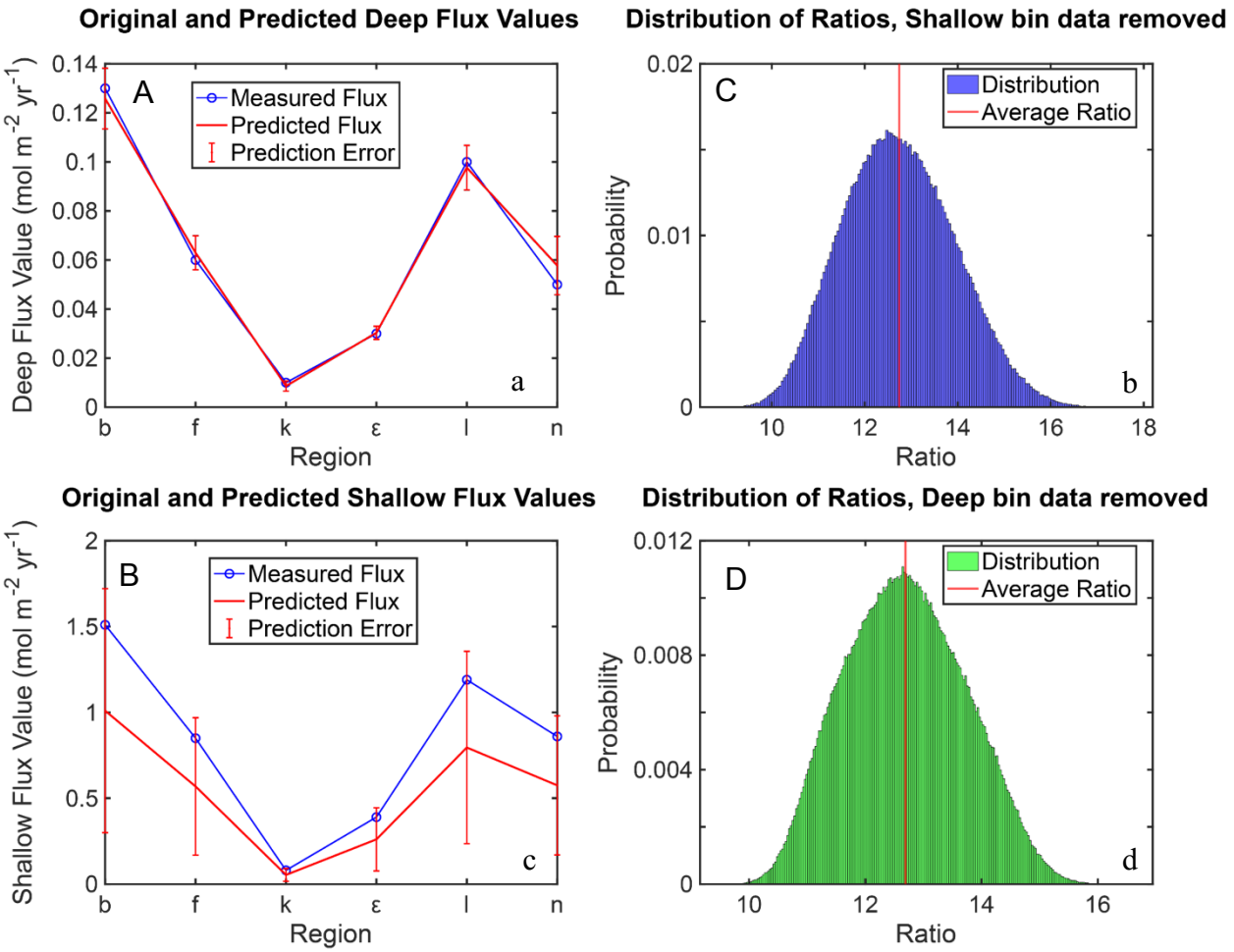

Figure 4(a-d). Uncertainty analysis on the ratio extrapolation method. Panels a and c show the measured flux from the test sites against the predicted values when they are removed and subsequently predicted using the relationships in the remaining data. Panels b and d show a histogram of the distribution of the ratios between the shallow and the deep bins. The average ratio is 12.7 with a standard deviation of 1.1 (n=500,000)

Table 4. Marine-only OC flux

General Region	Figure Code	Area in km² (0-1000 m)	Area in km² (1000-1500 m)	Max Flux (mol m^{-2} yr^{-1})	Min Flux (mol m^{-2} yr^{-1})	Max Tmol yr^{-1}	Min Tmol yr^{-1}	Method	Bin with sufficient data density
Northeast Pacific	a	5.74E+05	3.08E+04	2.28	1.69	1.38	1.02	Ratio	0-1000
Northeast Pacific	b	3.32E+05	6.96E+04	1.46	1.08	0.59	0.43	Binned	
Northeast Pacific	c	2.16E+05	5.28E+04	0.81	0.60	0.22	0.16	Ratio	0-1000
Southeast Pacific	e	2.27E+05	6.63E+04	2.04	1.27	0.60	0.37	Ratio	1000-1500
Southeast Pacific	f	2.66E+05	3.37E+04	0.88	0.65	0.26	0.19	Binned	
Southwest Atlantic	g	1.79E+06	1.69E+05	0.26	0.16	0.51	0.32	Ratio	1000-1500
Southwest Atlantic	h	6.50E+05	8.43E+04	0.23	0.14	0.17	0.10	Ratio	1000-1500
W.Equatorial Atlantic	i	2.94E+05	1.01E+05	0.17	0.17	0.07	0.12	Jahnke	NA
Gulf of Mexico	j	1.02E+06	2.17E+05	0.17	0.17	0.28	0.28	Jahnke	NA
NW Atlantic	k	1.79E+06	1.21E+05	0.08	0.06	0.16	0.12	Binned	
Arctic	l	7.48E+05	2.36E+05	1.07	0.79	1.05	0.78	Binned	
Northeast Atlantic	m	1.81E+06	3.52E+05	0.17	0.10	0.36	0.23	Ratio	1000-1500
Northeast Atlantic	n	4.23E+05	8.50E+04	0.83	0.61	0.42	0.31	Binned	
Southeast Atlantic	o	4.83E+05	9.44E+04	0.51	0.51	0.22	0.22	Jahnke	
Southeast Atlantic	p	3.98E+05	5.98E+04	0.60	0.38	0.28	0.17	Ratio	1000-1500
West Indian	q	4.82E+05	1.75E+05	1.46	0.91	0.96	0.60	Ratio	1000-1500
Red Sea	r	3.99E+05	5.59E+04	0.02	0.01	0.01	0.01	Ratio	0-1000
Black Sea	s	2.08E+05	3.39E+04	0.24	0.18	0.06	0.04	Ratio	0-1000
West Arabian Sea	t	3.61E+05	2.65E+04	0.25	0.19	0.10	0.07	Ratio	0-1000
East Arabian Sea	u	4.47E+05	7.36E+04	1.57	0.98	0.82	0.51	Ratio	1000-1500
Bay of Bengal	v	1.29E+06	2.31E+05	0.19	0.14	0.29	0.21	Ratio	0-1000
Australia (West)	w	5.81E+05	1.79E+05	0.12	0.12	0.09	0.09	Jahnke	NA
Australia (South)	x	5.75E+05	5.69E+04	0.21	0.21	0.08	0.08	Jahnke	NA
Australia (East)	y	7.20E+05	1.40E+05	0.23	0.23	0.2	0.20	Jahnke	NA
Australia (Tropical)	z	1.33E+06	2.49E+04	0.25	0.25	0.45	0.45	Jahnke	NA
W Equatorial Pacific	α	4.50E+06	5.07E+05	0.88	0.65	4.40	3.25	Ratio	0-1000
Northwest Pacific	β	2.03E+06	4.83E+05	0.63	0.39	1.59	0.99	Ratio	1000-1500
South Pacific	ɣ	1.03E+06	5.81E+05	0.26	0.19	0.42	0.31	Binned	
Antarctic	δ	4.03E+06	3.40E+05	0.63	0.46	2.73	2.02	Binned	
Arctic	ε	8.11E+06	2.98E+05	0.43	0.32	3.64	2.69	Binned	
Northeast Pacific	ζ	2.65E+04	2.78E+04	0.02	0.01	0.00	0.00	Ratio	0-1000
Mediterranean Sea	ϑ	1.07E+06	2.27E+05	0.05	0.03	0.06	0.04	Binned	
Sum						**22.45**	**16.40**		

accounts for the majority of total OC deposition (i.e., marine *and* terrestrial OC). The fluxes for each region are given in Table 4. As a check, we compare one of the flux estimates we ascertained using the ratio value to a recent paper, which estimated the OC accumulation flux in the North Sea from a machine-learning method (Diesing et al., 2021). This study suggests that 0.12 ± 0.17 Tmol r C yr^{-1} reaches the sediment in the North Sea and Skagerrak, although the authors argue that most of the deposition occurs in the Norwegian Trough. If we use our mean deposition flux estimate in this region (e.g., region m, ratio at 12.7, 0.14 mol m^{-2} yr^{-1}) and apply it to the area covered in that study (e.g., ~560,000 km^2), we get an estimate of ≈0.08 Tmol C yr^{-1}, which is in good agreement with (Diesing et al., 2021). Furthermore, it is important to note that each of these regional environments has important geographic textures to consider (Diesing et al., 2021). The North Sea shows heterogeneous OC arrival to the seafloor across the region (Diesing et al., 2021). However, despite this heterogeneity, our methods are still able to replicate the detailed regional estimate.

3.2 Quantifying uncertainties and utility of the carbon flux estimate

While our bottom-up approach has several benefits over previous top-down estimates of OC deposition, there are limitations. These include potential oversampling of unrepresentative regions, low data density from areas underlying very shallow water depths, OC deposition flux attenuation with sediment age, challenges in assigning uncertainty values, and inability to account for all processes. We explore these limitations and suggest that while these uncertainties will affect the *precision* of our estimates, they will have a minimal effect on the *accuracy* of our results.

3.2.1 Sample site bias

Study site selection is often driven by the desire to study specific phenomena (e.g., low-oxygen environments, upwelling, cross-shelf transport, ecology). Therefore, regions hosting certain phenomena may be overrepresented in our sample compilation. Constraining the uncertainty caused by this limitation is challenging since several factors determine site selection. However, when we compare the distribution of raw OC deposition flux data versus bottom water oxygen, one phenomenon we expected to potentially be oversampled, we find that the distribution is extremely similar (Figure S1). Additionally, we observe OC deposition flux follows anticipated trends: water depth is the dominant control over OC deposition fluxes. Thus, while we recognize

that a bias toward regions with unique depositional environments may influence our margin flux value, we do not see evidence for sample bias that influences the raw or extrapolated values.

3.2.2 Bathymetry, attenuation of OC deposition with depth, and areal extent of coverage

We recognize that a significant fraction of our compiled data comes from sediments underlying water columns deeper than 700 meters. Pelagic OC fluxes generally attenuate according to a power law as a function of water depth (Martin et al., 1987; Eq. 3). Thus, we may be underestimating the marine OC deposition flux to the margins by having only relatively few data from shallower water depths. If this problem were to persist in the sample sites, it could lead to OC deposition fluxes in shallow waters that are too low. This would result in an underestimate of the global marine OC deposition flux. However, the closer marine sediment gets to shore, the more sediment transport processes occur, including lateral advection. More terrestrial sourced material is also likely to be observed in this area, which may also artificially elevate the marine OC flux. Thus, even if we had more OC measurements closer to the continent, they would be exposed to additional physical processes that may not represent long-term deposition flux of marine organic matter (Dunne et al., 2007). For these reasons, it is not straightforward to determine if more sediment data from shallow water depths would increase overall confidence in the global OC deposition flux.

To explore the general character with which the sediment OC flux data are attenuating, we first calculated the best-fit *b* for the entire dataset. We perform this estimate to determine whether our core-top estimates faithfully represent the accumulation rate we might expect. This was achieved by log-transforming the OC deposition flux data and plotting as a function of depth. The OC flux at each depth was predicted using John Martin's iconic power-law function:

$$F = F_{100}\left(\frac{z}{100}\right)^{b} \quad (3)$$

We use the flux data from Figure 5d and set F_{100} equal to the top bin (e.g., 7.6 Tmol yr^{-1} in the 0-100 meter OC deposition flux) and solve for *b* for each depth. This exercise reveals a best-fit *b* of −1.3, which is within the range of −2.1 to −0.3 reported for sinking organic matter

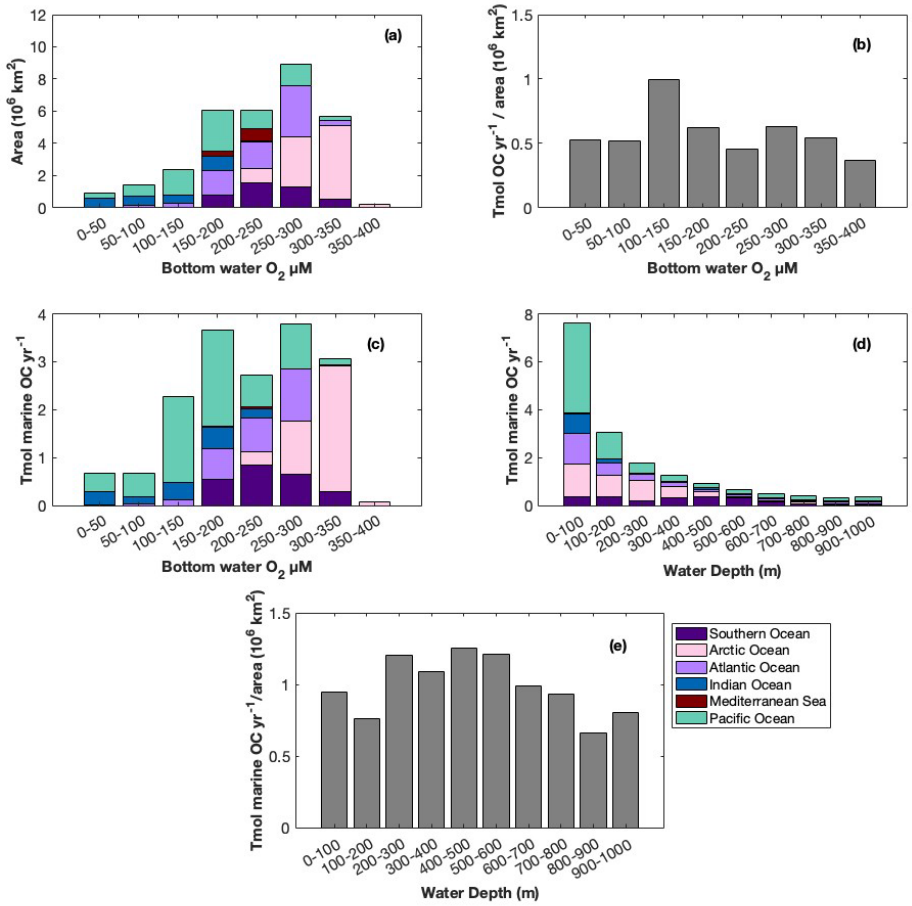

Figure 5: (a) shows the area of the seafloor in km^2 that falls under the O_2 bottom water bins, (b) shows the OC deposition per unit area in each O_2 bottom water bins on the global scale, not broken into region for ease of reading, (c) shows the total OC deposition for each O_2 bottom water bins, (d) shows OC deposition as a function of water depth above the sediment, and (e) shows the the OC deposition per unit area in each bathymetry bottom water bins on the global scale, not broken into region for ease of reading.

attenuation in the Atlantic, Indian, and Pacific Oceans (Buesseler et al., 2007; Martin et al., 1987; Rosengard et al., 2015). It is important to note that this OC flux from the water column is distinct from the deposition flux. However, deposition flux is, in large part, determined by how much OC arrives on the seafloor. Thus, we would expect the OC deposition flux to attenuate in a similar manner to that in the water column. Although this first approximation makes it appear that our OC is arriving to the seafloor as expected, further exploration suggests that our binning techniques impart an artifact. This artifact comes from the low data density and sampling bias that puts more data in the deeper bins coupled with the geography of the continental margin. Specifically, along the margin there is a greater areal extent of regions that underlie shallower water waters (the shelf) than deeper water depths (the slope and rise). Therefore, our approach likely attributes more area, and thus a higher OC deposition, onto the shelf. More bathymetric bins are needed to access whether OC fluxes are attenuating according to a power law.

3.2.3 Carbon deposition flux as a function of sediment age and oxidation processes

In this study, we only included sediment cores deposited during the Holocene (i.e., 0-11 kyr BP), which serves to eliminate the large changes in productivity and bottom-water conditions associated with the last glaciation and deglacial period (Jaccard & Galbraith, 2012). Although accumulation rates at any site may have changed somewhat over the Holocene, this period was generally stable with a climate relatively similar to modern and only minor changes in sea level (Stanford et al., 2011). Furthermore, we purposefully selected sediment cores with ages as close to modern as possible: core top and late Holocene were selected when data were available. By trying to ensure the samples were selected from the late Holocene, we assume that the rates of marine OC and terrestrial OC are similar to modern accumulation rates.

Another potential issue with using samples deposited within a relatively broad timeframe is that the organic carbon in the sediment will have been exposed to oxidation for variable amounts of time. These effects are particularly important where sediment oxygen penetration goes beyond the upper few centimeters. In these environments, the organic carbon in older sediment that has experienced oxidation for longer may better represent long-term OC burial, while OC in younger sediment may represent the flux of organic carbon to the seafloor, not what is ultimately buried there. As noted previously, our estimate of OC deposition likely represents the upper limit of the burial flux and does not account for when post-depositional remineralization ends. For these reasons, our OC deposition estimate likely represents a value between the rain rate and the long-

term burial flux. The best way to determine true OC burial would be to integrate OC burial fluxes over the last 11,000 years before the present. Unfortunately, this would require that every sample had an OC accumulation rate estimate for the entire period, which is not the case. As a mitigating factor, we note that oxygen penetration depth on continental margins is typically <5cm (Cai & Sayles, 1996). We infer that for the samples with an estimated linear sedimentation rate (approximately half of our samples), 90% of post-depositional respiration of oxic remineralization is limited to sediment 750 years before the present. At the very least, that means that the majority of our samples are no longer exposed to oxic remineralization.

3.2.4 Why inverse distance weighting (IDW) over other interpolation and extrapolation methods?

In this study we used inverse distance weighting to generate maps of OC deposition. While more advanced methods have been used in other studies to estimate OC accumulation or OC inventories in marine sediments (Atwood et al., 2020; Diesing et al., 2021; Lee et al., 2019; Smeaton et al., 2021), we believe that these methods are not good candidates for estimating global OC deposition fluxes along continental margins, at least for the time being. Broadly, these other studies were able to employ more advanced geostatistical techniques either because their datasets were made up of thousands of observations, and thus good candidates for machine learning, or because the datasets were in a specific region where a lot of information was available for each sample. Datasets that are hyper-regional can provide the many predictor variables (tidal speed, peak orbital velocity, the content of mud, gravel, and sand in the sediment, etc.) to model OC stock or OC burial/deposition within the sediment. But, while it is possible to have a robust set of predictor variables in a regional environment, such a compilation is currently impossible on a global scale. Thus, even though simple interpolation and extrapolation methods like inverse distance weighting have been associated with high uncertainties (Li & Heap, 2008), we contend that IDW is the best way to estimate fluxes in our case.

Indeed, one of the critical findings of this study is to illustrate how few OC deposition flux measurements exist. To get a better estimate of marine OC carbon deposition flux, the community needs more OC deposition measurements across the margin, not more sophisticated interpolation. Indeed, it is unlikely that model refinements can overcome the low data density limitation.

3.3. Synthesis and implications

3.3.1. Comparison with existing flux estimates

Our regionally and bathymetrically constrained margin flux estimate places total OC deposition between 16.4–22.5 Tmol OC yr^{-1}. This compares well with several top-down estimates established by previous studies of 24.2 and 15.6 Tmol OC yr^{-1} (Dunne et al., 2007; Jahnke, 2010). The convergence of these estimates bolsters our confidence that the uncertainties inherent to each approach do not compromise the ability to determine an accurate OC deposition flux to recent sediments. The accuracy of our estimate is ultimately limited by the number of OC deposition flux data in this compilation. Additional sediment samples will bolster confidence in our results.

3.3.2. Efficiency of the biological carbon pump

We can use our organic carbon flux to determine the overall long-term (i.e., millennial) efficiency of the marine biological carbon pump. This calculation is based on the fraction of NPP that reaches the seafloor rather than nutrient use efficiency (as in Volk & Hoffert, 1985). Marine biogeochemical models estimate that between ~800–850 Tmol C yr^{-1} are exported as particulate OC below the euphotic zone (Jin et al., 2006; Nowicki et al., 2022), which is roughly equivalent to current anthropogenic CO_2 emissions of ≈800 Tmol C yr^{-1} (Friedlingstein et al., 2022). Using our margin OC deposition flux estimate of $19.4^{+3.1}_{-3.0}$ Tmol marine-derived OC yr^{-1} and combining with OC deposition fluxes in the deep sea of 1.7 ± 0.5 Tmol C yr^{-1} (Hayes et al., 2021), we obtain a total flux of between 21.1 ± 3.1 Tmol OC yr^{-1}. Thus, we calculate that between 2.3–3.0 % of the organic matter exported below the euphotic zone escapes remineralization and is ultimately buried.

3.3.3 OC deposition flux as a function of oxygen bottom water and water depth

We explore whether the bottom water oxygen concentration plays an important role in determining the global sediment OC deposition flux magnitude and efficiency. In Figure 5, we compile our calculated amounts of OC deposition flux within different ranges of bottom water O_2 concentration and water depth. This allows us to identify the areas in the ocean with the highest sedimentary OC deposition fluxes. We use the deepest oxygen concentration measured in the 2018 World Ocean Atlas to first approximate the bottom water concentration on a 1 x 1˚ grid. We then

extrapolated these oxygen concentration values to align them with our OC deposition fluxes on a 10 by 10 km^2 grid, which was corrected for an equal area spherical projection. Interpolating the WOA18 oxygen data allows us to have a paired bottom water O_2 estimate for each OC deposition flux estimate. It is important to note that some of our regions are not included in the OC deposition flux versus O_2 concentration because there is not a high enough data density to extract OC deposition fluxes on a 10 by 10 km^2 grid. Regions d, o, s, w, x, y, and z, shown in Figure 2, do not have enough data in the 0–1000-meter bin to interpolate the OC deposition flux. Therefore, these regions are not included. However, these regions have overall low OC deposition fluxes and should not substantially change the observed trend. Thus, only 17 Tmol OC yr^{-1} (~88 % of global burial flux) are accounted for in this section.

We find that 43 % of OC deposition flux along the margins occurs in regions that have a bottom water concentration lower than 200 μM and approximately 57 % of OC deposition flux occurs in regions that have a bottom water content between 200 and 400 μM (Figure 5c). Most of the OC deposition flux that occurs under these higher oxygen conditions occurs in the Arctic and Southern Oceans. Regions with <50 μM O_2 at the sediment–water interface only account for <4% of global margin OC deposition (Figure 5c).

We examine OC deposition flux under a range of redox conditions and compare the fluxes to what would be expected if the areal extent of each redox environment alone controlled how much OC was deposited in a region (Figure 5a-d). Figure 5b shows that regions underlying 100-150 μM O_2 have the highest OC deposition relative to unit area. We do not see significant evidence to suggest that OC deposition is focused in the low-oxygen regions, as has been previously suggested. Instead, all of the regions appear to have a similar OC deposition when normalized by area. This distribution suggests that the oxygen content of the bottom water plays a relatively minor role in determining OC deposition fluxes on a global scale. We suggest other pelagic processes, like attenuation with depth (Martin et al., 1987) and productivity at the surface (Pedersen & Calvert, 1990) are likely a more dominant control on the ultimate OC deposition. However, such findings are hard to determine given the low data density. Figure 5e shows that the effects of bathymetry are muddied by areal extent. We expect that this lack of a bathymetric control has to do with extrapolating between bathymetric bins. However, we do not expect oxygen to be as affected by the binning methods as bathymetry is. Unlike bathymetry, low oxygen regions can be extrapolated with little changes in the values as certain regions are often defined as high or low

oxygen. Furthermore, the raw data have oxygen values that span the entire range of bottomwater oxygen. On the other hand, the samples in this study tend to have water depths greater than 700 meters. Therefore, extrapolating between bathymetric bins from east to west is likely too much of an extrapolation to move between bins. Indeed, this is why we only created two bins (e.g., 0-1,000 and 1,000-1,500) in the method.

Despite our findings that O_2 does not appear to be a dominant control on OC deposition, O_2 need not be unimportant. In regions with low bottom water oxygen and high OC deposition flux, the sediments can become anoxic within the first few centimeters. Once the organic carbon is buried in marine sediments, it is generally protected from remobilization on 1,000 year timescales (Hemingway et al., 2019). Furthermore, we do see that sediment underlying regions with 100-150 O_2 have increased deposition relative to their area. Therefore, this relationship is important in the context of understanding how anthropogenic climate change could impact long-term C deposition flux. However, other factors, such as transfer efficiency and surface productivity, are expected to have a more dominant control on global carbon storage on shorter timescales. One recent study suggested that global carbon export and transfer efficiencies are both expected to decrease by 2100 (Wilson et al., 2022). Carbon export and transfer efficiencies are the two parameters that our data suggest play the most important role in determining OC deposition flux to shallow marine sediments (i.e., <100 meters of water depth). Thus, assuming NPP stays constant, we expect that the overall OC burial will decrease in the coming century, despite projected increases in OMZs.

4 Conclusions

Carbon deposition to marine sediments removes carbon dioxide from the atmosphere on centennial-to-million-year timescales. Although several studies have used combined field measurements of sediments and modeling to estimate OC deposition flux in the deep sea, no such exercise has been undertaken along the continental margins, where most of the global OC deposition flux occurs. Here, we leveraged the wealth of OC and flux data for Holocene sediments supplied by literature values, the PANGEA and IODP databases combined with geospatial interpolation to produce a bottom-up estimate of the OC deposition flux to the margins. Our preferred estimate of marine margin OC *deposition* is $19.4^{+3.1}_{-3.0}$ Tmol C yr^{-1}. Combined with

previous estimates of deep-sea OC deposition of 1 to 2 Tmol C yr^{-1},we estimate the global *marine flux* over all water depths as 17.4 to 24.5 Tmol C yr^{-1}. Additionally, we estimated that the margins have a *total OC* deposition flux (i.e., combined marine-sourced and terrestrial-sourced OC) of 23.2 ± 3.5 Tmol C yr^{-1} along the margins, for a total OC deposition flux of terrestrial and marine OC of 24.9 ± 3.6 T mol C yr^{-1} (i.e., no bathymetric constraints, >1,500 meters included). Our estimates compare reasonably well with previous top-down approaches. We use our flux data to determine the efficiency of global OC export from the euphotic zone to the seafloor, which we estimate as between 2–3 %. Additionally, we show that OC deposition appears to depend primarily on particle transit distance to the seafloor and on productivity in the surface, whereas the oxygen contents of the marine bottom water only play a minor role. Future work may explore machine learning models once more data is available.

Acknowledgments

The project was funded by the National Science Foundation Graduate Research Fellowship (Grant #1122374; L.A.T). Further support was provided by NSF grants (e.g., GEO-NERC 1948716 S.G.N and T.J.H) and The Breene M. Kerr Early Career Scientist Endowment Fund (T.J.H). I would also like to thank the coauthors of this study: Sune Nielsen, Yi Wang, Shavonna Bent, Valier Galy and Tristan Horner.

Chapter 2 References

Archer, D. E., Morford, J. L., & Emerson, S. R. (2002). A model of suboxic sedimentary diagenesis suitable for automatic tuning and gridded global domains. *Global Biogeochemical Cycles*, *16*(1), 17-1-17–*21*. https://doi.org/10.1029/*20*00gb001288

Atwood, T. B., Witt, A., Mayorga, J., Hammill, E., & Sala, E. (2020). Global Patterns in Marine Sediment Carbon Stocks. *Frontiers in Marine Science*, *7*, 165. https://doi.org/10.*3*389/fmars.2020.00165

Bradley, J. A., Hülse, D., LaRowe, D. E., & Arndt, S. (2022). Transfer efficiency of organic carbon in marine sediments. *Nature Communications*, *13*(1), *7*297. https://doi.org/10.1038/s41467-022-*35*112-9

Buesseler, K. O., Lamborg, C. H., Boyd, P. W., Lam, P. J., Trull, T. W., Bidigare, R. R., et al. (2007). Revisiting Carbon Flux Through the Ocean's Twilight Zone. Science, *316*(5824), 567–*570*. https://doi.org/10.1126/science.1137959

Burdige, D. J. (2007). Preservation of Organic Matter in Marine Sediments: Controls, Mechanisms, and an Imbalance in Sediment Organic Carbon Budgets? *Chemical Reviews*, *107*(2), 467–485. https://doi.org/10.1021/cr050347q

Cai, W.-J., & Sayles, F. L. (*19*96). Oxygen penetration depths and fluxes in marine sediments. *Marine Chemistry*, *52*(2), 123–131. https://doi.org/10.1016/0304-4203(95)00081-x

Cartapanis, O., Bianchi, D., Jaccard, S. L., & Galbraith, E. D. (2016). Global pulses of organic carbon burial in deep-sea sediments during glacial maxima. Nature Communications, 7(1), 10796. https://doi.org/10.1038/ncomms10796

Diesing, M., Thorsnes, T., & Bjarnadóttir, L. R. (2021). Organic carbon densities and accumulation rates in surface sediments of the North Sea and Skagerrak. *Biogeosciences*, *18*(6), 2139–2160. https://doi.org/10.5194/bg-18-2139-2021

Dunne, J. P., Armstrong, R. A., Gnanadesikan, A., & Sarmiento, J. L. (2005). Empirical and mechanistic models for the particle export ratio. Global Biogeochemical Cycles, 19(4). https://doi.org/10.1029/2004gb002390

Dunne, J. P., Sarmiento, J. L., & Gnanadesikan, A. (2007). A synthesis of global particle export from the surface ocean and cycling through the ocean interior and on the seafloor. Global Biogeochemical Cycles, 21(4). https://doi.org/10.1029/2006gb002907

Falkowski, P. G., Barber, R. T., & Smetacek, V. (1998). Biogeochemical Controls and Feedbacks on Ocean Primary Production. Science, *281(5374), 200-206*

Friedlingstein, P., Jones, M. W., O'Sullivan, M., Andrew, R. M., Bakker, D. C. E., Hauck, J., et al. (2022). Global carbon budget 2021. *Earth System Science Data*, *4*(14), 1917–2005.

Galy, V., Peucker-Ehrenbrink, B., & Eglinton, T. (2015). Global carbon export from the terrestrial biosphere controlled by erosion. Nature, *521*(7551), 204–207. https://doi.org/10.1038/nature14400

Gershanovich, D. E., Gorshkova, T. I., & Koniukhov, A. I. (1974). Organic matter in recent sediments of continental margins. *Organic Matter in Recent and Fossil Sediments and Methods of Its Investigation*, 63–80.

Hayes, C. T., Costa, K. M., Anderson, R. F., Calvo, E., Chase, Z., Demina, L. L., et al. (2021). Global Ocean Sediment Composition and Burial Flux in the Deep Sea. Global Biogeochemical Cycles, 35(4). https://doi.org/10.1029/2020gb006769

Hedges, J. I., & Keil, R. G. (1995). Sedimentary organic matter preservation: an assessment and

speculative synthesis. Marine Chemistry, *49*(2–3), 81–115.
Hedges, J. I., Keil, R. G., & Benner, R. (1997). What happens to terrestrial organic matter in the ocean? *Organic Geochemistry*, *5–7*(27), 195–212.
Hemingway, J. D., Rothman, D. H., Grant, K. E., Rosengard, S. Z., Eglinton, T. I., Derry, L. A., & Galy, V. V. (2019). Mineral protection regulates long-term global preservation of natural organic carbon. Nature, 570(7760), 228–231. https://doi.org/10.1038/s41586-019-1280-6
Jaccard, S. L., & Galbraith, E. D. (2012). Large climate-driven changes of oceanic oxygen concentrations during the last deglaciation. *Nature Geoscience*, *5*(2), 151–156. https://doi.org/10.1038/ngeo1352
Jahnke, R. A. (1996). The global ocean flux of particulate organic carbon: Areal distribution and magnitude. Global Biogeochemical Cycles, 1(10), 71–88.
Jahnke, R. A. (2010). *"Global synthesis", in Carbon and nutrient fluxes in continental margins. Global change—the IGBP series.* (K. Liu, L. Atkinson, R. Quiñones, & and L. Talaue-McManus, Eds.). Berlin: Springer. https://doi.org/10.1007/978-3-540-92735-8
Jin, X., Gruber, N., Dunne, J. P., Sarmiento, J. L., & Armstrong, R. A. (2006). Diagnosing the contribution of phytoplankton functional groups to the production and export of particulate organic carbon, CaCO3, and opal from global nutrient and alkalinity distributions. Global Biogeochemical Cycles, 20(2) https://doi.org/10.1029/2005gb002532
Keil, R. (2015). Hoard of fjord carbon. Nature Geoscience, 8(6), 426–427. https://doi.org/10.1038/ngeo2433
Lamb, A. L., Wilson, G. P., & Leng, M. J. (2006). A review of coastal palaeoclimate and relative sea-level reconstructions using δ13C and C/N ratios in organic material. *Earth-Science Reviews*, *75*(1–4), 29–57. https://doi.org/10.1016/j.earscirev.2005.10.003
Lee, T. R., Wood, W. T., & Phrampus, B. J. (2019). A Machine Learning (kNN) Approach to Predicting Global Seafloor Total Organic Carbon. Global Biogeochemical Cycles, 33(1), 37–46. https://doi.org/10.1029/2018gb005992
Li, J., & Heap, A. D. (2008). *A review of spatial interpolation methods for environmental scientists* (Vol. 10). https://doi.org/10.1559/152304083783914958
Lutz, M., Dunbar, R., & Caldeira, K. (2002). Regional variability in the vertical flux of particulate organic carbon in the ocean interior. Global Biogeochemical Cycles, 16(3), 11-1-11–18. https://doi.org/10.1029/2000gb001383
Martin, J. H., Knauer, G. A., Karl, D. M., & Broenkow, W. W. (1987). VERTEX: carbon cycling in the northeast Pacific. *Deep Sea Research Part A. Oceanographic Research Papers*, *34*(2), 267–285. https://doi.org/10.1016/0198-0149(87)90086-0
Middelburg, J. J., Soetaert, K., & Herman, P. M. (1997). Empirical relationships for use in global diagenetic models. *Deep Sea Research Part I: Oceanographic Research Papers*, *2*(44), 327–344.
Muller-Karger, F. E., Varela, R., Thunell, R., Luerssen, R., Hu, C., & Walsh, J. J. (2005). The importance of continental margins in the global carbon cycle. *Geophysical Research Letters*, *32*(1).
Nowicki, M., DeVries, T., & Siegel, D. A. (2022). Quantifying the Carbon Export and Sequestration Pathways of the Ocean's Biological Carbon Pump. Global Biogeochemical Cycles, *36*(3). https://doi.org/10.1029/2021gb007083
Pedersen, T. F., & Calvert, S. E. (1990). Anoxia vs. Productivity: What Controls the Formation of Organic-Carbon-Rich Sediments and Sedimentary Rocks? *The American Association of Petroleum Geologists*, *74*(4), 454–466.

Rosengard, S. Z., Lam, P. J., Balch, W. M., Auro, M. E., Pike, S., Drapeau, D., & Bowler, B. (2015). Carbon export and transfer to depth across the Southern Ocean Great Calcite Belt. Biogeosciences, 12(13), 3953–3971. https://doi.org/10.5194/bg-12-3953-2015

Smeaton, C., Cui, X., Bianchi, T. S., Cage, A. G., Howe, J. A., & Austin, W. E. N. (2021). The evolution of a coastal carbon store over the last millennium. *Quaternary Science Reviews*, *266*, 107081. https://doi.org/10.1016/j.quascirev.2021.107081

Smith, W. H. F., & Sandwell, D. T. (1997). Global Sea Floor Topography from Satellite Altimetry and Ship Depth Soundings. Science, *277*(5334), 1956–1962.

Stanford, J. D., Hemingway, R., Rohling, E. J., Challenor, P. G., Medina-Elizalde, M., & Lester, A. J. (2011). Sea-level probability for the last deglaciation: A statistical analysis of far-field records. *Global and Planetary Change*, *79*(3–4), 193–203. https://doi.org/10.1016/j.gloplacha.2010.11.002

Urey, H. C. (1952). *The Planets: their Origin and Development*. New Haven: Yale University Press.

Volk, T., & Hoffert, M. I. (1985). The Carbon Cycle and Atmospheric CO 2 : Natural Variations Archean to Present. *Geophysical Monograph Series*, 99–110. https://doi.org/10.1029/gm032p0099

Wilson, J. D., Andrews, O., Katavouta, A., Viríssimo, F. de M., Death, R. M., Adloff, M., et al. (2022). The biological carbon pump in CMIP6 models: 21st century trends and uncertainties. *Proceedings of the National Academy of Sciences*, *119*(29), e2204369119. https://doi.org/10.1073/pnas.2204369119

Chapter 3. Refining the roles of productivity, redox, and remineralization on the cadmium isotope composition of marine sediments

Abstract

Cadmium (Cd) has a nutrient-like profile in the ocean, similar to the macronutrient phosphate. Significant isotopic fractionation induced by biological cycling of Cd makes it a potential tracer for nutrients and productivity. However, the quantity and Cd isotope composition of marine sediments can also be influenced by local redox conditions and partial remineralization of organically hosted Cd. These complicating factors are under-constrained and render it challenging to use Cd as a reliable proxy. To understand the relative importance of each of these processes, we examined the Cd isotope systematics of 69 modern sediments deposited across a wide range of environments. We complement these data with four profiles of particulate Cd isotope compositions from the Southern Ocean. We report three main results. First, we show that the global flux of Cd is closely coupled to that of organic matter. Likewise, most of the Cd burial occurs in regions with some bottom-water oxygen, and the flux of cadmium sulfides (CdS) to anoxic regions is, globally, minor. Second, we find that remineralization can substantially modify sedimentary Cd isotope compositions, though it is challenging to relate pelagic and sedimentary processes. For example, we find that the relationship between sedimentary Cd isotope compositions and surface seawater [Cd] is the reverse of that predicted by isotope reactor models. Likewise, sedimentary Cd isotope compositions are anti-correlated with bottom-water oxygen. While this pattern is consistent with preferential remineralization of isotopically heavy Cd, profiles of marine particulate matter reveal the reverse, whereby the Cd isotope composition of the large organic matter particles, which are most likely to reach the seafloor, becomes increasingly 'heavy' during export. Third, we combine our new data with literature values to estimate the global mass balance of Cd and its isotopes. While it is possible to derive a balanced Cd isotope budget, the result strongly depends on the approach taken. These results highlight how productivity, redox, and remineralization all influence the flux and isotope composition of Cd in marine sediments. While our study suggests that there is no simple way to relate sedimentary Cd isotopes to surface nutrient utilization, our data point toward several potential controls that could form the basis of novel proxies for local redox and remineralization.

1. Introduction

Cadmium (Cd) displays a nutrient-like profile in the ocean with a distribution similar to the macronutrient phosphate (Boyle et al., 1976; Bruland, 1980). Despite its nutrient-like behavior, there is considerable debate about whether Cd serves an important physiological function (Lane et al., 2005) or is simply mistakenly incorporated by microbes as they search for other biologically essential metals (Horner et al., 2013). Regardless of cadmium's biological function, Cd is intensely cycled by microbes in the upper water column (Sunda, 2012) and its relationship with P underpins its use as a proxy for nutrients and circulation (Boyle, 1988; Marchitto and Broecker, 2006).

Biological uptake of Cd is generally accompanied by a significant negative Cd isotopic fractionation, which can be traced throughout the water column. Studies have shown that phytoplankton preferentially take up the light isotope (Lacan et al., 2006; John and Conway, 2014), leaving the residual seawater more positive by up to $\delta^{114}Cd = +5$ ‰ relative to deep waters, (where $\delta^{114}Cd = (\delta^{114/110}Cd_{sample}/\delta^{114/110}Cd_{NIST\ SRM\ 3108}) - 1$). In contrast, the deep and intermediate ocean is nearly homogeneous with respect to $\delta^{114}Cd$, exhibiting values between +0.25 and +0.45 ‰ (Ripperger et al., 2007; Abouchami et al., 2014; Conway and John, 2015b; Sieber et al., 2023). The isotopic composition of Cd in surface waters can theoretically provide information about the relative degree of nutrient utilization in a region (i.e., the fraction of consumed nutrients), akin to carbon, nitrogen, or silicon isotopes (Farmer et al., 2021). In general, heavier Cd isotopic compositions in surface seawater imply a higher level of local nutrient use, whereas lighter Cd isotopic compositions indicate the reverse. However, studies have shown that this relationship does not hold true under very low surface Cd concentrations where small additions of Cd – either from upward mixing of deep Cd (Abouchami et al., 2011; Xue et al., 2013) or downward deposition of anthropogenic aerosols and dust particles (Yang et al., 2012; Bridgestock et al., 2017; Sieber et al., 2023) – may obfuscate the seawater biological $\delta^{114}Cd$ signal. However, little work has been done to investigate the relationship between surface water nutrient utilization and Cd isotope compositions recorded in marine sediments, which is a prerequisite for using Cd isotopes as a proxy for nutrient utilization (Georgiev et al., 2015).

Nearly all modern Cd burial is associated with organic matter-rich sediments (van Geen et al., 1995; Morford and Emerson, 1999; Little et al., 2015). While there are some minor sedimentary

sinks of Cd, including burial with marine carbonates (Boyle, 1988; Horner et al., 2010) and removal with Fe-Mn sediments (Schmitt et al., 2009; Horner et al., 2010), >90 % of Cd is burial occurs into organic-rich sediments deposited along continental margins (Rosenthal et al., 1995; van Geen et al., 1995; Little et al., 2015). Margins account for most global organic matter deposition and have enhanced Cd concentrations relative to the detrital background of Cd (e.g., 0.1 μg/g) (van Geen et al., 1995). While much of the Cd that is deposited along margins is supported by Cd incorporation into organic matter, some Cd in the sediment occurs in excess of this value and is likely associated with Cd sulfides.

Cadmium sulfide formation has been predicted to occur through three primary pathways. First, some studies have posited that an abiotic mechanism may allow CdS to form within sulfidic microenvironments of sinking particles (Janssen et al., 2014; Conway and John, 2015a). However, several recent studies have suggested that this mechanism does not exist; instead these studies suggest that the observed dissolved Cd deficiency in the water column may arise through biotic (e.g., Ohnemus et al., 2017) or physical processes, perhaps related to lower Cd: PO_4 in intermediate waters relative to deep waters (Ohnemus et al., 2017; de Souza et al., 2022; Sieber et al., 2023). Given the contentious nature of this supposed Cd sink, and difficulty in distinguishing it from other forms of CdS, we will not consider CdS formation within sinking particles in our study. Second, CdS formation may occur pelagically in bottom water in particularly in low-oxygen, or anoxic (no detectable oxygen) environments. A recent study indicated that cadmium sulfide minerals could be precipitated directly from seawater in the presence of dissolved H_2S (Plass et al., 2020), even if the dissolved H_2S has very low concentrations. Third, when Cd bound in organic matter is delivered to the seafloor, some of that organic matter can be remineralized within the sediment. If the Cd that was formerly bound in organic matter is liberated into porewaters that contains even trace levels dissolved H_2S, Cd can be recaptured into cadmium sulfide minerals (Gobeil et al., 1987; McCorkle and Klinkhammer, 1991).

The precipitation of Cd into sulfides is associated with a slight negative isotope fractionation (Guinoiseau et al., 2018). Thus, CdS formation in the environment has the potential to render changes in the Cd isotope composition of marine sediments. If, however, the capture of Cd is quantitative, the Cd isotope composition of sediments would reflect the source—bottom seawater or organic matter. The latter is noteworthy because it suggests that sediments may retain the Cd isotope composition of exported organic matter, even if the organic matter itself is no longer

present. Unfortunately, the relative importance of each of these last two CdS fluxes compared to organically bound fluxes are not well constrained. Isotope analysis may be able to help tease these sources of CdS apart.

Recent studies have indicated that continental margin sediments have Cd isotope compositions that are lighter than those of deep-water isotopic compositions when they are not impacted by the formation of CdS (Bryan et al., 2021; Chen et al., 2021). This finding is in line with the expectation that organic matter possesses low δ^{114}Cd values. Likewise, it is consistent with a potential relationship between Cd isotopes and nutrient utilization that could be used as a paleonutrient proxy (Georgiev et al., 2015; Hohl et al., 2019). However, a recent study showed that suspended particulate matter in the North Pacific Ocean had isotope compositions that were far lighter than were expected based on surface isotope values. The authors of this study attributed the light isotope signature to a few possible processes, including remineralization, which may alter the Cd isotope composition of the primary particles. If this process affects the particles that eventually settle in the seafloor, it would affect the isotope composition of sedimentary Cd isotopes, but this process has not been explored. Likewise, no study has systematically explored how the different sources of Cd–organic matter and CdS–affect sedimentary Cd isotope compositions on a global scale. Such a study is important both to close the marine Cd budget and to evaluate the potential of sedimentary Cd isotopes as a paleo nutrient proxy.

Here, we explore the role of redox, productivity, and remineralization in shaping the Cd isotope compositions of recent organic-rich sediments. We specifically aimed to answer three questions: (i) can we differentiate between regions that have substantial CdS formation from those that do not?, (ii) do regions that are dominated with Cd derived from organic matter record nutrient utilization from the surface waters?, and (iii) can we use our samples to close the global Cd isotope budget? To answer these questions, we examine sediments deposited under various bottom water redox conditions and consider these data alongside a recent data set for sediments from the California margin. Our dataset suggests that the local redox conditions influence the underlying sediment's Cd-isotopic composition. We argue that pelagic cadmium sulfide formation is only significant to sedimentary Cd budgets in regions with anoxic bottom water conditions with an episodic source of HS^-, such as the Peru Margin, rather than persistently euxinic basins. Finally, we quantify and apply relationships between Cd burial, O_2 content of the bottom water, and surface water Cd concentrations to calculate a global Cd isotope mass balance.

2. Samples, Sampling, and Site Description

2.1 Sediment Samples

Sixty-nine sediment samples were selected across the globe to cover a range of redox conditions (Figure 1, Table 1). The sediments in this study span a redox gradient from euxinic (anoxic and sulfidic waters, e.g., Black Sea and Cariaco Basin), anoxic (e.g., Cariaco Basin and Peru Upwelling Region), and oxic (e.g., Peru Upwelling, Santa Barbara Basin, Western Equatorial Pacific, Arabian Sea, and Namibian Margin) bottom water conditions. The samples will be briefly described here.

The 12 Black Sea sediment samples were collected on the R/V *Knorr* Cruise 134 Leg 8 in 1988. The Black Sea is the modern ocean's largest euxinic basin. The basin is defined by a constant halocline that restricts vertical mixing below 60-80 meters (Yakushev et al., 2010). Beneath the halocline, oxygen is depleted as it is used for microbial respiration. Subsequent anoxic respiration creates persistent hydrogen sulfide in the water column (Konovalov and Murray, 2001; Konovalov et al., 2001). The Black Sea has only limited exchange with open ocean seawater as it is an intracontinental basin. Thus, the Black Sea is likely to be heavily influenced by changes in riverine input. The subsamples collected were stored frozen in the Woods Hole Oceanographic (WHOI) Seafloor Samples Laboratory. Five of these are down core samples (i.e., non-coretop) taken from Station 39 box core 21 below the chemocline at a water depth of 2,092 m. These samples were described in detail elsewhere (Arthur et al., 1994; Owens et al., 2017). The remaining seven sub-samples collected from the core repository were taken at various water depths between 184 and 2215 meters. The sample depths (e.g., core-top or down core) for each of the samples are given in Table 1.

Cariaco Basin sediments were collected on the 1990 PLUME Cruise Leg 7 (R/V *Thomas Washington*). The Cariaco Basin is a large euxinic basin off the coast of Venezuela that spans about 7000 km^2 (Peterson et al., 1990). The basin is restricted from the Caribbean Sea by shallow sills to the west (146 m) and north (120 m) basin margins (Figure 1). There is high productivity in the region from seasonal upwelling along the coast, which, coupled to significant microbial respiration and lack of deep-water renewal, leads to the depletion of oxygen and the increase of hydrogen sulfide in the water. Thus, the basin water becomes euxinic at a water depth of ~300

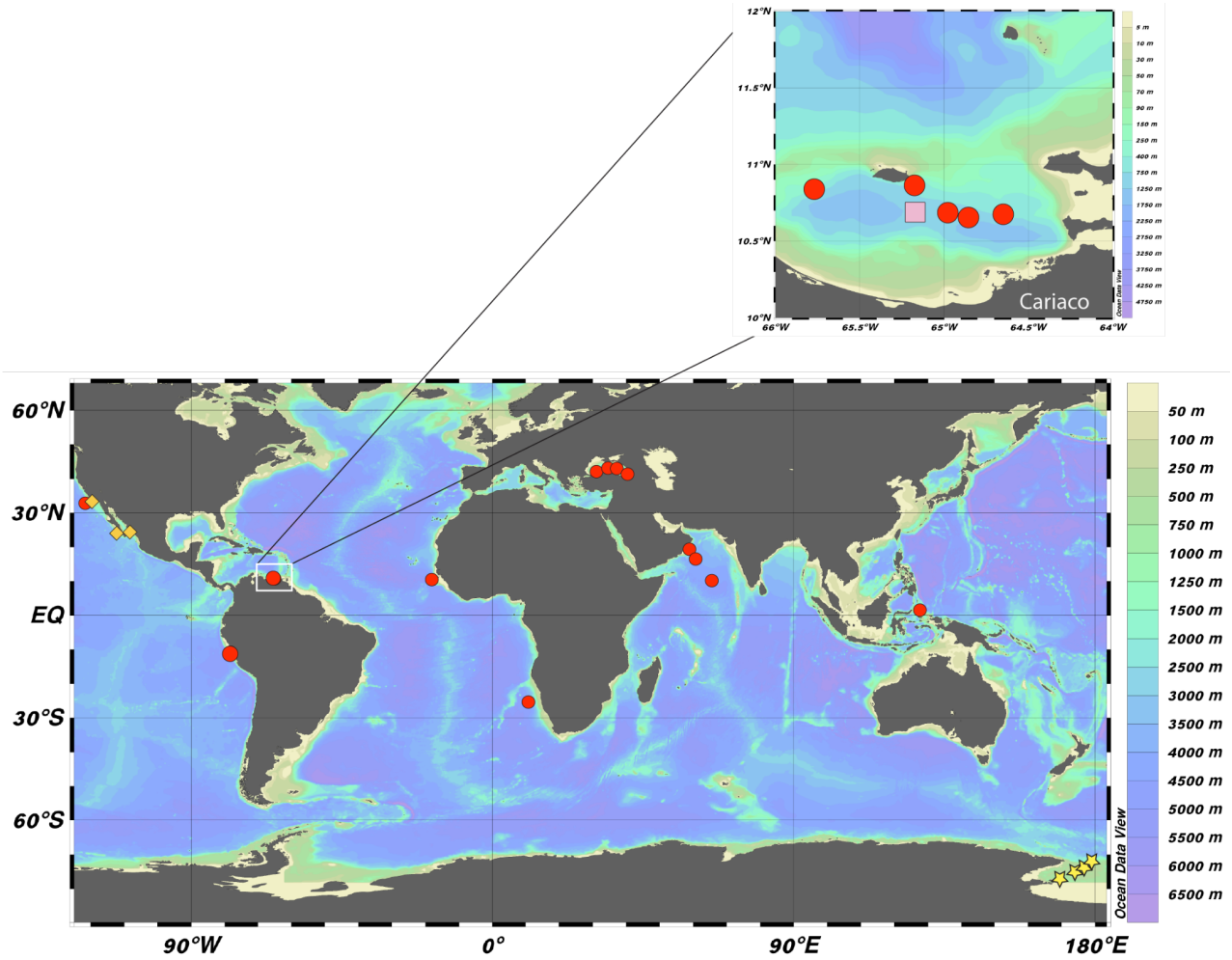

Figure 1. Circles indicate locations of the sites studied along the continental margins. Individual sample locations within a region are not always plotted due to close proximity to other samples within that region. Diamonds are locations of samples in the northeastern Pacific margin from Chen et al. (2021). Square data in the Cariaco Basin is from Little et al. (2015). Stars are seawater sample data collected in the Ross Sea. Maps were made using Ocean Data View (odv.awi.de; Schlitzer, 2017).

meters. Additional information on the seawater and sediments can be found in (Astor et al., 2011) and (Peterson et al., 1990), respectively. The samples measured in this study were box core top samples and were collected below the permanent chemocline (400 to 1400 m).

Peruvian Margin samples were collected along 11˚S in 2008 on the M77-1 Cruise (RV *Meteor*). The Peru Margin is defined by offshore Ekman transport off the coast of South America that creates coastal upwelling of nutrient-rich waters of oxygen-depleted water supplied by the Peru-Chile Undercurrent. The upwelling of nutrient-rich and oxygen-depleted waters leads to high levels of primary productivity in the region. The high levels of primary productivity are linked to high demands for oxygen during oxic microbial respiration (Pennington et al., 2006). Thus, the region is characterized by a perennial oxygen minimum zone (OMZ) off the coast of the Peruvian shelf between approximately 50 and 500 meters (Suess and Huene, 1988; Scholz et al., 2011). During periods of water stagnation, the water column can become anoxic and depleted in both nitrate and nitrite following denitrification (Sommer et al., 2016). When this depletion occurs, hydrogen sulfide (H_2S) that is generated in the sediments can be released to the bottom water and accumulate to micromolar levels (Schunck et al., 2013; Scholz et al., 2016; Ohde, 2018). Furthermore, due to low sulfide solubility, CdS can precipitate in these waters with trace amounts of hydrogen sulfide (Davies-Colley et al., 1985; Rosenthal et al., 1995). In essence, this creates an environment that can be, at times, both anoxic and sulfidic above the sediment. We measured twenty-six sediment samples from the margin shelf to the slope for water depths between 85 and 2025 meters and were analyzed from a core depth between 0 to 35cm. The sample sites span the reducing OMZ and the neighboring oxic deep water—the oxygen concentrations through the region range from 0 μM to 93.4μM.

Sediment samples from the Santa Barbara Basin were collected as a part of the CALMEX Cruise in 2001 (R/V *New Horizon*). The Santa Barbara Basin is a basin in the California Borderlands. It has a sill depth of ~475 meters and a maximum depth of 627 m (Bernhard and Reimers, 1991). There is a limited exchange with water outside the basin; thus, the oxygen concentration in the bottom waters is low, generally < 5 μM (Zheng et al., 2000). The core sites in this region have ferruginous porewaters, which indicates that iron and sulfate reduction are the dominant electron transfer pathways (McManus et al., 1997). The region also has relatively high sedimentation rates (~90 mg/cm^2/yr), which is partially attributed to high lithogenic input from the continent (Thunell et al., 1995). The sediment samples were collected in the basin center, where

the bottom water concentration was <20 μM (Bernhard et al., 1997). All the samples were collected near the core top but were from the same hole (between 0 to 3 cm). Thus, for some calculations, only the topmost sample was included.

Samples from the Arabian Sea were collected on the R/V *Thomas Thompson* Cruises 41 and 47 in November 1994 and May 1995, with multicore samples taken between 16 and 19˚N and 58 and 61 ̊E. The Arabian Sea is a highly productive region with a dynamic oxygen minimum zone (OMZ) driven by monsoon cycling, water mass mixing, and several sources of micro and macronutrients. Because we do not have paired overlying water column data or pore water data, we used the closest cast in the World Ocean Database to determine the approximate O_2 concentration near where the sediment was collected at a similar bottom water depth. All of the samples were taken from near the core top (0-5cm).

Western Equatorial Pacific samples were collected in July 2003 aboard the R/V *Baruna Jaya VIII*, Cruise 8 with a multicore and were subsequently stored in the WHOI Core Repository. The samples were taken in Kau Bay between the northern and northeastern edge of the Island of Halmahera at approximately 1˚N and 127˚E. The bay is highly productive and has bottom water oxygen concentrations of ~100μM, according to the nearest WOA18 hydrocast data and estimated at ~80 μM O_2 based on field measurements from the 1980's (Aken and Verbeek, 1988; van der Weijden et al., 1989). Core top samples were taken at water depths between 250 and 500 meters. All of the sediment samples were taken from 5 cm or shallower in the core and reflect coretop sediment.

Finally, samples from the Angola and Namibian margin were collected aboard the R/V *Chain* in May 1970 and January 1974. The samples are stored in the WHOI Seafloor Samples Laboratory, and core top or near core top material was collected for analysis. The western coast of the South African margin is characterized by the upwelling of nutrient-rich waters with high productivity (Shannon and Nelson, 1996). Although the biological activity leads to an intense oxygen minimum zone over large areas of the margin (Chapman and Shannon, 1987), the samples collected in these waters were collected at a water depth of ~4000 meters and were bathed by well-oxygenated waters. Like the samples from the Arabian Sea and Western Equatorial Pacific, we use the World Ocean Database 2018 to pair bottom water oxygen concentrations to these sediments. Sediment samples were taken between 0-5 cm below seafloor.

For any samples that did not have a published measurement of oxygen concentration, we estimated the bottom water oxygen value using the World Ocean Atlas (WOA) 2018 (Boyer et al., 2022). The values ascribed to each of our samples are shown in Table 1.

2.2 Marine particulate matter

We examined Cd isotope compositions of marine particulate matter collected from the Ross Sea in the Southern Ocean (Table 2). These samples were collected in January to February of 2011 aboard the R/V *Palmer* (NBP1101) using large-volume *in situ* filtration (McLane Research Laboratories, Inc.). Filters were acid cleaned prior to use following GEOTRACES protocols (Cutter et al., 2010). Between 97–439 L of seawater was pumped across each filter during pump deployment (mean of 298 L). Particulate samples were collected in two size fractions: a small size fraction (SSF; 0.8-51 μm), obtained using a 142 mm diameter polyethersulfone membrane filters, and a large size fraction (LSF; >51 μm), collected with a 142 mm diameter nylon screen. After collection, filters were sliced at sea using a ceramic blade in a laminar flow bench and placed in storage bags. Typically, 12.5 % (i.e., ⅛) of the small size fraction filter was set aside for Cd isotope analysis, whereas 74 % of the nylon screen was sampled (ranging from 50–88 %). The samples in this study come from four stations with water depths ranging from 398 to 1,887 meters, whereas the samples were collected between 0 and 600 meters. No sediment samples accompanied these water column samples.

3. Materials and Methods

3.1 Sample leaching

The total Cd content of sediment, $[Cd]_{total}$, can be considered as follows:

$$[Cd]_{total} = [Cd]_{lithogenic} + [Cd]_{biogenic} + [Cd]_{XS} \quad (1)$$

where $[Cd]_{lithogenic}$ is the lithogenic (or detrital) Cd in the sediment, $[Cd]_{biogenic}$ is the Cd that is associated bound with organic matter (i.e., not remineralized nor reprecipitated), and $[Cd]_{XS}$ is the concentration that cannot be supported by lithogenic Cd or Cd that would be expected from organic matter inputs where the OC is preserved in the sediment. Here, a leach of 2 M HNO_3 was used to

isolate: (i) Cd associated with organic matter ($Cd_{biogenic}$), (ii) Cd that was once hosted in organic matter, but was liberated to porewaters and recaptured as CdS, and (iii) CdS that formed pelagically in the water column of anoxic bottom waters in the presence of free H_2S. Both (ii) and (iii) constitute Cd_{XS}. Use of a leach ensured that biogenic and authigenic were sampled without liberating significant quantities of lithogenic Cd. We refer to this fraction as $Cd_{leachable}$, whereby:

$$[Cd]_{leachable} \approx [Cd]_{total} - [Cd]_{lithogenic} \quad (2)$$

thus

$$[Cd]_{leachable} \approx [Cd]_{biogenic} + [Cd]_{XS} \quad (3)$$

In order to differentiate between the biogenic and excess Cd, we calculated how much of the Cd was expected to be derived from organic material using a ratio of organic carbon to Cd:

$$[Cd]_{biogenic} = [OC] \times Cd{:}C \quad (4)$$

where [OC] is the total organic carbon measured in the sediment, and Cd:C is either estimated by an extended Redfield ratio (Ho et al., 2003) or measured ratios in field samples (Bourne et al., 2018). Thus,

$$[Cd]_{XS} \approx [Cd]_{leachable} - [OC] \times Cd{:}C \quad (5)$$

We assumed that the excess Cd, $[Cd]_{XS}$, was formed via one of two pathways. First, CdS can form near the sediment–seawater interface if the dissolved Cd encounters H_2S emanating from sediments. We refer to this as pelagic CdS. Alternatively, CdS can form within the sediment after the organic matter it was bound in is remineralized. If the liberated Cd encounters even trace amounts of H_2S, it can be quantitatively re-precipitated. We refer to this as porewater CdS. Since the latter process is generally quantitative, it likely captures ambient pore water $\delta^{114}Cd$ with no net Cd isotope fractionation. Either of these processes would elevate Cd above what is supported by $[Cd]_{biogenic}$.

3.2 Sediment samples

All samples were prepared in the NIRVANA clean laboratory facilities at WHOI. Acids were double distilled inhouse and were tested for their Cd content before use using methods described below. All water used in preparation was obtained from an 18.2 MΩ ultrapure, deionized water system (Milli-Q).

For each sample, approximately 20-30 mg of powdered sample was weighed into 7 mL perfluoroalkoxy vials (Savillex). The powder was treated with 2 M HNO_3 for 17 hours at 60˚C and centrifuged to separate the detrital material (Nielsen et al., 2011; Owens et al., 2017). The refractory organic matter was oxidized by reacting concentrated HNO_3 at 250˚C for two hours in a pressurized microwave digestion system (Multiwave PRO; Anton Parr). After oxidation, an aliquot of each sample was analyzed on an iCAP RQ-ICP-MS (Thermo Fisher Scientific™) in the WHOI Plasma Facility to determine approximate Cd concentrations for initial spiking. A ^{111}Cd–^{113}Cd double spike was then added to each sample so that the spike-to-sample ratio (S:N) would be between 1 and 2. Spiked samples were then reconstituted in 1 M HCl for chromatography.

Two-stage anion-exchange chromatography was performed to separate Cd from the sample matrix. The separation technique was modified from Conway et al. (2013). In brief, the samples were loaded in 1 M HCl onto columns with pre-cleaned 500 µL AG MP-1M anion-exchange resin (Bio Rad™). Matrix elements were eluted in increasing molarities of HCl, and Cd was eluted using 2 M HNO_3. Next, the samples were dried down and reconstituted in the Cl^- form and subsequently loaded in 1 M HCl onto pre-cleaned 180 µL AG MP-1M anion exchange resin. Following column chemistry, residual organic material was removed with a liquid–liquid organic extraction (Murphy et al., 2015). Here, any excess organic material–either from the resin or carried over from organic-rich sediment samples–was extracted by adding 1.2 mL of optima-grade heptane to the eluted samples, shaking for 30 seconds, and allowing them to sit for three minutes. After sitting for three minutes, the heptane was extracted and discarded, and the process was repeated. The samples were dried, reconstituted in 1.1 mL of 2 % HNO_3, and a subsample of 100µL was taken to ascertain the spike-to-sample ratio (S:N), Cd concentration, and chemistry concentration yields of the purified sample. Samples were diluted to achieve similar Cd concentrations (~20 ng/mL sample-derived Cd) and organized such that samples with similar S:N were analyzed together. Cadmium isotope compositions were then measured and reported relative to spiked aliquots of NIST SRM 3108

possessing similar S:N to those of the samples. Given that samples were spiked prior to purification, Cd concentrations were determined simultaneously to isotope compositions.

To monitor the measurement precision and accuracy, aliquots of USGS SGR-1, NOD-A-1 and NOD-P1 were processed alongside samples of unknown isotope composition. The USGS SGR-1 reference material was processed using the same steps described above, whereas the USGS NOD-A-1 and NOD-P-1 underwent a 6M HCl total digest at 50˚C for 10 minutes before separation (Horner et al., 2010). After the digestion, standards were processed alongside the samples of SGR-1 as samples in the protocols described above.

3.3 Marine particulate matter preparation

Particulate samples were leached in acid-cleaned PFA vials (Savillex) for 16 hours in 0.6 M HCl at 80˚C (Bishop and Wood, 2008; Horner et al., 2017). The small size fraction filters were leached in 10 mL, whereas the nylon screens were leached in 50 mL. Samples were leached in 0.6 M HCl as this method does not appreciably dissolve the filter, but nonetheless results in near-quantitative recovery of many elements including P, Mn, Ba, Cd, and Sr (Bishop et al., 2012; Planquette and Sherrell, 2012). A 100 µL aliquot was taken from the leachate and Cd and P contents were determined by means of an external calibration using an ELEMENT 2 ICP-MS (ThermoFisher Scientific), also situated in the WHOI Plasma Facility. Samples were then evaporated to dryness, spiked with the same ^{111}Cd –^{113}Cd double spike to ensure a S:N of 1–2, and reconstituted in 1 mL of 1 M HCl for ion-exchange chromatography. The protocol was similar to that used for sediment samples; however, instead of a second pass through anion-exchange resin, the samples were instead reconstituted in 8 M HCl and passed through 180 µL of Eichrom TRU resin to remove any residual tin (Wombacher et al., 2003; Ripperger et al., 2007). Following this step, the samples were reconstituted in 2 % HNO_3 acid in preparation for mass spectrometry.

3.4 Cadmium isotope analysis

Cadmium isotope ratios were measured on a multi-collector inductively-coupled mass spectrometer (MC-ICP-MS; ThermoFinnigan Neptune), situated in the WHOI Plasma Facility. Samples were aspirated into a desolvation system (Aridus II, CETAC) at approximately 140 µL minute$^{-1,}$ and the resultant aerosol was introduced into the ion source using a 1 L minute^{-1} Ar carrier gas. The ion currents from 110 to 117 AMU were measured in 30 four-second integrations and

processed with a MATLAB script to calculate the sample isotopic composition from the spike-to-sample mixture and the isobaric interferences (Horner et al., 2011). In this approach, isotope data were solved relative to the spike; however, Cd isotope data was reported relative to bracketing (spiked) aliquots of NIST SRM 3108 that were measured during the same analytical session (Abouchami et al., 2013). Within-run accuracy was monitored by analyzing appropriately spiked aliquots of BAM-I012, which we found possessed a Cd isotope composition of −1.33 ± 0.02 ‰ (± 2 SD, n = 25). These values are identical, within uncertainty, to the inter-laboratory consensus value of δ^{114}Cd= −1.31 ± 0.04 ‰ (Abouchami et al., 2013). Long-term accuracy for standards was monitored by processing standard reference materials alongside sample unknowns.

4. Results

4.1 Standard data and leach reproducibility

The accuracy of our Cd concentration and δ^{114}Cd data were determined by measuring three USGS reference standards: SGR-1, NOD-A-1, and NOD-P-1. The average SGR-1 leached concentration measured here was 704 ± 105 ng/g (2SD, n=8), which is reasonable for the leachate given the $[Cd]_{Total}$ of between 900 to 1,200 ng/g (Jochum et al., 2005). Since the average Cd concentration of the upper continental crust is ~ 100 ng/g (Wedepohl, 1995), we conclude that this leach extracts essentially the entire complement of non-lithogenic, leachable Cd—800 to 1,100 ng/g are expected to be leachable, which overlaps with our value within uncertainty. The SGR-1 USGS reference material had a mean δ^{114}Cd = −0.02 ± 0.03 ‰ (±2SD; n=7). Although there are no literature data for leached SGR-1, our reproducibility implies that the leach performed similarly each time in agreement with the quantitative extraction of leachable Cd from the samples.

The nodule standards were prepared using a different leach from the samples (Horner et al., 2010). The average bulk NOD-A-1 and NOD-P-1 we measured is 5.6 ± 0.9 µg/g (2SD, n=6) and 15.7 ± 1.7 µg/g (2SD, n=6), respectively. The accepted values for these two reference materials are slightly more concentrated than our measured values, falling between 6.8 - 8 µg/g (NOD-A-1) and 20.9 - 23.3 µg/g (NOD-P-1) (Jochum et al., 2005). However, the consistency of the standards' isotopic values suggests no appreciable fractionation during sample processing or analysis. NOD-A-1 and NOD-P-1 had average δ^{114}Cd = +0.11 ± 0.03 ‰ (n=6) and +0.13 ± 0.03 ‰ (n=6), respectively, and overlap with a study that compiled literature values and recommended that the

true $\delta^{114}Cd$ of the samples was + 0.129 ± 0.035 ‰ (NOD-A1) and +0.141 ± 0.052 ‰ (NOD-P1; Lu et al., 2021).

4.2 Cadmium concentration and isotope variations in sediment leachates

The 69 sediments in this study display leachable Cd concentrations between 0.09 and 59 μg g^{-1} (Table 1, Figure 2a-b). Sediments with the highest and lowest values are from the Peru Upwelling Region and the Western Equatorial Pacific, respectively.

The Cd isotope composition of the samples fall between $\delta^{114}Cd$ = −0.18 and +0.35 ‰ (Table 1). Except for the Peru Margin, the measured isotope compositions are similar within a given region. The heaviest isotope compositions occur in the Peru Margin at low bottom water oxygen concentrations and the lightest in the Namibian Margin at high oxygen concentrations.

4.3 Marine particulate Cd concentrations and isotopes from the Ross Sea

Four stations in the Ross Sea were selected to measure particulate $\delta^{114}Cd$ ($p\delta^{114}Cd$). The profiles of small size fraction (SSF) $p\delta^{114}Cd$ are like those observed in the Northeast Pacific by Janssen et al. (2019), whereby the surface $p\delta^{114}Cd$ sample is the heaviest for all four stations, and the $p\delta^{114}Cd$ becomes lighter with depth (Figure 3e-h). For three of the stations, the final small fraction of marine particulate samples returns to heavier values, albeit the last sample is still lighter than the surface value. The only profile that does not show this trend is Station 0, but this station was not sampled deeper than 250 meters, so we cannot rule out the possibility that it would have followed the same trend as the other four samples deeper in the water column. The O_2 profiles for Station 2, 14 and 24 are shown in Figure 3(b-d). Unlike the samples from the Northeast Pacific, all of the water column profiles in the Ross Sea are well oxygenated, with $[O_2]$ >175 μM. Particulate Cd concentrations (p[Cd]) for all 8 profiles show that the particulate Cd concentrations are highest in the surface and decrease with depth (Figure 3i-l), similar to profiles of particulate P (Figure 3m-b; Bishop and Wood, 2008).

The large size fraction particles (LSF) follow the same trends that were observed in the SSF (Figure 3). Stations 0, 2 and 24 show that the samples become isotopically lighter with depth, but not as much as the SSF particles, and are often within uncertainty of the other samples collected at the same station. Station 14, the most offshore region samples, shows the largest change of Cd isotopes with depth: the top 250 meters of water have a similar $p\delta^{114}Cd$ value,

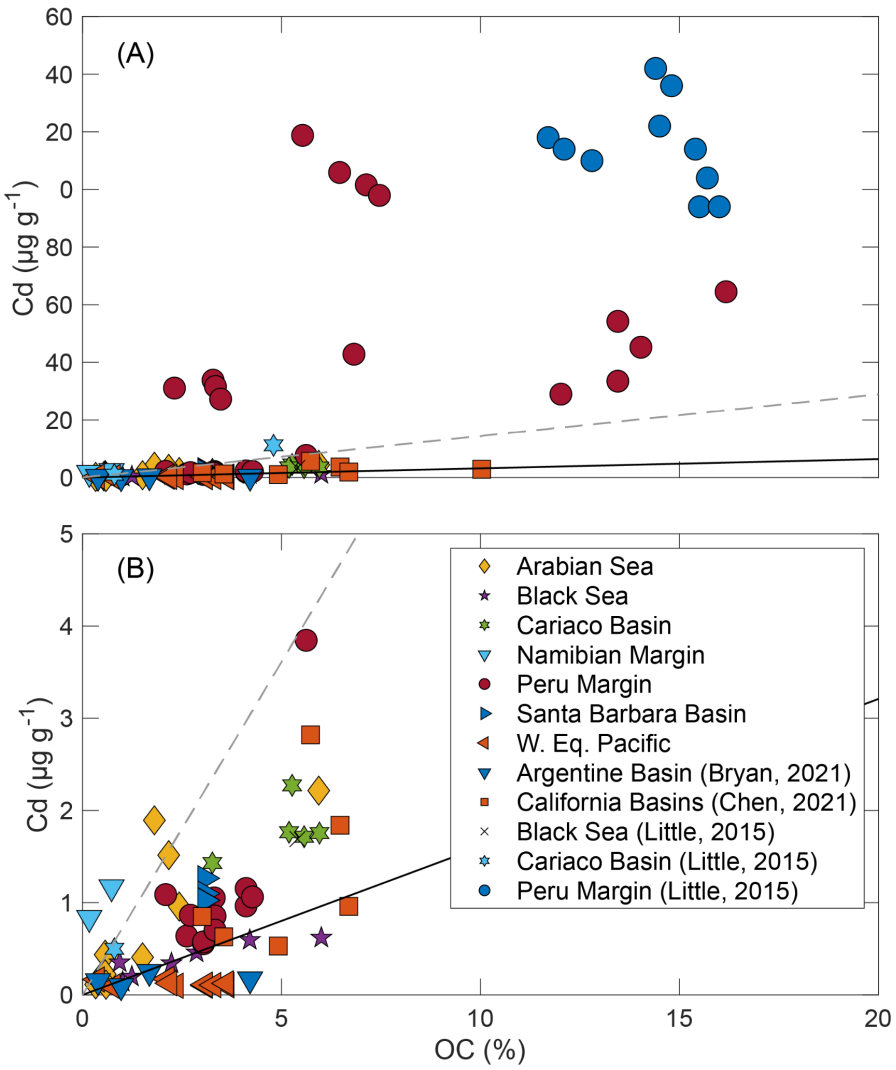

Figure 2. (A) All leachable Cd concentrations versus organic carbon concentrations. For comparison, the dashed gray line is the average molar Cd:C ratio from euphotic particles in the Peru Margin (7.66×10^{-6}; Bourne et al., 2018) the solid black line is the Cd:C ratio in the 'average' phytoplankton (1.69×10^{-6}; Ho et al., 2003). Samples in the Peru Margin have increased Cd concentrations, suggesting an input of excess CdS (B) Zoomed in on the leachable Cd concentrations that fall between 0 and 5 µg g^{-1}

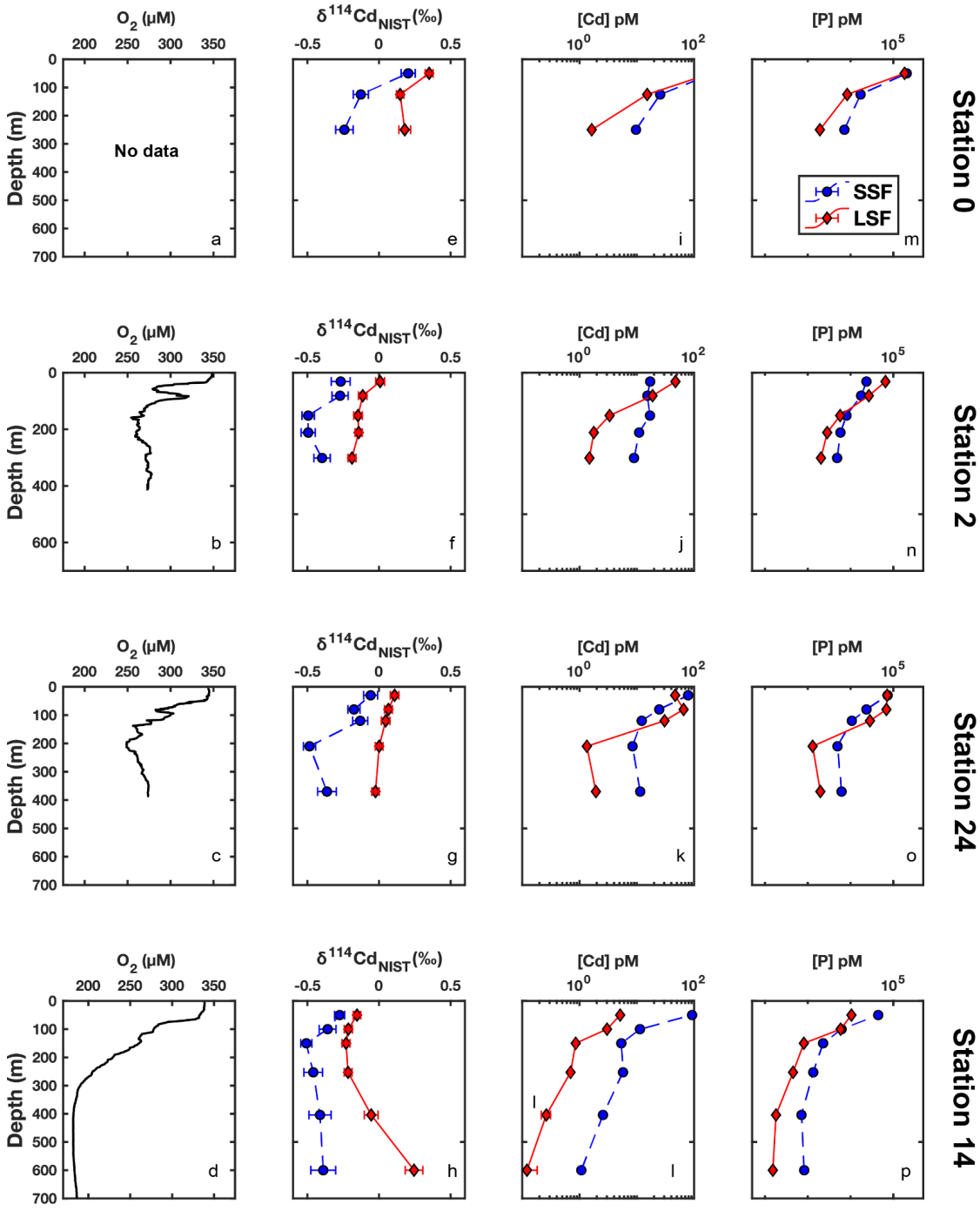

Figure 3. Profiles from four stations in the Ross Sea. The first column shows the O_2 composition of the water column at stations 0, 2, 24 and 14 (a-d). The second column shows the $\delta^{114}Cd$ (‰) (e-h). The third and fourth columns show the Cd concentration and P concentrations, respectively (i-p). The large size fraction particles are shown in red diamonds with a solid line, the small-size fraction particles are shown in a blue circle with a dashed line.

whereas deeper samples become isotopically heavier. Indeed, the deepest sample at 600 meters is heavier than the surface sample by 0.40 ‰

5. Discussion

5.1. Cadmium sulfide incorporation into marine sediments

In this section, we quantify the amount of CdS delivered to anoxic marine sediments, constrain its Cd isotope composition, and assess the significance of CdS to global Cd budgets. We explore results from three anoxic regions: the Peru Margin, the Cariaco Basin, and the Black Sea. We show that pelagically precipitated CdS significantly contributes to the sedimentary Cd inventory of the Peru Margin, but not the permanently restricted Cariaco Basin or Black Sea. We examine the impact of CdS precipitation on the Cd isotope composition and highlight the interplay between redox conditions, organic matter delivery, and regional hydrography. This analysis reveals that pelagic CdS precipitation can impact the overall Cd isotope signature of certain sediments. Despite pelagic CdS precipitation being a significant contributor to sedimentary Cd inventories in certain settings, it plays only a minor role in the global Cd marine cycle.

5.1.1 Evidence for cadmium sulfide incorporation into sediments

As described previously, CdS can be incorporated into sediments via two mechanisms: pelagic and porewater. First, Cd can precipitate directly out of seawater under anoxic conditions with a permanent or transient source of dissolved H_2S (Plass et al., 2020). Second, Cd that was originally bound by organic matter can be transformed into CdS if it is remineralized and then recaptured by sulfide-containing porewaters (Gobeil et al., 1987; McCorkle and Klinkhammer, 1991). This process can elevate the amount of Cd in the sediment relative to OC. We analyzed samples from three anoxic regions: the Peru Margin, the Cariaco Basin, and the Black Sea, each with varying geographic restriction conditions. The Black Sea and Cariaco Basin are both euxinic (e.g., anoxic and sulfidic). Meanwhile, although the Peru Margin is not classified as a euxinic basin, H_2S may episodically accumulate in the bottom waters when the conditions become stagnant, and nitrate and nitrite are depleted. We examine these three regions together because all three are defined by low oxygen and have evidence for H_2S accumulation, even if the H_2S accumulation is transient.

Our twenty-six samples from the Peru Upwelling region range from the margin (85 m water depth) to the slope (2,025 m water depth) traversing the anoxic margin bottom waters and the nearby oxic bottom waters, making them ideal to examine the enrichments from cadmium sulfide to the sediments, both from pelagic precipitation of CdS out of the bottom water and from Cd that is captured during organic matter remineralization in the sediment.

In a recent study, Plass et al. (2020) used benthic chamber incubation data to show that Cd sulfides could precipitate in near bottom waters and could account for the majority (up to 60 %) of the excess Cd accumulation in Peru Margin sediments. In a follow up study, sequential extraction data provided more evidence that Cd sulfide precipitation from the bottom waters was important to account for Cd delivery and burial in the sediment (Plass et al., 2021). However, while the extraction data illustrated that most of the Cd hosted in the sediment was in the CdS form, additional work was needed to determine whether the CdS was formed in the water column near the sediment-water interface or as a result of organic matter being deposited under conditions where only a portion of OC is retained while Cd burial is more efficiently trapped within the sulfidic porewaters as CdS. The authors of this study calculated the amount of Cd in the sediment from both the organic carbon rain rate and the carbon accumulation rate at 10 cm in the sediment from the same stations along the Peruvian transect from other studies (Dale et al., 2015, 2021). We take a similar approach here for a direct comparison. We multiply our leachable Cd concentrations by the MAR rate given in Dale et al. (2021) from the same station in the Peruvian transect (only five of our samples had an associated MAR). Next, we estimate the Cd arriving in the rain rate and the accumulation rate at 10 cm by using the same Cd:C ratio used in Plass et al. (2021) (e.g., Ho et al., 2003; Moore et al., 2013). The amount of Cd in the sediment that arrived from organic matter should fall between these two values. If the Cd burial reflects the OC that remains in the sediment without any preferential retention of Cd as CdS, then the Cd will reflect the organic matter that has accumulated within the sediment (i.e., the Cd estimated in the accumulation rate). However, if the flux equals the Cd expected from the carbon rain rate, it suggests excess Cd was captured during remineralization beyond the OC that is retained in the sediment. If the flux is greater than the rain rate, it would suggest pelagic CdS precipitation. The findings from the calculation are shown in Table 3 and Figure 4. We find that for sediments that fall within or near the OMZ (85 m

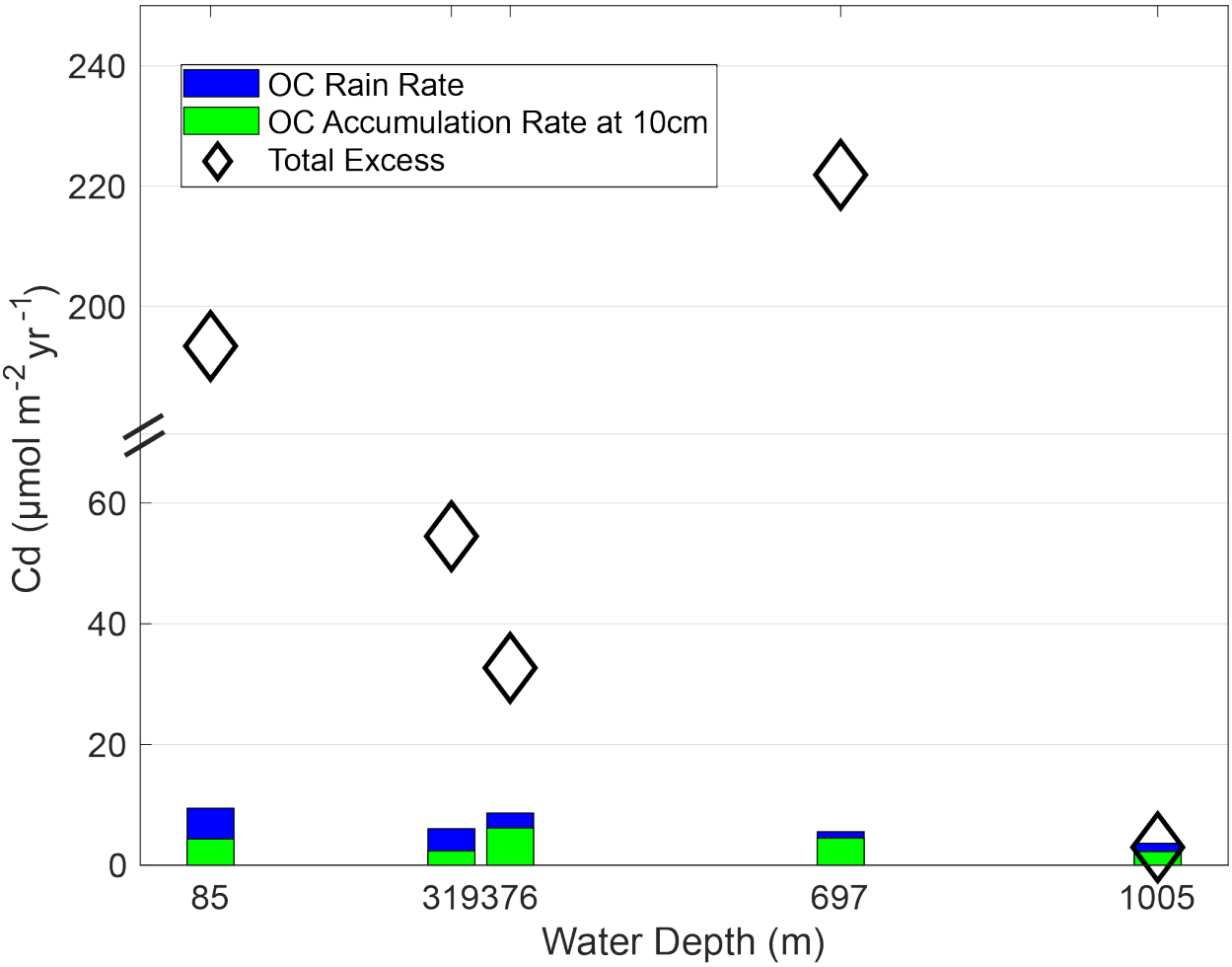

Figure 4. Cadmium excess accumulation is shown by the diamonds and this contribution can come from Cd incorporation from organic matter and CdS pelagic precipitation in the bottom water. The entire bar represents the Cd that can come from the OC rain rate while the green represents what is expected from OC that is accumulated in the sediment at 10 cm. The reader is referred to Plass et al. (2021) to see an analogous figure in the same region. In order of left to right, the Peru Margin stations collected along the 11˚S transect are Station 568, 449, 481, 459, 549. More information on these stations can be found in Dale et al. (2015) and Scholz et al. (2011). The station numbering scheme is from Scholz et al. (2011)

to 697 m), Cd from the rain rate of OC can account for a maximum of ~20 % of the Cd hosted in the leachable fraction. The Cd fluxes that we estimate in the sediment are far higher than what can be explained by organic matter rain rates alone. Thus, our data suggest that CdS formation in the bottom waters is an important delivery vector of Cd to the sediment within the core of the Peru Margin OMZ.

Figure 5 shows that the Cd:OC relationship develops as the samples transition from sediment that is bathed in anoxic bottom water where CdS may form to sediment that underlies oxic waters where CdS is not delivered pelagically to the sediment. Two sediment samples show enrichment of Cd outside of the defined OMZ (e.g., 100 - 500 meters water depth). However, both of these samples are near the OMZ (at 85 meters and 697 meters). Because these samples are close to the OMZ boundary, we suggest that they formed from the same processes that are driving CdS formation within the core of the OMZ.

Unlike in the Peru Margin, the samples from the Black Sea and the Cariaco Basin do not suggest that pelagic precipitation of CdS is an important delivery mechanism. The Cariaco Basin samples have Cd:OC values on the order of 4 μmol Cd/ mol OC, which is within the range of Cd:OC values that are supported by organic matter delivery (Ho et al., 2003; Bourne et al., 2018). Likewise, the Cd:C ratio in the Black Sea can be reasonably explained by organic delivery of Cd as well (e.g., ~2 μmol Cd/ mol OC; Figure 2).

Since all of these regions have anoxic bottom waters with a presence of free sulfides, it may at first be surprising that they do not all exhibit evidence for pelagic precipitation of CdS to the sediment. However, these data suggest that the degree of restriction likely influences whether CdS is a primary vector of delivery of Cd to a basin. Unlike the Peru Margin, the Cariaco Basin and the Black Sea are restricted and have limited mixing with open ocean seawater. We suggest that any dissolved Cd that does enter into the euxinic bottom waters may be stripped out of the water column soon after it encounters the euxinic bottom waters. Thus, the dissolved Cd may not persist long enough to be a vector of Cd delivery over the entire basin. This theory is supported by the Cd concentrations observed in both the Black Sea and the Cariaco Basin. Studies have shown that in the modern Cariaco Basin, Cd concentrations of water below the chemocline are generally <0.02 nM Cd, and in the modern Black Sea concentrations are even lower below the chemocline

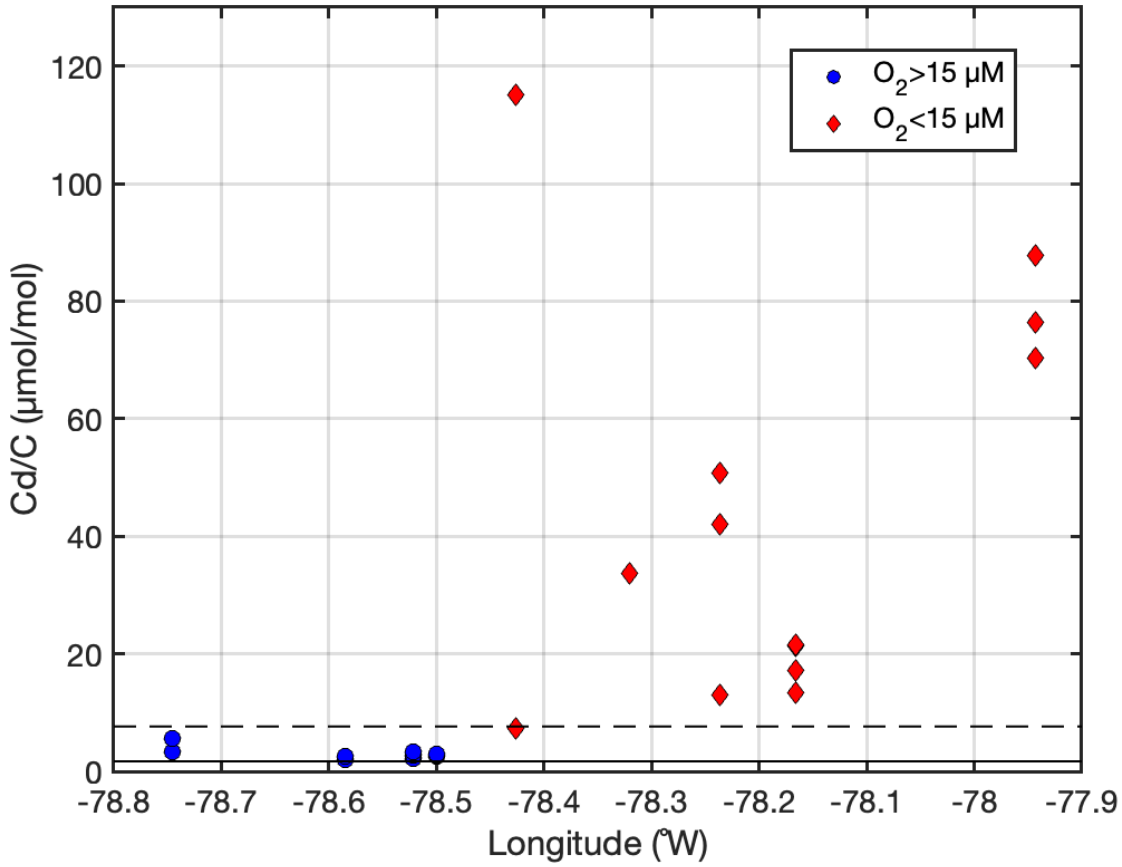

Figure 5. Data color coded by bottom water oxygen content (i.e., < 15µM as red diamonds and > 15 µM as blue circles). The dotted lines represent the range of expected Cd:OC via delivery with organic matter based on previous studies (e.g., Ho et al., 2003; Bourne et al., 2018). The data was collected along the 11˚S transect in the Peru Upwelling Zone. Station numbering is found in Table 1 under sample name.

(e.g., <0.01 nM; Tankéré et al., 2001; Little et al., 2015). The sediment samples measured in this study all come from substantially deeper than the chemocline. Therefore, as there is no upwelled supply of Cd, we expect the Cd that formed CdS to be stripped out and deposited in the sediment closer to where the Cd first encounters the euxinic water (e.g., in proximity to the edges of the basin). For example, Little et al. (2015) suggested that a minor amount of seawater-derived CdS was present in sediment from a core in the Cariaco Basin located near to the Tortuga bank between two local deepwater maxima (Fig. 1). However, in the other samples measured in the Cariaco Basin and the Black Sea, it appears that little, if any, CdS makes it to the sediments through pelagic precipitation because of the low Cd supply.

5.1.2 Impact of pelagic cadmium sulfide precipitation on Peru Margin cadmium isotope compositions

Pelagic CdS also influences sedimentary Cd isotope compositions along the Peru Margin. As suggested in Section 5.1.1, we expect the leachable Cd in sediments from the Cariaco Basin and the Black Sea to primarily reflect organically derived Cd. The restricted nature of these basins likely results in Cd being primarily influenced by local inputs. Indeed, the surface water dissolved Cd in the Cariaco Basin is very low (Roshan et al., 2017; Roshan and DeVries, 2021), which is coupled with sediment Cd isotope compositions that are heavy (on average, $\delta^{114}Cd = +0.28 \pm 0.03$ ‰, n=12). The isotope composition of the Black Sea sediments is isotopically lighter than the Cariaco Basin sediments, with an average value of = +0.11 ± 0.05 ‰ (n=5). These Cd isotope compositions are complemented by Black Sea surface water Cd concentrations that are higher than the Cariaco Basin (Roshan and DeVries, 2021). We suggest that the restricted nature of both basins limit physical mixing of Cd replete waters into the surface as there is no shortage of sulfide in the water column. Therefore, the Cd isotope composition of organic matter produced in the surface waters most likely reflects the source of Cd to each region (i.e., open ocean seawater with $\delta^{114}Cd$ = +0.25 ‰ for the Cariaco Basin and riverine inputs with $\delta^{114}Cd$ = +0.1 ‰ in the Black Sea (Lambelet et al., 2013). Isotope fractionation during biological uptake is also possible, although less likely given the similarities with the Cd isotope compositions of likely Cd source material.

Unlike the Cariaco Basin and the Black Sea, the high excess Cd in the Peru Margin sediments is evidence for pelagic precipitation of cadmium sulfides in parts of the region, which will impact the isotope composition of the sediment. Figure 6 shows the distribution of the $\delta^{114}Cd$

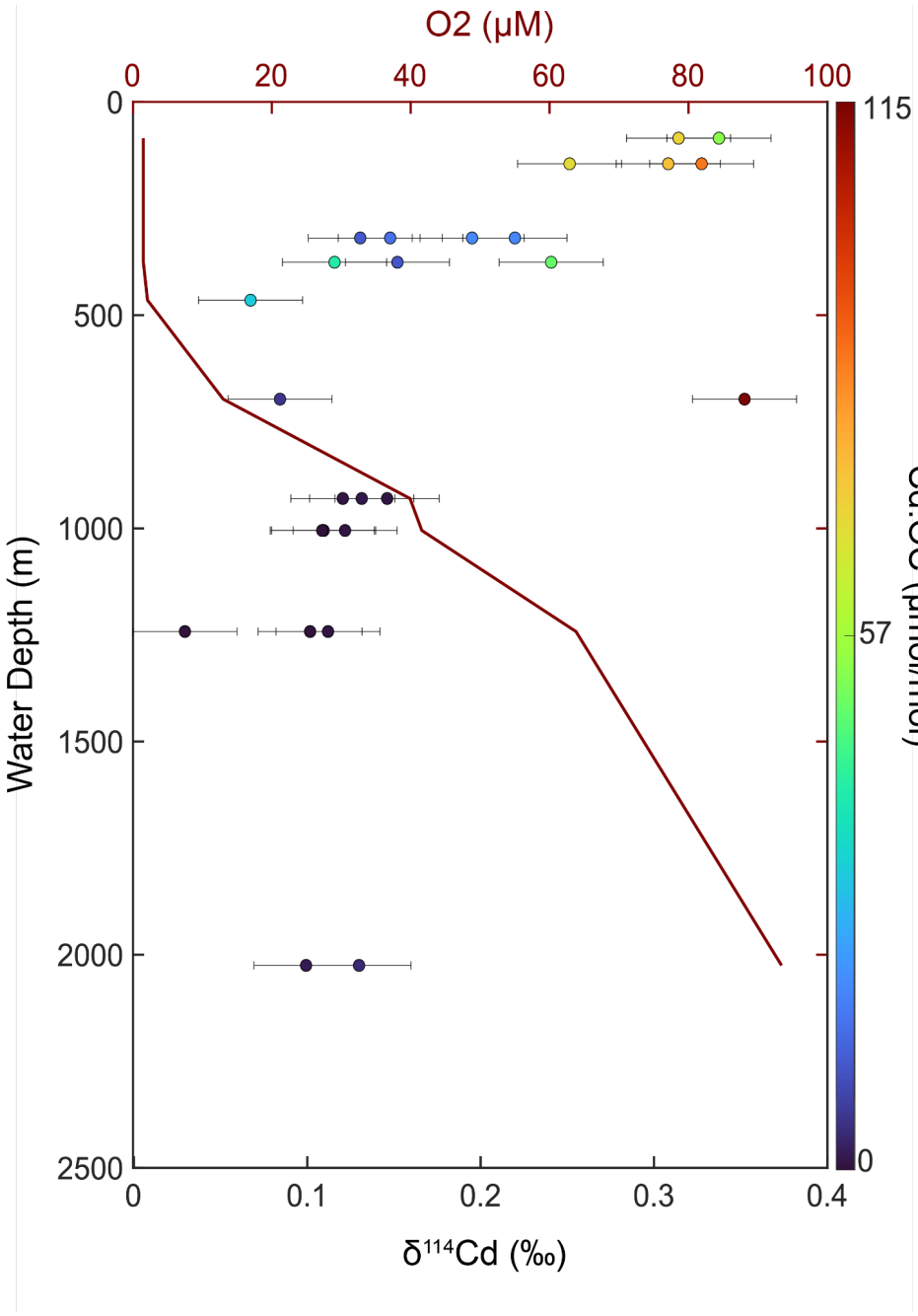

Figure 6. All data points plotted from Peru Margin Sediments (including some values measured within the same core, see Table 1 for sample details). Top axis and red line show the bottom water oxygen content against water depth. Data points show the isotopic composition relative to water depth. The color bar shows the Cd:OC ratios. The darkest blue values are wholly supported by organic matter whereas all other colors have excess Cd.

isotope composition across the margin. The samples that underlie the OMZ and have anoxic bottom waters and experience transient sulfidic water, have δ^{114}Cd isotope values between +0.12 and +0.35 ‰. In the oxic bottom waters outside the OMZ (e.g., no evidence of free sulfides and oxic bottom waters), the δ^{114}Cd values span a narrower range from +0.03 to +0.15 ‰, with an average value of +0.11 ‰.

We propose that the isotope composition of the sediments throughout this region reflects the combined compositions of CdS precipitated directly from seawater and Cd that was incorporated into organic matter, where the region outside of the OMZ should be dominated by Cd incorporation into organic matter. In Section 5.1.1, we argued that the predominant formation of excess Cd in the sediment underlying the OMZ is from CdS that forms in the bottom waters. This finding is corroborated by the differences in isotope composition of these two regions. Cadmium sulfide reprecipitation in the porewater is expected to quantitatively capture Cd from organic matter. If it were a dominant source, we would not expect large deviations in the isotope compositions of the sediments underlying the OMZ versus those in the oxic regions.

We can determine the relative importance of CdS formation and Cd that is still bound by organic matter by examining the sedimentary Cd:OC ratio. Values for Cd:OC ratios from organic-derived sources range between 1.69 to 7.66 μmol Cd/ mol C. Here, we use a ratio of 7.66 because those were the ratios measured in Peruvian samples (Bourne et al., 2018). We construct a mixing line between the sulfide and organic matter components. We observe that our two samples dominated by cadmium sulfide (i.e., greater than 90 % CdS) possess a mean δ^{114}Cd value of +0.31 ± 0.03 ‰ (Figure 7). Our average organic matter dominated samples (i.e., 0 % CdS) have an average δ^{114}Cd of +0.11 ± 0.03 ‰ (2SD; n= 8). Two recent studies suggested that the Cd isotope composition in the Peru Margin above 500 meters of water depth is ~ +0.5 ‰ (John et al., 2018; Xie et al., 2019). This offset implies a Cd isotope fractionation, $\Delta^{114}Cd_{CdS\text{-}medium}$, of approximately –0.2‰. This finding aligns well with previous laboratory based studies that found that the observed isotope fractionation factor for CdS precipitation between the CdS solid phase and the medium ($\Delta^{114}Cd_{CdS\text{-}medium}$) is approximately –0.3‰ (Guinoiseau et al., 2018).

Figure 7 does show that some of the samples fall off of the mixing line between OC:Cd and δ^{114}Cd. We suggest that these samples may have more influence from reprecipitation of Cd that was derived from organic matter and this reprecipitation could be the reason for the lighter Cd isotope signature that is observed.

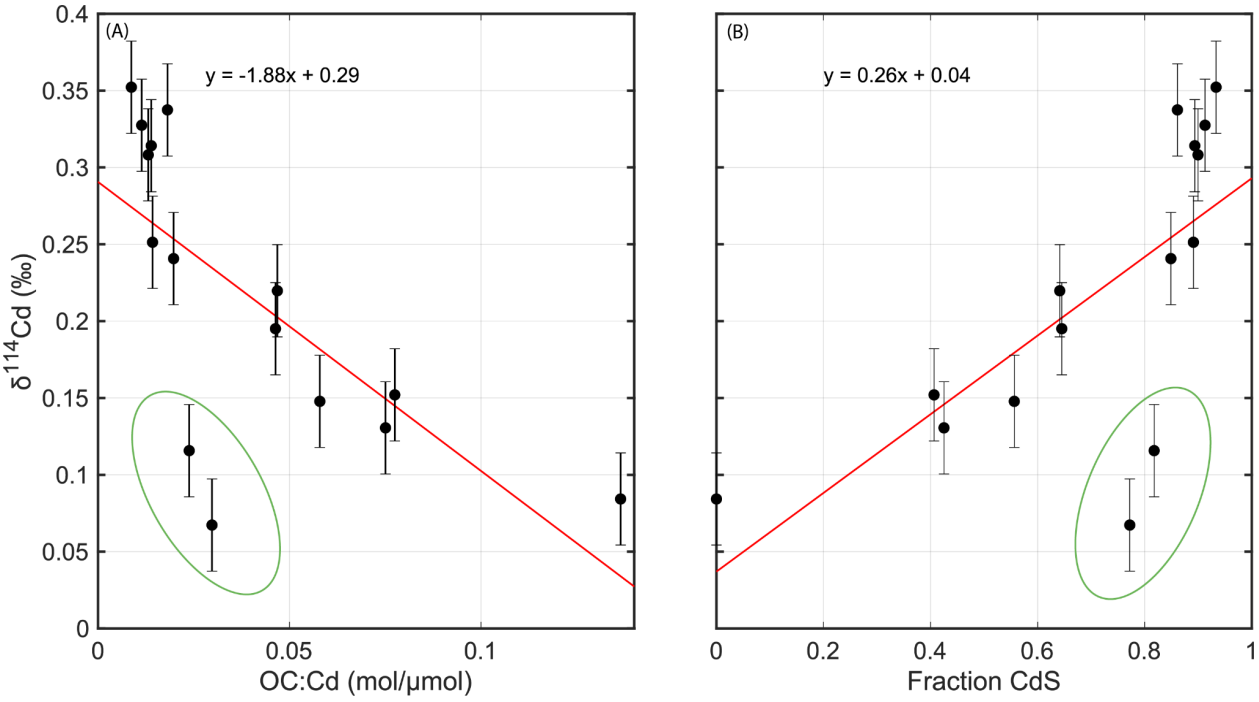

Figure 7. (A) Shows the trend between δ^{114}Cd and Cd:OC ratio for all samples that have Cd concentrations that are higher than those supported by organic matter inputs alone (i.e., have evidence for CdS inputs). The red line is the trend line that shows the relationship between the δ^{114}Cd and Cd:OC ratio. (B) Assumes that any Cd:OC that is in excess of the range of values from Ho et al. (2003) and Bourne et al. (2018) is from inputs of CdS. The fraction of this excess is shown versus δ^{114}Cd. The trend line shows the relationship between this fraction and δ^{114}Cd. The two points highlighted in green fall off of both trend lines. We posit that these samples may have CdS that forms from remineralized matter instead of bottom water CdS precipitation.

5.1.3 Is CdS formation important to the global marine mass balance of Cd?

The three anoxic and (periodically) euxinic regions showcase how the $\delta^{114}Cd$ of sediments depends on redox conditions, organic matter delivery, and regional hydrography. The presence of free sulfides and a supply of dissolved Cd to the bottom water results in elevated Cd concentrations and heavier $\delta^{114}Cd$ isotope values. However, free sulfides without a supply of dissolved Cd prevents significant CdS from forming. Regions where both these conditions are met (e.g., anoxic and at least periodic H_2S accumulation in the bottom waters *and* a supply of Cd) are small compared to the rest of the margins where the bottom waters tend to have measurable oxygen concentrations and/or no evidence for free sulfide in the bottom waters. Indeed, the only place found to date with ample evidence for the formation of cadmium sulfides from seawater is on the Peru Margin. It is certainly possible that the Namibian margin, which also has sulfidic events (Brüchert et al., 2006; Currie et al., 2018), experiences a similar CdS drawdown. However, we measure two samples from this region, which are albeit from the oxic portion, and do not see evidence for CdS formation. While one study examined Cd concentrations along the Namibian margin in a region where sediments are expected to emit H_2S, the paper concluded that the Cd that reached the sediments was from primary productivity and reprecipitation in the porewaters (Borchers et al., 2005), despite suggesting other elements may pelagically precipitate as sulfides in the bottom water. More work should be done on the Namibian margin where sulfidic events occur to interrogate whether the Peru Margin has an analog.

Despite not having samples from the region of the Namibian margin that experience sulfidic events, we do measure several samples from the low oxygen portions of the Arabian Sea and the California margin. We do not see any similar excess of CdS that can be linked to pelagic bottom water CdS formation. Therefore, we do not believe that this formation of CdS is a general OMZ feature that can account for a substantial portion of CdS deposition on the margins. It appears that sulfidic buildup in bottom waters is essential for excess CdS to become significant.

To estimate the amount of CdS that is buried in sediment on the Peru Margin we approximate the amount of CdS that may be expected to form during a sulfidic event. Schunck et al. 2013 reported a sulfidic plume in the Peru Margin that was 5,500 km^2 in size from 12˚S to 14˚S, and was the largest plume observed in ocean waters. Tegler et al. *(subm.)* suggests that the OC flux to the Peru Margin area is on the order of 1.7 mol OC m^{-2} yr^{-1}, which would correspond to a deposition of 13 μmol Cd yr^{-1} over such an area, using the ratio of 7.6 μmol Cd: mol OC. On

average, our samples in the Peru Margin that show evidence of CdS deposition are between 2 and 15 times higher than what is expected from organic matter alone, with an average value of 6 times higher. Thus, the Cd deposition in that region would be a maximum of 1.8×10^6 mol Cd yr^{-1}. However, if the total global organic matter flux of Cd is on the order of 5.7×10^7 mol Cd yr^{-1}(calculated in section 5.3.1) this would only account for 2 % of global Cd deposition. If the same process exists to the same extent in the Namibian margin, this would still account for ~ 4% of global Cd deposition. Thus, we conclude that pelagic CdS deposition is minimal in the global marine Cd cycle. For this reason, we turn to regions with oxygen at the sediment-water interface to understand the global Cd fluxes into the sediment.

5.2. Cadmium deposition under oxic conditions

In the previous section, we suggested that pelagic precipitation of CdS, while important locally, is not important to the global mass balance. We now turn to sediments deposited under oxic conditions, which, given their vast areal extent, are expected to be important for the global Cd mass balance. In these settings, most Cd arrives at the sediment associated with organic matter. Precipitation of CdS still occurs, but only in porewaters. We use a multiple linear regression analysis to show that the sediment's Cd isotope composition is significantly related to surface water [Cd] and bottom water [O_2]. Surprisingly, the relationship between surface [Cd] and sediment isotope composition is contrary to what is expected from the uptake of Cd in the surface water by microbes. We propose that this trend may reflect additions of Cd from other sources and that the relationship between the isotope composition of the sediments and [O_2] could relate to remineralization.

5.2.1 Cadmium concentrations and δ^{114}Cd in oxic environments

The quantity of Cd deposited in sediments underlying oxic regions depends primarily on the amount of organic matter present (Fig. 2b). While there is no evidence for pelagic precipitation of CdS out of bottom water in these regions, it is certainly possible that some CdS may form in porewaters after remineralization of organic matter within the sediments. The two lines included in Figure 2 are the Cd:OC ratio expected from the extended Redfield value (Ho et al., 2003) and measured field particle data (Bourne et al., 2018). All of our data fit on or near these estimated values, so a significant subsidy of pelagic or porewater CdS is not needed to explain the data.

Although we cannot conclusively state that these samples are free from CdS formation during remineralization of organic matter, such effects are clearly secondary and are unlikely to affect the measured leachable sediment Cd isotope compositions as sulfides in the porewater are expected to quantitatively capture any liberated Cd.

The range of δ^{114}Cd in the 34 oxic sediment samples falls between −0.18 and +0.25 ‰. In order to estimate the global average Cd isotope composition of sediment organic matter, it is important to understand what processes may control the isotopic variation of the organic matter that arrives at the seafloor. Because δ^{114}Cd in seawater and marine particles are thought to be controlled by parameters such as primary productivity, relative nutrient utilization in surface waters, and the length scale and intensity of remineralization, we performed a multiple linear regression analysis using variables related to these properties: leachable Cd concentrations in the sediment ($[Cd]_{leachable}$), Cd concentration of the surface water above a sediment site ($[Cd]_{surface}$), the O_2 concentration of the bottom water at the site of sedimentation ($[O_2]_{BW}$), the OC (%) content of the sediment (OC %), and the depth of the overlying water column (z). We used this analysis to determine which of these variables are most strongly related to the leachable Cd isotope composition of the sediment. The analysis involved compiling the oxic data into the following Equation 6:

$$\delta^{114}Cd_{sed} = \boldsymbol{\alpha} \times [Cd]_{leachable} + \beta \times [Cd]_{surface} + \gamma \times [O_2]_{bw} + \varepsilon \times water\ depth + \boldsymbol{\zeta} \times OC\ (\%) + b \quad (6)$$

where are $\boldsymbol{\alpha}$, β, γ, ε, and $\boldsymbol{\zeta}$ are the coefficients subject to optimization and b is a constant. All parameters were measured or, in the case of $[O_2]_{BW}$, extrapolated from the WOA 2018. All values used in the analysis are compiled in Table 4.

We optimized the equations for every combination of parameters (n=63 equations) to explore the range of the parameter space. We determined which coefficients provided the best offset by minimizing the root mean squared deviation between the measured and predicted sedimentary Cd isotope values. The results reveal that only two parameters, $[Cd]_{surface}$ and $[O_2]_{bw}$, are significantly related to the Cd isotope composition of the sediment. We performed an F-test to identify that using the model that includes both $[Cd]_{surface}$ and $[O_2]_{bw}$ are not statistically different from using the model with all of the variables. However, using the two parameters together is statistically distinct from using the two parameters separately. While these

variables appear to be codependent (i.e., they have a better correlation with the δ^{114}Cd of the sediment when used together than when applied independently) we will treat them as independent parameters as well as co-dependent variables. We recognize that these variables likely do depend on one another, but in order to understand their role theoretically, it is necessary to explore them independently to better understand what physical underpinning may drive their relationship to δ^{114}Cd. Thus, we examine three models that predict the isotope composition of the sediment: linear regressions using each of the variables individually and a linear combination of the two variables together.

The first two models can be described with a simple linear regression: The r^2 value of $[Cd]_{surface}$and δ^{114}Cd is 0.4 and the r^2 value of $[O_2]_{bw}$and δ^{114}Cd is 0.6. We can quantify the significance of r^2 by determining the likelihood that correlations are statistically significant. We use statistical tables given in (Taylor, 1982) to determine the correlation of individual parameters with the isotope composition. We find that the surface water Cd concentrations and sediment isotope compositions have a 92 % probability of being meaningfully correlated. The oxygen bottom water and isotope compositions have a 99.5 % chance of being meaningfully correlated. We also calculate an adjusted r^2 of 0.65 for the combination of both variables and find greater than 99.5 % that both of these variables are significantly correlated with δ^{114}Cd of the sediments.

Though these parameters are correlated with our sedimentary data, the mechanisms underpinning these correlations are complex. In the following section, we examine the extent to which these correlations may be used to predict the isotope composition of the sediment.

5.2.2 Relationship between surface seawater [Cd] and sedimentary δ^{114}Cd

The linear regression shows that surface Cd concentrations are correlated with δ^{114}Cd (Figure 8). The correlation suggests that as the Cd surface concentrations increase, sedimentary δ^{114}Cd increases. However, this behavior is the opposite to the relationship expected based on biological uptake of Cd from surface seawater. Our sediment samples underlie surface waters with some of the lowest Cd concentrations observed in global seawater (e.g., <0.15 nM). If we extrapolate our relationship over the entire range of surface Cd concentrations in the ocean (up to 1.2 nM), the resulting δ^{114}Cd of sedimentary organic matter at the highest surface water [Cd] reaches values of ~+1.3 ‰, which is unrealistic and underscores that the relationship observed in this study (i.e., biased toward samples that underlie low surface Cd concentrations). This trend is

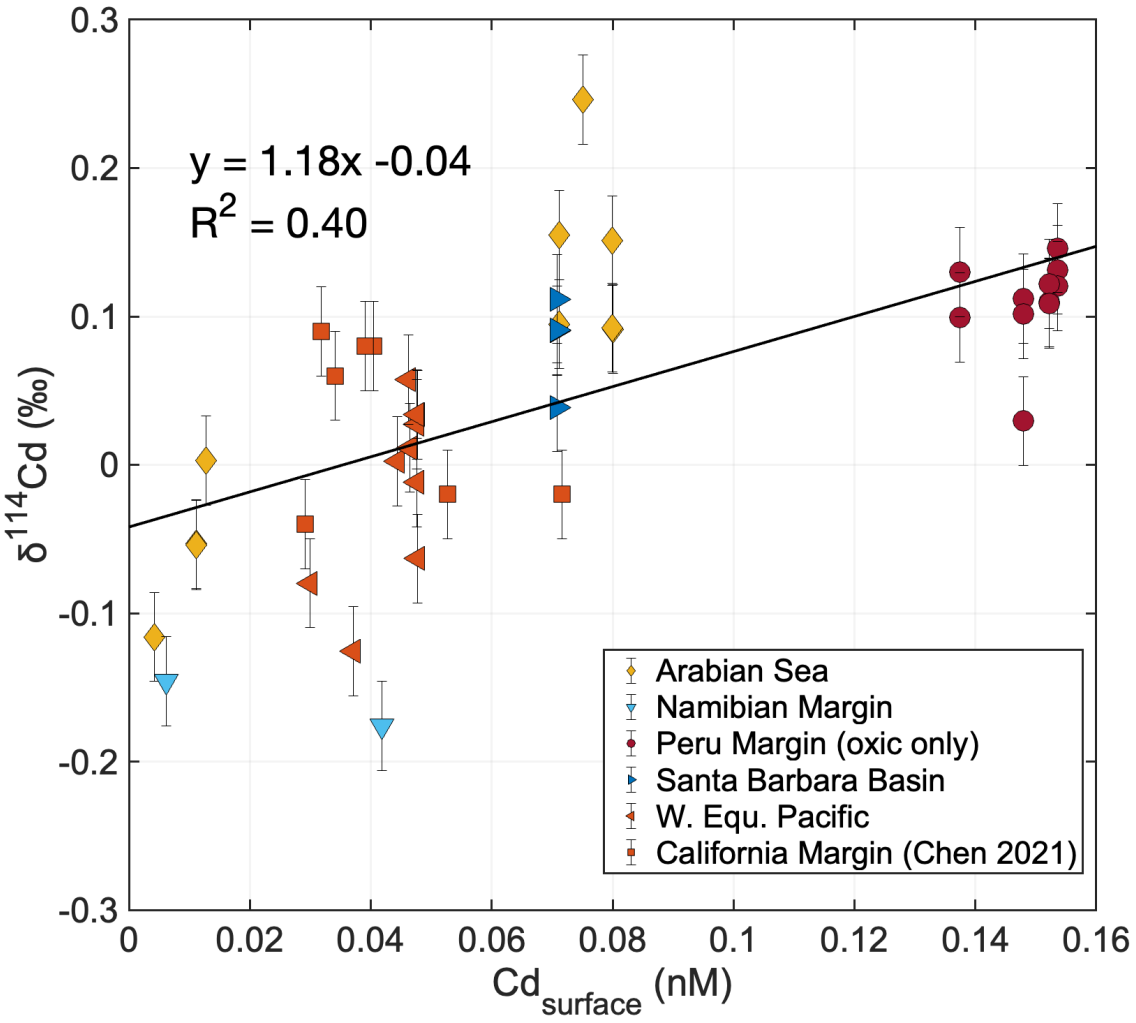

Figure 8. Surface water concentration from Roshan et al. (2021) against the sediment $\delta^{114}Cd$ composition. This correlation suggests that under low surface water Cd concentrations (between 0 and 0.15 nM), the isotope composition becomes heavier as Cd becomes more concentrated. This is likely from the addition of upward mixing of waters or aerosol sources of Cd, both sources are expected to be light relative to the biologically fractionated material.

unlikely to continue at higher surface Cd concentrations. Instead, we suggest that the Cd isotope compositions of sediments underlying Cd-depleted surface seawater behave differently to those underlying Cd-replete regions. This is analogous to the observations made in the water column. Indeed, cadmium isotope fractionation in seawater varies between high-[Cd] HNLC regions, such as the Subarctic North Pacific and Southern Oceans (e.g., Sieber et al., 2023; Xue et al., 2013), and low-[Cd] oligotrophic regions, including the South Pacific and South Atlantic (Gault-Ringold et al., 2012; Xie et al., 2017; George et al., 2019).

A number of explanations have been proposed for these different fractionation behaviors. In regions with low concentrations of Cd in the surface water, the surface isotope composition may be increasingly influenced by vertical inputs of Cd. Cadmium may be added to the surface waters via two mechanisms. First, additions of Cd from aerosols may influence the Cd isotope composition of surface waters (Sieber et al., 2023). Aeolian deposition of Cd is isotopically light (ranging from −1.91 ‰ and −0.07 ‰; Rehkämper et al., 2011; Sieber et al., 2023). Lateral inputs of dust to low Cd surface waters have caused Cd trends to deviate from the biologically mediated trends toward these lighter values, like what we observe in the sediment. Additionally, the upward mixing of deep waters may also contribute to the lighter-than-expected δ^{114}Cd in these low [Cd] regions. This process has been previously documented for multiple regions of the ocean (Abouchami et al., 2011; Xue et al., 2013): whereas δ^{114}Cd of surface seawater follows a Rayleigh- or Rayleigh-like trend at high [Cd], this relationship breaks down at very low Cd surface seawater concentrations (Figure 9). When plotted together, the dissolved and sedimentary global data suggest that there is a broad positive trend of sedimentary δ^{114}Cd below Cd surface seawater concentrations of ~0.15 nM (Figure 10), which is consistent with the process of additions of light aerosol Cd particles and/or upward mixing of deep water with lighter isotope values (relative to the heavier surface values). The more Cd in the surface waters, the less the Cd isotope composition may be affected by upward mixing processes. However, individual surface seawater samples provide only a snapshot of the upward mixing processes that are variable both geographically and temporally. Sediment samples will average these processes over longer time periods (in our case decades or more depending on sedimentation rates). The substantially stronger relationship between $[Cd]_{surf}$ and δ^{114}Cd sediment than for seawater samples may suggest that aeolian deposition of isotopically light particles or upward mixing of deeper waters, over decadal time scales, is a dominant process at low surface Cd concentrations.

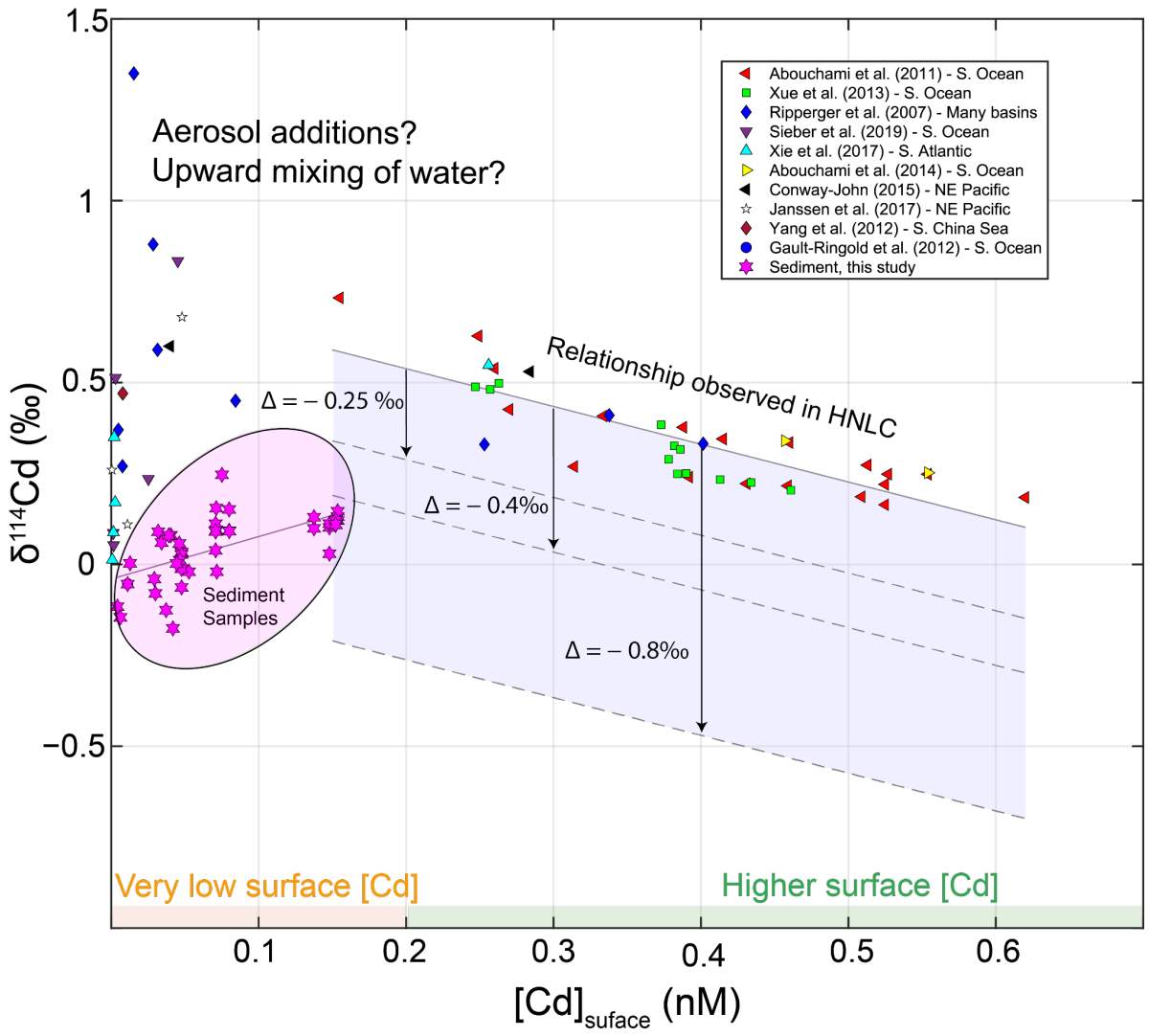

Figure 9. Dissolved δ^{114}Cd surface seawater samples versus surface Cd concentrations are shown alongside δ^{114}Cd sediment samples (highlighted in pink). The seawater data at [Cd] concentrations <0.15 nM fall off of the expected HNLC Rayleigh fractionation relationship. The pink stars are sediment data from this study. They show in regions with low surface Cd that the sediment samples are characterized by a broad positive trend. This is likely related to additions from deepwater and aerosols. The shaded blue region is the range of expected sediment values if the seawater rayleigh-like behavior is preserved in the sediment underlying regions with higher surface Cd concentrations. The fractionation factors shown here include Δ^{114}Cd = −0.25, −0.4, or −0.8 ‰. The general location for the seawater samples is given in the legend name and the sediment locations can be seen in Figure 8.

Aeolian deposition and upward mixing of deepwater may explain how our sedimentary Cd appears to become isotopically lighter at lower Cd surface concentrations, despite predictions that the opposite pattern is expected. However, it is possible that sediments deposited underneath regions with significantly higher Cd surface concentrations (i.e., 0.15-1.2 nM) do follow the seawater trends that suggest Rayleigh fractionation or open-system steady state fractionation in Cd-replete conditions. The missing sediment Cd isotope data deposited in high [Cd] regions of the ocean may be particularly important because these regions encompass nearly all of the high latitude areas (Roshan and DeVries, 2021), which also accounts for ~35 % of global OC deposition (Tegler et al., *subm.*).

We can gain insight into the sedimentary isotope composition underlying Cd replete conditions by considering studies characterizing the Cd isotope systematics in surface waters of Cd-replete regions (Abouchami et al., 2011; Xue et al., 2013). As noted, these studies illustrate that in the surface waters with a Cd concentration greater than 0.15 nM, higher Cd concentrations are negatively correlated with δ^{114}Cd seawater compositions (Figure 9). The application of a constant fractionation factor would allow us to predict, to a first order, the Cd isotope composition of sedimentary organic matter in Cd replete regions of the ocean. According to modeling and field studies, an appropriate fractionation factor for a Cd-replete region would likely fall between Δ^{114}Cd = −0.25‰ and −0.8‰ (Xue et al., 2013), with a value of −0.4 ‰ dominating in the Southern Ocean. Figure 9 shows the two relationships, the measured values under the low concentration seawater and the theoretical values under Cd-replete conditions, that may set the Cd isotope composition of the sediment: a broad positive trend for conditions with Cd<0.15 nM and a negative trend for Cd>0.15 nM. In section 5.3.2, we will estimate the isotope mass balance assuming that these trends together govern the Cd isotope composition of the sediment.

5.2.3 Correlations between O_2 and δ^{114}Cd

The second significant correlation is between the bottom water [O_2] and leachable sedimentary δ^{114}Cd. The trend suggests that as bottom water [O_2] increases, the δ^{114}Cd of sediments becomes lighter (Figure 10). One plausible process that is likely to govern this trend is Cd isotope fractionation that occurs during organic matter remineralization. In order to better understand the role that remineralization may play in modifying the δ^{114}Cd of sinking particles, we examined profiles of pδ^{114}Cd from the fully oxic water column of the Ross Sea and compare

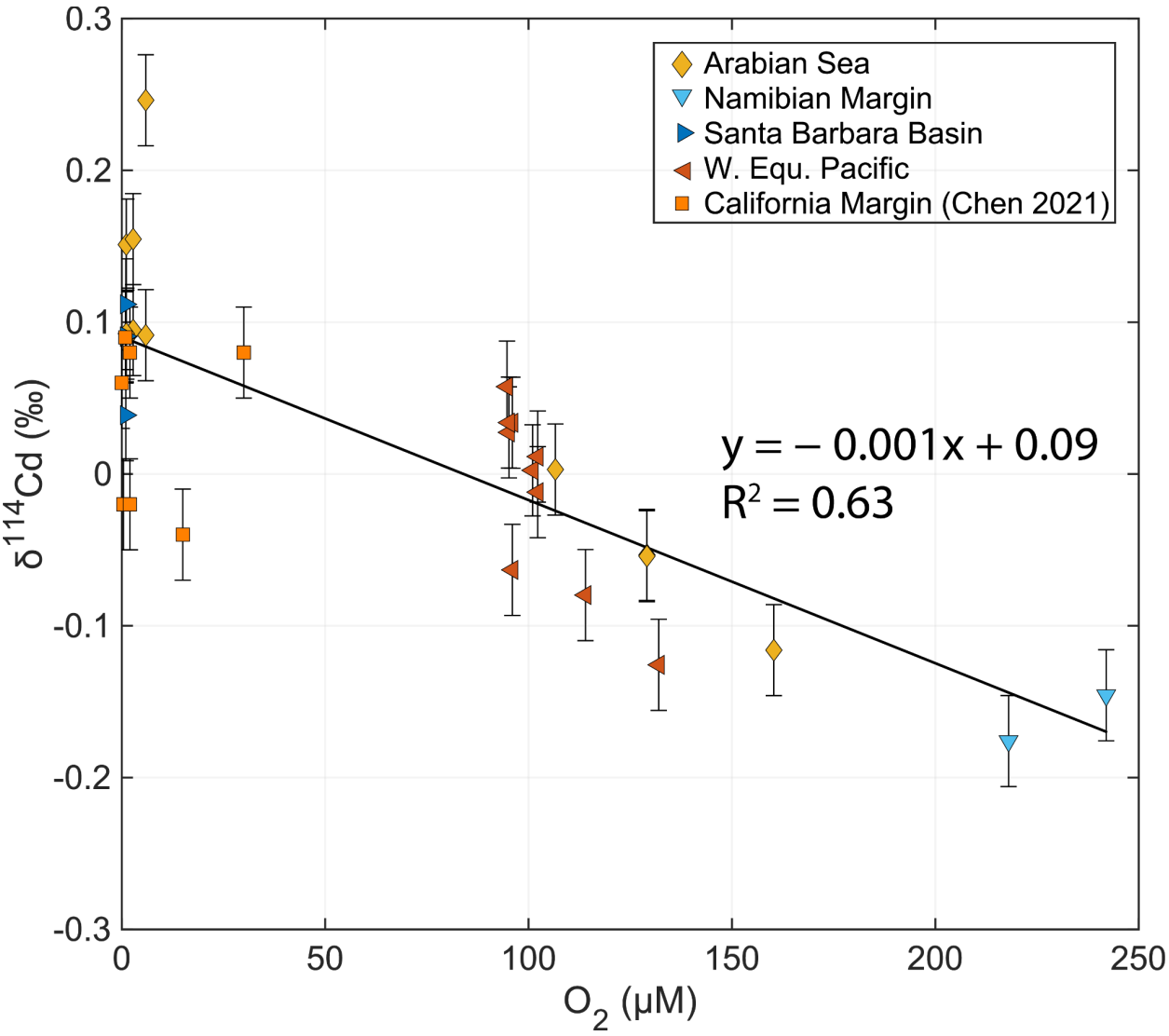

Figure 10. Bottom water oxygen value measured or estimated from WOA18, against sediment $\delta^{114}Cd$. All sediments with evidence for CdS influences are removed. Only oxic and suboxic sediments are included in this figure.

them with $p\delta^{114}Cd$ from OMZs. We compare these two regions as they serve as endmembers of oxygen concentrations in the water column.

The profiles from the Ross Sea were collected in a fully oxic water column ($[O_2]$ >160 μM; Figure 3a-d). In contrast, two other studies in the northeast Pacific and North Atlantic have measured $p\delta^{114}Cd$ in regions with lower oxygen. Samples from Janssen et al., (2019) covered a region with expansive low O_2 subsurface waters, at times reaching an O_2 concentration on the order of ~ 10 μM. Janssen et al. (2014) measured $p\delta^{114}Cd$ in a region with O_2 concentration that reached a minimum of ~50 μM.

The Ross Sea, the northeast Pacific profiles (0.8 - 51μm size fraction), and the North Atlantic profiles (>0.2μm size fraction) all show that there is a change in the isotopic composition of $p\delta^{114}Cd$ with depth. Broadly, each of the profiles exhibit a similar shape: the surface samples are heavy, the subsurface samples evolve toward lighter values, and the deepest samples return to heavier values (albeit never as heavy as the surface value). These profiles cover different depth ranges: the Ross Sea and North Atlantic data are measured to 400-600 m, while the two Pacific profiles extend to ~1,500 m. Despite the differences, there is substantial and similar vertical variation in $p\delta^{114}Cd$ in both fully oxic water conditions and within the OMZ. The evolution of these particles likely points to Cd isotope fractionation during remineralization or preferential remineralization of pools of Cd with variable lability (e.g., Bourne et al., 2018; Janssen et al., 2019).

However, the small size particles may not be a good representation of what particles ultimately arrive at the seafloor. The small size fraction particles may sink much more slowly than the large size fraction particles, if at all, and may undergo more processing before arriving at the seafloor. The $p\delta^{114}Cd$ of large size particles appear to be less modified during their transit through the upper part of the water column. Indeed, at stations 0, 2 and 24 all of the samples, except the surface sample, are within uncertainty of one another (Figure 4e-h). These data suggest that the LSF samples are not as influenced by remineralization as the SSF under oxic conditions. However, most of the samples in the Ross Sea data were taken on the continental shelf and thus cover only the upper ~400 meters of water depth. Deeper data from Station 14, which was located beyond the shelf break with water depth of 1,887 m, suggests that there may be other processes that modify the $p\delta^{114}Cd$ of large particles deeper in the water column. At St. 14, the $p\delta^{114}Cd$ of the LSF increases with depth. Assuming that sinking particles represent the residual material that is not

remineralized, these paired data would suggest that remineralization tends to concentrate 'light' Cd isotopes in the SSF and render exported LSF material 'heavy.' This finding would implicate microbial processes in setting the $p\delta^{114}Cd$ of exported matter and points toward a potential mechanism that explains why water column [O_2] can predict sedimentary $\delta^{114}Cd$. Future studies should examine the large size fraction particles across various redox conditions and over the entirety of the water column to determine if remineralization is likely to induce substantial Cd isotope fractionation that is incorporated into sediments.

While the particulate data support a link between remineralization and Cd isotope fractionation, the $p\delta^{114}Cd$ values themselves do not explain the trends observed in the sediments. The suspended SSF particles have light $p\delta^{114}Cd$ regardless of the [O_2] in the water column, as shown by the similar relationships in the oxic Southern Ocean and the OMZ in the Pacific Ocean (Janssen et al., 2019). In contrast, the sediments themselves show that the $p\delta^{114}Cd$ decreases with increasing [O_2] bottom water. Therefore, there is currently no obvious way to relate the correlation between sedimentary $\delta^{114}Cd$ with the water column particulate profiles.

Despite not having a clear explanation for the link between bottom water oxygen and sedimentary $\delta^{114}Cd$, our sediment data do show a correlation that might be related to some aspect of organic matter remineralization. Even if we are unable to explain the correlation with water column particulate data mechanistically, we can use the empirical relationship to estimate what the global isotope mass balance would be if the relationship holds true globally. We will calculate the isotope mass balance based on this relationship in Section 5.3.3.

5.3. Estimating global cadmium burial

Here we estimate the global Cd mass balance of Cd and its isotopes. We first establish likely Cd fluxes based on estimates of OC burial and Cd:OC ratios. Then we explore the isotope mass balance into margin sediments based on two approaches: one based on relationships to surface water [Cd] and another to bottom water [O_2]. This exercise reveals the need for more measurements of $\delta^{114}Cd$ in sediments in oxic regions with high surface Cd concentrations to further validate and refine these results.

5.3.1. Cadmium buried with organic matter

Our samples, together with literature data, reveal that leachable sedimentary Cd contents deposited under oxic conditions are, on a global basis, mostly controlled by delivery of organic matter because their Cd:OC ratios (2.9 ± 2.2 μmol Cd/mol OC; n=32, 2SD) are similar to published values for marine organic particles (1.69 and 7.66 μmol Cd/mol OC) (Ho et al., 2003; Bourne et al., 2018). It is important to note that samples from the Namibian Margin have Cd:OC ratios substantially higher than all other oxic sediments above this ratio. These samples are low in both Cd and OC, thus uncertainty in measurement may skew their final ratios. Therefore, they are not included in estimating the Cd:OC ratios but are still expected to represent Cd derived from organic matter. Recent studies have suggested that the total organic matter flux onto the continental margins is 19.4 Tmol OC yr^{-1} (e.g., Tegler et al., subm.). Using our Cd:OC ratio of 2.9 ± 2.2 μmol Cd/mol OC, we estimate that the global Cd flux into the margin sediment is $(5.6 \pm 4.3) \times 10^7$ mol Cd yr^{-1}. This value aligns well with other global estimates of 6.2×10^7mol/yr (Chen et al., 2021).

5.3.2 Global isotope mass balance based on surface [Cd]

Here, we perform a theoretical isotope mass balance that is only partially based on our sedimentary measurements. It is important to note that because we only have sedimentary isotope measurements for regions that are underlie Cd depleted regions (<0.15 nM Cd), we need to extrapolate the Cd isotope values from seawater isotope measurements for regions that have Cd concentrations greater than 0.15 nM, e.g., Figure 9). Therefore, the isotope mass balance estimated here needs to be verified with sediments deposited below waters with [Cd] >0.15 nM in order to determine if our model reflects the global Cd isotope mass balance.

We employ two separate trendlines to estimate the global outflux of δ^{114}Cd to the margins (i.e., [Cd] < 0.15 nM and [Cd] > 0.15 nM, shown in Figure 9). We couple the surface Cd concentrations (Roshan and DeVries, 2021) with OC flux estimates from (Tegler et al., *subm.*). This allows us to determine the Cd flux and Cd isotope composition using the Cd:OC relationship and the δ^{114}Cd and $[Cd]_{surf}$ trend, respectively. We estimate that the average Cd isotope composition of the global sedimentary organic matter flux would vary between $\delta^{114}Cd = -0.04$ and +0.17 ‰, depending on which fractionation factor is used (i.e., $\Delta^{114}Cd = -0.80$ and -0.25 ‰). We choose those values as they cover a range of different fractionation scenarios from closed

system Rayleigh fractionation conditions (between Δ^{114}Cd = −0.5 and −0.2 ‰) to open-system fractionation at steady state (between Δ^{114}Cd = −0.8 and −0.4 ‰; Xue et al., 2013). These fractionation factors were selected as they cover the entire range of values proposed in previous work that investigated the Cd isotope fractionation during biological uptake in the ocean (Lacan et al., 2006; Abouchami et al., 2011; Xue et al., 2013; Horner et al., 2013; John and Conway, 2014). When −0.25 ‰ is used as the fractionation factor, the global output balances an input value of ≈+0.2 ‰ (Lambelet et al., 2013; Bridgestock et al., 2017).

While this method shows that the marine Cd isotope budget can be balanced, these values are not based only on sedimentary data. To verify whether this method is plausible, it is critical that sediment samples are measured from Cd replete regions.

5.3.3 Global isotope mass balance based on bottom water O_2 concentration

Despite uncertainty about the mechanism underpinning the relationship between δ^{114}Cd and bottom water oxygen, we can use the empirical relationship in Figure 10 to estimate the Cd isotope composition of the global OC flux. The mass balance should be reassessed once more Cd sedimentary data are obtained from regions with high bottom water oxygen concentrations.

Unlike the Cd surface water concentrations, our data span a relatively broad range of bottom water O_2 compositions. However, we must make inferences for higher bottom water concentrations because our data is limited to O_2 bottom water concentrations between 1 and 250 µM. Therefore, we conduct two isotope mass balance approaches: (1) assume that the same trend line extends to the highest O_2 bottom waters, and (2) cap the relationship at 250 µM and treat all regions of the margins with a higher bottom water concentration as if they had 250 µM of O_2.

We used the gridded 10 by 10 km^2 OC flux provided by Tegler et al. *(subm.)* to create the mass flux. Then, the Cd isotope composition was calculated using the relationship defined in Section 5.2.3. The equation used to estimate the global Cd isotope flux is shown in Equation 7.

$$\delta^{114}Cd_{sed,global} = \sum \left(f_{Cd,n} \times \left(-1.1 \times 10^{-3} \times [O_2]_n + 0.09\right)\right) \quad \text{Eq. 7}$$

where $f_{Cd,n}$ is the fraction of Cd burial for a 10 by 10 square kilometer area and $[O_2]_n$ is the bottom water concentration of O_2 from the WOA18 gridded to align with the OC flux described in Tegler et al. (*subm.*).

In the first global approximation, we allow the trend to extrapolate over the entire 0 to 390 µM O_2 range, resulting in an estimated global Cd isotope composition = −0.13 ‰. When we limit

the extrapolation from 0 to 250 and force all values with oxygen bottom water greater than 250 to act as if it were 250, we achieve a global mass flux of $\delta^{114}Cd = -0.11$ ‰. These values are within analytical uncertainty, and therefore, for a first-order estimate, whether we extrapolate or assume that the relationship falls off asymptotically at higher oxygen bottom water concentrations does not impact the results. It is important to note that these values do not balance the current estimated input values (e.g., $\delta^{114}Cd \approx +0.2$ ‰; Chen et al., 2021). For this reason, it is important to explore what other processes could govern the isotope mass balance.

5.3.4 Global Mass Balance Comparison

Figure 11A estimates the global isotope trends using a fractionation factor of − 0.4 ‰ for the sediments underlying waters with surface [Cd] >0.15 nM. As expected, the areas with the most Cd replete seawater, the polar regions, including Antarctica and parts of the Arctic have some of the lightest $\delta^{114}Cd$ values. Conversely, some of the heaviest values are located at latitudes above 40˚N and around the southern tip of South America. The overall mass balance flux using this estimation is $\delta^{114}Cd \approx +0.1$ ‰.

Figure 11B shows a narrower span of isotope values for the values determined by the O_2 relationship. As expected, the lightest values are in the high oxygen polar regions and the heaviest values are in regions with substantial OMZs. It is important to note that our inability to estimate the $\delta^{114}Cd$ values along the Namibian Margin and the Peru Upwelling Zone likely leaves out regions with lower oxygen and thus heavier Cd from our mass balance. If these regions were included, we might expect the isotope mass balance to be heavier than $\delta^{114}Cd \approx -0.1$ ‰.

6. Conclusions and implications

In this paper, we consider three questions: (1) can we differentiate between regions that have substantial CdS formation from those that do not?, (2) do regions that are dominated with Cd derived from organic matter record nutrient utilization from the surface waters?, and (3) can we use our samples to close the Cd mass balance?

We first show that we can diagnose regions with significant CdS input by examining Cd content relative to what would be supported by organically derived Cd and the isotope composition of the sediment. We show that the regions with the highest [Cd] are from the regions with the most CdS formation. Geographically these regions are connected to a source of upwelled dissolved Cd

and have a supply of dissolved H_2S. However, regions with CdS influence are small and likely have little impact on the global Cd budget.

Next, we investigated the Cd isotope composition of sediments in both oxic and suboxic regions. Our findings reveal that almost all sediments exhibit light Cd isotope compositions, not just those underlying OMZs. Moreover, we find that more oxic bottom waters are generally associated with lighter Cd isotope compositions. We also observe that sedimentary Cd isotope compositions are positively correlated with surface water [Cd], which we attribute to upward mixing of deeper waters downward inputs from aerosols. However, our study lacks sediments underlying Cd replete regions, where sedimentary Cd isotope compositions are expected to follow biologically driven fractionation trends. We encourage future studies to analyze samples from these regions to determine whether sediments can record the fractionation observed in the surface waters.

We establish a first-order mass and isotope balance for Cd by utilizing observed correlations between sedimentary δ^{114}Cd and bottom-water [O_2] and surface water [Cd]. We draw on a recent study and published Cd:OC ratios to estimate Cd fluxes along the global margins. We use the observed relationship between δ^{114}Cd and bottom water [O_2] to estimate the isotope composition of buried organic matter. This results in a global output of ≈ -0.1 ‰. We also attempt to estimate the global mass balance using surface water [Cd], seawater isotope data and sedimentary δ^{114}Cd values. Variable fractionation factors suggest that the range of potential Cd isotope compositions could fall between −0.11 and +0.17 ‰. Obtaining more sediment samples underlying Cd-replete regions would facilitate a more robust estimate of the global mass balance. Likewise, a deeper understanding of the processes modifying the Cd isotope composition of particulate matter is essential to constrain the Cd isotope composition of material delivered to sediments.

Our data show that there is no simple relationship between nutrient utilization and the Cd isotope composition of marine sediments. Instead, we show that sedimentary Cd isotope systematics are influenced by multiple variables, each driven by different processes. This complexity in teasing out a unique driving process introduces uncertainty when establishing the global mass balance of Cd isotopes. Should the relationships with surface-water [Cd] and bottom-water [O_2] be subsequently refined, sedimentary Cd isotopes may still offer valuable insights as a biogeochemical proxy.

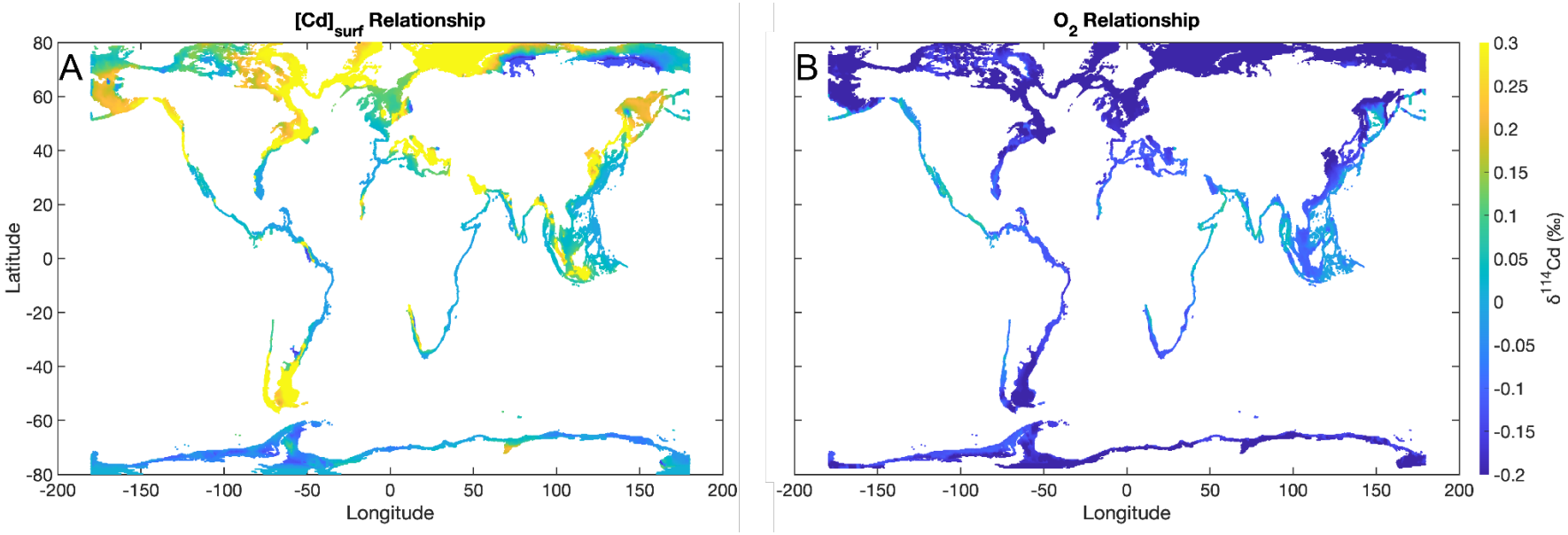

Figure 11. (A) Shows the range of $\delta^{114}Cd$ globally assuming that there is a relationship governed by a broadly positive trend for [Cd] < 0.15 nM and a negative trend related to seawater isotope systematics with a constant fractionation factor of − 0.4 ‰ for [Cd] > 0.15 nM (B) Shows the range of $\delta^{114}Cd$ globally if we extrapolate the bottom water oxygen concentrations over the entire oxygen range (~0 – 350 µM O_2)

Acknowledgments

I would like to acknowledge Jurek Blusztajn for his invaluable help running the MC-ICP-MS. The project was funded by the National Science Foundation Graduate Research Fellowship (Grant #1122374; L.A.T). TJH acknowledges support from NSF (OCE-1443577) and *The Breene M. Kerr Early Career Scientist Endowment Fund*. I would like to thank the coauthors of this study: Sune Nielsen, Yi Wang, Florian Scholz, Jeremy D. Owens, Larry Peterson, Maureen Auro, Phoebe Lam, and Tristan J. Horner.

Table 1: Summary of results, including sample information and leached Cd concentrations and isotopes

Location	Sample Name	Latitude	Longitude	Depth in sediment (top)	Depth in sediment (bottom)	Coring Depth	Bottom Water O2 (µM)	O_2 estimate	OC (%)	Cd (µg/g)	δ114Cd (‰)	2SD	[Cd]surf (nM)	Reference
Arabian Sea	TOM41 MC32C	19.50	58.47	0	1	611	1	WOA18	1.81	1.89	0.15	0.03	0.080	This study
Arabian Sea	TOM41-17E	15.99	61.53	2	3	3985	129	WOA18	0.57	0.22	-0.05	0.03	0.011	This study
Arabian Sea	TOM41-32G	19.50	58.47	0	1	611	1	WOA18	2.17	1.52	0.09	0.03	0.080	This study
Arabian Sea	TOM41-MC17A	15.99	61.53	2	3	3985	129	WOA18	0.53	0.23	-0.05	0.03	0.011	This study
Arabian Sea	TOM41-MC22E	10.03	65.08	2	3	4426	160	WOA18	0.33	0.11	-0.12	0.03	0.004	This study
Arabian Sea	TOM41-MC29G	17.20	59.95	3	4	2431	107	WOA18	0.59	0.11	0.00	0.03	0.013	This study
Arabian Sea	TOM47 26F	19.21	58.27	1	2	513	3	WOA18	1.51	0.41	0.15	0.03	0.071	This study
Arabian Sea	TOM47 MC26D	19.21	58.27	3	4	513	3	WOA18	2.43	0.96	0.09	0.03	0.071	This study
Arabian Sea	TOM47 MC30H	19.22	58.02	5	6	71	6	WOA18	0.57	0.44	0.25	0.03	0.075	This study
Arabian Sea	TOM47 MC34D	19.52	58.49	5	6	719	6	WOA18	5.94	2.22	0.09	0.03	0.080	This study
Black Sea	BS1-2CM	43.09	32.03	1	2	2092	0	Measured	6.00	0.62	0.12	0.02	0.820	This study
Black Sea	BS2-3CM	43.09	32.03	2	3	2092	0	Measured	6.00	1.14	0.03	0.04	0.820	This study
Black Sea	BS3-4CM	43.09	32.03	3	4	2092	0	Measured	6.00	1.06	0.18	0.02	0.820	This study
Black Sea	BS30-31CM	43.09	32.03	30	31	2092	0	Measured	6.00	0.22	0.19	0.02	0.820	This study
Black Sea	BS48-49CM	43.09	32.03	48	49	2092	0	Measured	6.00	1.68	0.18	0.02	0.820	This study
Black Sea	BSBC47	41.45	40.36	0	1	184	0	WOA18	0.93	0.35	-0.01	0.02	0.792	This study
Black Sea	BSBC84	42.37	31.89	0	1	2212	0	WOA18	1.24	0.20	0.09	0.02	0.800	This study
Black Sea	BSGGC14	41.79	30.48	11	12	1916	1	WOA18	1.18	0.17	0.04	0.02	0.762	This study

Location	Sample Name	Latitude	Longitude	Depth in sediment (top)	Depth in sediment (bottom)	Coring Depth	Bottom Water O2 (μM)	O_2 estimate	OC (%)	Cd (μg/g)	δ114Cd (‰)	2SD	[Cd]surf (nM)	Reference
Black Sea	BSGGC16	42.43	30.65	6	7	2170	0	WOA18	1.01	0.14	0.02	0.02	0.820	This study
Black Sea	BSGGC68	42.99	34.01	0	1	2221	0	WOA18	4.20	0.60	0.19	0.02	0.806	This study
Black Sea	BSWHGGC-80	42.51	33.22	0	1	2215	1	WOA18	2.23	0.34	0.11	0.02	0.795	This study
Black Sea	BSWHGGC32	43.10	36.60	21	22	2186	0	WOA18	2.87	0.46	0.12	0.02	0.831	This study
Cariaco	CB111BC	10.84	-65.78	0	1	411	0	Measured	3.26	1.43	0.28	0.03	0.014	This study
Cariaco	CB22BC	10.87	-65.17	0	1	656	0	Measured	5.27	2.27	0.26	0.02	0.007	This study
Cariaco	CB67BC	10.69	-64.66	0	1	400	0	Measured	5.57	1.72	0.27	0.02	0.007	This study
Cariaco	CB82BC	10.66	-64.86	0	1	1342	0	Measured	5.95	1.76	0.25	0.02	0.010	This study
Cariaco	CB89BC	10.69	-64.97	0	1	818	0	Measured	5.19	1.76	0.34	0.02	0.010	This Study
Namibian	CHN115- 17PH	-25.01	10.67	0	1	4254	218	WOA18	0.17	0.84	-0.18	0.03	0.042	This study
Namibian	CHN99 8 PG	10.51	-18.31	2	5	4014	242	WOA18	0.73	1.17	-0.15	0.03	0.006	This study
Peru Margin	PM-Stn481-30-34	-11.00	-78.24	30	34	376	2	Measured	3.34	15.81	0.24	0.02	0.194	This study
Peru Margin	PM-Stn449-14-18	-11.00	-78.17	14	18	319	2	Measured	13.45	16.73	0.13	0.02	0.246	This study
Peru Margin	PM-Stn549-7	-11.00	-78.52	7	7	1005	42	Measured	3.33	0.86	0.12	0.02	0.152	This study
Peru Margin	PM-Stn449-8-10	-11.00	-78.17	8	10	319	2	Measured	16.17	32.25	0.22	0.02	0.246	This study
Peru Margin	PM-Stn568-10	-11.00	-77.80	10	10	85	2	Measured	2.31	15.53	0.31	0.02	0.326	This study

Location	Sample Name	Latitude	Longitude	Depth in sediment (top)	Depth in sediment (bottom)	Coring Depth	Water O2 (µM)	O_2 estimate	OC (%)	Cd (µg/g)	δ114Cd (‰)	2SD	[Cd]surf (nM)	Reference
Peru Margin	PM-Stn462-14	-11.00	-78.75	14	14	2025	93	Measured	2.09	1.09	0.13	0.03	0.137	This study
Peru Margin	PM-Stn568-14	-11.00	-77.80	14	14	85	2	Measured	3.28	16.90	0.34	0.02	0.326	This study
Peru Margin	PM-Stn470-18-22	-11.00	-77.94	18	22	145	2	Measured	7.13	50.80	0.31	0.02	0.294	This study
Peru Margin	PM-Stn459-22-26	-11.00	-78.43	22	26	697	13	Measured	5.62	3.85	0.08	0.03	0.162	This study
Peru Margin	PM-Stn470-22-26	-11.00	-77.94	22	26	145	2	Measured	7.46	48.97	0.25	0.02	0.294	This study
Peru Margin	PM-Stn481-22-26	-11.00	-78.24	22	26	376	2	Measured	12.02	14.49	0.15	0.02	0.194	This study
Peru Margin	PM-Stn449-30-34	-11.00	-78.17	30	34	319	2	Measured	14.03	22.62	0.15	0.02	0.246	This study
Peru Margin	PM-Stn460-6	-11.00	-78.59	6	6	1242	64	Measured	3.04	0.56	0.03	0.03	0.148	This study
Peru Margin	PM-Stn445-6-8	-11.00	-78.50	6	8	930	40	Measured	4.11	1.15	0.13	0.02	0.154	This study
Peru Margin	PM-Stn462-7	-11.00	-78.75	7	7	2025	93	Measured	2.71	0.86	0.10	0.02	0.137	This study
Peru Margin	PM-Stn459-14-18	-11.00	-78.43	14	18	697	13	Measured	5.53	59.39	0.35	0.02	0.162	This study
Peru Margin	PM-Stn460-8	-11.00	-78.59	8	8	1242	64	Measured	3.04	0.58	0.10	0.02	0.148	This study
Peru Margin	PM-Stn549-8	-11.00	-78.52	8	8	1005	42	Measured	3.33	0.70	0.11	0.02	0.152	This study
Peru Margin	PM-Stn445-8	-11.00	-78.50	8	8	930	40	Measured	4.11	0.97	0.15	0.02	0.154	This study
Peru Margin	PM-Stn445-10-12	-11.00	-78.50	10	12	930	40	Measured	4.27	1.06	0.12	0.02	0.154	This study
Peru Margin	PM-Stn449-12-14	-11.00	-78.17	12	14	319	2	Measured	13.45	27.11	0.20	0.02	0.246	This study
Peru Margin	PM-Stn470-12-14	-11.00	-77.94	12	14	145	2	Measured	6.46	52.95	0.33	0.02	0.294	This study
Peru Margin	PM-Stn455-14-18	-11.00	-78.32	14	18	465	2	Measured	6.82	21.41	0.07	0.02	0.175	This study
Peru Margin	PM-Stn481-14-18	-11.00	-78.24	14	18	376	2	Measured	3.47	13.61	0.12	0.02	0.194	This study

Location	Sample Name	Latitude	Longitude	Depth in sediment (top)	Depth in sediment (bottom)	Coring Depth	Bottom Water O2 (μM)	O_2 estimate	OC (%)	Cd (μg/g)	δ114Cd (‰)	2SD	[Cd]surf (nM)	Reference
Peru Margin	PM-Stn460-15	-11.00	-78.59	15	15	1242	64	Measured	2.62	0.64	0.11	0.02	0.148	This study
Peru Margin	PM-Stn549-15	-11.00	-78.52	14	14	1005	42	Measured	3.31	1.05	0.11	0.02	0.152	This study
Santa Barbara	SBB1-2CM	34.23	-120.03	1	2	594	1	Measured	3.08	1.10	0.09	0.02	0.071	This study
Santa Barbara	SBB2-3CM	34.23	-120.03	2	3	594	1	Measured	3.08	1.03	0.04	0.02	0.071	This study
Santa Barbara	SBB0.1CM	34.23	-120.03	0	0	594	1	Measured	3.08	1.27	0.11	0.02	0.071	This study
Santa Barbara	SBB3-4CM	34.23	-120.03	3	4	594	1	Measured	3.08	1.03	0.09	0.02	0.071	This study
W. Equ. Pacific	BJ8 103A	0.87	127.76	2	3	377	96	WOA18	3.08	0.10	-0.06	0.03	0.048	This study
W. Equ. Pacific	BJ8 MC98B	1.06	127.89	2	3	341	101	WOA18	2.35	0.10	0.00	0.03	0.044	This study
W. Equ. Pacific	BJ8-101B	0.87	127.76	2	3	377	96	WOA18	3.08	0.11	0.03	0.03	0.048	This study
W. Equ. Pacific	BJ8-105B	0.92	127.71	3	4	401	95	WOA18	3.61	0.13	0.03	0.03	0.048	This study
W. Equ. Pacific	BJ8-108A	0.94	127.69	0	1	272	102	WOA18	3.62	0.11	-0.01	0.03	0.048	This study
W. Equ. Pacific	BJ8-111A	0.99	127.74	0	1	268	102	WOA18	2.12	0.17	0.01	0.03	0.047	This study
W. Equ. Pacific	BJ8-MC106B	0.92	127.71	2	3	401	95	WOA18	3.30	0.11	0.03	0.03	0.048	This study
W. Equ. Pacific	BJ8-MC116A	0.97	127.81	0	2	472	95	WOA18	2.18	0.13	0.06	0.03	0.046	This study
W. Equ. Pacific	BJ8-MC94A	2.35	127.82	0	2	501	114	WOA18	0.37	0.17	-0.08	0.03	0.030	This study

Location	Sample Name	Latitude	Longitude	Depth in sediment (top)	Depth in sediment (bottom)	Coring Depth	Bottom Water O2 (μM)	O_2 estimate	OC (%)	Cd (μg/g)	δ114Cd (‰)	2SD	[Cd]surf (nM)	Reference
W. Equ. Pacific	BJ8-MC96A	1.45	128.17	1	2	386	132	WOA18	0.76	0.09	-0.13	0.03	0.037	This study
Magadalena	MagD_0	23.50	-111.60	0	1	692	1	Measured	10.03	1.45	0.09	0.05	0.032	Chen (2021)
Pescadero	Pesc_2	24.30	-108.20	2	3	616	0	Measured	3.55	0.63	-0.02	0.05	0.053	Chen (2021)
San Nicolas Basin	MC37 2.5-3	32.80	-118.80	3	3	1750	15	Measured	4.92	0.53	-0.04	0.05	0.029	Chen (2021)
Santa Barbara	MC17_1	34.30	-120.00	1	2	493	2	Measured	3.01	0.85	-0.02	0.07	0.072	Chen (2021)
Santa Monica	8B3	33.70	-118.80	1	2	905	2	Measured	5.73	2.82	0.08	0.05	0.040	Chen (2021)
Soledad	Sol2_1	25.20	-112.70	1	2	544	0	Measured	6.47	1.84	0.06	0.08	0.034	Chen (2021)
Tanner	12B3	33.00	-119.70	1	2	1514	30	Measured	6.69	0.96	0.08	0.04	0.039	Chen (2021)

Table 2. Data summary from the Ross Sea

Station	Depth	Lat	Lon	Bottom depth	$\delta^{114/110}$Cd (‰)	± 2 SE	[Cd]	[P]	$\delta^{114/110}$Cd (‰)	± 2 SE	[Cd]	[P]
	m	deg	deg	(m)	SSF	SSF	pM (SSF)	pM (SSF)	LSF	LSF	pM (LSF)	pM (LSF)
0	250	-76.50	170.00	737	-0.24	0.06	10	7169	0.18	0.04	2	1919
0	125	-76.50	170.00	737	-0.13	0.05	26	17142	0.15	0.03	15	8349
0	50	-76.50	170.00	737	0.20	0.05	218	204876	0.35	0.03	198	182999
2	402	-75.19	174.00	428	0.16	0.19	6	4531	-0.19	0.03	2	2478
2	302	-75.19	174.00	428	-0.40	0.06	9	4846	-0.19	0.03	1	2032
2	212	-75.19	174.00	428	-0.49	0.05	11	5801	-0.14	0.02	2	2846
2	152	-75.19	174.00	428	-0.49	0.04	17	8015	-0.15	0.03	3	5701
2	82	-75.19	174.00	428	-0.27	0.06	15	17653	-0.11	0.03	19	26707
2	32	-75.19	174.00	428	-0.27	0.07	17	23481	0.01	0.03	47	65339
24	370	-74.14	176.66	398	-0.36	0.07	11	6157	-0.02	0.03	2	1968
24	210	-74.14	176.66	398	-0.49	0.04	8	4938	0.00	0.03	1	1299
24	120	-74.14	176.66	398	-0.13	0.05	12	10701	0.05	0.03	31	28381
24	80	-74.14	176.66	398	-0.17	0.04	25	23483	0.07	0.03	66	68832
24	30	-74.14	176.66	398	-0.06	0.05	78	73479	0.11	0.03	47	71616
24	600	-72.58	178.50	1887	-0.39	0.09	1	825	0.24	0.06	0	152

Table 2. Data summary from the Ross Sea *(cont.)*

Station	Depth	Lat	Lon	Bottom depth	$\delta^{114/110}$Cd (‰)	± 2 SE	[Cd]	[P]	$\delta^{114/110}$Cd (‰)	± 2 SE	[Cd]	[P]
	m	deg	deg	(m)	SSF	SSF	pM (SSF)	pM (SSF)	LSF	LSF	pM (LSF)	pM (LSF)
14	404	-72.58	178.50	1887	-0.41	0.08	3	712	-0.05	0.05	0	181
14	253	-72.58	178.50	1887	-0.46	0.06	6	1343	-0.22	0.03	1	453
14	150	-72.58	178.50	1887	-0.51	0.04	5	2281	-0.23	0.03	1	810
14	100	-72.58	178.50	1887	-0.36	0.06	11	6161	-0.21	0.03	3	5858
14	50	-72.58	178.50	1887	-0.27	0.04	92	44207	-0.15	0.03	5	10475

Table 3. Cd excess and the range of contributions that can reasonably expected to be from Cd that arrived in association with organic carbon

Station	Depth (cm)	Type	MAR g m^{-2} yr^{-1}[a]	POC rain rate, mmol C m^{-2} d^{-1}[b]	POC accumulation rate at 10 cm, g C m^{-2} yr^{-1}[b]	Rain Rate µmol Cd m^{-2} yr^{-1}[c]	Accumulation Rate at 10 cm µmol Cd m^{-2} yr^{-1}[c]	Excess µmol Cd m^{-2} yr^{-1}
M77-1 549 *MUC53	7	Oxic	390	5.9	16	3.6	2.3	3.0
M77-1 BIGO-05	10	OMZ	1400	15.3	31	9.4	4.4	193.4
M77-1 MUC19	8-10	OMZ	190	9.8	17	6.0	2.4	54.5
M77-1 MUC25	14-18	Transition	420	9	32	5.6	4.5	221.9
M77-1 MUC33	14-18	OMZ	270	14	44	8.6	6.2	32.7

[a] from (Dale et al., 2021)

[b] from (Dale et al., 2015)

[c] Value determined by multiplying the Cd:C ratio in average phytoplankton (Ho et al., 2003) with the particulate organic carbon rain rates (max^b) value and the organic carbon accumulation rates (min^b). The excess Cd is calculated by multiplying the MAR by the measured leached Cd. A similar calculation is found in (Plass et al., 2021).

Table 4. Coefficients for each model minimizing RMSE

$[Cd]^{-1}$	$[Cd]_{surf}$	O_2	Depth (m)	OC (%)	b-intercept	RMSE	RSS	MAD	r^2
α	β	ɣ	ε	**ζ**	b				
4.5E-04	8.8E-01	-8.5E-04	-4.1E-06	-2.1E-03	4.2E-02	0.05	0.10	0.04	0.70
	8.8E-01	-8.4E-04	-3.8E-06	-2.1E-03	4.2E-02	0.05	0.10	0.04	0.70
1.1E-03	8.4E-01	-9.2E-04		-2.2E-03	4.3E-02	0.05	0.10	0.04	0.70
	8.2E-01	-9.1E-04		-2.3E-03	4.7E-02	0.05	0.10	0.04	0.70
	8.2E-01	-8.0E-04	-4.4E-06		3.9E-02	0.05	0.10	0.04	0.70
4.4E-04	8.4E-01	-8.2E-04	-4.0E-06		3.6E-02	0.05	0.10	0.04	0.70
1.2E-03	8.5E-01	-8.9E-04			3.3E-02	0.05	0.10	0.04	0.70
	8.3E-01	-8.6E-04			3.7E-02	0.05	0.10	0.04	0.70
3.1E-03	1.0E+00	-7.9E-04		2.7E-03		0.05	0.11	0.04	0.69
4.8E-03	1.0E+00	-9.2E-04	6.4E-06			0.05	0.11	0.04	0.69
3.8E-03	1.1E+00	-8.1E-04				0.05	0.11	0.04	0.69
	9.9E-01	-6.9E-04		3.7E-03		0.05	0.11	0.04	0.68
	9.8E-01	-6.6E-04	-1.8E-06	4.1E-03		0.05	0.11	0.04	0.68
3.1E-03	8.4E-01	-8.0E-04	3.3E-06	5.3E-03		0.05	0.11	0.04	0.68
	1.1E+00	-6.5E-04	-2.8E-06			0.05	0.12	0.04	0.68
	1.1E+00	-6.8E-04				0.05	0.11	0.04	0.68
-1.1E-02	6.5E-01		-3.5E-05	6.0E-04	6.7E-02	0.05	0.13	0.04	0.62
-8.2E-03	7.4E-01		-3.4E-05		5.3E-02	0.06	0.13	0.04	0.62
-5.9E-03	9.1E-01		-2.5E-05	7.0E-03		0.06	0.14	0.04	0.60
-1.0E-02		-6.0E-04	-2.6E-05	-5.6E-03	1.6E-01	0.06	0.15	0.05	0.58
-4.8E-03	1.1E+00		-2.4E-05			0.06	0.15	0.05	0.58

Table 4. Coefficients for each model minimizing RMSE *(cont.)*

$[Cd]^{-1}$	**$[Cd]_{surf}$**	**O_2**	**Depth (m)**	**OC (%)**	**b-intercept**	**RMSE**	**RSS**	**MAD**	**r^2**
α	β	ɣ	ε	**ζ**	b				
-9.8E-03		-5.4E-04	-2.3E-05		1.3E-01	0.06	0.15	0.05	0.57
	9.8E-01		-2.6E-05	6.8E-03	-1.7E-02	0.06	0.15	0.04	0.56
	9.2E-01		-2.9E-05	4.7E-03		0.06	0.16	0.05	0.55
-4.8E-03		-1.0E-03		-3.9E-03	1.3E-01	0.06	0.16	0.05	0.55
-4.6E-03		-9.7E-04			1.2E-01	0.06	0.16	0.05	0.54
	1.0E+00		-3.2E-05		5.0E-03	0.06	0.16	0.05	0.54
	1.1E+00		-2.8E-05			0.06	0.16	0.05	0.54
-1.7E-02			-4.4E-05	-2.3E-03	1.5E-01	0.06	0.16	0.05	0.54
-1.6E-02			-4.3E-05		1.4E-01	0.06	0.16	0.05	0.54
		-1.0E-03	-8.5E-06	-3.9E-03	1.3E-01	0.06	0.16	0.05	0.53
		-9.8E-04	-7.4E-06		1.1E-01	0.06	0.16	0.05	0.53
		-1.1E-03		-3.4E-03	1.2E-01	0.06	0.17	0.05	0.53
		-1.1E-03			1.1E-01	0.06	0.17	0.05	0.53
		-1.6E-04				0.10	0.43	0.09	0.53
-4.9E-03	9.8E-01			1.1E-02	-4.5E-02	0.06	0.18	0.05	0.49
	1.1E+00			1.2E-02	-7.3E-02	0.06	0.18	0.05	0.48
-9.0E-03	7.7E-01			6.0E-03		0.07	0.19	0.05	0.47
-7.3E-03	9.8E-01				-6.5E-03	0.07	0.19	0.05	0.45
-8.0E-03	9.3E-01					0.07	0.19	0.05	0.45

Table 4. Coefficients for each model minimizing RMSE *(cont.)*

$[Cd]^{-1}$	$[Cd]_{surf}$	O_2	Depth (m)	OC (%)	b-intercept	RMSE	RSS	MAD	r^2
α	β	ɣ	ε	**ζ**	b				
	7.1E-01			2.4E-03		0.07	0.23	0.05	0.44
	1.2E+00				-4.2E-02	0.07	0.21	0.05	0.40
	7.8E-01					0.07	0.23	0.05	0.40
-4.7E-04		-4.6E-04		2.0E-02		0.07	0.24	0.06	0.34
		-4.9E-04	1.5E-06	2.0E-02		0.07	0.24	0.06	0.34
		-4.7E-04		2.0E-02		0.07	0.24	0.06	0.34
-4.3E-04		-4.7E-04	8.8E-07	2.0E-02		0.07	0.24	0.06	0.34
-5.6E-03			-1.5E-05	2.1E-02		0.08	0.25	0.06	0.31
			-3.5E-05	8.1E-03	6.1E-02	0.07	0.25	0.06	0.30
			-7.0E-07			0.10	0.44	0.09	0.27
			-4.1E-05		9.3E-02	0.08	0.25	0.06	0.27
-1.3E-02				1.0E-02	5.0E-02	0.08	0.25	0.06	0.27
			-1.9E-05	1.9E-02		0.08	0.27	0.06	0.25
-7.7E-03				1.9E-02		0.08	0.27	0.06	0.24
-1.5E-02					8.7E-02	0.08	0.27	0.06	0.23
2.4E-04						0.10	0.44	0.09	0.23
		-4.5E-04	1.8E-05			0.10	0.42	0.09	0.16
6.5E-03		-3.9E-04				0.10	0.42	0.08	0.14
				1.7E-02	-5.0E-03	0.08	0.31	0.07	0.13

Table 4. Coefficients for each model minimizing RMSE *(cont.)*

$[Cd]^{-1}$	$[Cd]_{surf}$	O_2	Depth (m)	OC (%)	b-intercept	RMSE	RSS	MAD	r^2
α	β	ɣ	ε	**ζ**	b				
				1.5E-02		0.08	0.31	0.07	0.13
1.1E-02		-1.1E-03	3.1E-05			0.09	0.38	0.08	0.11
4.8E-04			-1.3E-06			0.10	0.44	0.09	0.00
					4.4E-02	0.09	0.35	0.07	0.00

Chapter 3 References

Abouchami, W., Galer, S. J. G., De Baar, H. J. W., Alderkamp, A. C., Middag, R., Laan, P., Feldmann, H., and Andreae, M. O. (2011). Modulation of the Southern Ocean cadmium isotope signature by ocean circulation and primary productivity. *Earth Planet Sc. Lett.*, **305** (1-2), 83-91.

Abouchami, W., Galer, S. J. G., De Baar, H. J. W., Middag, R., Vance, D., Zhao, Y., Feldmann, H., and Andreae, M. O. (2014). Biogeochemical cycling of cadmium isotopes in the Southern Ocean along the Zero Meridian. *Geochim. Cosmochim. Ac*, **127**, 348-367.

Abouchami, W., Galer, S. J., Horner, T. J., Rehkämper, M., Wombacher, F., Xue, Z., Lambelet M., Gault-Ringold M., Stirling C. H., Schönbächler M., Shiel A. E., Weis D. and Holdship P. F. (2013). A common reference material for cadmium isotope studies–NIST SRM 3108. *Geostand. Geoanal. Res.*, **37**, 5-17.

Arthur M. A., Dean W. E., Neff E. D., Hay B. J., King J. and Jones G. (1994) Varve calibrated records of carbonate and organic carbon accumulation over the last 2000 years in the Black Sea. *Global Biogeochem Cy* **8**, 195–217.

Astor Y. M., Lorenzoni L. and Scranton M. (2011) Handbook of methods for the analysis of oceanographic parameters at the Cariaco time series station. Available on line at: https://repository.oceanbestpractices.org/.

Bernhard, J. M., Sen Gupta, B. K., & Borne, P. F. (1997). Benthic foraminiferal proxy to estimate dysoxic bottom-water oxygen concentrations; Santa Barbara Basin, US Pacific continental margin. *J. Foramin. Res.* , *27*(4), 301-310.

Bernhard, J. M., & Reimers, C. E. (1991). Benthic foraminiferal population fluctuations related to anoxia: Santa Barbara Basin. *Biogeochemistry*, *15*, 127-149.

Bishop, J. K., Lam, P. J., & Wood, T. J. (2012). Getting good particles: Accurate sampling of particles by large volume in-situ filtration. *Limnology Oceanogr. Methods*, *10*(9), 681-710.

Bishop, J. K., & Wood, T. J. (2008). Particulate matter chemistry and dynamics in the twilight zone at VERTIGO ALOHA and K2 sites. *Deep Sea Res. Part : Oceanogr. Res. Pap.*, *55*(12), 1684-1706.

Borchers, S. L., Schnetger, B., Böning, P., & Brumsack, H. J. (2005). Geochemical signatures of the Namibian diatom belt: Perennial upwelling and intermittent anoxia. *Geochem. Geophys. Geosystems*, ***6***

Bourne, H. L., Bishop, J. K., Lam, P. J., & Ohnemus, D. C. (2018). Global spatial and temporal variation of Cd: P in euphotic zone particulates. *Global Biogeochem. Cy.*, **32**,1123-1141.

Boyer, Garcia T. P. ;, Locarnini H. E. , Zweng R. A. , Mishonov M. M. , Reagan A. V. , Weathers J. R., Baranova K. A. , Seidov O. K. , Smolyar D. and V. I. (2022) *World Ocean Atlas 2018. NOAA National Centers for Environmental Information. Dataset.*

Boyle E. A. (1988) Cadmium: Chemical tracer of deepwater paleoceanography. *Paleoceanography* **3**, 471–489.

Boyle, E. A., Sclater, F., and Edmond J. (1976) On the marine geochemistry of cadmium. *Nature,* **263**, 42-44.

Bridgestock, L., Rehkämper, M., Van De Flierdt, T., Murphy, K., Khondoker, R., Baker, A. R., ... & Achterberg, E. P. (2017). The Cd isotope composition of atmospheric aerosols from the Tropical Atlantic Ocean. *Geophys Res. Lett.*, **44**, 2932-2940.

Brüchert, V., Currie, B., Peard, K. R., Lass, U., Endler, R., Dübecke, A., ... & Zitzmann, S. (2006). Shelf anoxia in the Namibian coastal upwelling system. Biogeochemical and physical

control on shelf anoxia and water column hydrogen sulphide in the Benguela coastal upwelling system off Namibia. *Past and present water column anoxia. NATO Science Series. Kluwer Springer*, 161-193.

Bruland, K. W. (1980). Oceanographic distributions of cadmium, zinc, nickel, and copper in the North Pacific. *Earth Planet Sc. Lett.*, **47**, 176-198.

Bryan, A. L., Dickson, A. J., Dowdall, F., Homoky, W. B., Porcelli, D., & Henderson, G. M. (2021). Controls on the cadmium isotope composition of modern marine sediments. *Earth Planet Sc. Lett.*, **565,** 116946.

Chapman, P., & Shannon, L. V. (1987). Seasonality in the oxygen minimum layers at the extremities of the Benguela system. *South Afr. J. Mar. Sci.*, **5**, 85-94.

Chen, L., Little, S. H., Kreissig, K., Severmann, S., & McManus, J. (2021). Isotopically light Cd in sediments underlying oxygen deficient zones. *Frontiers Earth Sci.*, **9**, 623720.

Conway, T. M., & John, S. G. (2015a). Biogeochemical cycling of cadmium isotopes along a high-resolution section through the North Atlantic Ocean. *Geochim. Cosmochim. Ac*, **148**, 269-283.

Conway, T. M., & John, S. G. (2015b). The cycling of iron, zinc and cadmium in the North East Pacific Ocean–Insights from stable isotopes. *Geochim. Cosmochim. Ac*, **164**, 262-283.

Conway, T. M., Rosenberg, A. D., Adkins, J. F., & John, S. G. (2013). A new method for precise determination of iron, zinc and cadmium stable isotope ratios in seawater by double-spike mass spectrometry. *Analytica Chimica Acta*, **793**, 44-52.

Currie, B., Utne-Palm, A. C., & Salvanes, A. G. V. (2018). Winning ways with hydrogen sulphide on the Namibian shelf. *Front. Mar. Sci.*, **5**, 341.

Cutter, G., Andersson, P., Codispoti, L., Croot, P., Francois, R., Lohan, M. C., ... & Rutgers vd Loeff, M. (2010). Sampling and sample-handling protocols for GEOTRACES cruises.

Dale, A. W., Paul, K. M., Clemens, D., Scholz, F., Schroller-Lomnitz, U., Wallmann, K., ... & Sommer, S. (2021). Recycling and burial of biogenic silica in an open margin oxygen minimum zone. *Global Biogeochem. Cy.*, **35**, e2020GB006583.

Dale, A. W., Sommer, S., Lomnitz, U., Montes, I., Treude, T., Liebetrau, V., ... & Wallmann, K. (2015). Organic carbon production, mineralisation and preservation on the Peruvian margin. *Biogeosciences*, **12**, 1537-1559.

Davies-Colley, R. J., Nelson, P. O., & Williamson, K. J. (1985). Sulfide control of cadmium and copper concentrations in anaerobic estuarine sediments. *Mar. Chem.*, **16**, 173-186.

de Souza, G. F., Vance, D., Sieber, M., Conway, T. M., & Little, S. H. (2022). Re-assessing the influence of particle-hosted sulphide precipitation on the marine cadmium cycle. *Geochim. Cosmochim. Ac*, **322**, 274-296.

Farmer, J. R., Hertzberg, J. E., Cardinal, D., Fietz, S., Hendry, K., Jaccard, S. L., ... & GEOTRACESPAGES Biological Productivity Working Group Members. (2021). Assessment of C, N, and Si isotopes as tracers of past ocean nutrient and carbon cycling.

Gault-Ringold, M., Adu, T., Stirling, C. H., Frew, R. D., & Hunter, K. A. (2012). Anomalous biogeochemical behavior of cadmium in subantarctic surface waters: mechanistic constraints from cadmium isotopes. *Earth Planet Sc. Lett.*, **341**, 94-103.

George, E., Stirling, C. H., Gault-Ringold, M., Ellwood, M. J., & Middag, R. (2019). Marine biogeochemical cycling of cadmium and cadmium isotopes in the extreme nutrient-depleted subtropical gyre of the South West Pacific Ocean. *Earth Planet Sc. Lett.*, **514**, 84-95.

Georgiev, S. V., Horner, T. J., Stein, H. J., Hannah, J. L., Bingen, B., & Rehkämper, M. (2015).

Cadmium-isotopic evidence for increasing primary productivity during the Late Permian anoxic event. *Earth Planet Sc. Lett.*, **410**, 84-96.

Gobeil, C., Silverberg, N., Sundby, B., & Cossa, D. (1987). Cadmium diagenesis in Laurentian Trough sediments. *Geochim. Cosmochim. Ac*, **51**, 589-596.

Guinoiseau, D., Galer, S. J., & Abouchami, W. (2018). Effect of cadmium sulphide precipitation on the partitioning of Cd isotopes: Implications for the oceanic Cd cycle. *Earth Planet Sc. Lett.*, **498**, 300-308.

Ho, T. Y., Quigg, A., Finkel, Z. V., Milligan, A. J., Wyman, K., Falkowski, P. G., & Morel, F. M. (2003). The elemental composition of some marine phytoplankton. *J. Phycol*, **39**, 1145-1159.

Hohl, S. V., Jiang, S. Y., Wei, H. Z., Pi, D. H., Liu, Q., Viehmann, S., & Galer, S. J. (2019). Cd isotopes trace periodic (bio) geochemical metal cycling at the verge of the Cambrian animal evolution. *Geochim. Cosmochim. Ac*, **263**, 195-214.

Horner, T. J., Lee, R. B., Henderson, G. M., & Rickaby, R. E. (2013). Nonspecific uptake and homeostasis drive the oceanic cadmium cycle. *Proc. National Acad. Sci.* , **110**, 2500-2505.

Horner T. J., Pryer H. V., Nielsen S. G., Crockford P. W., Gauglitz J. M., Wing B. A. and Ricketts R. D. (2017) Pelagic barite precipitation at micromolar ambient sulfate. *Nat. Commun.* **8**, 1342.

Horner, T. J., Rickaby, R. E., & Henderson, G. M. (2011). Isotopic fractionation of cadmium into calcite. *Earth Planet Sc. Lett.*, **312**, 243-253.

Horner T. J., Schönbächler M., Rehkämper M., Nielsen S. G., Williams H., Halliday A. N., Xue Z. and Hein J. R. (2010) Ferromanganese crusts as archives of deep water Cd isotope compositions. *Geochem Geophys Geosystems* **11.**

Janssen, D. J., Abouchami, W., Galer, S. J., Purdon, K. B., & Cullen, J. T. (2019). Particulate cadmium stable isotopes in the subarctic northeast Pacific reveal dynamic Cd cycling and a new isotopically light Cd sink. *Earth Planet Sc. Lett.*, **515**, 67-78.

Janssen, D. J., Conway, T. M., John, S. G., Christian, J. R., Kramer, D. I., Pedersen, T. F., & Cullen, J. T. (2014). Undocumented water column sink for cadmium in open ocean oxygen-deficient zones. *Proc. National Acad. Sci.* , **111**, 6888-6893.

Jochum, K. P., Nohl, U., Herwig, K., Lammel, E., Stoll, B., & Hofmann, A. W. (2005). GeoReM: a new geochemical database for reference materials and isotopic standards. *Geostand. Geoanal. Res.*, **29**, 333-338.

John, S. G., & Conway, T. M. (2014). A role for scavenging in the marine biogeochemical cycling of zinc and zinc isotopes. *Earth Planet Sc. Lett.*, **394**, 159-167.

John, S. G., Helgoe, J., & Townsend, E. (2018). Biogeochemical cycling of Zn and Cd and their stable isotopes in the Eastern Tropical South Pacific. *Mar. Chem.*, **201**, 256-262.

Konovalov, S. K., Ivanov, L. I., & Samodurov, A. S. (2001). Fluxes and budget of sulphide and ammonia in the Black Sea anoxic layer. *J. Marine Syst.*, **31**, 203-216.

Konovalov, S. K., & Murray, J. W. (2001). Variations in the chemistry of the Black Sea on a time scale of decades (1960–1995). *J. Marine Syst.*, **31**, 217-243.

Lacan, F., Francois, R., Ji, Y., & Sherrell, R. M. (2006). Cadmium isotopic composition in the ocean. *Geochim. Cosmochim. Ac*, **70**, 5104-5118.

Lambelet, M., Rehkämper, M., van de Flierdt, T., Xue, Z., Kreissig, K., Coles, B., ... & Andersson, P. (2013). Isotopic analysis of Cd in the mixing zone of Siberian rivers with the Arctic Ocean—New constraints on marine Cd cycling and the isotope composition of riverine Cd. *Earth Planet Sc. Lett.*, **361**, 64-73.

Lane, T. W., Saito, M. A., George, G. N., Pickering, I. J., Prince, R. C., & Morel, F. M. (2005). A cadmium enzyme from a marine diatom. *Nature*, **435**, 42-42.

Little, S. H., Vance, D., Lyons, T. W., & McManus, J. (2015). Controls on trace metal authigenic enrichment in reducing sediments: insights from modern oxygen-deficient settings. *Am. J. Sci.* , **315**, 77-119.

Lu, Z., Zhu, J. M., Tan, D., Wang, X., & Zheng, Z. (2021). δ114/110Cd values of a suite of different reference materials. *Geostand. Geoanal. Res.*, **45**, 565-581.

Marchitto, T. M., & Broecker, W. S. (2006). Deep water mass geometry in the glacial Atlantic Ocean: A review of constraints from the paleonutrient proxy Cd/Ca. *Geochem., Geophys., Geosystems*, **7**.

McCorkle, D. C., & Klinkhammer, G. P. (1991). Porewater cadmium geochemistry and the porewater cadmium: δ13C relationship. *Geochim. Cosmochim. Ac*, **55**, 161-168.

McManus, J., Berelson, W. M., & Coale, K. H. (1998). Phosphorus regeneration in continental margin sediments. *Oceanogr. Lit. Rev.*, **1**, 61.

Moore, C. M., Mills, M. M., Arrigo, K. R., Berman-Frank, I., Bopp, L., Boyd, P. W., ... & Ulloa, O. (2013). Processes and patterns of oceanic nutrient limitation. *Nat. Geosci.*, **6**, 701-710.

Morford, J. L., & Emerson, S. (1999). The geochemistry of redox sensitive trace metals in sediments. *Geochim. Cosmochim. Ac*, **63**, 1735-1750.

Murphy, K., Rehkämper, M., Kreissig, K., Coles, B., & van de Flierdt, T. (2016). Improvements in Cd stable isotope analysis achieved through use of liquid–liquid extraction to remove organic residues from Cd separates obtained by extraction chromatography. *J. Anal. Atom. Spectrom.* **31**, 319-327.

Nielsen, S. G., Goff, M., Hesselbo, S. P., Jenkyns, H. C., LaRowe, D. E., & Lee, C. T. A. (2011). Thallium isotopes in early diagenetic pyrite–A paleoredox proxy?. *Geochim. Cosmochim. Ac*, **75**, 6690-6704.

Ohde, T. (2018). Coastal sulfur plumes off Peru during El Niño, La Niña, and neutral phases. *Geophys Res. Lett.*, **45**, 7075-7083.

Ohnemus, D. C., Rauschenberg, S., Cutter, G. A., Fitzsimmons, J. N., Sherrell, R. M., & Twining, B. S. (2017). Elevated trace metal content of prokaryotic communities associated with marine oxygen deficient zones. *Limnol. Oceanogr.* , **62**, 3-25.

Owens, J. D., Nielsen, S. G., Horner, T. J., Ostrander, C. M., & Peterson, L. C. (2017). Thallium-isotopic compositions of euxinic sediments as a proxy for global manganese-oxide burial. *Geochim. Cosmochim. Ac*, **213**, 291-307.

Pennington, J. T., Mahoney, K. L., Kuwahara, V. S., Kolber, D. D., Calienes, R., & Chavez, F. P. (2006). Primary production in the eastern tropical Pacific: A review. *Prog. Oceanogr.y*, **69**, 285-317.

Peterson, L. C., Overpeck, J. T., & Murray, D. W. (1990). A High-Resolution Paleoenvironmental Study of the Cariaco Basin, Venezuela: Late Quaternary to Present-Preliminary Report on R/V Thomas Washington Cruise PLUME-07. *RSMAS/University of Miami Technical Report*, *50*.

Planquette, H., & Sherrell, R. M. (2012). Sampling for particulate trace element determination using water sampling bottles: methodology and comparison to in situ pumps. *Limnology Oceanogr. Methods*, **10**, 367-388.

Plass, A., Dale, A. W., & Scholz, F. (2021). Sedimentary cycling and benthic fluxes of manganese, cobalt, nickel, copper, zinc and cadmium in the Peruvian oxygen minimum zone. *Mar. Chem.*, **233**, 103982.

Plass, A., Schlosser, C., Sommer, S., Dale, A. W., Achterberg, E. P., & Scholz, F. (2020). The control of hydrogen sulfide on benthic iron and cadmium fluxes in the oxygen minimum zone off Peru. *Biogeosciences*, **17**, 3685-3704.

Rehkämper M., Wombacher F., Horner T. J. and Xue Z. (2011) Handbook of Environmental Isotope Geochemistry. *Adv. Isot. Geochem.*, 125–154.

Ripperger, S., Rehkämper, M., Porcelli, D., & Halliday, A. N. (2007). Cadmium isotope fractionation in seawater—A signature of biological activity. *Earth Planet Sc. Lett.*, **261**, 670-684.

Rosenthal, Y., Lam, P., Boyle, E. A., & Thomson, J. (1995). Authigenic cadmium enrichments in suboxic sediments: Precipitation and postdepositional mobility. *Earth Planet Sc. Lett.*, **132**, 99-111.

Roshan, S., & DeVries, T. (2021). Global contrasts between oceanic cycling of cadmium and phosphate. *Global Biogeochem. Cy.*, **35**, e2021GB006952.

Roshan, S., Wu, J., & DeVries, T. (2017). Controls on the cadmium-phosphate relationship in the tropical South Pacific. *Global Biogeochem. Cy.*, **31**, 1516-1527.

Schlitzer, R. (2017). Ocean data view. Retrieved from http.*odv.awi.de*.

Schmitt, A. D., Galer, S. J., & Abouchami, W. (2009). Mass-dependent cadmium isotopic variations in nature with emphasis on the marine environment. *Earth Planet Sc. Lett.*, **277**, 262-272.

Scholz, F., Hensen, C., Noffke, A., Rohde, A., Liebetrau, V., & Wallmann, K. (2011). Early diagenesis of redox-sensitive trace metals in the Peru upwelling area–response to ENSO-related oxygen fluctuations in the water column. *Geochim. Cosmochim. Ac*, **75**, 7257-7276.

Scholz, F., Löscher, C. R., Fiskal, A., Sommer, S., Hensen, C., Lomnitz, U., ... & Canfield, D. E. (2016). Nitrate-dependent iron oxidation limits iron transport in anoxic ocean regions. *Earth Planet Sc. Lett.*, **454**, 272-281.

Schunck, H., Lavik, G., Desai, D. K., Großkopf, T., Kalvelage, T., Löscher, C. R., ... & LaRoche, J. (2013). Giant hydrogen sulfide plume in the oxygen minimum zone off Peru supports chemolithoautotrophy. *PLoS One*, **8**, e68661.

Shannon L. V. and Nelson G. (1996) The Benguela: large scale features and processes and system variability. In The south atlantic. In *The South Atlantic* pp. 163–210.

Sieber, M., Lanning, N. T., Bunnell, Z. B., Bian, X., Yang, S. C., Marsay, C. M., ... & Conway, T. M. (2023). Biological, physical, and atmospheric controls on the distribution of cadmium and its isotopes in the Pacific Ocean. *Global Biogeochem. Cy.*, **37**, e2022GB007441.

Sommer, S., Gier, J., Treude, T., Lomnitz, U., Dengler, M., Cardich, J., & Dale, A. W. (2016). Depletion of oxygen, nitrate and nitrite in the Peruvian oxygen minimum zone cause an imbalance of benthic nitrogen fluxes. *Deep Sea Res. Part : Oceanogr. Res. Pap.*, **112**, 113-122.

Suess, E., & von Huene, R. (1988). Ocean Drilling Program Leg 112, Peru continental margin: Part 2, Sedimentary history and diagenesis in a coastal upwelling environment. *Geology*, **16**, 939-943.

Sunda, W. G. (2012). Feedback interactions between trace metal nutrients and phytoplankton in the ocean. *Front. Microbiol.* , **3**, 204.

Tankéré, S. P. C., Muller, F. L. L., Burton, J. D., Statham, P. J., Guieu, C., & Martin, J. M. (2001). Trace metal distributions in shelf waters of the northwestern Black Sea. *Cont. Shelf Res.* , **21**, 1501-1532.

Taylor J. R. (1982) *An introduction to error analysis: the study of uncertainties in physical measurements*. ed. Ann, Univ. Sci. Books, Mill Valley, California.

Tegler, L. A., Horner, T. J., Galy, V., Bent, S. M., Wang, Y., Nielsen, S. G., (sumb.) Constraining the margin organic C flux. *AGU Adv*.

Thunell, R. C., Tappa, E., & Anderson, D. M. (1995). Sediment fluxes and varve formation in Santa Barbara Basin, offshore California. *Geology*, **23**, 1083-1086.

Van Aken, H. M., & Verbeek, H. (1988). The hydrography and ventilation of Kau Bay in Halmahera. *Neth. J. Sea Res.*, **22**, 403-413.

van der Weijden, C. H., de Lange, G. J., Middelburg, J. J., van der Sloot, H. A., Hoede, D., & Shofiyah, S. (1989). Geochemical characteristics of Kau Bay water. *Neth. J. Sea Res.*, **24**, 583-589

van Geen, A., McCorkle, D. C., & Klinkhammer, G. P. (1995). Sensitivity of the phosphate-cadmium-carbon isotope relation in the ocean to cadmium removal by suboxic sediments. *Paleoceanography*, **10**, 159-169.

Wedepohl, K. H. (1995). The composition of the continental crust. *Geochim. Cosmochim. Ac*, **59**, 1217-1232.

Wombacher, F., Rehkämper, M., Mezger, K., & Münker, C. (2003). Stable isotope compositions of cadmium in geological materials and meteorites determined by multiple-collector ICPMS. *Geochim. Cosmochim. Ac*, **67**, 4639-4654.

Xie, R. C., Galer, S. J., Abouchami, W., Rijkenberg, M. J., De Baar, H. J., De Jong, J., & Andreae, M. O. (2017). Non-Rayleigh control of upper-ocean Cd isotope fractionation in the western South Atlantic. *Earth Planet Sc. Lett.*, **471**, 94-103.

Xie, R. C., Rehkämper, M., Grasse, P., van de Flierdt, T., Frank, M., & Xue, Z. (2019). Isotopic evidence for complex biogeochemical cycling of Cd in the eastern tropical South Pacific. *Earth Planet Sc. Lett.*, **512**, 134-146.

Xue, Z., Rehkämper, M., Horner, T. J., Abouchami, W., Middag, R., van de Flierd, T., & de Baar, H. J. (2013). Cadmium isotope variations in the Southern Ocean. *Earth Planet Sc. Lett.*, **382**, 161-172.

Yakushev, E., Chelysheva, M., Podymov, O., Velikova, V., Chasovnikov, V., & Belokopytov, V. (2010). On the recent decadal changes of the Black Sea nutrient regime and oxic/anoxic boundary position. *CIESM*, 25-34.

Yang, S. C., Lee, D. C., & Ho, T. Y. (2012). The isotopic composition of cadmium in the water column of the South China Sea. *Geochim. Cosmochim. Ac*, **98**, 66-77.

Zheng, Y., Anderson, R. F., Van Geen, A., & Kuwabara, J. (2000). Authigenic molybdenum formation in marine sediments: a link to pore water sulfide in the Santa Barbara Basin. *Geochim. Cosmochim. Ac*, **64**, 4165-4178.

Chapter 4. Cadmium isotope variations across a ‘whiff’ of O_2 at 2.5 Ga

Abstract

Numerous geochemical proxies suggest that transient 'whiffs' of molecular oxygen (O_2) predated the Great Oxidation Event (GOE; ~2.4 billion years ago, or Ga). Because the 'whiffs' of oxygen are suspected to be of a cyanobacterial origin, we might expect that these changes in atmospheric oxygenation were associated with concurrent perturbations to the marine nutrient biogeochemistry. Evidence for such perturbations is presently lacking. Here, we explore cadmium (Cd) abundance and isotopic compositions in the sedimentary rocks that host perhaps the most compelling evidence for a pre-GOE "whiff" event: the ~2.5 Ga organic-rich Mt. McRae Shale (Western Australia).

In the modern ocean, dissolved Cd displays a nutrient-like profile. To briefly summarize, uptake by phytoplankton fractionates Cd: the light isotopes are assimilated into organic matter and the residual seawater is enriched in heavy isotopes. Because the Cd ultimately delivered to sediments is primarily associated with organic matter and sulfides, the Cd isotopic compositions of certain marine sediments could potentially elucidate changes in the composition of ancient seawater and thus nutrient biogeochemistry. However, recent work has shown that Cd use as a paleo nutrient proxy may be difficult if the conditions of the basin are not well-constrained (i.e., redox conditions and Cd concentrations in the surface waters), diagenesis modifies the shale after deposition, or external supply of Cd obfuscates the signal in Cd-deplete regions.

We observe minimally varying Cd-isotopic compositions in the USI of the Mt. McRae Shale despite pronounced Cd enrichments associated with the 'whiff' interval. The entire interval is characterized by Cd-isotopic compositions comparable to light isotope values in some modern organic-rich sediments. We attribute the Cd isotope composition to depleted Cd surface waters over the entire 'whiff' interval and suggest that Cd isotopes do not reflect nutrient utilization in the Hamersley Basin.

1. Introduction

Multiple lines of evidence suggest that minor amounts of molecular oxygen (O_2) were present on Earth's surface before rapidly accumulating in the atmosphere during the Great Oxidation Event (GOE; ~2.5 Billion years ago; Anbar et al., 2007; Bekker et al., 2004). Some models suggest that under anoxic conditions cyanobacteria can produce up to 25 μM of dissolved oxygen in the surface ocean and may be responsible for the "whiffs" of atmospheric oxygen

observed in the late Archean (Olson et al., 2013). Because these transient oxygenation events are thought to be of a cyanobacterial origin, one might expect to observe associated changes in the nutrient biogeochemistry over the same period. However, evidence for changes in nutrient supply and/or utilization has not been substantiated because few geochemical proxies that can be employed in ancient shales are capable of tracking changes in nutrient biogeochemistry. Cadmium (Cd), however, is strongly enriched in organic matter and is primarily preserved in organic-rich sediments (Little et al., 2015; Morford & Emerson, 1999; van Geen et al., 1995). Here, we will employ Cd concentrations and isotopic analyses to probe our ability to relate nutrient cycling to the whiff of oxygen observed in the Mt. McRae Shale from Western Australia, an organic-rich shale deposited approximately 100 Myr before the GOE.

In the modern ocean, Cd, a post-transitional trace metal, exhibits a nutrient-like profile that mimics dissolved inorganic phosphorus, an essential macronutrient. Interestingly, this profile suggests that Cd is subject to biological cycling in seawater, despite being toxic to microbes (Waldron & Robinson, 2009). While many explanations have been posited to explain why this toxic trace metal is biologically cycled, two prevailing theories dominate: microbes mistakenly remove Cd from seawater while trying to uptake biologically relevant trace metals such as iron and zinc (Horner et al., 2013) or microbes require Cd for an undiscovered Cd-centered metalloenzyme (Lane et al., 2005; Price & Morel, 1990). Regardless of the ultimate fate of Cd in a microbe, Cd has been shown to be actively cycled in the water column. In the surface ocean, Cd is taken up by microbial activity and subsequently exported to the deep as particulate organic matter (POM) where it is remineralized at depth (Boyle et al., 1976). Upon remineralization, most of the fixed Cd is released to the surrounding seawater, but the fraction that remains in the particulate phase is delivered to the seafloor.

Isotopic analyses have revealed significant variations associated with Rayleigh-like fractionation during biological assimilation, which affects the vertical distribution of Cd-isotopes in seawater (Ripperger et al., 2007; Xue et al., 2013). In the upper water column, phytoplankton preferentially uptake isotopically light Cd (John & Conway, 2014; Lacan et al., 2006) and leave the residual seawater enriched in heavy isotopes. Measurements of modern seawater reveal that deep water is homogeneous after the remineralization of organic matter, and maintains a Cd isotopic value on the order of +0.3 ‰ (Abouchami et al., 2014; Conway & John, 2015; Ripperger et al., 2007b; Sieber et al., 2023) where $\delta^{114}Cd = (\delta^{114}Cd_{sample}/\delta^{114}Cd_{NIST\ SRM\ 3108}) - 1$. Ultimately,

the Cd isotope compositions in the underlying sediment are sensitive to changes in the physical and biological processes occurring in the water column, which might allow for some sedimentary archives (such as carbonates and organic-rich shales) to be used as a proxy for past nutrient cycling and utilization efficiency (Georgiev et al., 2015; Hohl et al., 2019)

Organic-rich sediments are a potential archive for observing changes associated with nutrient biogeochemistry as they are a major sink of dissolved Cd in the modern oceans (Little et al., 2015; Morford & Emerson, 1999; Tegler et al., *submitted;* van Geen et al., 1995). Cadmium enrichment in these sediments is primarily controlled by two processes: the delivery of organic matter from sinking particles and the formation of Cd sulfides (Tegler et al., *submitted*). The first vector of Cd enhancement in the margins is simply related to the organic carbon flux to the sediment. As organic matter is delivered and preserved in the sediment, so is Cd. However, under conditions where porewaters become sulfidic when organic matter is remineralized in the sediment, Cd is subsequently released to the surrounding porewaters. Under these conditions, Cd co-precipitates with sulfides in the sediments as CdS (e.g., Greenockite; Gobeil et al., 1987; McCorkle & Klinkhammer, 1991). However, because Cd is chalcophile, CdS can precipitate in these waters with trace amounts of hydrogen sulfide (Davies-Colley et al., 1985; Rosenthal et al., 1995). Thus, if the Cd capture is near-quantitative, dissolution and recapture of Cd as a CdS would have a minimal effect on the isotope composition of the sediment. Finally, Cd can arrive in the sediment if CdS formed pelagically in anoxic bottom waters with even trace accumulation of free hydrogen sulfide (Plass et al., 2020, 2021). However, this vector of Cd delivery requires both periodically sulfidic conditions and advection of dissolved Cd to the depositional site (Tegler et al., submitted). If an ancient record does not meet these conditions, then it is probable that the Cd isotope composition of the sediments reflects the organically-bound Cd that arrives at the seafloor.

Unfortunately, the isotope composition of the organically-bound Cd that arrives at the seafloor may be more complex than simply reflecting the Cd isotope signature of biological activity in the surface waters. Physical processes such as the upward mixing of Cd-rich water, as well as the dissolution of dust, may affect the Cd isotope composition of surface waters when Cd concentrations are overall very low (Tegler et al., *submitted.*). Furthermore, evidence from marine particulates suggests that organic matter may undergo a modification of the Cd isotope values during remineralization as it sinks to the seafloor (Tegler et al., submitted; Janssen et al., 2019). While remineralization is possible, there are currently no studies that compare particulate Cd

isotopes in the water column with marine sediments. Therefore, we will not discuss the role remineralization may play in setting the Cd isotope composition of the seafloor but urge for more studies to examine the effects of remineralization in the modern.

Here, we apply Cd concentration and isotope measurements over a "whiff" of oxygen 2.5 billion years ago observed in the Mt. McRae Shale. We examine this "whiff" in the context of presumed changes in nutrient utilization and preservation that are hypothesized to occur during a reorganization of biogeochemical pathways. Our data allow us to conjecture some of the possibilities that lead to the prolonged burial of isotopically light Cd. We conclude that since Cd:OC ratios are similar to modern-day sediments, pelagic CdS precipitation in euxinic bottom waters is unlikely. Furthermore, the consistently light Cd isotopes rule out quantitative uptake of Cd in the surface waters and suggest either very high or very low surface Cd concentrations. We posit the external Cd sources coupled with low surface Cd concentrations are the most promising conditions to explain the Cd trends observed in the Archean.

2. Methods and Methodology

2.1 Geological Context

Core ABDP-9 was drilled in 2004 as a part of the NASA Astrobiology Institute Deep Time Drilling Program. It is located in the Pilbara craton of Western Australia, spans 1000 meters, and comprises banded iron formations, kerogenous shales, cherts, carbonates, and clastics (Figure 1). The section comprises four distinct units, as shown in Fig. 1 (Raiswell et al., 2011). The base of the shale is the lower shale interval (LSI; 189.65 - 173 m) and is made up of interbedded organic-rich marl and laminated shale (Anbar et al., 2007; Kaufman et al., 2007). Above LSI is a sideritic banded iron formation (BIF) (up to 153.5 m) with thinly laminated shales at the top and marl near the base. After LS1, there is an upper shale interval (USI) up to 125.5 m. The final section is mainly carbonate (125.5 to 110 m; Raiswell et al., 2011).

The Mt. McRae Shale shows periods of broad-scale redox changes likely brought on by weathering in response to the onset of an oxidative sulfur cycle (Anbar et al., 2007). Minimal oxidative weathering began during LS1, and likely contributed to enrichment in authigenic trace metals in the shales during US1, the main "whiff" interval (Anbar et al., 2007). Trace metal

analysis has indicated increased concentrations and isotopic variability during the US1 interval (Anbar et al., 2007; Kaufman et al., 2007; Ostrander et al., 2017; Reinhard et al., 2009).

2.2 Sample Preparation

All samples were prepared in the NIRVANA Clean lab facilities at the Woods Hole Oceanographic Institution (WHOI). Acids were distilled and tested for their Cd concentration before use, and water was obtained from an 18.2 ΩM Milli-Q grade system.

Approximately 20-30 mg of sample from the drill core ABDP9 was weighed into 7 mL perfluoroalkoxy vials (Savillex). The powder was first treated with 2 M HNO_3 for 17 hours at 60˚C and centrifuged to separate the detrital material (Ostrander et al., 2017). The leachate was subsequently oxidized in an Anton Parr Microwave for 2 hours at 250 ˚C to dissolve any remaining organic material. After oxidation, an aliquot of each sample was taken, and the Cd content was measured on a Thermo quadrupole inductively-coupled mass spectrometer (Q-ICP-MS) located in the WHOI Plasma Facilitates. An appropriate amount of double spike was added to each sample such that the Cd spike-to-sample ratio would be between 1 and 2. The samples were brought up in 1 mL of 1 M HCl after the addition and dry-down of 6 M HCl.

Two-stage anion-exchange chromatography was performed to separate Cd from the geological matrix (Table 1). Particularly, separation from In, Sn, and Pd is important as these elements are isobaric interferences with Cd. The separation technique was modified from (Wombacher et al., 2003). In brief, the samples were loaded in 1 M HCl onto columns with pre-cleaned 500 µL AG MP-1M anion-exchange resin. Following the first column, the samples were dried down and reconstituted in the Cl^- form and subsequently loaded in 1 M HCl onto pre-cleaned 180 µL AG MP-1M anion-exchange resin. Following column chemistry, residual organic material was removed with a liquid-liquid organic extraction, which was modified from (Murphy et al., 2015). Here, any excess organic material from the resin was extracted by adding 1.2 mL of Optima-grade heptane to the eluted samples, shaking for 30 seconds, and allowing them to sit for three minutes. The heptane was shaken and allowed to sit three times. Subsequently, the heptane was extracted and discarded, and the process was repeated once. The samples were dried and brought up in 1.1 mL of 2 % HNO_3 and prepared for mass spectrometry.

2.3 Isotopic Analysis of Cd

The Cd isotope ratios were measured at the WHOI Plasma Mass Spectrometry Facility on a Thermo Finnigan Neptune multi-collector inductively-coupled mass spectrometer. Samples were introduced into the instrument at a rate of 140 μL minute^{-1}. The ion currents from 110 AMU to 117 AMU were measured in 30 four-second integrations and processed with a MATLAB script to elicit the sample isotopic composition from the spike-to-sample mixture and the isobaric interferences, which included ^{112}Sn, ^{113}In, and ^{114}Sn.

The samples were externally normalized to NIST SRM (Standard Reference Material) 3108, the 'zero-delta' reference material, and BAM 1020, a secondary reference material. To assess the long-term uncertainty and precision of the Cd isotopic measurements, the USGS Green River Shale (SGR) was processed several times in each standard run. The long-term 2SD of unknown samples is ± 0.03 ‰, which was determined by repeated measurements of standards over several instrumental runs.

3. Results

3.1 Cadmium Concentrations and leach validation

The data are summarized in Figure 2. The record shows that, despite an increase in Cd concentration, there is prolonged burial of invariant isotopically light Cd across the whiff interval. The LS1shows a trend toward isotopically heavy values before returning to the characteristic light values.

On average, the leaching method released 82 % Cd contents compared to the bulk measurements made for elements throughout the shale (Figure 3). Throughout the record, the concentration of Cd in the leached samples mirrors the trends in the bulk data, implying that the leach removes the majority of the authigenic Cd in the sediment with minimal release of lithogenic material. Similar results have been found for modern organic-rich sediments (Tegler et al., submitted), which suggests that the leach efficiently produces a chemical separation of organic and sulfidic Cd from lithogenic.

Our analyses reveal a significant rise in Cd concentrations centered on the previously identified whiff interval whereby the concentrations rise and fall from 1-10 ppm (Figure 2a). There is a less-pronounced rise in Cd concentrations at the end of the LS1.

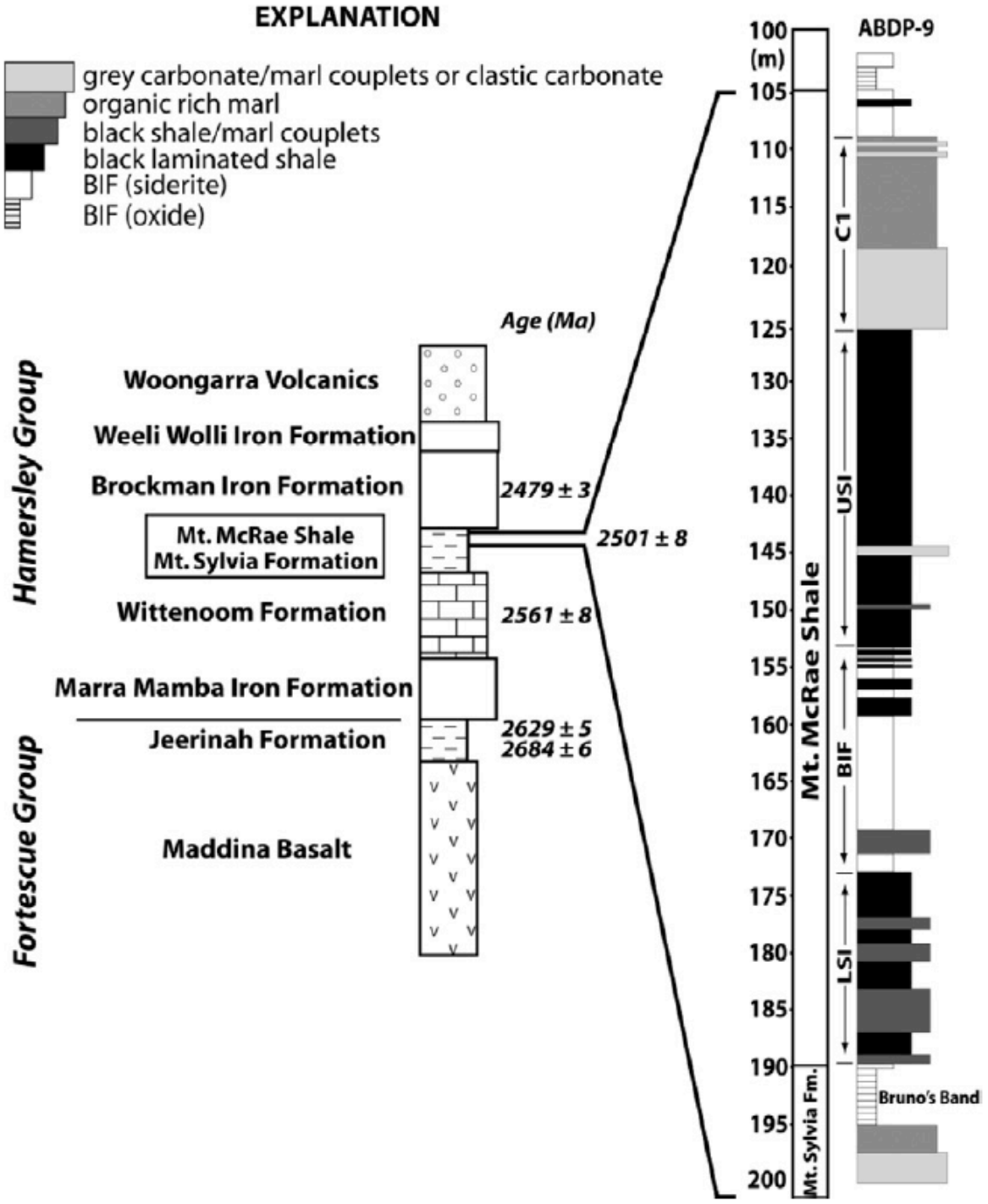

Figure 1. Stratigraphy for the Mt. McRae Shale in Western Australia. Figure is reproduced from Raiswell et al. (2011) and references therein. The associated radiometric ages are from Ono et al. (2003) and Anbar et al. (2007).

Table 1: Cd purification procedure

Biorad AG-1X8 anion-exchange resin (100-200 mesh)		
Stage 1 column chemistry		
Eluent	Quantity (μL)	Purpose
2 M HNO_3	3750	Clean resin
H_2O	250	Resin rinse
6 M HCl	5500	Conversion to Cl- form
0.5 M HCl	3750	Resin equilibration
Load samples	variable	Samples loaded in 1 M HCl
0.5 M HCl	7750	Elute matrix
1 M HCl	3250	Elute matrix
2 M HCl	3250	Elute matrix
6 M HCl	3250	Elute Ag
0.5 M HNO_3 + 0.1 M HBr	3750	Elute Zn
2 M HNO3	3750	Elute Cd
Stage 2 column chemistry		
2 M HNO_3	1320	Clean resin
H_2O	60	Resin rinse
6 M HCl	1920	Conversion to Cl- form
0.5 M HCl	1320	Resin equilibration
Load samples	variable	Samples loaded in 1 M HCl
0.5 M HCl	2760	Elute matrix
1 M HCl	1200	Elute matrix
2 M HCl	1200	Elute matrix
6 M HCl	1200	Elute Ag
0.5 M HNO_3 + 0.1 M HBr	1200	Elute Zn
2 M HNO3	1380	Elute Cd
Heptane Extraction		
Optima Heptane	1200	Extract organics
Optima Heptane	1200	Extract organics

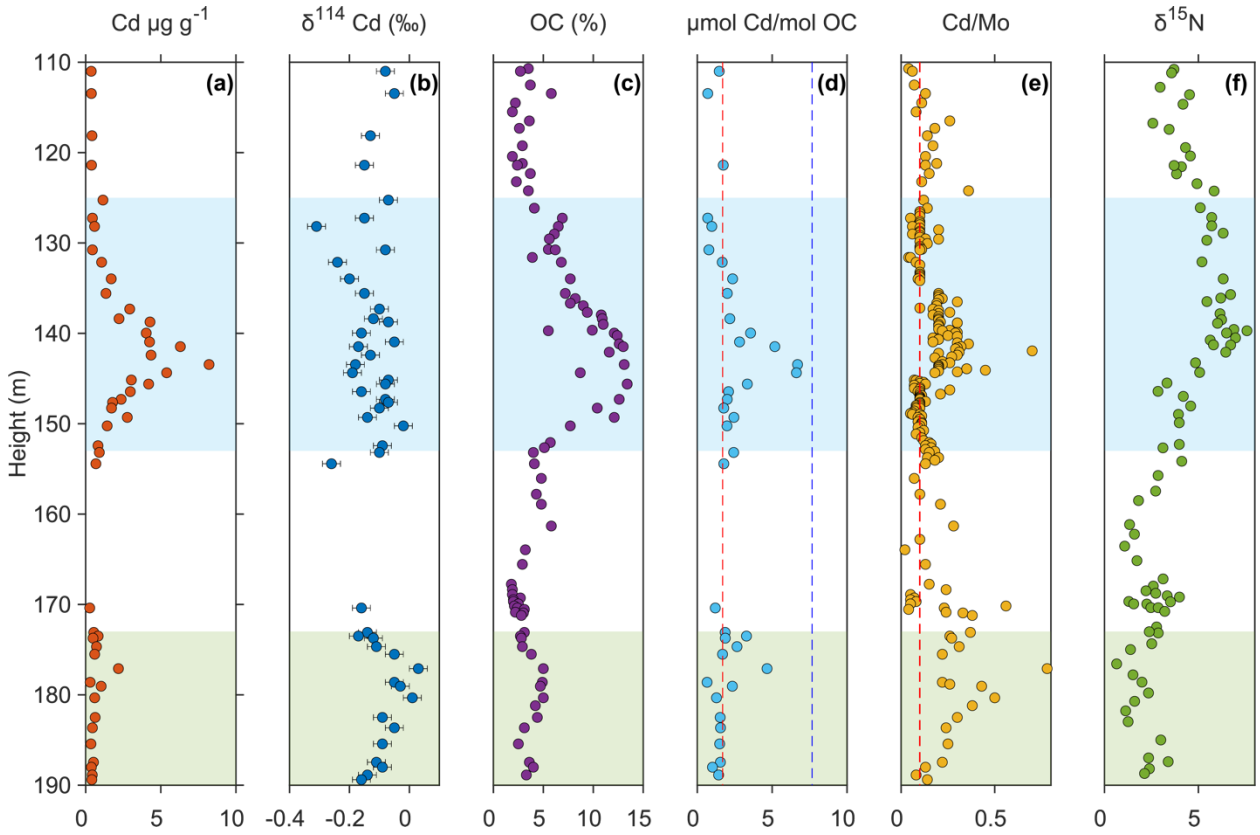

Figure 2. (a) leached concentrations of Cd, featuring a marked increase over the 'whiff' interval, (b) the Cd isotope composition throughout the Mt. McRae Shale, (c) OC content in the shale from (Anbar et al., 2007), (d) ratio of µmol Cd relative to mol OC where the dotted lines are estimates of Cd:OC ratios in phytoplankton from Ho et al. (2003) and Bourne et al. (2018), (e) Cd:Mo ratios throughout the section, dotted line indicates 0.1 cut off between restricted and upwelling regions, (f) $\delta^{15}N$ data from (Garvin et al., 2009).

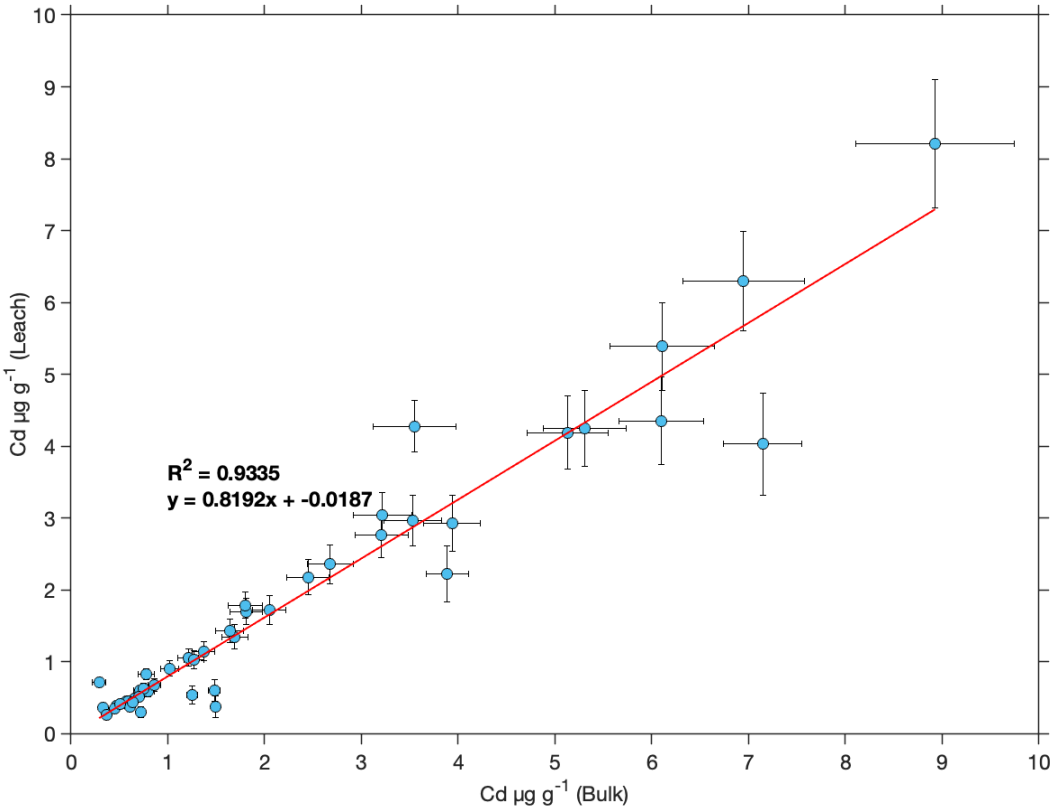

Figure 3. Bulk versus leached samples show that the leach captured the majority of the Cd, but some of the detrital material was left behind.

3.2 Cadmium Isotopic Composition

In USI, the $\delta^{114}Cd$ values fall between −0.31 ± 0.03 ‰ and −0.02 ± 0.03 ‰ and an average value of $\delta^{114}Cd$ = -0.13 ± 0.06 ‰ (1 SD; n=31). Meanwhile, the LSI reveals a trend from 190-178m toward heavier values from −0.17 to +0.03 ‰ returning to −0.17‰ ~172m depth (Figure 2b). The average value of the LSI is δ^{114} Cd = −0.09 ± 0.06 ‰ (1 SD; n = 17).

An SGR-1 standard was also run once for every 10 samples. The standard values between δ^{114} Cd = −0.01 and 0.05 ‰ with an average value of δ^{114} Cd = 0.02 ‰ ± 0.03 (e.g., 1 SD; n = 6).

4. Discussion

4.1 Cadmium Incorporation in the Mt. McRae Shale

To briefly review, in modern marine sediment, Cd can be incorporated into the sediment via three mechanisms. First, it can arrive in association with organic matter, where both the Cd and organic matter are preserved in the sediment. Second, it can be released to the porewaters as the organic material is remineralized. If these porewaters are sulfidic, the Cd can be captured as CdS and preserved in the sediment even as the organic material is remineralized. Finally, Cd can precipitate directly out of seawater, assuming (i) there is a source of dissolved H_2S in the bottom water and (ii) there is a supply of dissolved Cd. Tegler et al. (submitted) showed that the depositional environment plays an important role in determining whether pelagic precipitation of CdS occurs. For example, while the Peru Margin shows ample evidence for pelagic CdS precipitation, regions with high degrees of restriction and no source of dissolved Cd, like the Cariaco Basin and the Black Sea, do not have evidence for pelagic precipitation despite having euxinic bottom waters. We assume that each of these mechanisms for Cd incorporation in sediments existed in the Archean. However, before we interpret our records, we will explore whether diagenesis is expected to add or modify the Cd that is recorded in the Mt. McRae Shale.

4.1.1. Did Cd in the Mt. McRae Shale experience diagenetic alteration?

Recent studies have suggested that the Mt. McRae shale may have been affected by post-depositional processes. Slotznick et al. (2022) hypothesized that elements were introduced to the Mt. McRae shale as volcanic glasses and were altered during diagenesis to form sulfide minerals during secondary fluid flow through the shale. If true, this could suggest that the Cd concentration and isotope signatures in the sediment were set during post-depositional processes and do not represent Archean Cd. However, our data suggest that Cd is not significantly impacted by post-depositional remineralization.

Slotznick et al. (2022) argue that the Cd incorporations come from volcanic rocks. However, Cd concentrations from volcanic rocks are expected to be an order of magnitude lower than the concentrations observed in the Mt. McRae Shale (Cannon et al., 1978). Thus, even if volcanic Cd is incorporated in the sediment after deposition, it is unlikely that such a Cd source would significantly impact the Cd concentrations or isotope signatures. Secondly, Slotznick et al. (2022) suggested that the diagenetic processes are expected to be most pronounced over the 'whiff' interval. However, the Cd isotope values are invariant before, after, and during the whiff section, even as the Cd concentrations rise. If there was more influence during the whiff interval, and the increased Cd concentrations are owed to the input of volcanic glass, we would expect these isotope values to change during the whiff interval. This is not the case. Thus, our data suggest that Cd and its isotopes are minimally impacted by post-depositional processes.

4.1.2. Did the Mt. McRae have pelagic CdS precipitation?

In modern marine settings, CdS can precipitate pelagically if certain conditions are met. The bottom waters have at least episodic euxinia and there must be a fresh supply of Cd from upwelled waters (e.g., Plass et al., 2020, 2021; Tegler et al., submitted). Studies have used Fe speciation to suggest that the Mt. McRae Shale was deposited under euxinic conditions (Reinhard et al., 2009). If true, this would suggest that the Hamersley Basin meets the first condition needed for pelagic CdS precipitation. Additionally, Ostrander et al. (2019) proposed that portions of the continental margins were fully oxic in the Hamersley Basin—from the air-sea surface to below the sediment-water interface. This suggests that Mt. McRae itself may have been positioned under a stratified water column, with oxic surface waters and euxinic bottom waters. Therefore, it is possible that the euxinic sediments had a source of oxic waters with dissolved Cd to be upwelled

into a region where pelagic CdS could precipitate, similar to the modern Peru Margin (e.g., Plass et al., 2020, 2021; Tegler et al., submitted). To probe whether pelagic precipitation was possible, we examine the Cd/OC ratios and the δ^{114}Cd of the record.

Several studies have indicated that the range of Cd:OC ratio in organic matter spans from 1.69 to 7.66 μmol Cd: mol OC (Ho et al., 2003; Bourne et al., 2018; Chen et al., 2021; Tegler et al., submitted). Cadmium that is pelagically precipitated from seawater have Cd:OC ratios that surpass this ratio. Tegler et al. (submitted) suggests that the average Cd:OC ratio in the Peru Margin is ~47 and the highest observed Cd:OC ratio in the Peru Margin is 115. Thus, the Cd:OC ratios that depict pelagic CdS precipitation should be easily identified. Figure 2d shows the range of Cd:OC in the Mt. McRae Shale. The dotted lines of the figure indicate the range of ratios that are attributed to organic matter. The expected Cd:OC ratio of pelagically precipitated CdS is not shown in the figure because it is nearly 5 times higher than the greatest Cd:OC ratio observed in the Mt. McRae shale. Therefore, we suggest that there no evidence of pelagic CdS precipitation in the Hamersley Basin.

Additionally, the δ^{114}Cd of the shale argues against pelagic CdS precipitation. If we assume that (i) the Cd inputs had an isotope composition similar to today (e.g., +0.1 to + 0.2 ‰; Lambelet et al., 2013; Bridgestock et al., 2017). and (ii) the Archean did not have a process that preferentially removes the heavy isotopes into marine sediment, any pelagic Cd precipitation should be isotopically heavy. As a modern analog, the isotope composition of the sediments in the modern Peru Margin are all heavier than + 0.1 ‰ and are often on the order of + 0.3 ‰. Instead, we observe isotopically light Cd isotopes over the entire 'whiff' interval (e.g., −0.15 ‰). Thus, we conclude that the Cd in the Mt. McRae Shale represents organically-derived Cd.

4.2 What does the δ^{114}Cd signature in the Mt. McRae Shale represent?

Cadmium has been proposed as a proxy for nutrient utilization in marine sediments (e.g., Georgiev et al., 2015). However, recent studies have suggested this proxy may not be easily applied to marine sediments. In the proposed proxy, Georgiev et al. (2015) suggested that as long as the deep water has an isotopic composition of δ^{114}Cd = +0.3 ‰, sediment with the same composition signifies the quantitative removal of Cd in the surface waters of these regions. Likewise, in regions where there is incomplete nutrient uptake from low biological activity or enhanced supply of Cd through upwelling, the particulate organic matter can be substantially

lighter on the order of $\delta^{114}Cd = -0.1$ ‰ (Georgiev et al., 2015). Thus, according to this proxy, the overall range of $\delta^{114}Cd$ in organic-rich sediments is between +0.3‰ (reflecting quantitative removal) and −0.1‰ (signifying non-quantitative removal; Figure 4).

However, while this proxy has been applied to ancient marine sediments, it has never been tested with modern deposits. Several studies have now measured the isotope composition of Cd in organic-rich marine sediments. For sediments that are not influenced by pelagic Cd precipitation, the $\delta^{114}Cd$ compositions of the marine sediments have always been lighter than ~ +0.15 ‰ (Chen et al., 2021; Tegler et al., submitted). Sediments with a Cd isotope values that suggest quantitative uptake have never been observed. Moreover, isotopically light signatures have been observed in regions that have extreme Cd depletion in the surface waters due to external inputs (Tegler et al., 2023). This discovery is at odds with the theoretical use of the paleonutrient proxy.

Over the entirety of the record in the Mt. McRae shale, we observe the invariant burial of isotopically light $\delta^{114}Cd$, despite increased Cd concentrations over the 'whiff' interval. This light signature could arise from two scenarios. First, the Mt. McRae could reflect a sediment deposit that underlies a Cd-replete region. In this scenario, Rayleigh-like uptake could be expressed in the sinking particles and reflect low nutrient utilization. Unfortunately, no modern data exists for Cd-replete conditions. So, this explanation is currently speculative. Alternatively, the shale could have been deposited under Cd-deplete conditions. The Mt. McRae average $\delta^{114}Cd$-value in this section (δ^{114} Cd = − 0.13 ‰) is comparable to isotope compositions found in the modern, including in the California margin (Chen et al., 2021), the Arabian Sea, the Namibian Margin and the Western Equatorial Pacific (Tegler et al., submitted). Each of these modern regions has Cd depleted surface waters and an external supply of Cd that obfuscates the biological signals. Here, we discuss the two Cd surface water conditions that are possible in the Archean. First, we consider that the Hamersley Basin had Cd-replete conditions in the surface waters. Next, we consider that the basin had Cd-deplete surface waters.

4.3 Cd-replete versus Cd-deplete surface conditions

The Hamersley Basin may have had high Cd surface water concentrations above the Mt. McRae depositional site. Unfortunately, there are currently no modern data from regions that have Cd-replete surface waters, so no current analog for such a scenario exists. However, Tegler et al., (submitted) speculate that Cd-replete regions may follow Rayleigh-like trends in the surface

waters. If true, the observed light Cd isotopes would indicate low surface nutrient utilization. While it is possible that these Cd-replete conditions could set the observed δ^{114}Cd signatures, we expect that Cd-replete conditions in the Hamersley Basin were unlikely. In section 4.1, we suggest that upwelling of waters containing dissolved Cd was unlikely because we did not observe pelagic precipitation of Cd in the euxinic bottom waters of the deposition site. If there was an open basin with a supply of Cd to the euxinic bottom waters overlying the deposition site, we might expect to see pelagic CdS precipitation instead of primarily organically-derived Cd. Thus, we expect that replete Cd conditions in a restricted basin are unlikely, but not impossible. Such a scenario should be evaluated when measurements from modern sediments underlying Cd-replete surface waters are available.

Modern studies have shown that if [Cd] in surface waters is low, the Cd isotope compositions of sediment underlying such regions can be significantly influenced by external inputs, including aeolian deposition (Yang et al., 2012; Bridgestock et al., 2017; Sieber et al., 2023) and upward mixing of deeper waters (Abouchami et al., 2011; Xue et al., 2013). Because both deeper waters and aeolian deposition add Cd to surface waters that are isotopically significantly lighter than the values expected based on Rayleigh depletion by uptake into phytoplankton (Schmitt et al 2009; Rehkämper et al., 2011; Sieber et al., 2023), sediment deposited underneath low [Cd] regions exhibit mostly light Cd isotope values with δ^{114} Cd = −0.2 to +0.15 ‰ (Tegler et al submitted). This range of values are consistently offset by ~0.2−0.8‰ from surface waters with [Cd] in the same range, implying that Cd deposition underneath regions with low [Cd] surface water likely adhere to isotope fractionation patterns observed for Cd uptake into phytoplankton.

The light values observed throughout the Mt McRae shale succession could, therefore, be consistent with the deposition of organic matter in a region of the ocean with overall low [Cd] in the surface waters. Given the high contents of OC in the Mt McRae shale (Fig. 2), it is possible that [Cd] surface waters were low due to biological uptake. In turn, these low [Cd] in the surface waters likely resulted in light Cd isotope values in the exported organic matter, similar to what is observed in modern organic-rich sediments underlying regions with low [Cd] in the surface waters (Tegler et al submitted). We posit that this is the best current explanation for the δ^{114} Cd observed in the Mt. McRae Shale.

4.4 What does the change in Cd:OC in USI the Mt. McRae Shale represent?

Figure 2 shows that Cd concentrations, OC (%) and Cd μmol: OC mol all increase during the 'whiff' interval, despite being within the range of Cd and OC from modern marine particles. This change in Cd:OC occurs even as the isotopes remain invariant. There are two scenarios that may explain this phenomenon. First, it is possible that more Cd was liberated during this interval. Anbar et al. (2007) suggested that oxidative weathering increases the weathering of Mo-bearing sulfides in crustal minerals. Thus, more Mo entered the oceans during this interval. If oxidative weathering also increased the amount of Cd that reached the ocean, it could have increased the reservoir of Cd in the surface waters. However, if Cd increased, and the surface Cd was depleted, we may have expected to see an associated change in the Cd isotopes during this time (e.g., b we may have expected the isotopes to become heavier). However, it is possible that the increased Cd was small, and thus the Cd in the surface waters, while increased, remained low enough that Rayleigh-like behavior was not observed. On the other hand, it is possible that the 'whiff' interval was also marked by porewaters that more efficiently captured Cd in the porewater relative to OC. If that were the case, we would expect for the Cd isotopes to remain the same even as Cd was preserved more efficiently relative to OC.

4.5. The Lower Shale Member and Potential Productivity Signature

For the majority of the record, a light, unsystematic Cd isotopic signature dominates, but a small systematic excursion is observed in LS1 (between 170-190 m, Fig 2a). This section shows values that tend toward heavier values, with a maximum of an $\delta^{114}Cd = +0.03 \pm 0.02$ ‰ before returning to the standard lighter composition in US1. This could represent a change in Cd surface concentrations wherein the conditions were Cd-deplete and then became slightly more replete and allowed Rayleigh fractionation to be expressed, if only marginally. Such a possibility is likely if the Hamersley basin experienced less restriction during LS1 compared to US1.

We can roughly distinguish between unrestricted and restricted basins by comparing the ratios of Cd to Mo in the sediment. Specifically, biologically active regions and hydrologically restricted regions have distinct Cd and Mo enrichment patterns. Upwelling regions are often associated with high productivity. Thus, the regions tend to show high Cd enrichment in the underlying sediment as Cd-rich microbes are exported to the seafloor. Conversely, Mo, a

conservative element, is unaffected by increased biological activity and is not enriched in regions with enhanced productivity (Little et al., 2015). Therefore, in areas with high productivity, the Cd:Mo ratios are high, whereas, in restricted regions, the differences between the concentrations are much subtler. Sweere et al. (2016) use an empirical ratio of 0.1 to define the cut-off between a restricted basin and an upwelling setting. We employ the same ratio with the caveat that a ratio of Cd:Mo of 0.1 is calibrated for modern settings and may not hold for ancient sediments.

The Cd:Mo ratios in LSI suggest that the period may have been defined by a local upwelling event that could have stimulated productivity or increased Cd in the surface waters, allowing Rayleigh like fractionation to be expressed. Thus, the excursion in LS1 may be interpreted as a local productivity signature. Here, almost all of the Cd:Mo ratios are much higher than those observed in US1. These higher Cd:Mo ratios imply that deposition took place during a period of enhanced organic matter production. The isotopic and geochemical evidence corroborates such a conclusion. The Cd isotopes at the onset and conclusion of the excursion show a light signature but tend toward heavier values that coincide with the peak of the Cd:Mo ratios. This excursion implies that there was a change in the fractionation factor between the seawater and the sediment as a result of increased Cd utilization. Furthermore, OC and $\delta^{15}N$ also show small deviations during LS1 that signal biological activity (Garvin et al., 2009). The nitrogen isotopes below 161 m represent an anoxic N cycle with a small fractionation that may have been imparted during N_2 fixation. Thus, although significant nitrogen isotopic excursions occur between 139-153 meters owing to an increase in fixed N loss through denitrification (Garvin et al., 2009), the small excursion below 161 m hints at small-scale biological activity. Furthermore, although OC and Cd:Mo ratios are independent proxies, the fact that they increase together signals increased productivity over this interval, as both would be preserved similarly under euxinic conditions. Such a productivity event would be interesting as it appears to occur before the major 'whiff' event where most of the redox elements show variability (Anbar et al., 2009), and this indicator noticeably absent in the main interval. We propose that this discrepancy is due to a potential hydrological shift in the basin that caused the Cd dynamics to change between the lower shale member and the upper shale member.

Conclusions

Here, we show that the late Archean Mt. McRae Shale was characterized by an isotopically light signature of ~ −0.15 ‰. We argue against the formation of post-depositional remineralization, pelagic precipitation of CdS, and deposition of Cd under a continuously Cd replete marine environment. Instead, we propose that the data are most compatible with a strongly Cd depleted surface ocean throughout the deposition of the Mt. McRae shale. While the whiff event may have caused an increase in Cd supply to the surface ocean that was synchronous with other elements such as Mo and Re, this did not change the overall low availability of Cd in the surface waters in the Hamersely Basin at 2.5 Ga.

Acknowledgments

I would like to acknowledge Jurek Blusztajn for his invaluable help running the MC-ICP-MS. I would like to thank the coauthors of this study: Chadlin Ostrander, Brian Kendall, Ariel Anbar, Sune Nielsen and Tristan Horner

Chapter 4 References

Abouchami, W., Galer, S. J. G., De Baar, H. J. W., Alderkamp, A. C., Middag, R., Laan, P., Feldmann, H., and Andreae, M. O. (2011). Modulation of the Southern Ocean cadmium isotope signature by ocean circulation and primary productivity. *Earth Planet Sc. Lett.*, **305** (1-2), 83-91.

Abouchami, W., Galer, S. J. G., De Baar, H. J. W., Middag, R., Vance, D., Zhao, Y., Feldmann, H., and Andreae, M. O. (2014). Biogeochemical cycling of cadmium isotopes in the Southern Ocean along the Zero Meridian. *Geochim. Cosmochim. Ac*, **127**, 348-367

Anbar, A. D., Duan, Y., Lyons, T. W., Arnold, G. L., Kendall, B., Creaser, R. A., ... & Buick, R. (2007). A whiff of oxygen before the great oxidation event?. *Science*, *317*(5846), 1903-1906.

Bekker, A., Holland, H. D., Wang, P. L., Rumble Iii, D., Stein, H. J., Hannah, J. L., ... & Beukes, N. J. (2004). Dating the rise of atmospheric oxygen. *Nature*, *427*(6970), 117-120.

Bourne, H. L., Bishop, J. K., Lam, P. J., & Ohnemus, D. C. (2018). Global spatial and temporal variation of Cd: P in euphotic zone particulates. *Global Biogeochem. Cy.*, **32**,1123-1141.

Boyle E. A. (1988) Cadmium: Chemical tracer of deepwater paleoceanography. *Paleoceanography* **3**, 471–489.

Boyle, E. A., Sclater, F., and Edmond J. (1976) On the marine geochemistry of cadmium. *Nature,* **263**, 42-44.

Bridgestock, L., Rehkämper, M., Van De Flierdt, T., Murphy, K., Khondoker, R., Baker, A. R., ... & Achterberg, E. P. (2017). The Cd isotope composition of atmospheric aerosols from the Tropical Atlantic Ocean. *Geophys Res. Lett.*, **44**, 2932-2940.

Cannon, H. L., Connally, G. G., Epstein, J. B., Parker, J. G., Thornton, I., & Wixson, G. (1978). Rocks: geological sources of most trace elements. In *report to the workshop at south scas plantation Captiva Island, FL, US. Geochem Environ* (Vol. 3, pp. 17-31).

Chen, L., Little, S. H., Kreissig, K., Severmann, S., & McManus, J. (2021). Isotopically light Cd in sediments underlying oxygen deficient zones. *Frontiers Earth Sci.*, **9**, 623720.

Conway, T. M., Rosenberg, A. D., Adkins, J. F., & John, S. G. (2013). A new method for precise determination of iron, zinc and cadmium stable isotope ratios in seawater by double-spike mass spectrometry. *Analytica Chimica Acta*, *793*, 44-52.

Conway, T. M., & John, S. G. (2015). Biogeochemical cycling of cadmium isotopes along a high-resolution section through the North Atlantic Ocean. *Geochimica et Cosmochimica Acta*, *148*, 269-283.

Davies-Colley, R. J., Nelson, P. O., & Williamson, K. J. (1985). Sulfide control of cadmium and copper concentrations in anaerobic estuarine sediments. *Mar. Chem.*, **16**, 173-186.

Emerson, S. R., & Huested, S. S. (1991). Ocean anoxia and the concentrations of molybdenum and vanadium in seawater. *Marine Chemistry*, *34*(3-4), 177-196.

Garvin, J., Buick, R., Anbar, A. D., Arnold, G. L., & Kaufman, A. J. (2009). Isotopic evidence for an aerobic nitrogen cycle in the latest Archean. *Science*, *323*(5917), 1045-1048.

Georgiev, S. V., Horner, T. J., Stein, H. J., Hannah, J. L., Bingen, B., & Rehkämper, M. (2015). Cadmium-isotopic evidence for increasing primary productivity during the Late Permian anoxic event. *Earth and Planetary Science Letters*, *410*, 84-96.

Gobeil, C., Silverberg, N., Sundby, B., & Cossa, D. (1987). Cadmium diagenesis in Laurentian Trough sediments. *Geochim. Cosmochim. Ac*, **51**, 589-596.

Guinoiseau, D., Galer, S. J., Abouchami, W., Frank, M., Achterberg, E. P., & Haug, G. H. (2019). Importance of cadmium sulfides for biogeochemical cycling of Cd and its isotopes in oxygen deficient zones—A case study of the Angola Basin. *Global Biogeochemical Cycles*, *33*(12), 1746-1763.

Ho, T. Y., Quigg, A., Finkel, Z. V., Milligan, A. J., Wyman, K., Falkowski, P. G., & Morel, F. M. (2003). The elemental composition of some marine phytoplankton 1. *Journal of phycology*, *39*(6), 1145-1159.

Hohl, S. V., Jiang, S. Y., Wei, H. Z., Pi, D. H., Liu, Q., Viehmann, S., & Galer, S. J. (2019). Cd isotopes trace periodic (bio) geochemical metal cycling at the verge of the Cambrian animal evolution. *Geochimica et Cosmochimica Acta*, *263*, 195-214.

Horner, T. J., Lee, R. B., Henderson, G. M., & Rickaby, R. E. (2013). Nonspecific uptake and homeostasis drive the oceanic cadmium cycle. *Proc. National Acad. Sci.* , **110**, 2500-2505.

Horner, T. J., Rickaby, R. E., & Henderson, G. M. (2011). Isotopic fractionation of cadmium into calcite. *Earth Planet Sc. Lett.*, **312**, 243-253.

Janssen, D. J., Conway, T. M., John, S. G., Christian, J. R., Kramer, D. I., Pedersen, T. F., & Cullen, J. T. (2014). Undocumented water column sink for cadmium in open ocean oxygen-deficient zones. *Proc. National Acad. Sci.* , **111**, 6888-6893

Janssen, D. J., Abouchami, W., Galer, S. J., Purdon, K. B., & Cullen, J. T. (2019). Particulate cadmium stable isotopes in the subarctic northeast Pacific reveal dynamic Cd cycling and a new isotopically light Cd sink. *Earth Planet Sc. Lett.*, **515**, 67-78

John, S. G., & Conway, T. M. (2014). A role for scavenging in the marine biogeochemical cycling of zinc and zinc isotopes. *Earth Planet Sc. Lett.*, **394**, 159-167.

John, S. G., Helgoe, J., & Townsend, E. (2018). Biogeochemical cycling of Zn and Cd and their stable isotopes in the Eastern Tropical South Pacific. *Mar. Chem.*, **201**, 256-262.

Kaufman, A. J., Johnston, D. T., Farquhar, J., Masterson, A. L., Lyons, T. W., Bates, S., ... & Buick, R. (2007). Late Archean biospheric oxygenation and atmospheric evolution. *Science*, *317*(5846), 1900-1903.

Lambelet, M., Rehkämper, M., van de Flierdt, T., Xue, Z., Kreissig, K., Coles, B., ... & Andersson, P. (2013). Isotopic analysis of Cd in the mixing zone of Siberian rivers with the Arctic Ocean—New constraints on marine Cd cycling and the isotope composition of riverine Cd. *Earth and Planetary Science Letters*, *361*, 64-73.

Lacan, F., Francois, R., Ji, Y., & Sherrell, R. M. (2006). Cadmium isotopic composition in the ocean. *Geochim. Cosmochim. Ac*, **70**, 5104-5118.

Lane, T. W., Saito, M. A., George, G. N., Pickering, I. J., Prince, R. C., & Morel, F. M. (2005). A cadmium enzyme from a marine diatom. *Nature*, *435*(7038), 42-42.

Little, S. H., Vance, D., Lyons, T. W., & McManus, J. (2015). Controls on trace metal authigenic enrichment in reducing sediments: insights from modern oxygen-deficient settings. *American Journal of Science*, *315*(2), 77-119.

McCorkle, D. C., & Klinkhammer, G. P. (1991). Porewater cadmium geochemistry and the porewater cadmium: δ13C relationship. *Geochim. Cosmochim. Ac*, **55**, 161-168.

Morford, J. L., & Emerson, S. (1999). The geochemistry of redox sensitive trace metals in sediments. *Geochim. Cosmochim. Ac*, **63**, 1735-1750.

Murphy, K., Rehkämper, M., Kreissig, K., Coles, B., & van de Flierdt, T. (2016). Improvements in Cd stable isotope analysis achieved through use of liquid–liquid extraction to remove organic residues from Cd separates obtained by extraction chromatography. *Journal of Analytical Atomic Spectrometry*, *31*(1), 319-327.

Nielsen, S. G., Goff, M., Hesselbo, S. P., Jenkyns, H. C., LaRowe, D. E., & Lee, C. T. A. (2011). Thallium isotopes in early diagenetic pyrite–A paleoredox proxy?. *Geochimica et Cosmochimica Acta*, *75*(21), 6690-6704.

Olson, S. L., Kump, L. R., & Kasting, J. F. (2013). Quantifying the areal extent and dissolved oxygen concentrations of Archean oxygen oases. *Chemical Geology*, *362*, 35-43.v

Ono, S., Eigenbrode, J. L., Pavlov, A. A., Kharecha, P., Rumble III, D., Kasting, J. F., & Freeman, K. H. (2003). New insights into Archean sulfur cycle from mass-independent sulfur isotope records from the Hamersley Basin, Australia. *Earth and Planetary Science Letters*, *213*(1-2), 15-30.

Ostrander, C. M., Owens, J. D., & Nielsen, S. G. (2017). Constraining the rate of oceanic deoxygenation leading up to a Cretaceous Oceanic Anoxic Event (OAE-2:~ 94 Ma). *Science advances*, *3*(8), e1701020.

Ostrander, C. M., Nielsen, S. G., Owens, J. D., Kendall, B., Gordon, G. W., Romaniello, S. J., & Anbar, A. D. (2019). Fully oxygenated water columns over continental shelves before the Great Oxidation Event. *Nature Geoscience*, *12*(3), 186-191.

Plass, A., Dale, A. W., & Scholz, F. (2021). Sedimentary cycling and benthic fluxes of manganese, cobalt, nickel, copper, zinc and cadmium in the Peruvian oxygen minimum zone. *Mar. Chem.*, **233**, 103982.

Plass, A., Schlosser, C., Sommer, S., Dale, A. W., Achterberg, E. P., & Scholz, F. (2020). The control of hydrogen sulfide on benthic iron and cadmium fluxes in the oxygen minimum zone off Peru. *Biogeosciences*, **17**, 3685-3704.

Price, N. M., & Morel, F. M. M. (1990). Cadmium and cobalt substitution for zinc in a marine diatom. *Nature*, *344*(6267), 658-660.

Raiswell, R., Reinhard, C. T., Derkowski, A., Owens, J., Bottrell, S. H., Anbar, A. D., & Lyons, T. W. (2011). Formation of syngenetic and early diagenetic iron minerals in the late Archean Mt. McRae Shale, Hamersley Basin, Australia: New insights on the patterns,

controls and paleoenvironmental implications of authigenic mineral formation. *Geochimica et Cosmochimica Acta*, *75*(4), 1072-1087.

Redfield, A. C. (1958). The biological control of chemical factors in the environment. *American scientist*, *46*(3), 230A-221.

Reinhard, C. T., Raiswell, R., Scott, C., Anbar, A. D., & Lyons, T. W. (2009). A late Archean sulfidic sea stimulated by early oxidative weathering of the continents. *Science*, *326*(5953), 713-716.

Rehkämper M., Wombacher F., Horner T. J. and Xue Z. (2011) Handbook of Environmental Isotope Geochemistry. *Adv. Isot. Geochem.*, 125–154.

Ripperger, S., Rehkämper, M., Porcelli, D., & Halliday, A. N. (2007). Cadmium isotope fractionation in seawater—A signature of biological activity. *Earth Planet Sc. Lett.*, **261**, 670-684.

Rosenthal, Y., Lam, P., Boyle, E. A., & Thomson, J. (1995). Authigenic cadmium enrichments in suboxic sediments: Precipitation and postdepositional mobility. *Earth and Planetary Science Letters*, *132*(1-4), 99-111.

Schmitt, A. D., Galer, S. J., & Abouchami, W. (2009). Mass-dependent cadmium isotopic variations in nature with emphasis on the marine environment. *Earth Planet Sc. Lett.*, **277**, 262-272.

Slotznick, S. P., Johnson, J. E., Rasmussen, B., Raub, T. D., Webb, S. M., Zi, J. W., ... & Fischer, W. W. (2022). Reexamination of 2.5-Ga "whiff" of oxygen interval points to anoxic ocean before GOE. *Science advances*, *8*(1), eabj7190.

Sieber, M., Lanning, N. T., Bunnell, Z. B., Bian, X., Yang, S. C., Marsay, C. M., ... & Conway, T. M. (2023). Biological, physical, and atmospheric controls on the distribution of cadmium and its isotopes in the Pacific Ocean. *Global Biogeochem. Cy.*, **37**, e2022GB007441.

Sweere, T., van den Boorn, S., Dickson, A. J., & Reichart, G. J. (2016). Definition of new trace-metal proxies for the controls on organic matter enrichment in marine sediments based on Mn, Co, Mo and Cd concentrations. *Chemical Geology*, *441*, 235-245.

Tegler, L. A., Nielsen, S. G., Wang, Y., Scholz, F., Owens, J. D., Peterson, L., Auro, M., Lam, P., Horner, T.J. (submitted.) Refining the roles of productivity, redox, and remineralization on the cadmium isotope composition of marine sediments. *Geochim. Cosmochim. Ac.*

van Geen, A., McCorkle, D. C., & Klinkhammer, G. P. (1995). Sensitivity of the phosphate-cadmium-carbon isotope relation in the ocean to cadmium removal by suboxic sediments. *Paleoceanography*, *10*(2), 159-169.

Waldron, K. J., & Robinson, N. J. (2009). How do bacterial cells ensure that metalloproteins get the correct metal?. *Nature Reviews Microbiology*, *7*(1), 25-35.

Wombacher, F., Rehkämper, M., Mezger, K., & Münker, C. (2003). Stable isotope compositions of cadmium in geological materials and meteorites determined by multiple-collector ICPMS. *Geochim. Cosmochim. Ac*, **67**, 4639-4654.

Xue, Z., Rehkämper, M., Horner, T. J., Abouchami, W., Middag, R., van de Flierd, T., & de Baar, H. J. (2013). Cadmium isotope variations in the Southern Ocean. *Earth Planet Sc. Lett.*, **382**, 161-172.

Yang, S. C., Lee, D. C., & Ho, T. Y. (2012). The isotopic composition of cadmium in the water column of the South China Sea. *Geochim. Cosmochim. Ac*, **98**, 66-77.

Chapter 5. Evolution of the Southern Ocean's Iron Cycle over the Cenozoic

Abstract

Iron (Fe) availability influences primary productivity in marine ecosystems. Indeed, in regions where Fe is limiting, the efficiency of the biological pump is stunted along with its ability to sequester atmospheric carbon dioxide. Thus, Fe availability in many ocean regions can influence the global climate. Isotope analysis has emerged as a tool to understand how Fe is sourced and cycled in the water column. Iron sources (including dust, sediment dissolution along margins, and hydrothermal) exhibit characteristic isotope signatures that enable their tracing. However, after processing within the water column, the isotope compositions of Fe can overlap, making it challenging to determine where the Fe originated. Therefore, additional tools are needed to understand how the sources and cycling of Fe have changed over time.

To account for Fe cycling over the Cenozoic, we analyze Fe isotopes and leverage the multi-element geochemistry of pelagic clays from three sites in the South Pacific. Backtrack paths indicated that the sites originated in the Southern Ocean at the beginning of the Cenozoic and migrated tectonically northward to the South Pacific. In order to dissolve Fe that was sourced from the water column and not from detrital Fe, sediment samples were leached to amplify the hydrogenous signals. The leachates were analyzed for Fe isotopes and over 30 elemental concentrations. By applying Q-mode factor analysis to element concentrations of Mg, Ca, Ti, V, Mn, Fe, Y, La, and Pb in 137 samples, we find that five factors account for over 97 % of the variability in the dataset. We interpret the factors as dust, an organically-bound distal background source, two sources of hydrothermalism, and a Mg-rich volcanic ash. Taken together, we observe that the sites have a similar depositional history. Early in each record, the sites experienced Fe input from near-field hydrothermalism. As the sites migrated northward, they experienced more influence from dust deposition. Additionally, throughout the sites depositional histories we see periods where there are minor sources of Fe. These minor sources are from highly-processed Fe that traveled far from its origin, an additional hydrothermal source, and Fe derived from volcanic ash. Ultimately, we combine the components of our study–isotope analysis, statistical modeling, and geological settings, to untangle the history of Fe cycling to the South Pacific over the Cenozoic.

1. Introduction

Iron (Fe) is an essential micronutrient that exerts control over the productivity of many marine ecosystems. In high-nutrient, low-chlorophyll (HNLC) regions, Fe is the limiting nutrient that restricts CO_2 drawdown (Moore et al., 2013). Thus, understanding the sources and cycling of Fe over geological timescales provide context for the relationship between Fe and the climate. Previous studies suggested that dust was the predominant source of Fe to the Southern Ocean over the last four million years (Martínez-Garcia et al., 2011). However, recent studies have shown that hydrothermal and sediment porewater emanations from continental margins can be important sources of Fe, especially in regions that are far from significant dust deposition, like in the South Pacific Ocean (Tagliabue et al., 2010). Indeed, the presence of hydrothermal Fe has been observed thousands of kilometers away from hydrothermal vent sites (Resing et al., 2015). Once Fe from each of these sources is in the marine ecosystem, however, the cycling is complex, and pinpointing the original source, or the importance of that source, can be challenging (Tagliabue et al., 2017).

Isotope analysis has emerged as a powerful tool to trace the sources and cycling of Fe (Conway and John, 2014; Buck et al., 2017; John et al., 2018). Each of the main sources of Fe—dust deposition, hydrothermal inputs, and continental margin supply—have a characteristic isotope signature. However, the sources do not keep their end-member isotope composition but are modified by internal cycling in the water column. Processes such as oxide- and sulfide-precipitation, ligand binding, and biological uptake modify the initial Fe isotope signature (Severmann et al., 2004; Lough et al., 2017; Marsay et al., 2018) and make tracing the Fe measured in the water column back to its source more complicated. When the internal cycling processes and their effect on the isotope composition of Fe in sediments are considered, dust-derived Fe has a narrow range of allowable Fe isotope values (Beard et al., 2003a; Waeles et al., 2007; Conway and John, 2014). The sources of hydrothermal and non-reductive margin supply are more challenging to define on isotope analysis alone because their modified signatures can overlap. Thus, previous studies have interpreted Fe isotope records within a site's palaeoceanographic context (Horner et al., 2015; Dunlea et al., 2021) to determine whether Fe deposition was primarily from dust, hydrothermal input, or continental supply.

Understanding how Fe sources and cycling have changed requires a suitable archive of Fe isotopes. A desirable archive must faithfully record the Fe isotope composition of the overlying seawater, be minimally impacted by diagenesis, and be amenable to stratigraphic dating. Pelagic

clays meet each of these requirements. Dunlea and Tegler et al. (2021) performed leaching experiments on the Fe isotope composition of core-top samples to investigate how the isotope composition of seawater was preserved in sediments. Combined with evidence from the water column (Marsay et al., 2018) and ferromanganese nodules (Marcus et al., 2015), Dunlea and Tegler et al. (2021) concluded that pelagic clays reliably record the average $\delta^{56}Fe$ of the particles in the overlying water column and the isotope signature could be reliably extracted from the sediment via a mild leach. Pelagic clays are the dominant marine sediment lithology in slowly accumulating sediment below the calcite compensation depth (CCD). These clays are not expected to be significantly affected by diagenesis. The slow sedimentation rates and low abundances of organic matter common in pelagic clays cause them typically to be oxygenated from the seawater interface to deep into the sediment, often all the way to the underlying basalt (D'Hondt et al., 2011). Unlike Fe deposited under reducing conditions, where Fe is significantly remobilized during diagenesis, iron is minimally remobilized in oxic sediments. Indeed, the Fe porewater concentrations were found to be low in oxic sediments in the South Pacific Gyre (<10 μM Fe; D'Hondt et al., 2011). Solid-phase sediment is less sensitive to diagenesis than the surrounding porewaters. Any oxic exchange between porewater and Fe-oxyhydroxides occurs slowly enough to be negligible in the solid-phase sediment and is particularly negligible for the isotope record spanning millions of years. Thus, once the Fe isotope signature is laid down in the sediment, it is not expected to change substantially during oxic diagenesis.

In order for these records to be useful in recording changes in Fe sources through time, they must be amenable to age determination. Although pelagic clays preserve very limited microfossils and, therefore, cannot be dated using biostratigraphy, they can be dated using non-traditional techniques. Osmium (Os) isotopes in pelagic sediments can be used to provide age constraints in pelagic. Osmium from the water column is scavenged by Fe and Mn oxide minerals (Klemm et al., 2005; Nielsen et al., 2009) and preserved in the hydrogenous fraction of the sediment (Pegram et al., 1992; Peucker-Ehrenbrink et al., 1995; Peucker-Ehrenbrink and Ravizza, 2000; Peucker-Ehrenbrink and Ravizza, 2012, 2020). When the hydrogenous fraction of the sediment is measured for Os isotopes, it can be compared to the global marine $^{187}Os/^{188}Os$ seawater record, and the age of the sediment can be approximated. Methods can also be employed to account for the slow sedimentation rates and potential bioturbation within the sediments.

Although we have an archive of Fe isotopes that can be dated, understanding the complex sources of Fe cycling over the site depositional history of a pelagic clay is challenging to do with isotope analysis alone. Dunlea, Tegler et al. (2021) analyzed a downcore profile of Fe isotopes in pelagic clays from Site U1366, which revealed significant Fe isotope variations over time. In this study, the context of the site's paleogeographic location was used to make inferences about the changes in the Fe supply and cycling. While this approach provides useful context, it lacks a robust way to validate or quantify the relative importance of different Fe sources. One way to achieve this is using Q-mode factor analysis of elemental abundance data. Here, the goal is to identify the smallest number of factors that can account for the largest amount of variability in the dataset. Statistics were computed using MATLAB algorithms for geochemical applications (Pisias et al., 2013; Dunlea and Murray, 2015). We interpret the VARIMAX-rotated factor loadings, which indicate the importance of each factor in each sample, to compare each factor to the iron isotope value. Thus, we constrain the sources of Fe to each sample both quantitatively and within the geochemical framework of the site history.

The objective of this study is to combine Fe isotope analysis and Q-mode factor analysis on hydrogenous elemental concentrations in three cores in the South Pacific Gyre. We use these techniques to explore the evolution of Fe sources as these sites migrated tectonically from near the mid-ocean ridges, where hydrothermal inputs are expected, to further north, where Australian dust inputs likely dominate. This work will lay the foundation for exploring other pelagic clay records and can ultimately be used to explore global Fe cycling over the Cenozoic in different locations.

2. Sample Description and Methods

2.1 Sample Description

The samples analyzed in this study are from three sediment cores in the South Pacific (Sites U1366, U1369, U1370) drilled during the Integrated Ocean Drilling Program (IODP) Expedition 329. The lithology of these sediments is described in detail elsewhere (e.g., D'Hondt et al., 2011; Dubois et al., 2014). Briefly, these sediments are metalliferous pelagic clays with homogenous grain sizes. The clays are primarily comprised of smectite, zeolites, mica-group end-members, and red-brown to yellow-brown semi-opaque oxides (D'Hondt et al., 2011; Yang et al., 2016). The

porewaters from the cores are oxygenated to the basement, and the Fe concentrations are consistently low in the porewaters, suggesting minimal post-depositional reductive remobilization of Fe (e.g., < 10μM Fe; e.g., South Pacific Gyre D'Hondt et al., 2011). Previous work on these sediments has modeled the aluminosilicate provenance qualities and provided age estimates with cobalt-based age modeling (Dunlea et al., 2015a). Furthermore, a previous study verified that the elemental concentrations of trace metals and the isotope composition of Fe in the hydrogenous fraction of the sediment can be extracted using an acid leach (Dunlea and Tegler et al., 2021). Additionally, the study illustrated that hydrogenous Os isotopes are also preserved in the sediment, and the sediments are, therefore, amenable to Os chronostratigraphy.

2.2 Sample Preparation – Leaching for Fe and Os Isotopes and Trace Metal Concentrations

Some studies have suggested isolating hydrogenous Fe by using an oxalate-EDTA as a leaching protocol (Revels et al., 2015). However, at least one study has suggested that when oxalate leaches are used on Fe-bearing pelagic clays it may unintentionally release detrital iron (Slotznick et al., 2020). Therefore, we chose not to use the oxalate-EDTA leaching protocol to prevent release of Fe from detrital material. Instead, we used a leach tested by Dunlea and Tegler et al. (2021). This study determined that a 1 M HCl leach successfully extracted the hydrogenous Os and Fe isotope signatures. The details of this leaching procedure, and documentation of its effectiveness, can be found in Dunlea and Tegler et al. (2021).

In brief, after sample collection, several grams of sediment were freeze-dried from each site, and hand-powdered and homogenized with an agate mortar and pestle. After being powdered, approximately 200 mg of powder was weighed into high-density polyethylene (HDPE) vials and leached with 5 mL of reagent grade 1 M HCl. The samples were placed on a shaker table at 20˚C for 24 hours to allow for the exchange of the solution and the sediment. Subsequently, the leachate was separated from the sediment via centrifugation (3000 rpm or ~1,500 g for 10 minutes). Small aliquots of the leachate were taken for Fe isotope and trace metal analyses, respectively.

Previous studies indicate that Os isotope analyses could be obtained using the same leach procedure as described above. However, due to the low Os concentration in these samples coupled with the loss of Os during the heating process through volatilization, we opted to use a leach that increased Os recoveries. We weighed approximately 200 mg of powered sediment into perfluoroalkoxy alkane (PFA) vials. Subsequently, 2 mL of reagent-grade concentrated nitric acid

was added to the samples. The rims of the vials were wrapped liberally with polytetrafluoroethylene (PTFE) thread-seal tape to prevent loss of volatized Os. The samples were then capped tightly, lightly agitated to promote adequate mixing between the leach solution and sediment and placed on a hot plate at 90˚C for 17 hours. The samples were chilled for ~15 minutes, diluted with 8mL of 18.2 MΩ deionized water, and immediately capped. They were left capped and on ice until directly before analysis.

2.3 Analyses

2.3.1 Element concentrations

Major and trace element concentrations were measured using the Thermo iCAP-Q inductively coupled plasma mass spectrometer (ICP-MS) in the Woods Hole Oceanographic Institution (WHOI) Plasma Facility (Supplementary Table S1). To prepare for elemental analysis, approximately 100 µL of leachate was diluted to 2 mL with 2 % nitric acid and 100 µL of an internal indium standard. The ion beam intensities were corrected for drift and ionization attenuation using indium as an internal standard. A suite of six multi-element standards were prepared to cover the range of element concentrations in the samples. The standards were used to construct calibration curves ($r^2 > 0.999$) that convert ion counts per second of the samples to concentrations. To assess long-term precision, we leached two in-house standards with every run.

2.3.2 Osmium isotope compositions

Analytical procedures broadly followed methods described elsewhere (Sen and Peucker-Ehrenbrink, 2014). Osmium isotopes were measured on a Thermo Finnigan Neptune multi-collector inductively coupled mass spectrometer (MC-ICP-MS) at the WHOI Plasma Facility. After samples were leached in their oxidizing solution, they were chilled, diluted, wrapped with PTFE thread-seal tape, and sparged into the MC-ICP-MS using argon (Ar) as the carrier gas, which allows the solution to be introduced directly into the instrument (Hassler et al., 2000). The instrument was tuned to maximize the ion beam intensity on *m/z* 192 (Os, Pt). Gas flow was generally optimized at a rate of 1.2 Ar L min^{-1}. Osmium isotope data were acquired dynamically using three continuous-dynode ion counters to serially measure *m/z* 185 (Re), 187 (Os, Re), 188 (Os), 190 (Os, Pt), 192 (Os, Pt); 190, 192, and 194 (Pt); and 192, 194, 196 (Pt). Data acquisition

uses the three dynodes attached in a rack with fixed spacing (2 Da at the mass/charge values of a single charged Os). The 2-Da spacing between the ion counters allowed for the detection of all the relevant mass to charge ratios on four blocks of data acquisition. These lines were as follows: 185–187–188 (8 seconds), 188–190–192 (4 seconds), 190–192–194 (4 seconds), and 192–194–196 (4 seconds). Thirty repeat measurements were made for each sample, which allowed for correction of offsets in counting efficiency between detectors, decay in transmission over the run, and isobaric interferences. We found that contributions from the procedural blanks were negligible. Further information about the Os isotope procedure can be found elsewhere (Sen and Peucker-Ehrenbrink, 2014).

To assess the accuracy of Os isotope measurements, we measured several standards. A dilute in-house LoOs standard reference ([Os] = 0.61 pg/g) yielded similar results at the beginning of each session. Additionally, four standards (NOD-A1, NOD-P1, an in-house standard from the South Pacific Gyre, and an in-house core top sample from the North Atlantic) were processed with each batch of samples and were accurate within uncertainty. We used these samples to check for precision and accuracy from run to run. NOD-A1 yielded a long term value of $^{187}Os/^{188}Os = 1.01 \pm 0.04$ (2SD, n = 10) and NOD-P1 had a long-term value of $^{187}Os/^{188}Os = 0.95 \pm 0.04$ (n = 10). These values are within the accepted value of $^{187}Os/^{188}Os = 0.9733 \pm 0.02$ (NOD-A1) and $^{187}Os/^{188}Os = 0.9418 \pm 0.02$ (NOD-P1) (Jochum et al., 2005). The South Pacific Gyre sample had a value of $^{187}Os/^{188}Os = 0.61 \pm 0.07$ (2SD, n = 17) and the North Atlantic core top sample composition was $^{187}Os/^{188}Os = 1.03 \pm 0.1$ (2SD, n = 4).

2.3.3 Iron isotope composition

Iron isotope compositions were measured at both Rutgers University and the WHOI Plasma Facility. The two labs processed the data using MC-ICP-MS, albeit using slightly different methods.

The majority of the iron isotope analyses were performed at the WHOI Plasma Facility. These samples were dried after leaching and treated with 1 mL HNO_3 and 500 µL of H_2O_2 to oxidize any residual organic matter. To ensure that no HNO_3 remained, the samples were dried down, reconstituted in 1 mL 1 M HCl, dried, and reconstituted into 1 mL 6 M HCl. Iron was purified from the sample matrix following an established ion exchange technique (Dauphas et al., 2009; Craddock and Dauphas, 2011). Briefly, the samples were loaded onto acid-cleaned AG1-X8

resin (200-400 mesh size; chloride form). The matrix elements were eluted in 6 M HCl, and Fe was eluted in 0.4 M HCl. The eluted Fe was collected and oxidized and reconstituted in 6 M HCl using the method described above. Once dissolved in 6 M HCl, the sample was passed through the ion-exchange protocol again to ensure that all of the matrix had been removed.

Isotope analysis was performed on a Thermo Neptune MC-ICP-MS in the WHOI Plasma Facility. The mass spectrometer was operated in wet plasma mode using a quartz spray chamber and a platinum skimmer cone for added signal stability. Each sample was measured between five and seven times using sample-standard bracketing relative to IRMM-524A (Institute for Reference Materials and Measurements, Geel, Belgium). This standard has the same Fe isotope composition as IRMM-014, which was originally defined as the δ = 0 ‰ standard for Fe (Craddock and Dauphas, 2011). Iron isotope compositions are reported using the delta notation (δ^{56}Fe; Coplen, 2011):

$$\delta^{56}Fe\ (‰) = \left(\frac{\delta^{56/54}Fe_{sample}}{\delta^{56/54}Fe_{IRMM-524A}} - 1\right)$$

The Fe isotope method at Rutgers differed slightly. Here, Fe splits were dried and refluxed in H_2O_2 and HNO_3 to oxidize the remaining organic matter. The samples were dried and reconstituted in 6 M HCl. Iron was purified from the sample matrix using established chromatography techniques (deJong et al., 2007; Majestic et al., 2009). In brief, the samples were loaded onto acid-clean columns with acid-cleaned AG1-X8 200-400 micron chloride resin, and the matrix was eluted in 6 M HCl. The sample was finally eluted with *0.5 M HCl* into trace-metal clean PTFE vials. The quantitative yields were measured spectrophotometrically using the *Ferrozine* method (e.g., (Stookey, 1970). This method uses a UV-Vis spectrophotometer. Samples with yields ± 20 % of the pre-column concentrations were prepared for isotope analysis.

Isotope compositions of these samples were measured on a Thermo Neptune MC-ICP-MS at Rutgers University. The purified samples and standards were analyzed using an external normalization to Cu. Instrument mass bias was quantified by monitoring $^{65}Cu/^{63}Cu$ and calculating an instrumental mass fractionation scalar. This scalar was then used to correct Fe isotope ratios in

samples and standards, before converting final isotope data to a delta value relative to IRMM-524A.

Some samples were analyzed at both institutions and these all fell within uncertainty of each other. For these samples, final Fe isotope compositions were calculated by compiling the two datasets. The final isotope compositions reflect 2SE of the repeat measurements of each sample. The uncertainty and Fe isotope values range from ± 0.05 to 0.06 ‰.

To ensure that the leach was consistent in this study, an in-house pelagic clay standard from the North Atlantic was processed. Four individual standard leaches were passed through column chemistry, and each was measured at least one time, although several were measured more times to ensure that there was no instrumental drift. The average in-house standard was −0.25 ± 0.05 ‰ (2SD, n=7). Additionally, for the samples processed at WHOI, the bulk digested geo-standard, IFG, was processed alongside the samples to ensure instrument accuracy. We report a mean IFG value of 0.64 ± 0.06 ‰ (2SD, n=7). This value is within the expected IFG value of 0.639 ± 0.013‰ (Craddock and Dauphas, 2011).

2.4 Q-mode factor analysis methodology and choosing the optimal model

Multivariate statistics were computed using MATLAB algorithms created for geochemical mixing problems (Pisias et al., 2013). The algorithms have been successfully used in geological and oceanographic contexts (Leinen and Pisias, 1984; Dunlea et al., 2015a; Longman et al., 2023). Q-mode factor analysis (QFA) was performed on element concentrations of the leached pelagic clay samples from Sites U1366, U1369, and U1370. QFA is a statistical technique that allows for the identification of features that covary in a dataset and helps determine the number of factor groupings that are needed to explain the variance of the dataset. Before QFA was performed on the samples, we pretreated the data set by normalizing the sample concentrations to the range of concentrations for each element. Once the dataset was pretreated, the QFA MATLAB codes were used to group the elements into factors (Pisias et al., 2013; Dunlea et al., 2015a). These factors then underwent a VARIMAX rotation that kept the factors orthogonal to one another and maximized the variance that was explained by each factor. These factors can *loosely* be interpreted as “end-members” of the material contributing to sedimentary chemistry. By examining which elements covary, we can interpret which sources contributed to the sediment in what relative proportions. The elements that covary strongly within a factor have a high VARIMAX factor *score*

(e.g., a large magnitude), and the importance of each factor to the variability in an individual sample is recorded by the factor *loading* (e.g., a loading closer to one has a higher importance). These factor *loadings* can be used to determine the relative importance of each factor to a sample. This is essential for understanding how the dominant factors may have changed over a site's history or between sites. However, it is critical to stress that while these may be loosely considered as end members, factor loadings are not equivalent to quantitative mass fractions.

Our initial analysis included 137 samples and a broad range of elements that allowed us to discern as many potential factors as possible. The element menu we tested included the following elements: Al, Ti, Fe, Mn, Ca, Mg, P, Li, V, Cr, Co, Ni, Cu, Zn, Sr, Y, Mo, Ba, La, Ce, Nd, Sm, Gd, Dy, Er, Yb, Pb, Th, U and Tl. To start, all elements were included in the QFA to explore the overall structure of the dataset. Then, the number of elements were reduced to < 10 elements and between four and six factors for a more statistically robust and stable model (Reimann et al., 2002). Millions of models were created using a combination of elements to find the model that maximized the amount of variability the model could explain and represented the majority of the observed sources in the other models. Ultimately, there were many models that explained a high amount of the variability of the data. We selected one that produced geologically reasonable results and was representative of the factors that were commonly repeated in the iterations of the model testing the robustness and sensitivity of the model output. This model included 9 elements: Mg, Ca, Ti, V, Mn, Fe, Y, La, and Pb. The QFA results indicated that five factors explain 97 % of the variability between the three sites. Factor 1 explained 46 % of the variance and shows that Ti, Fe, and Pb covary strongly. The second factor, which explains 22 % of the variability, shows covariance between Ca, Y and La. The third factor explains 17 % of the variability and Mn, V and Fe covary most strongly. The fourth and fifth factors explain 9 and 3 % of the variability, respectively. Factor four is dominated by Mg while Factor five shows covariation between Ti, Mn, and Fe (Figure 1 & 2).

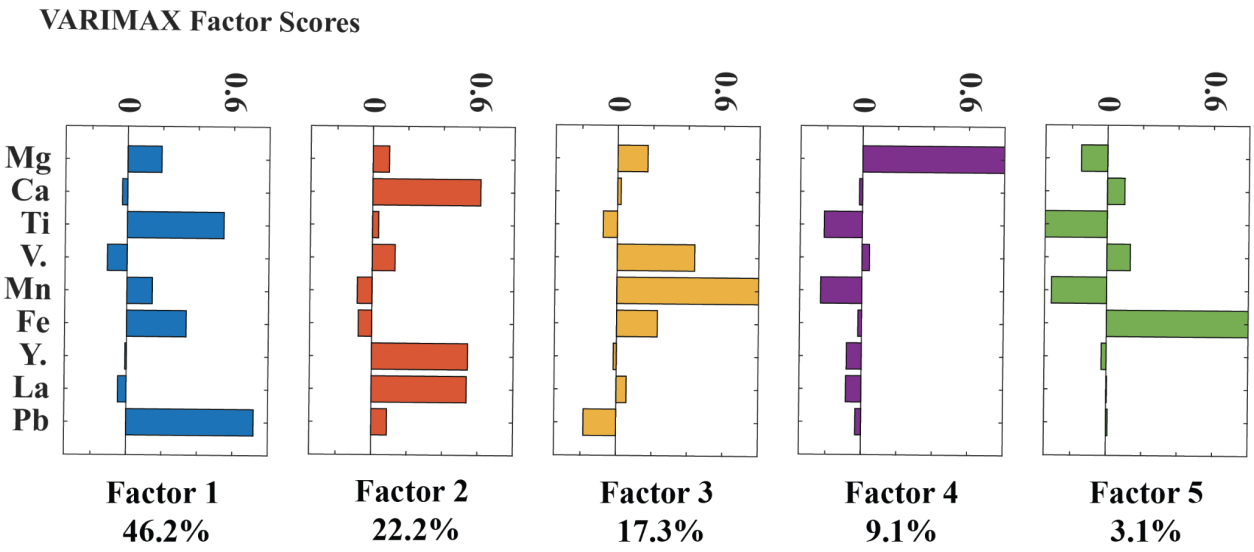

Figure 1. The VARIMAX factor scores from the Q-mode factor analysis. Elements associated with the hydrogenous fraction if the sediment produced five factors that explain 97.8 % of the data (46.2%, 22.2 %, 17.3 %, 9.1 %, and 3.1 %, respectively)

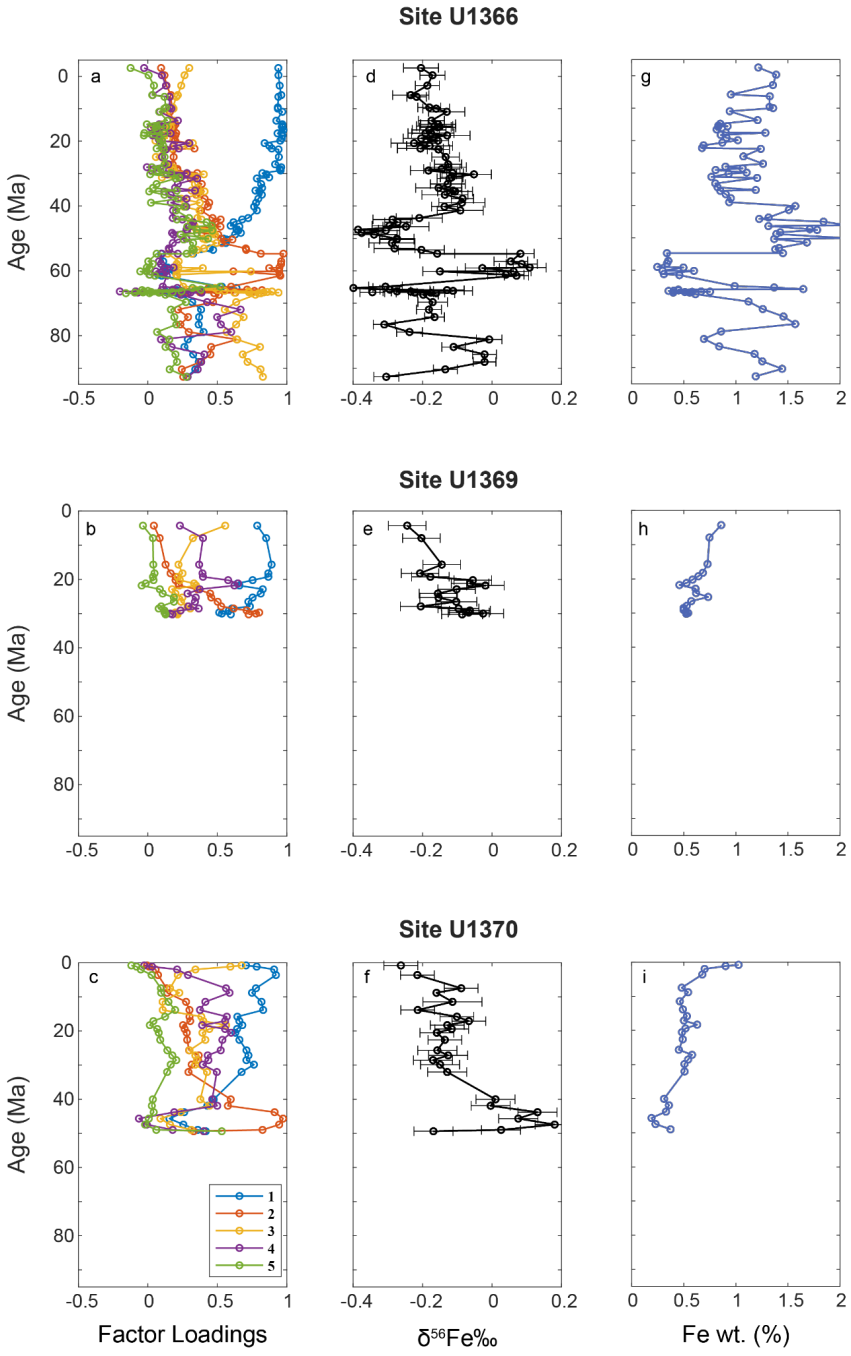

Figure 2. Ages plotted on the y axis were determined using $^{187}Os/^{188}Os$ chronostratigraphy. The first column (a-c) shows the factor loadings produced from the QFA along with color-coded factor scores. The second column (d-f) shows the $\delta^{56}Fe$ measurements for each site and the last column (g-i) shows the Fe wt. % for each sediment core

3. Results

The Fe concentrations and isotopes vary downcore at all three sites. Together, the samples have an δ^{56}Fe range between −0.40 and +0.18 ‰ (Figure 2d-f). The Fe wt. % ranges between 0.12 and 2.26 wt % (Figure 2g-i). Specifically, the Fe concentrations over Site U1366 range from 0.12 wt % to 2.07 wt. %, Site U1370 has Fe concentrations between 0.19 and 2.26 wt %, and Site U1369 has the most consistent Fe concentrations, ranging from 0.46 to 0.86 wt. %. Iron isotopes are also variable at each site. The Fe isotopes at Site U1366 range from −0.40 to +0.11 ‰, Site U1370 has Fe isotopes values between −0.26 and +0.18 ‰. Site U1369 has the most consistent Fe isotope values, ranging from −0.24 to −0.02 ‰.

On a site-by-site basis, we can observe trends in the downcore profiles. At Site U1366, there are four periods that are defined by changes in the Fe isotopes. From 0-40 Ma the Fe isotopes fall close to −0.1 ‰, from 40-60 Ma, the isotopes become lighter to around −0.2 ‰, then from 55-65 Ma the Fe isotopes reach the heaviest values at around +0.1 ‰, and from between 70-90 Ma the Fe isotope signatures change somewhat stochastically throughout the core before settling at approximately 0 ‰. Site U1370 shows variability as well. From 0-30 Ma, an isotope signature of −0.1 ‰ dominates. Then, the isotope value becomes heavier from 30-50 Ma (e.g., up to 0 ‰). The isotope composition becomes lighter at the oldest part of the record on the order of −0.2 ‰. Finally, Site U1369 gives a range of Fe isotope values between −0.25 and + 0.01 ‰ but does not show the smooth transitions that were observed in the other two sites.

4. Discussion

4.1. Assigning ages to pelagic clay sequences

In this section, we detail the construction of the Os age model using SOsAGES and *rBacon*. We then compare our age model to an age model constructed using Co concentrations.

4.1.1 Os Age Model Construction

We processed 131 oxic pelagic clay samples from Sites U1366 (n=89), U1369 (n=24), and U1370 (n=18). Forty-five samples from Site U1366 were previously reported in Dunlea and Tegler et al. (2021). These samples are included here for a complete record. The results from each of the downcore sections show downcore variation in Os (Figure 3). For all three cores, the $^{187}Os/^{188}Os$ value tends to decrease with depth toward more non-radiogenic values. All $^{187}Os/^{188}Os$ values are between 0.20 and 0.99 (Figure 3a-c).

The age model constructed here follows a probabilistic approach. Marine $^{187}Os/^{188}Os$ seawater ratios were compiled over the Cenozoic and the Late Cretaceous (Peucker-Ehrenbrink and Ravizza, 2020). While the global marine Os record broadly allows for interrogations of Os changes on the order of 20,000 years, the sediment samples in this study do not allow us to date over these short time intervals. On average, the sedimentation rate of pelagic clays in the South Pacific Gyre is ~1 m/Myr (Dunlea et al., 2015a). Thus, a 10 cm sediment sample spans ~100,000 years. If we assume a bioturbation depth of ~40 cm in either direction, each of our 10 cm sediment samples may span up to one–million years. The slow sedimentation rate and a high degree of bioturbation will create an Os isotope curve in the sediment that appears smooth relative to the global marine Os reference curve. Due to the smoothing, we anticipate that we will not be able to discern the sharp peaks and valleys that are observed in the global reference curve. Thus, to best fit our data to the marine Os reference curve, we fit the global reference curve with the LOESS function provided in MATLAB™ (Figure 4). This plot reflects the isotope values we might expect after considering the sedimentation rates and bioturbation. After smoothing, an Os isotope value was assigned million-year intervals by interpolating between points on the smoothed curve. An uncertainty of 0.04 was assigned in either direction as this is equivalent to our typical measurement uncertainty.

These smoothed age values were loaded into a software package named *SOsAGES* (Sedimentary Osmium Ages Generated by Enforcing Stratigraphy). This software explores the permitted age space of a sample based on its Os isotope composition. The model extracts a subset of 10 Os isotope values from the core and calculates all allowable ages for each 10 points. One of the allowable ages is selected for each sample and an age-depth curve constructed. If the age-depth curve satisfies the law of superposition, that deeper samples are older than the ones above it, the model is noted, and the process is repeated for 10 more randomly selected samples. If the superposition requirement is not met (i.e., a deeper point is younger than a shallower one), the model is rejected. At this point, the software will select another set of allowable ages for each of the 10 samples and test whether this new age-depth curve is satisfactory. The model will attempt to fit a given set of 10 samples 100,000 times before abandoning that subset of the data and selecting 10 more samples at random. Once 10,000 age-depth curves have been constructed, we can assign a probabilistic age for every sample in the core (Figure 5d-f).

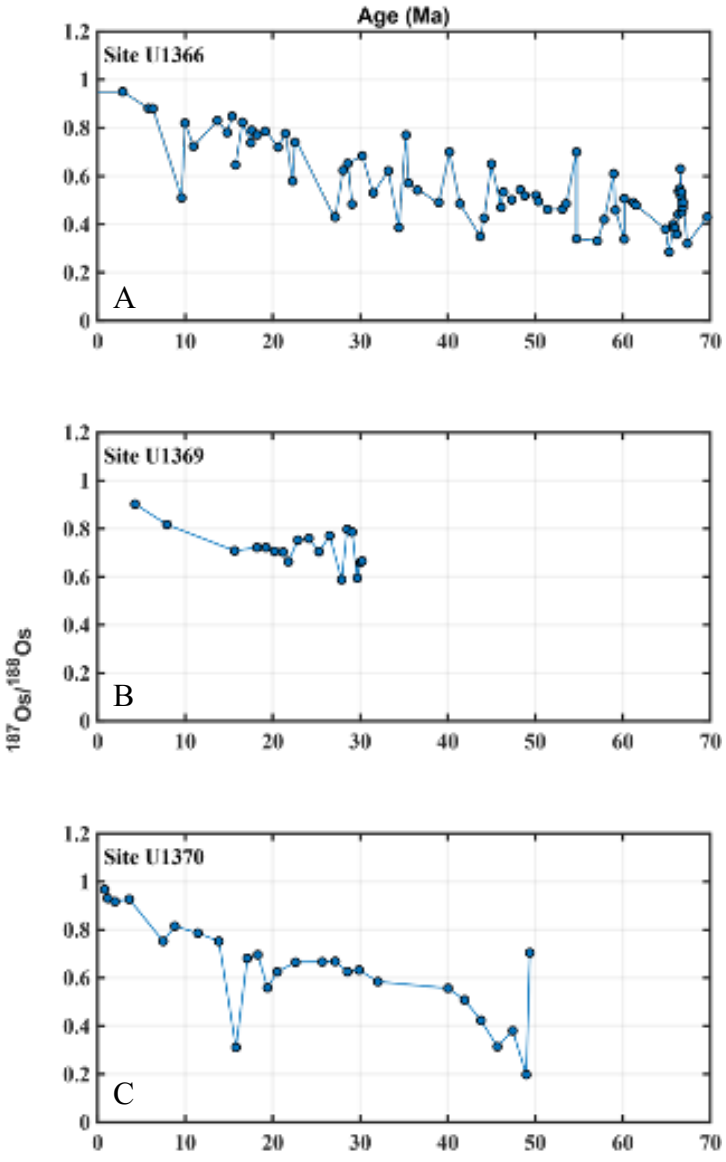

Figure 3(A-C). The raw $^{187}Os/^{188}Os$ profiles for Sites U1366, U1369 and U1370. Broadly, the data show a smoothed Os curve relative to the marine Os reference curve. The records start with unradiogenic values and tend toward radiogenic values in the modern.

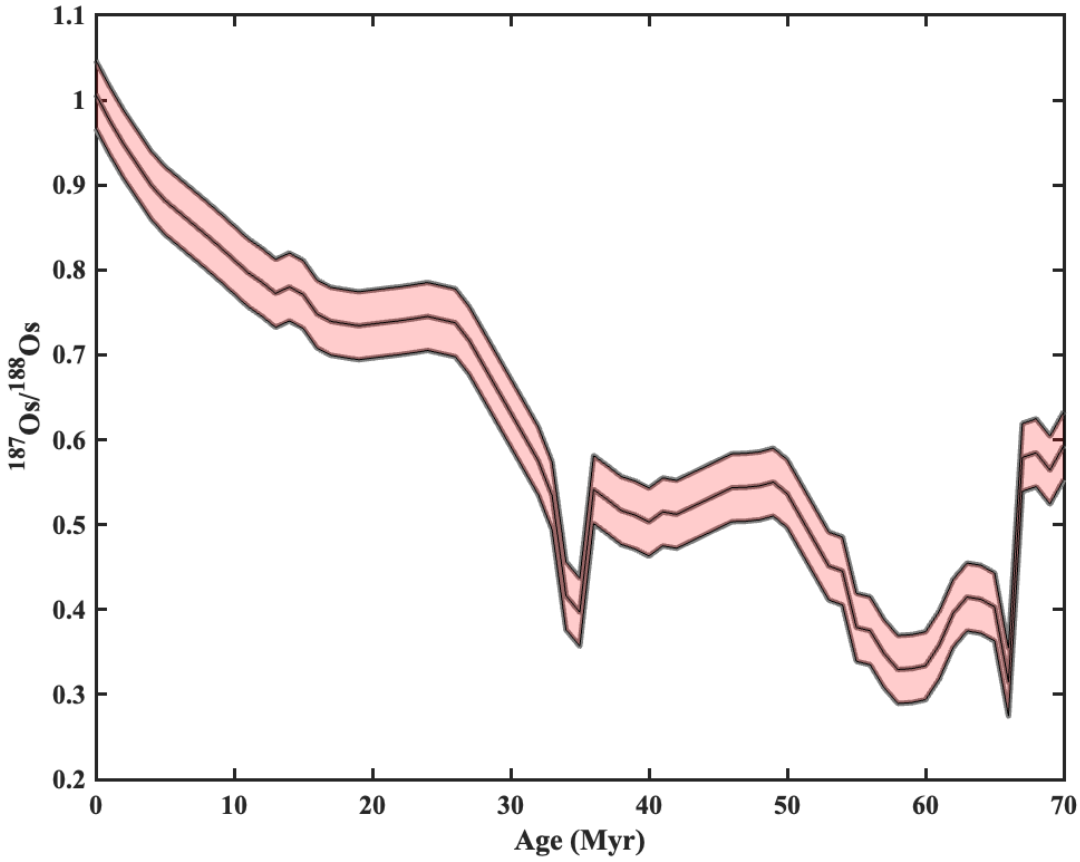

Figure 4. The red shading shows the allowable $^{187}Os/^{188}Os$ values for a given age when considering bioturbation, sedimentation rates, and instrument uncertainty in the pelagic clays in the South Pacific Gyre.

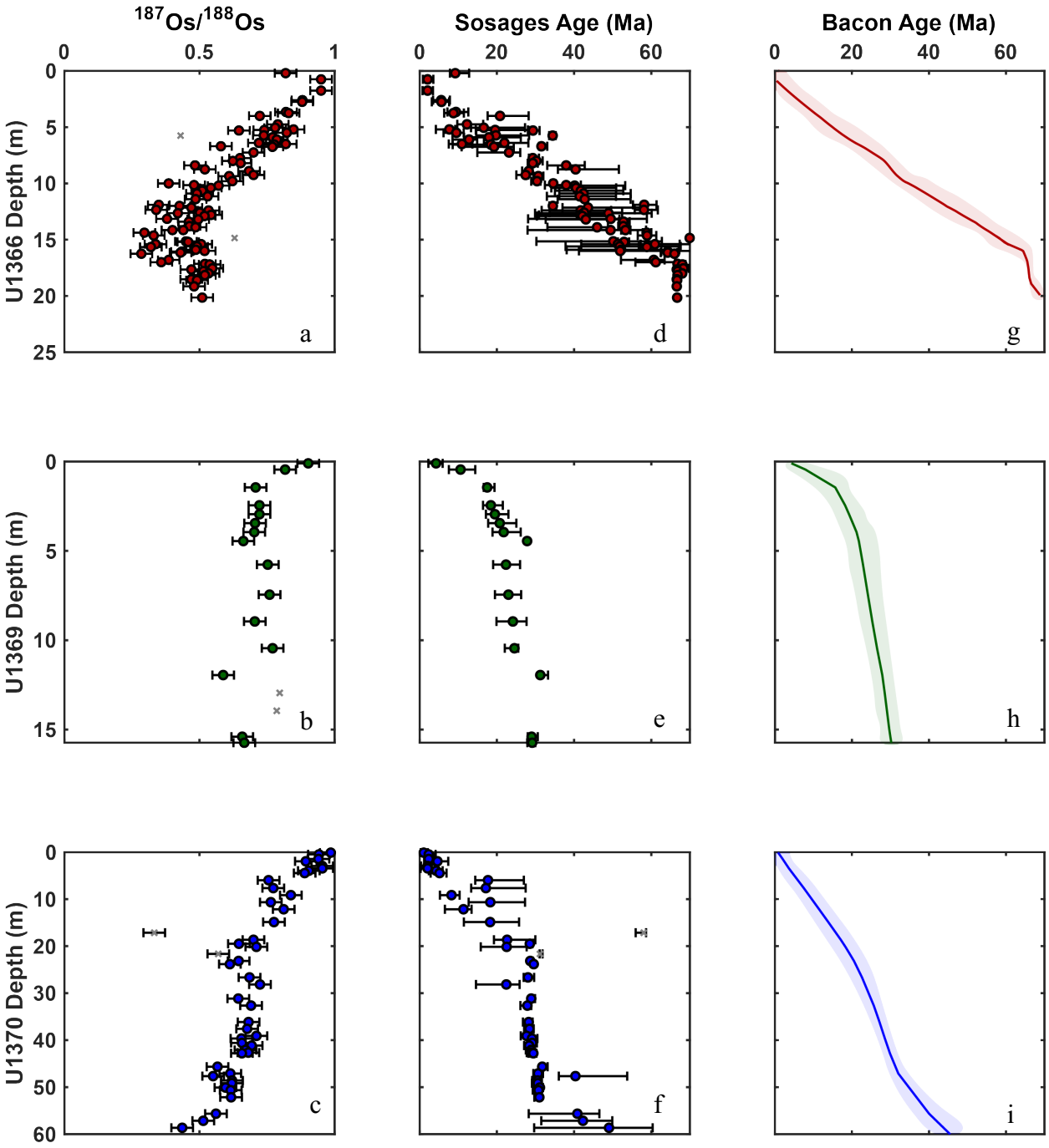

Figure 5(a-i). Panels a-c show the $^{187}Os/^{188}Os$ measured values as a function of depth in the sediment at Sites U1366, U1369 and U1370. Panels d-f show the rough estimated ages from the sOsages model against depth that were loaded, with their uncertainties into 'rbacon', Panels g-I show the final age estimates generated using rBacon as a function of depth with a cloud of uncertainty around the median age estimate.

After employing the dating technique and accounting for sedimentation rate and bioturbation, Site U1366 is dated between 0 to 95 Ma, U1369 is between 4 and 30 Ma, and U1370 is between 1 and 49 Ma (Figure 5g-i). It important to note that U1369 and U1370 are dated entirely using Os chronostratigraphy. U1366 was dated primarily using Os chronostratigaphy. However, the oldest part of the record was unable to be dated with Os isotopes without damaging the mass spectrometer (the matrix of these samples caused the plasma to be extinguished on several attempts to measure the samples), so a linear sedimentation was applied over these samples. The oldest age was set to the age of the basement age.

SOsAGES was also used to identify outliers. Specifically, if a datum was not fitted to a model at least 5 % of the time it was selected, it was removed from the dataset. However, before elimination, these data were observed to ensure that they fell outside of the expected Os values and were not being erroneously removed. In all cases, the flagged $^{187}Os/^{188}Os$ value fell outside the expected values for the global Os isotope reference curve. Thus, we expect that these values had an additional source of Os, which was not derived from seawater. The samples with the largest deviations exhibited unradiogenic Os values relative to their stratigraphic height. We expect these samples may have had micrometeorite contamination. A few samples were removed for having values that were more radiogenic than expected. Here, we suppose that the outliers may have been an increased local continental delivery or the samples experienced contamination. A total of 6 samples were removed out of a total of 157 samples during this process (e.g., n=3 U1366, n=4 U1369, n=3 U1370).

The discrete samples ages determined using *SOsAGES* were then used to create a continuous age model, also premised on Bayesian statistical methods called *rBacon* (Blaauw and Christen, 2011). Using the "rBacon" package and the "bacon" function, we input each of the sites' "sOsages" output estimated ages and associated 1s uncertainties for each of the cores. The *rBacon* model defined the age, accumulation rate, and valid gateway dates for all the samples. *rBacon* allows the user to change the parameters to best fit their record. Here, we adjusted the following parameters: "cc", "ssize", "acc.mean", "acc.shape", "mem.strength", and "thickness". In order, these parameters do the following: turn offs ^{14}C age adjustments, adjust the number of iterations run, changes starting accumulation rate, modifies the range of allowed accumulation rate, adjusts how much the code remembers the past accumulation rates, and changes how abruptly the

accumulation rate can change. The adjustments were made in line with the documentation supplied by Blaauw and Christen (2011) and represented the broad trends reflected in the iterations of *rBacon* we ran while building the age mode.

Unfortunately, not all the samples were able to be measured with Os isotopes. Some of the samples from U1366 had elemental matrices that affected the plasma on the mass spectrometer and caused the plasma to become unstable. Rather than risk compromising the instrument, the stratigraphically lowest 11 samples from Site U1366 were not measured for Os isotopes. Instead, the basement age of 95 Ma was applied at Site U1366 (Dunlea et al., 2015a) and we assumed a linear sedimentation rate from the last measured sample to the basement.

4.1.2 Evaluation of the $^{187}Os/^{188}Os$ age model and comparison to the existing Co age model

As described in Section 4.1.1, the $^{187}Os/^{188}Os$ in our pelagic clay sediments are smoothed relative to the rapid transitions in the marine Os isotope reference curve because of bioturbation and slow sedimentation rates. Although we are unable to account for fine-scale resolutions marked by short-term excursions, our samples do follow the broad general trend where Os isotopes become more radiogenic over the Cenozoic.

We compare our final age models to a cobalt-based age model that was previously used to date these sites. Cobalt-based age models are useful for dating pelagic sediments that are not amenable to other traditional dating techniques. However, these methods assume that the flux of non-detrital Co to the seafloor is constant, both in time and space. While many studies have shown that Co can be a useful tool to date sediments, it cannot detect hiatuses or intervals of rapid biogenic deposition. Conversely, the $^{187}Os/^{188}Os$ record is able to account for both of these processes. Despite these advantages, the $^{187}Os/^{188}Os$ record presented in this study is not without uncertainty. The slow sedimentation rates, bioturbation, and presence of micrometeorites can impact the sedimentary Os curve relative to the marine record, and any inputs from micrometeorites can obscure true Os isotope signals. We are unable to account for these uncertainties directly. But, by placing constraints on sedimentation and bioturbation, we were are able to identify the outliers that most likely have inputs of Os from non-seawater sources. By flagging and excluding these outliers, we can produce an Os curve that permits dating the clays.

.

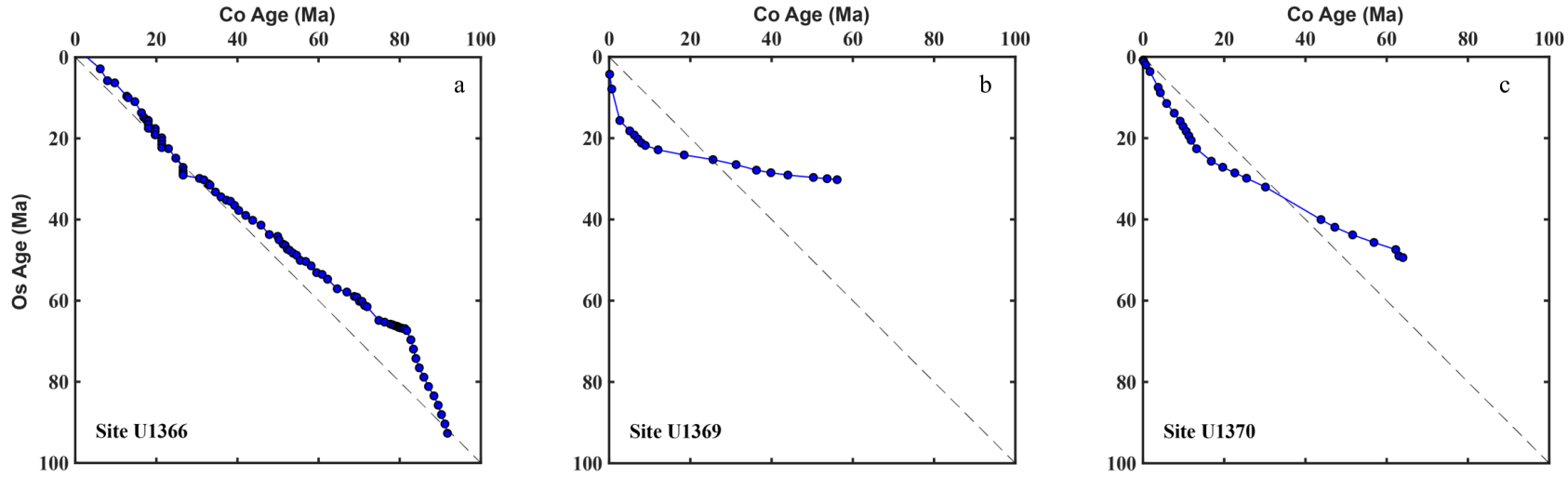

Figure 6 (a-c). Cobalt age model plotted (Dunlea et al., 2015a) against the Os age model (this study). The grey line in the background represents a 1:1 relationship.

At Site U1366, the Os and Co-based methods align well. Figure 6 shows that the two methods agree within uncertainty of each other between 0-35 Ma. In sediments older than 35 Ma, the techniques begin to diverge. The $^{187}Os/^{188}Os$ method suggests a slower sedimentation from 35-60 Ma and a possible hiatus at ~65 Ma. The Co-based method is unable to pinpoint hiatuses, thus, it is likely the reason for the discrepancy. Thus, we employ a linear sedimentation rate between the final $^{187}Os/^{188}Os$ sample and the basement age of 95 Ma to maintain independence from the Co dating method.

At Site U1369, the two age models diverge (Figure 6b). Despite the records converging at ~25 Ma, the Os isotope record predicts consistently older age values at the most recent part of the record (0-25 Ma) while the Co method depicts an older core later in the record (> 25 Ma). Ultimately, the Co method dates the oldest sample from Site U1369 at 56 Ma while the Os record suggests the core is only 30 Ma. We suggest that this discrepancy is due to a massive ~28 Ma hiatus from 58 Ma (age of the basalt) to 30 Ma. If true, this would suggest that there was no sediment deposition for the first 25 Ma of the site's history. Such an interpretation is consistent with the Co dating method, which was stretched to fit the age of the basement, and the Co method is unable to detect hiatuses. Indeed, areas of the seafloor have been shown to have little sediment coverage (Rea et al., 2006).

Finally, Site U1370 shows broadly similar age estimates, but implied sedimentation rates are variable. From 0-35 Ma the Os age model suggests a slower sedimentation rate than the Co age model. However, from 35 Ma onward, the Os age models shows a faster sedimentation rate. For this site, the Co-based age model estimates that the oldest sample in this study is ~62 Ma, while the Os model predicts a younger age for that sample at nearly 50 Ma. There were unusually high fluxes of hydrogenous Co at Site U1370 (Dunlea et al., 2015a), thus we expect the Os age model to give more accurate ages than the Co age estimates.

Our age model takes the factors that can impact Os isotopes into account: inputs of non-seawater derived Os (principally micrometeorites), bioturbation, and the smoothing of the Os marine record. Furthermore, Os isotopes have long been used as a reliable means to date pelagic sediments. We report an uncertainty estimate with each value. These estimated uncertainties are from the minimum and maximum ages that are provided after running *rBacon*. The average error for all three records is ±2.1 Ma, the median error is ±2.3 Ma and the maximum error is ±4.2 Ma.

4.2 Sources of Fe to the South Pacific over 95 Ma

It is challenging to use only sedimentary Fe isotope compositions to disentangle sources of Fe that were once in the water column. This is difficult because sedimentary Fe isotopes values reflect a weighted sum of Fe contributions from various sources, each possessing a unique isotope signature. Furthermore, end-member Fe isotope compositions of the different sources may be modified within the water column. Depending on which modifications happened, the different sources could end up having indistinguishable Fe isotope compositions. This creates an unmixing problem where neither the relative importance of the end-members nor the end-member compositions are explicitly known. Therefore, we need to rely both on the Fe isotope composition of the original sources as well as a method that allows us to unmix the Fe sources.

Here we use a combination of Fe isotope analysis and statistical analysis. Section 4.2.1 provides an overview of known processes that modify the Fe isotopes from their original sources, Section 4.2.2 discusses QFA analysis and use chemical heuristics to determine the different chemical components in the sediment leaches and interpret these as Fe sources, and Section 4.3 compares our independently determined Fe isotopes and QFA analysis and interprets our findings within the geological context of the South Pacific over 90 Ma.

4.2.1 Iron isotope characterization of major Fe sources

Although the end-member isotope values for the dominant sources of Fe to seawater (e.g., dust, margin dissolution, and hydrothermal fluids) are somewhat well-characterized, secondary processes in the water column can modify the end-member compositions. In this section, we describe the isotope composition of each Fe sources that is ultimately likely to reach the seafloor.

When dust ($\delta^{56}Fe \approx 0.1 \pm 0.1$ ‰) is released into seawater, some of it is stabilized by organic ligands like siderophores. This stabilizing mechanism fractionates the Fe: generally, the heavier Fe isotope is stabilized by the ligand. The ligand, which is functionally dissolved in seawater, causes seawater to become heavier than the crustal composition (e.g., $\Delta_{Seawater\text{-}crust} \approx +0.6 \pm 0.1$ ‰;(Dideriksen et al., 2008; Conway and John, 2014). When Fe-oxyhydroxides form from this heavier pool of ligand-stabilized Fe, they preferentially incorporate the light Fe isotopes (e.g., $\Delta_{Fe\text{-}oxide\text{-}Seawater} \approx -0.8 \pm 0.1$ ‰; Horner et al., 2015). The net effect of these processes leaves dust-derived Fe deposited in pelagic clays with an isotope composition of $\sim -0.1 \pm 0.1$ ‰.

Hydrothermal end-member fluids fall between $\delta^{56}Fe \approx -0.6$ ‰ to −0.2 ‰ (Beard et al., 2003b, a; Severmann et al., 2006; Rouxel et al., 2016; Marsay et al., 2018). In the first approximately 10 meters, the plume rises. Initially, Fe sulfides precipitation dominates, and these particles preferentially incorporate the isotopically light Fe. As the plume rises above the first 10 meters, Fe oxyhydroxides, which favor isotopically heavy Fe, dominant precipitation (Severmann et al., 2004; Lough et al., 2017). Severmann et al. (2004) measured δ^{56}pFe in Rainbow vent fluids, which hosts very little sulfides. The authors of this study found that within the buoyant plume, the particulate Fe isotopes varied substantially from +0.24‰ to +1.29‰. Neutrally-buoyant plume particles were also collected, and these had an isotope composition on the order of $\delta^{56}pFe \approx -0.09 \pm 0.03$ ‰ relative to IRMM-014. We suggest that this represents the range of Fe isotope composition from Fe-oxyhydroxide particles that hosted within a hydrothermal plume. Conversely, Fe particles resulting from sulfide precipitation are isotopically lighter. Particles settling out of the East Pacific Rise showed a range of -0.43 ± 0.08‰ and between 42-86 % of the Fe in the particles was in FeS_2 (Rouxel et al., 2016). As the plume moves even farther from the ridge in the East Pacific Rise, the Fe is stabilized by ligands and exchanging with reactive particulate Fe (Fitzsimmons et al., 2017). The GEOTRACES GP16 cruise showed that at distances farther than 100 km from the ridge, the dissolved Fe isotope composition was constant (e.g., -0.25 ± 0.14 ‰), which suggests that no further fractionation occurs within the plume. Unpublished measurements from leached particles from coretop sediments collected along the GP16 cruise showed that leached hydrothermal sediments had an isotope composition on the order of −0.35 ‰ (Tegler et al., *unpublished*). Because of all of the processes that modify the Fe isotopes in hydrothermal systems, it is challenging to predict what the Fe isotope composition should be recorded in the sediment. However, the range for δ^{56}pFe is quite broad–ranging from −0.43 to +1.29‰.

Continental margins offer another source of Fe to the marine environment. Non-reductive sediment dissolution has an Fe isotope composition on the order of $\delta^{56}Fe \approx \sim 0.2$ ‰ while reductive sediment dissolution has an isotope composition of between $\delta^{56}Fe \approx -3$ and −4 ‰ (Severmann et al., 2004, 2006; John et al., 2012). Additional processes modify these Fe isotope compositions. However, the reducing margin sediment ultimately supply light dissolved and particulate δ^{56}Fe to the margins. The non-reductive margins supply δ^{56}Fe similar to dust (i.e., −0.1 ‰). However, despite this being an importance source near the continent, data from the GEOTRACES program

suggests that continental margins do not carry Fe as far as hydrothermal plumes (1000s of km), as shown by evidence that Fe concentrations are only elevated near the margins before tapering off (within kilometers). Thus, it is likely that the sources of Fe from the margins are not readily observed far from the continents.

Low Fe concentrations exists far from any known source in the open ocean with an isotope composition on the order of >+0.5 ‰ (Fitzsimmons et al., 2017; Marsay et al., 2018). These isotope signatures have been interpreted as ligand-bound background Fe (Fitzsimmons et al., 2017; Marsay et al., 2018). We expect that when this distal background Fe settles to the seafloor, it will be isotopically heavy, likely between 0 and 0.66 ‰. We choose this range as we expect the background to be heavier than crustal values, but lighter or equal to the heavy dissolved δ^{56}Fe observed in Fitzsimmons et al. (2017).

In addition to these well-known sources, volcanism may also provide an important episodic input of Fe to the oceans (Olgun et al., 2011; Longman et al., 2022). Explosive volcanic events can result in 1 km^3 of tephra released and as much as 45 % of the tephra-bound Fe may ultimately enter into the marine environment (Longman et al., 2022). The isotope composition of this material is hard to characterize as few studies have examined the Fe isotope compositions associated with dissolution of erupted volcanic material. One study suggested that fresh tephra that had not experienced oxic diagenesis had an $\delta^{56}Fe \approx 0.02‰$ while buried tephra that had experienced diagenesis had a composition of down to $\delta^{56}Fe \approx -0.26‰$ (Longman et al., 2023), suggesting that tephra dissolution would preferentially liberate isotopically heavy Fe. However, there is no direct information about whether the Fe isotope composition of tephra is variable or whether it is modified by various water column processes. We speculate the tephra-derived Fe becomes ligand-bound and may precipitate as an Fe oxide, similar to dust. However, since tephra has a lighter starting composition than dust, we might expect the tephra value to be slightly lighter, perhaps between ~ -0.3 and -0.15 ‰.

In our downcore profiles, which were detailed in Section 2.3.3 and shown in Figure 2, we observe Fe isotope changes that can be explained by a combination of these processes. However, because of the overlapping isotope values, it is impossible to determine which process dominated for a given sample without additional information. Therefore, before we can interpret the origin of the observed Fe isotope variations, we will use QFA modeling to help us determine the nature of the different sediment components found in our leachates.

4.2.2 Statistical characterization of major hydrogenous components

Q-mode factor analysis is a dimension reduction technique that is used to unmix geochemical datasets to help infer end members. QFA allows for the identification of elements that covary in a dataset and allows us to explain the variability within a dataset. The groupings of these end-members provide clues about the source that each factor represents. The relative importance is described by the factor loadings. The loading values reveal how the importance of each source has changed over time and between the different sites. It is important to note that QFA did not consider any of the Fe isotope measurements, it considered only relationships between the 9 element concentrations.

Factor 1: "Dust component"

Factor one, which accounts for 46 % of total variability of the three sites, is denoted by covariation between Ti, Fe and Pb, all of which are expected to be found in the dissolution of dust components. We thus interpret this factor as a dust-like source. However, because we leached the sediment, it is possible that the dust component comes from two scenarios (i) partial dissolution of detrital material, much of which will represent dust that arrived at the seafloor, or (ii) dissolved or ligand-bound dust that took part in the biological cycle of Fe (e.g., truly seawater-derived).

As shown in Dunlea and Tegler et al., (2021), the leach used in this study is not expected to dissolve detrital aluminosilicates that would significantly influence the hydrogenous signals. Dunlea and Tegler et al. (2021) showed that the Fe:Ti ratios were elevated above the bulk ratios at Site U1366. We show that the same is true for Site U1369 and U1370 (Figure 7). Additionally, if the Fe associated with the dust component was of a detrital origin (i.e., not formerly dissolved in seawater), we would expect for it to have an isotope signature on the order of 0 to +0.1 ‰. Here, we estimate the δ^{56}Fe for dust by equating it to the sediment that have factor loadings for factor 1 greater than 0.9. We observe that the Fe isotopes in regions where factor 1 dominates are on the order of -0.17 ± 0.09 ‰ (Figure 8a), which is similar to what is predicted for dust-sourced Fe that was bound to ligands in the water column prior to precipitation as Fe-oxyhydroxides. This similarity suggests that we preferentially liberated the dust signal of a hydrogenous origin during our leach procedure. Additionally, other studies have measured similar Fe isotope values in Fe-Mn nodules from the same site and arrived at similar conclusions. Marcus et al. (2015) measured the composition of a hydrogenetic ferromanganese nodule with an isotope composition within the

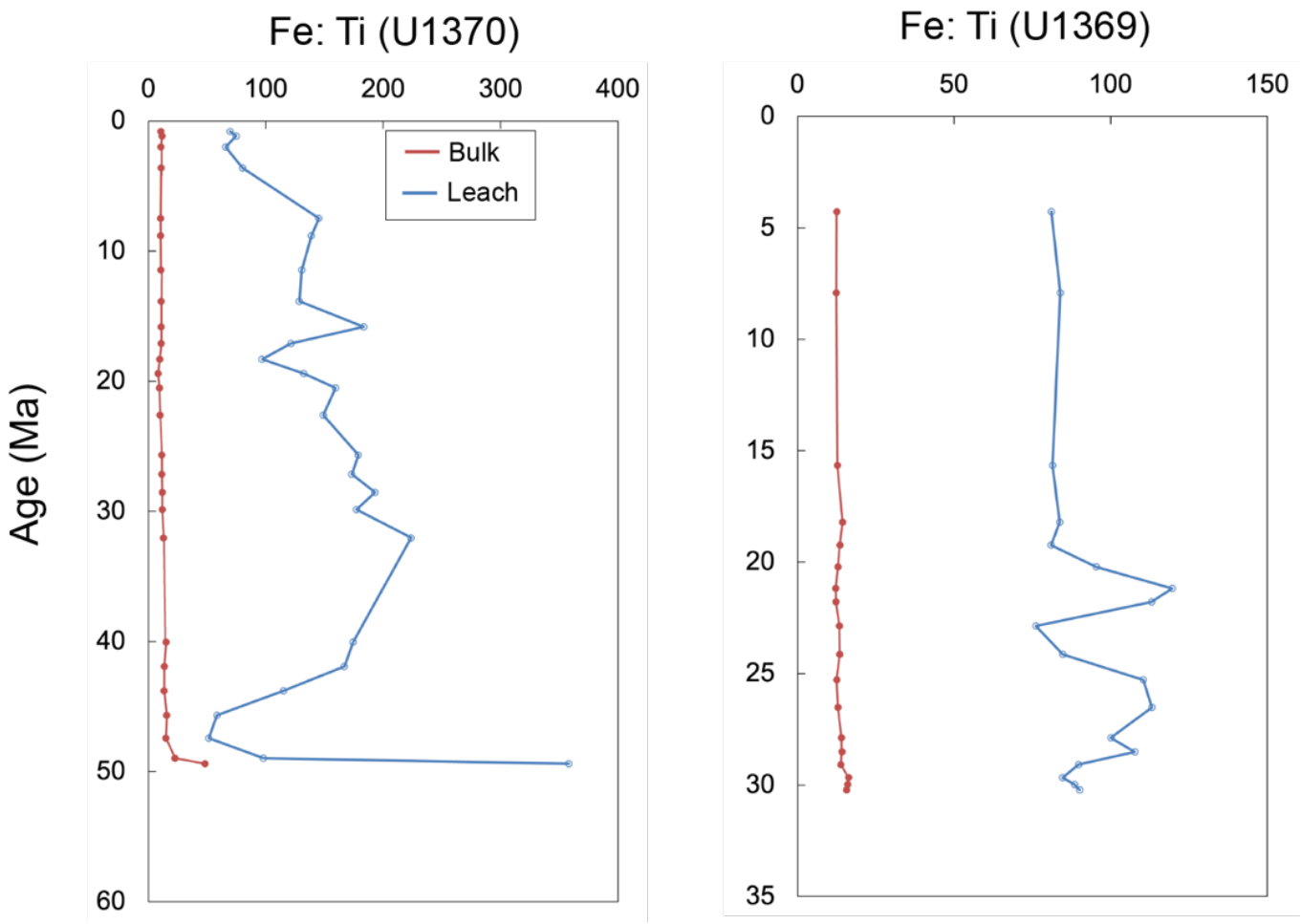

Figure 7. Ratio of Fe (wt. %) to Ti (wt %) in the leach (blue) and the bulk (red). Note that the leach has an elevated Fe:Ti relative to the bulk samples

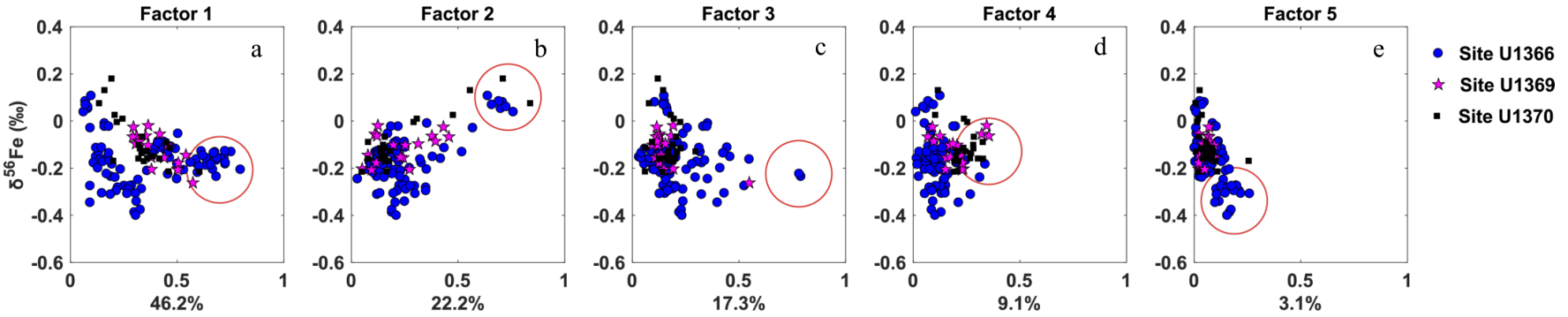

Figure 8. Shows the $\delta^{56}Fe$ of each sample against the factor loading relative to the sum of all factor loadings, such that the sum of all factor loadings is 1. This plot illustrates the isotope composition of factors when the factor is contributing its maximum. While these factor loadings *do not* constitute end-members, we can use them to approximate the isotope composition for each of the factor scores.

same range (e.g., − 0.07 and − 0.17 ± 0.09 ‰) and Dunlea and Tegler et al. (2021) measured the same pelagic clays in this study. Both studies suggested that the Fe from this region, deposited within the last 40 Ma, was primarily derived from a dust source.

Factor 2: "Distal Background Component"

The second factor, which we interpret as a distal background component, accounts for 22 % of the variability of the three sites. In our model, it is defined by strong covariance between Ca, Y, and La. However, when we tested out various iterations of the QFA models with different elements and sample subsets all of the REEs and P covaried in this factor. The observation is important because these elements are expected to accumulate in sediments with slow sedimentation rates. This factor dominates between 60 and 55 Ma, 50 and 40 Ma, and 33 and 30 Ma in Sites U1366, U1370, and U1369.

Factor 2 dominates at the same time intervals where Fe concentrations are the lowest and the Fe isotope compositions are the heaviest. There is only one interval for each of the three sites where the second factor's relative importance is nearly 1 (Figure 8b, Figure 9b), which we interpret as making up the majority of the leached Fe in that region. We take the average isotope composition when the component two factor loading is > 0.9 and suggest that factor two has an isotope composition of +0.09 ± 0.04 ‰.

These heavy Fe isotope values cannot be explained by Fe in near-field hydrothermal plumes or from reducing sediment, both of which are isotopically lighter than this range. Particles with heavy Fe isotope compositions have been observed along the GEOTRACES GP16 transect far from the mid-ocean ridge where particulate Fe concentrations were lowest. This Fe isotope signature has been suggested to represent particles precipitated from ligand-bound background Fe (Fitzsimmons et al., 2017; Marsay et al., 2018). The background source is always present to some degree in our VARIMAX factor loadings. But, in regions that are far from other sources of Fe, with low Fe concentrations (Figure 2a-c), this source is directly observed, despite being associated with low Fe concentrations. Thus, during periods of slow sedimentation, the background ligand-bound Fe is dominant.

Factor 3: "Near-field hydrothermal Component"

This factor is characterized by a covariance between Mn, Fe and V, with a lesser relationship between Mg and Pb. Factor 3 accounts for 17.3 % of the total variability of the dataset. Given that hydrothermal particles typically exhibit strong covariations between Fe and V (Feely et al., 1998; Wu et al., 2022), we interpret this component as indicating a near-field hydrothermal source to the sediment. This factor is most prominent early in the sediment core depositional history of Site U1366 (95-68Ma), which is when Site U1366 would have been closest to the spreading ridge. Additionally, the Fe isotopes over this interval at Site U1366 are isotopically light. There is only one instance when factor 3 has a factor loading of > 0.9. This sample has an isotope composition of −0.22 ‰. The values are identical when we take an average of samples with a factor loading on factor 3 of > 0.8. Here, the δ^{56}Fe is −0.19 ± 0.07 ‰ (Figure 8c). Therefore, the Fe isotopes in this section point to an isotopically light source of Fe. It is interesting to note that this hydrothermal component appears to increase slightly at Sites U1369 and U1370 sites from 0-5 Ma. In this interval, the Fe isotopes also become slightly lighter. It will be important to measure δ^{56}Fe within different hydrothermal systems and core-top sediments near vent systems to narrow in on the range expected to be found in sedimentary archives with distance from the ridge.

Factor 4: "Mg-Ash Component"

Factor 4 accounts for 9.1 % of the variability in the dataset. Factor 4 has very high VARIMAX factor scores for Mg and low to moderate scores for Mn and Ti, suggesting covariation of these elements amongst the samples. Additionally, when Co was used as an element in the model, it was also shown to be correlated with this component. While each of these elements comes from multiple sources, the common source shared by these elements is detrital aluminosilicates. Recent studies at other sites have interpreted the covariations of Mg and Co as being associated with an ash component (Longman et al., 2023). Similar to Longman et al. (2023), we suggest that this component represents a source of volcanic ash to the sediment. Given that Sites U1366, U1369, and U1370 exhibit volcanic ash components in each record (Dunlea et al., 2015b), interpreting factor 4 as volcanic ash is reasonable.

The factor loadings suggest that this component is most relevant from 70-90 Ma at Site U1366, at 20 Ma and Site U1369 and is relatively important from 40-10 Ma at Site U1370 (Figure 9d). Few studies have explored the Fe isotope composition of ash. However, accounting for the

$\delta^{56}Fe$ composition of this component in the sediment is challenging as it never is the dominant source of Fe in our study. Longman et al. (2023) examined the Fe isotope composition of tephra. The study showed that buried volcanic ash that experienced oxic diagenesis exhibited $\delta^{56}Fe \sim -0.26$ ‰. Fresh tephra measured in Montserrat, that had not undergone diagenesis, had an isotope composition of 0.02 ± 0.02 ‰. The ultimate source of Fe in our three pelagic Sites would fall between these two values. The factor loadings associated with factor 4 are all less than 0.7, but the three with the highest factor 4 loadings have an $\delta^{56}Fe \sim -0.16$ ‰. When we apply approximate weighting to the other factor loadings (by using their factor loadings multiplied by the $\delta^{56}Fe$ we defined for each), we can very roughly estimate that the $\delta^{56}Fe$ may be even lighter, between ~ -0.37 ‰ and -0.20 ‰. This is a broad range that would be bolstered by isolating and measuring tephra in the clays. However, this crude estimate is broadly in line with tephra that was ligand bound and could have undergone oxic diagenesis. Olgun et al. (2011) showed that ash potentially contributes a significant supply of dissolved Fe globally. Therefore, our identified ash component may well indicate a significant dissolved sedimentary component from ash deposition at the sites of sedimentation.

Factor 5: "Other hydrothermal Component"

Our last factor is perhaps the most challenging to describe since it only accounts for 3 % of the variability in our dataset. It shows covariation between Fe, Mn and Ti. If only the samples from Site U1366 are included in a QFA, a factor very similar to this factor 5 explains a higher amount of the variability of the dataset. Thus, we consider it a robust factor and include it in our study, while acknowledging that it may only be significant at Site U1366. While this factor is never the most important relative to the other factors, there are intervals where it is notable and likely important to the Fe isotope composition. Between approximately 45 and 62 Ma at Site U1366, this factor shows an increase in its relative importance, similar to the increase seen in Factor 3 (eg., near-field hydrothermal).

We speculate that factor 5 is an additional hydrothermal fluid source of sediment and Fe. Hydrothermal fluids can be modified depending on the composition of the crust they travel through (e.g., pillow basalts, grabbros, ultramafic rocks), which can modify the redox state of the chemistry of the fluids and dictate what precipitates at a sediment site (German & Seyfried, 2014). This second hydrothermal fluid factor may represent a fluid that had a different source than the near-

field hydrothermal fluid, an off-axis hydrothermal fluid source, or a modified near-field hydrothermal source that has been distally advected because Fe is behaving in a somewhat unique manner relative to Mn and Ti.

4.3 Unraveling the factors in paleoceanographic context: How did Fe sources evolve over the Cenozoic?

4.3.1 The evolution of dust in the South Pacific over the Cenozoic

Our factor loads indicate the dust is low from 95-45 Ma for Sites U1366 and U1370. However, at 45 Ma, dust input begins increasing gradually (Figure 9a). All three of the sites experienced gradual increases in the relative amount of dust they were receiving until ~30 Ma, when the two sites achieve the maximum amount of relative dust deposition compared to the other sources. Dust remains the dominant source for the rest of the record.

To interpret these records in context, it is important to understand the backtrack paths of the three sites and the climate history of the Southern Ocean and South Pacific over the Cenozoic. At the start of the Cenozoic, Australia was situated farther south than it is today. Studies suggest that 65 million years ago, Australia was warm, humid and covered in rainforests, and fell at a latitude approximately 60 ˚S (Figure 10; Martin 2006). However, terrestrial vegetation records have suggested that Australia cooled and became more arid over the course of the Cenozoic. The first major transition from a wet-humid climate to a cool-dry one took place in the Mid-Miocene (Martin, 2006).

The aridification of Australia could have been linked to two factors: its northward migration into the 'desert latitudes' or because the Earth as a whole became cooler during this interval. In the early Cenozoic, Australia was entirely situated in the westerlies. Over time, the northern part of the continent migrated into the tropical easterlies. If the same atmospheric wind patterns were constant over the Cenozoic, we might expect for Australia to have become a desert as its northern region migrated across the 30˚S latitude, which is where the Hadley cells descend upon Earth with arid air. The desertification of Australia was likely also aided by the cooling of the Earth over the course of the Cenozoic. However, regardless of which of these conditions played the dominant role in creating the drier, dustier region, it is clear that Australia became an important source of mineral dust to the South Pacific starting between 36 and 30 Ma when Australia moved

northward and the Tasman gateway deepened (Mackie 2008). The fact that the dust factor loadings stay constant over time likely suggests that the amount of dust deposited to the ocean reflects the aridification of Australia, rather than the Sites' proximity to the continent.

4.3.2 Hydrothermalism

Our analysis shows that there are two sources of hydrothermal Fe, called 'near-field hydrothermal' and 'other hydrothermal'. In this section, we will first explore the ways in which we may expect hydrothermal sources to change of the Cenozoic. Next, we will speculate what the two different sources of hydrothermalism could represent.

The near-field hydrothermal factor is most important at Site U1399 from 95-68 Ma. It then has a period of low-to-moderate importance for all three sites until ~10 Ma. The near-field hydrothermal source shows an increase in importance at ~10 to 0 Ma, especially at Site U1370. We use our data and knowledge of the Sites' history to suggest that local hydrothermal processes, not broad tectonic changes, determine whether near-field hydrothermal is important to a site at a given time. Conversely, the 'other hydrothermal' appears at ~55 Ma and disappears at ~35 Ma for Site U1366 and, to a lesser extent, Site U1370. We suggest this factor may be related to broad tectonic changes.

The Cenozoic experienced changes in ocean circulation when both Australia and South America migrated northward and created two passageways—the Drake Passage and the Tasman Gateway. Seafloor magnetic anomalies in the Scotia Sea have been used to reconstruct the tectonic plate history of South America and Antarctica (e.g., Eagles, 2003; Livermore et al., 2005, Eagles et al., 2005; Livermore et al., 2005). These studies suggest that the Drake Passage, which created an oceanic connection between the Pacific and the Atlantic, slowly opened at ~50 Ma through continental stretching and seafloor spreading (Eagles et al., 2006). The opening of the Drake Passage is thought to have been quite shallow when it first opened and it deepened over time (~36 Ma; van de Lagemaat et al., 2021). Additionally, another oceanic passage, the Tasman Gateway opened between Australia and Antarctica, opened at ~35 Ma (e.g., Stickley et al., 2004). These changes fundamentally reorganized the ocean circulation of deep-water and may change how hydrothermal Fe was transported to the three sites. The 'other hydrothermal' factor shows a period of importance that coincides with the opening of the Drake Passage. Thus, this source may indicate a change in the hydrothermal supply of sediments (and Fe) during tectonic realignments. During

the intervals where factor 5 has an increased importance important at Site U1366 and U1370 (e.g., 65-62 Ma and 55-40 Ma), the Fe isotope composition becomes lighter (on the order of − 0.3 ‰). However, the isotopes observed here are marginally lighter than the isotope values as seen during hydrothermalism early in the site's history. Because this other hydrothermal source only accounts for a small portion of the factor loadings, we assume that the Fe isotope composition of mysterious hydrothermal is significantly lighter than the other sources, perhaps on the order of − 0.4 ‰. This Fe isotope composition is similar to the coretop sediments measured in Tegler et al. (*unpublished*) collected along GP16 (e.g., ~ − 0.35 ‰).

In addition to these major tectonic reorganizations, the three sites examined here also likely had variable inputs from local hydrothermalism over the course of the Cenozoic. For example, Site U1366 may have experienced additional hydrothermal input from multiple vent sources. Site U1366 was born amid a region that may have with multiple vent sources and was close to the Osbourne trough, a failed ridge system that stopped spreading in the late Cretaceous (Billen and Stock, 2000). This source of hydrothermal Fe would not be expected to be observed at Sites U1370 or U1369, which were born after the Osbourne trough went extinct. The interval from 95-68 Ma at Site U1366 may have been because it was close to the vent origin or vent fluids from the Osbourn trough followed by decreased importance as the site migrated away from where they plume was being advected. Likewise, the uptick in importance in the modern could suggest that U1370 moved into a flow path of a distal hydrothermal plume. The light Fe isotopes observed during periods where near-field hydrothermal is high (e.g., ~ − 0.19 ‰) is within what would be expected from hydrothermal Fe that was advected from its origin.

So, why do we see two distinct hydrothermal sources of Fe? We consider three factors that could be responsible. First, these sources could be modified versions of each other. The ‘other hydrothermal’ may be a modified fluid that was derived from near-field hydrothermal that became progressively isotopically lighter with distance from the ridge. However, we do not expect this to be the case because of the timing of when the factors become important. Near-field hydrothermal appears to be important when it is close to a local source of hydrothermalism at Site U1366 and becomes less important as the site migrates away from the mid-ocean ridge. Furthermore, the ‘other hydrothermal’ source becomes important at the same time major reorganizations of the tectonic plates are occurring. Alternatively, these hydrothermal sources represent vents with distinct chemistry. Different hydrothermal vents have unique chemical compositions based on the

host rock, temperature, pressure, amount of time the water spent in contact with the rock, and fluid-rock ratios (Humphris and Klein, 2017). We suggest that the distinct Fe isotope compositions derive from different processes that occurred at the vent plume (e.g., various amounts of FeS_2 precipitation and Fe-oxyhydroxide precipitation) and during biological progressing. Finally, we suggest that the other hydrothermal factor could represent an off-axis hydrothermal fluid. We offer this possibility because, unlike near-field hydrothermal, the 'other hydrothermal' never appears to be a dominant source to the sediments. Instead, it consistently appears in the background of all three sites. More work is needed to determine what isotope compositions of Fe are expected in off-axis hydrothermal fluids.

4.3.3 Volcanic Ash

While we cannot estimate the fluxes of volcanic ash to the sites in this study, we observe periods of increase in the relative importance of ash. Site U1366 shows that volcanic ash was more important from 80-70 Ma, Site U1369 shows increased importance near 20 Ma, and Site U1370 shows that volcanic ash was more important than other sources for a longer interval of 40-10 Ma. There are four potential ways for our sites to experience Fe inputs from ash deposition. First, the sites could be situated adjacent to subareal volcanic activity and experience ash deposition during eruption events. We believe this is unlikely since our sites are far from land. Second, there could be a general ash input to the Pacific that deposits ash continuously. However, since we do not see an ash component dominate at the same time for the three sites, we rule out this possibility. Third, it is possible that a site moves downwind of an active volcanic area. This is a likely possibility as it allows for the sites to experience unique intervals of increased ash. Finally, a fourth possibility is that the sites have volcanic ash inputs from subaqueous eruptions. Underwater eruptions can produce large amount of floating pumice and can travel long distance in ocean currents across the Pacific. If this pumice is eroded over time, some of it may become dissolved and rain down to the seafloor. The fourth possibility is also likely but would be hard to trace without histories of subaqueous volcanism.

The Pacific Ocean is encircled by many active, explosive and ash-emitting volcanoes (in particular New Zealand and the Tonga-Kermedec subduction zone that are both upwind of our sites). Although major eruptions are often thought of as episodic events, over geological time, ash emitted to the Pacific ocean can be thought of as quasi-continuous. Several studies examined sites

from the South Pacific Gyre to estimate the periods of increased volcanic activity. Dunlea et al. (2015b) quantified the dispersed ash in U1366, U1369, and U1370. The work found that the inputs of volcanic ash rivaled that of dust.

According to Dunlea et al. (2015b) periods of increased episodes of volcanism in the South Pacific occurred during the following intervals: 110-70 Ma, 40-35 Ma, 26-24 Ma, 15-10 Ma, 4 Ma, and 2-0 Ma. Site U1366 experienced increased volcanic ash inputs from 80-70 Ma. This increased input may be from widespread intraplate volcanism that begin at the beginning of the Cretaceous and lasted from approximately 40 Ma (Schlanger et al., 1981; Straub and Schmincke, 1998). It is possible that Site U1366 experienced similar levels of ash from 95-70 Ma, but the factor loadings from the ash source were muted by relatively higher hydrothermal inputs. Increasing volcanism in the Mid Micoene (~ 12 Ma) may account for some of the ash inputs seen at Sites U1369 and U1370. Carter et al. (2004) showed that tephras become thicker and more frequent from the late Micoene into the Quaternanry. This trend likely reflected more frequent and intense volcanism. Likewise, the Sites U1369 and U1370 were moving closer to New Zealand during this interval, but Site U1366 had already moved north of New Zealand.

Of course, in our Sites, it is difficult to quantify ash deposition because we are working with relative importance, not end-member compositions. Furthermore, we are unable to account for subaqueous processes or the delivery of pumice-derived Fe sources to the sediment. Future work on ash sources over the Cenozoic will be needed to better quantify ash deposition to our sediments.

5. Summary and Future Directions

In this study, we analyzed an operationally defined hydrogenous fraction of pelagic clays from three sediment sites in the South Pacific Gyre. In addition to creating new more robust age models for these sediments, we also measured their iron isotope compositions; determined concentrations of a suite of major, minor, and trace elements in the hydrogenous fraction of the sediments; and performed statistical modeling to attribute sources of material to the sediment. The downcore trends in the Fe isotopes and statistically determined sediment components correlate with each other, underscoring that five sources of Fe to the South Pacific Gyre were significant over the last 95 Ma: dust, a distal background source, two sources of hydrothermal material, and

volcanic ash. Early in the sites' depositional histories hydrothermal Fe sources dominate, whereas the last ~30 million years have seen dust sources become most important. However, throughout each core volcanic ash, distal Fe, and hydrothermal sources vary substantially, documenting a dynamic evolution of Fe sources to the Southern Ocean and South Pacific over the Cenozoic.

There are several future directions that should be addressed. First, pelagic clays from different ocean basins should be analyzed. In particular, it would be interesting to observe whether the identified Fe sources are universal to pelagic sediments or whether other sources of Fe arise in different basins. Additionally, it will be important to examine volcanic ash inputs to sediments in other basins – what is the extent of volcanic ash inputs across basin-wide scales? Finally, more work is needed to quantitatively disentangle the sources of Fe. Because this study used a leach to access the sources of Fe, we were unable to use a constrained least squares approach to quantify each of the sources. More work will be needed to address the importance of each of these factors.

While our findings suggest that dust deposition has become increasingly important from 35 Ma to present, sources of hydrothermalism and volcanic ash are also important, especially when far from the continents. This is particularly true before 35 Ma, where these factors were more significant Fe sources than dust. Further work should attempt to measure sediments that are currently in the Southern Ocean to explore how much Fe could currently be coming from hydrothermal sources. Although we expect that aridification of Australia led to the late Cenozoic becoming dustier, our sediments have also migrated away from mid-ocean spreading ridges, so they are likely less impacted by hydrothermal sources of Fe. In order to assess the importance of Fe from hydrothermalism in the modern Southern Ocean, which is Fe-limited, it will be key to measure sediment near vent systems in the Southern Ocean, many of which, have yet to even be discovered.

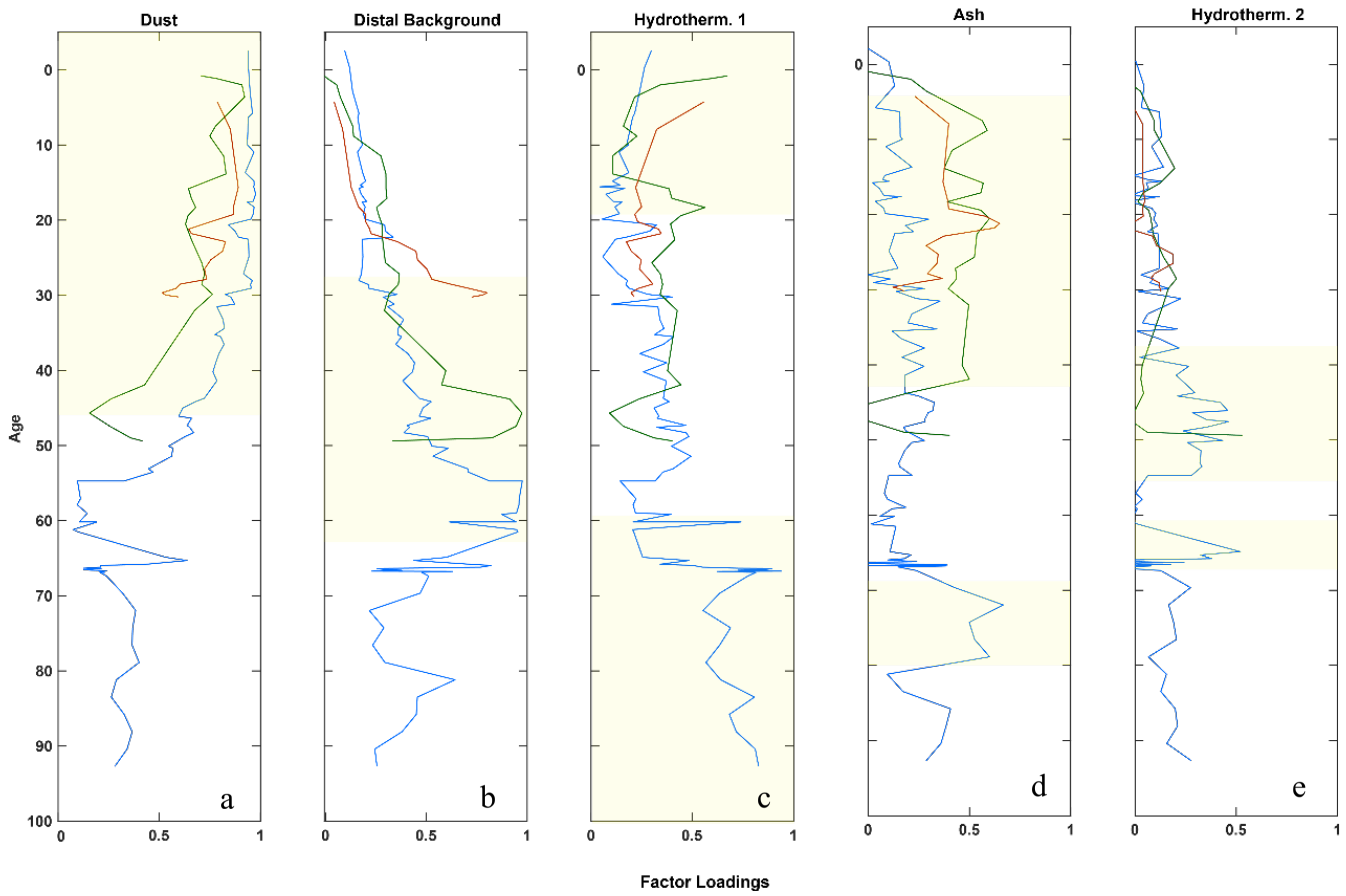

Figure 9. Factor loadings for each site broken out by factor scores (A: dust, B: background, C: hydrothermal 1, D: ash, E: hydrothermal 2). Blue lines represent Site U1366, green lines represent Site U1370 and redlines are Site U1369. The yellow shaded region notes periods of increased relative importance.

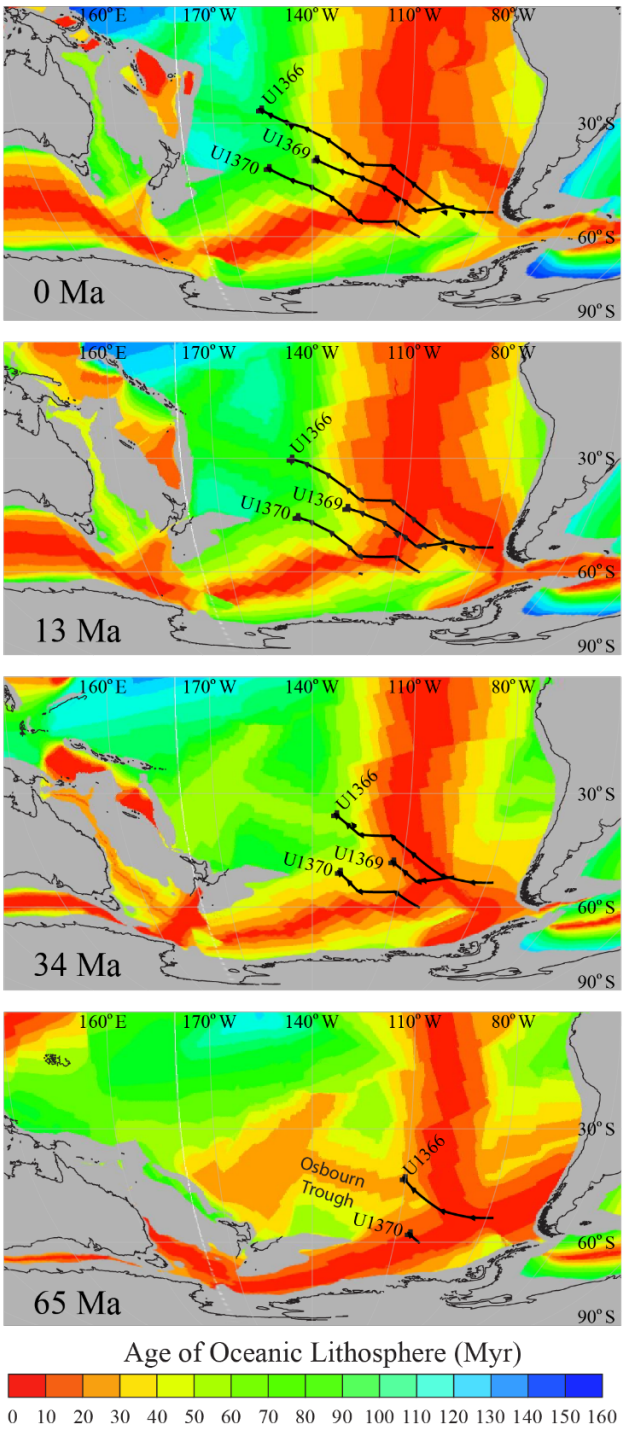

Figure 10. Location and backtrack paths of Sites U1366, U1370 and U1369 at (a) 65 Ma, (b) 34 a, (c) 13 Ma and (d) 0 Ma. Maps were generated by Ann Dunlea in GPlates. Backtrack plots are plotted against a latitude and longitude reference frame.

Acknowledgments

I would like to thank my coauthors for this study: Tristan J. Horner, Sune G. Nielsen, Andy Heard, Silke Severmann, Bernhard Peucker-Ehrenbrink, Jurek Blusztajn, Ann G. Dunlea

Chapter 5 References

Beard B. L., Johnson C. M., Damm K. L. V. and Poulson R. L. (2003a) Iron isotope constraints on Fe cycling and mass balance in oxygenated Earth oceans. *Geology* **31**, 629–632.

Beard B. L., Johnson C. M., Skulan J. L., Nealson K. H., Cox L. and Sun H. (2003b) Application of Fe isotopes to tracing the geochemical and biological cycling of Fe. *Chem Geol* **195**, 87–117.

Billen, M. I., & Stock, J. (2000). Morphology and origin of the Osbourn Trough. *Journal of Geophysical Research: Solid Earth*, **105**(B6), 13481-13489.

Blaauw M. and Christen J. A. (2011) Flexible paleoclimate age-depth models using an autoregressive gamma process. *Bayesian Anal* **6**, 457–474.

Buck K. N., Lohan M. C., Sander S. G., Hassler C. and Pižeta I. (2017) Editorial: Organic Ligands—A Key Control on Trace Metal Biogeochemistry in the Ocean. *Frontiers Mar Sci* **4**, 313.

Carter L., Alloway B., Shane P. and Westgate J. (2004) Deep-ocean record of major late Cenozoic rhyolitic eruptions from New Zealand. *N. Zealand J. Geol. Geophys.* **47**, 481–500.

Conway T. M. and John S. G. (2014) Quantification of dissolved iron sources to the North Atlantic Ocean. *Nature* **511**, 212–215.

Coplen T. B. (2011) Guidelines and recommended terms for expression of stable-isotope-ratio and gas-ratio measurement results. *Rapid Commun. Mass Spectrom.* **25**, 2538–2560.

Craddock P. R. and Dauphas N. (2011) Iron Isotopic Compositions of Geological Reference Materials and Chondrites. *Geostand Geoanal Res* **35**, 101–123.

D'Hondt, S., Inagaki, F., Alvarez Zarikian, C. A., Expedition 329 Scientists, 2011. Expedition 329 Reports, in Proceedings of the Integrated Ocean Drilling Program. vol. 329. Integrated Ocean Drilling Program Management International, Inc., Tokyo. https://doi.org/10.2204/iodp.proc.329.2011.

deJong J., Schoemann V., Tison J.-L., Becquevort S., Masson F., Lannuzel D., Petit J., Chou L., Weis D. and Mattielli N. (2007) Precise measurement of Fe isotopes in marine samples by multi-collector inductively coupled plasma mass spectrometry (MC-ICP-MS). *Anal Chim Acta* **589**, 105–119.

Dauphas N., Pourmand A. and Teng F.-Z. (2009) Routine isotopic analysis of iron by HR-MC-ICPMS: How precise and how accurate? *Chem. Geol.* **267**, 175–184.

Dideriksen K., Baker J. A. and Stipp S. L. S. (2008) Equilibrium Fe isotope fractionation between inorganic aqueous Fe(III) and the siderophore complex, Fe(III)-desferrioxamine B. *Earth* Planet. Sci. Lett. **269**, 280–290.

Dubois, N., Mitchell, N.C. , Ha ll, I.R., 2014. Data report: particle size distribution for IODP Expedition 329 sites in the South Pacific Gyre. Proc. IODP 329 doi:10.2204-iodp.proc.329.201.2014.

Dunlea A. G. and Murray R. W. (2015) Optimization of end-members used in multiple linear regression geochemical mixing models. *Geochem Geophys Geosystems* **16**, 4021–4027.

Dunlea A. G., Murray R. W., Sauvage J., Pockalny R. A., Spivack A. J., Harris R. N. and D'Hondt S. (2015a) Cobalt-based age models of pelagic clay in the South Pacific Gyre. *Geochem Geophys Geosystems* **16**, 2694–2710.

Dunlea A. G., Murray R. W., Sauvage J., Spivack A. J., Harris R. N. and D'Hondt S. (2015b) Dust, volcanic ash, and the evolution of the South Pacific Gyre through the Cenozoic. *Paleoceanography* **30**, 1078–1099.

Dunlea A. G., Tegler L. A., Peucker-Ehrenbrink B., Anbar A. D., Romaniello S. J. and Horner T. J. (2021) Pelagic clays as archives of marine iron isotope chemistry. *Chem Geol* **575**, 120201.

Eagles, G., Livermore, R. A., Fairhead, J. D., & Morris, P. (2005). Tectonic evolution of the west Scotia Sea. *Journal of Geophysical Research: Solid Earth*, **110**(B2).

Eagles, G., Livermore, R., & Morris, P. (2006). Small basins in the Scotia Sea: the Eocene Drake passage gateway. *Earth and Planetary Science Letters*, **242**, 343-353.

Feely R. A., Trefry J. H., Lebon G. T. and German C. R. (1998) The relationship between P/Fe and V/Fe ratios in hydrothermal precipitates and dissolved phosphate in seawater. *Geophys. Res. Lett.* **25**, 2253–2256.

Fitzsimmons J. N., John S. G., Marsay C. M., Hoffman C. L., Nicholas S. L., Toner B. M., German C. R. and Sherrell R. M. (2017) Iron persistence in a distal hydrothermal plume supported by dissolved–particulate exchange. *Nat Geosci* **10**, 195–201.

German, C. R., & Seyfried, W. E. (2014). 8.7-Hydrothermal Processes, Treatise on Geochemistry, Holland, HD, Turekian, KK, Eds.

Hassler D. R., Peucker-Ehrenbrink B. and Ravizza G. E. (2000) Rapid determination of Os isotopic composition by sparging OsO4 into a magnetic-sector ICP-MS. *Chem Geol* **166**, 1–14.

Horner T. J., Williams H. M., Hein J. R., Saito M. A., Burton K. W., Halliday A. N. and Nielsen S. G. (2015) Persistence of deeply sourced iron in the Pacific Ocean. *Proc National Acad Sci* **112**, 1292–1297.

Humphris S. E. and Klein F. (2017) Progress in Deciphering the Controls on the Geochemistry of Fluids in Seafloor Hydrothermal Systems. *Annu. Rev. Mar. Sci.* **10**, 1–29.

Jochum K. P., Nohl U., Herwig K., Lammel E., Stoll B. and Hofmann A. W. (2005) GeoReM: A New Geochemical Database for Reference Materials and Isotopic Standards. *Geostand Geoanal Res* **29**, 333–338.

John S. G., Helgoe J., Townsend E., Weber T., DeVries T., Tagliabue A., Moore K., Lam P., Marsay C. M. and Till C. (2018) Biogeochemical cycling of Fe and Fe stable isotopes in the Eastern Tropical South Pacific. *Mar Chem* **201**, 66–76.

John S. G., Mendez J., Moffett J. and Adkins J. (2012) The flux of iron and iron isotopes from San Pedro Basin sediments. *Geochim Cosmochim Ac* **93**, 14–29.

Klemm V., Levasseur S., Frank M., Hein J. R. and Halliday A. N. (2005) Osmium isotope stratigraphy of a marine ferromanganese crust. *Earth Planet Sc Lett* **238**, 42–48.

Leinen M. and Pisias N. (1984) An objective technique for determining end-member compositions and for partitioning sediments according to their sources. *Geochim Cosmochim Ac* **48**, 47–62.

Livermore, R., Nankivell, A., Eagles, G., & Morris, P. (2005). Paleogene opening of Drake passage. *Earth and Planetary Science Letters*, **236**, 459-470.

Longman J., Dunlea A. G., Böning P., Palmer M. R., Gernon T. M., McManus J., Manners H. R., Homoky W. B. and Pahnke K. (2023) Release of tephra-hosted iron during early diagenesis fingerprinted by iron isotopes. *Earth Planet. Sci. Lett.* **605**, 118016.

Longman J., Palmer M. R., Gernon T. M., Manners H. R. and Jones M. T. (2022) Subaerial volcanism is a potentially major contributor to oceanic iron and manganese cycles. *Commun. Earth Environ.* **3**, 60.

Lough A. J. M., Klar J. K., Homoky W. B., Comer-Warner S. A., Milton J. A., Connelly D. P., James R. H. and Mills R. A. (2017) Opposing authigenic controls on the isotopic signature of dissolved iron in hydrothermal plumes. *Geochim Cosmochim Ac* **202**, 1–20.

Mackie, D. S., Boyd, P. W., McTainsh, G. H., Tindale, N. W., Westberry, T. K., & Hunter, K. A. (2008). Biogeochemistry of iron in Australian dust: From eolian uplift to marine uptake. *Geochemistry, Geophysics, Geosystems*, **9.**

Majestic B. J., Anbar A. D. and Herckes P. (2009) Elemental and iron isotopic composition of aerosols collected in a parking structure. *Sci Total Environ* **407**, 5104–5109.

Marcus M. A., Edwards K. J., Gueguen B., Fakra S. C., Horn G., Jelinski N. A., Rouxel O., Sorensen J. and Toner B. M. (2015) Iron mineral structure, reactivity, and isotopic composition in a South Pacific Gyre ferromanganese nodule over 4Ma. *Geochim Cosmochim Ac* **171**, 61–79.

Marsay C. M., Lam P. J., Heller M. I., Lee J.-M. and John S. G. (2018) Distribution and isotopic signature of ligand-leachable particulate iron along the GEOTRACES GP16 East Pacific Zonal Transect. *Mar Chem* **201**, 198–211.

Martin, H. A. (2006). Cenozoic climatic change and the development of the arid vegetation in Australia. *Journal of Arid Environments*, **66**, 533-563.

Martínez-Garcia A., Rosell-Melé A., Jaccard S. L., Geibert W., Sigman D. M. and Haug G. H. (2011) Southern Ocean dust–climate coupling over the past four million years. *Nature* **476**, 312–315.

Moore C. M., Mills M. M., Arrigo K. R., Berman-Frank I., Bopp L., Boyd P. W., Galbraith E. D., Geider R. J., Guieu C., Jaccard S. L., Jickells T. D., Roche J. L., Lenton T. M., Mahowald N. M., Marañón E., Marinov I., Moore J. K., Nakatsuka T., Oschlies A., Saito M. A., Thingstad T. F., Tsuda A. and Ulloa O. (2013) Processes and patterns of oceanic nutrient limitation. *Nat Geosci* **6**, 701–710.

Nielsen S. G., Mar-Gerrison S., Gannoun A., LaRowe D., Klemm V., Halliday A. N., Burton K. W. and Hein J. R. (2009) Thallium isotope evidence for a permanent increase in marine organic carbon export in the early Eocene. *Earth Planet Sc Lett* **278**, 297–307.

Olgun N., Duggen S., Croot P. L., Delmelle P., Dietze H., Schacht U., Óskarsson N., Siebe C., Auer A. and Garbe-Schönberg D. (2011) Surface ocean iron fertilization: The role of airborne volcanic ash from subduction zone and hot spot volcanoes and related iron fluxes into the Pacific Ocean. *Glob. Biogeochem. Cycles* **25**, n/a-n/a.

Pegram W. J., Krishnaswami S., Ravizza G. E. and Turekian K. K. (1992) The record of sea water 187Os/186Os variation through the Cenozoic. *Earth Planet Sc Lett* **113**, 569–576.

Peucker-Ehrenbrink B. and Ravizza G. (2012) The Geologic Time Scale. , 145–166.

Peucker-Ehrenbrink B. and Ravizza G. (2000) The marine osmium isotope record. *Terra Nova* **12**, 205–219.

Peucker-Ehrenbrink B. and Ravizza G. E. (2020) Geologic Time Scale 2020. , 239–257.

Peucker-Ehrenbrink B., Ravizza G. and Hofmann A. W. (1995) The marine187Os/186Os record of the past 80 million years. *Earth Planet Sc Lett* **130**, 155–167.

Pisias N. G., Murray R. W. and Scudder R. P. (2013) Multivariate statistical analysis and partitioning of sedimentary geochemical data sets: General principles and specific MATLAB scripts. *Geochem Geophys Geosystems* **14**, 4015–4020.

Reimann C., Filzmoser P. and Garrett R. G. (2002) Factor analysis applied to regional geochemical data: problems and possibilities. *Appl. Geochem.* **17**, 185–206.

Resing J. A., Sedwick P. N., German C. R., Jenkins W. J., Moffett J. W., Sohst B. M. and Tagliabue A. (2015) Basin-scale transport of hydrothermal dissolved metals across the South Pacific Ocean. *Nature* **523**, 200–203.

Rouxel O., Toner B. M., Manganini S. J. and German C. R. (2016) Geochemistry and iron isotope systematics of hydrothermal plume fall-out at East Pacific Rise 9°50′N. *Chem Geol* **441**, 212–234.

Schlanger S. O., Jenkyns H. C. and Premoli-Silva I. (1981) Volcanism and vertical tectonics in the Pacific Basin related to global Cretaceous transgressions. *Earth Planet. Sci. Lett.* **52**, 435–449.

Sen I. S. and Peucker-Ehrenbrink B. (2014) Determination of Osmium Concentrations and 187Os/188Os of Crude Oils and Source Rocks by Coupling High-Pressure, High-Temperature Digestion with Sparging OsO4 into a Multicollector Inductively Coupled Plasma Mass Spectrometer. *Anal Chem* **86**, 2982–2988.

Severmann S., Johnson C. M., Beard B. L., German C. R., Edmonds H. N., Chiba H. and Green D. R. H. (2004) The effect of plume processes on the Fe isotope composition of hydrothermally derived Fe in the deep ocean as inferred from the Rainbow vent site, Mid-Atlantic Ridge, 36°14′N. *Earth Planet Sc Lett* **225**, 63–76.

Severmann S., Johnson C. M., Beard B. L. and McManus J. (2006) The effect of early diagenesis on the Fe isotope compositions of porewaters and authigenic minerals in continental margin sediments. *Geochim Cosmochim Ac* **70**, 2006–2022.

Slotznick S. P., Sperling E. A., Tosca N. J., Miller A. J., Clayton K. E., Helmond N. A. G. M., Slomp C. P. and Swanson-Hysell N. L. (2020) Unraveling the Mineralogical Complexity of Sediment Iron Speciation Using Sequential Extractions. *Geochem Geophys Geosystems* **21**.

Stickley, C. E., Brinkhuis, H., Schellenberg, S. A., Sluijs, A., Röhl, U., Fuller, M., ... & Williams, G. L. (2004). Timing and nature of the deepening of the Tasmanian Gateway. *Paleoceanography*, **19**.

Stookey L. L. (1970) Ferrozine---a new spectrophotometric reagent for iron. *Anal. Chem.* **42**, 779–781.

Straub S. M. and Schmincke H. U. (1998) Evaluating the tephra input into Pacific Ocean sediments: distribution in space and time. *Geol. Rundsch.* **87**, 461–476.

Tagliabue A., Bopp L., Dutay J.-C., Bowie A. R., Chever F., Jean-Baptiste P., Bucciarelli E., Lannuzel D., Remenyi T., Sarthou G., Aumont O., Gehlen M. and Jeandel C. (2010) Hydrothermal contribution to the oceanic dissolved iron inventory. *Nat Geosci* **3**, 252–256.

Tagliabue A., Bowie A. R., Boyd P. W., Buck K. N., Johnson K. S. and Saito M. A. (2017) The integral role of iron in ocean biogeochemistry. *Nature* **543**, 51–59.

Waeles M., Baker A. R., Jickells T. and Hoogewerff J. (2007) Global dust teleconnections: aerosol iron solubility and stable isotope composition. *Environ Chem* **4**, 233–237.

Wu F., Owens J. D., German C. R., Mills R. A. and Nielsen S. G. (2022) Vanadium isotope fractionation during hydrothermal sedimentation: Implications for the vanadium cycle in the oceans. *Geochim. Cosmochim. Acta* **328**, 168–184.

van de Lagemaat, S. H., Swart, M. L., Vaes, B., Kosters, M. E., Boschman, L. M., Burton-Johnson, A., ... & Van Hinsbergen, D. J. (2021). Subduction initiation in the Scotia Sea region and opening of the Drake Passage: When and why?. *Earth-Science Reviews*, **215**, 103551.

Yang K., Kim J., Kogure T., Dong H., Baik H., Hoppie B. and Harris R. (2016) Smectite, illite, and early diagenesis in South Pacific Gyre subseafloor sediment. *Appl Clay Sci* **134**, 34–43.

Conclusions and Future Directions

This thesis examines four elemental cycles in the ocean: carbon, cadmium, osmium and iron. We use each of these elements to learn about the biological pump, past or present. In Chapter 2, I constrain depositional fluxes of organic carbon in ~800 sediment samples from the continental margins. I encounter several challenges including choosing how to best define OC fluxes to sediment, having low data density, and distinguishing between terrestrial. Despite these challenges, I estimate that marine-derived OC deposition fluxes are on the order of 19.4 Tmol OC yr^{-1}. Furthermore, our study challenges the paradigm that most OC is buried in regions with low bottom water oxygen content. Instead, I find that OC deposition primarily relies upon particle distance to the seafloor and productivity within the surface waters. There is a plethora of future work that must be done to refine our estimates. Most importantly, more measurements of OC deposition fluxes are needed. While our data set is vastly more than was included in previous work, the number is still sparse compared to the relative size and heterogeneity of the margins. Moreover, some margins have few or no OC deposition information. It is my impression that many more OC deposition fluxes already exist, but as a footnote in studies that explore other important topics. Researchers should compile a repository of all OC deposition flux values and update our model estimates. More advanced interpolation or machine learning techniques may be applied if enough data are eventually acquired. Getting a precise estimate of OC deposition fluxes is of the utmost importance as humans proceed valiantly into the Anthropocene. Policymakers will be concerned with fluxes of carbon out of the atmosphere and geoengineering start-ups will likely lean on such values as they construct solutions to atmospheric carbon. It will be important to put forward the most robust flux estimates possible. Moreover, getting a handle on this flux estimate will be useful for determining whether increasing the efficiency of the biological pump is a reasonable means for atmospheric carbon dioxide removal (CRD) over long timescales. My study suggests that the global OC deposition flux is on the order of ~20 Tmol C per year, which is about 40 times smaller than current anthropogenic emissions. Thus, it is possible that focusing too much effort on marine export as a primary CDR removal technique may not offset human activities.

In Chapter 3, I explore Cd isotopes as a proxy for nutrient utilization and determine that using such a proxy is fraught. The original idea for such a proxy was that since significant Cd isotope fractionation is associated with the biological uptake of Cd, the export of biological particles to the seafloor should reflect how much Cd was taken up, which can be used to infer the

degree of nutrient utilization in the surface waters. However, the early studies that deployed Cd isotopes as a paleonutrient proxy in the sediment, did not compare the Cd isotopes in the surface water to those in the sediment. Recent studies have indicated that there is dynamic processing of Cd isotopes within the water column from redox and remineralization. So, to test whether Cd isotopes in sediments record nutrient utilization in the surface waters, I measured over one-hundred sediment and seawater Cd isotopes. I reported three key findings. First, I showed that the flux of Cd to the sediments is strongly coupled to the flux of organic matter, and the pelagic precipitation of Cd under reducing redox conditions is minor. Second, I found that remineralization did affect the Cd isotope compositions of sinking particles in the Southern Ocean. However, I was unable to interrogate whether those values were recorded in the underlying sediment. Finally, and perhaps most importantly, I found that when surface Cd concentrations are low, the Cd isotopes in the underlying sediment show the opposite trend than what would be expected from the paleonutrient proxy paradigm. I suggest, as has been suggested in seawater Cd isotope studies, that the Cd isotopes in these regions are set by the isotope composition of externally supplied Cd, not by biological activity. This third finding jeopardizes the use of Cd as a paleonutrient proxy as it suggests that scientists must know the Cd surface water concentrations before applying the proxy. Such knowledge would require additional information (e.g., Cd:Ca in forams) or would be nearly impossible to obtain in Archean settings. In addition to our findings, I also suggest that more research is needed to characterize the isotope composition of sediment underlying Cd-replete surface waters and sediments buried beneath regions with high bottom-water oxygen. It is possible that the paleonutrient proxy does work in these regions, but no sediments have been tested. Finally, it will be critical to explore these regions in order to close the Cd isotope mass balance. Despite finding that there is no simple way to relate sedimentary Cd isotopes to nutrient utilization, I suggest that Cd may be used as an indicator of remineralization and redox if these processes are explored in more detail.

In Chapter 4, I perform a Cd isotope case study on the 2.5 billion-year old Mt. McRae Shale. This study highlights just how challenging it is to apply Cd isotopes to the ancient sedimentary record. The Mt. McRae Shale was deposited 100 Ma before the Great Oxidation Event during transient oxidation events. Because the interval is thought to be concurrent with the evolution of photosynthesis, it is possible that there was a change in nutrient utilization in the surface waters. However, we do not observe changes in the Cd isotope record that suggest Cd is

reflecting ancient nutrient utilization. Instead, based on the conclusions of Chapter 3, I suggest that it is most likely that the Hamersley Basin was underlying Cd-depleted surface seawater for the duration of the whiff interval. Thus, I suggest that the Cd isotopes merely reflect external additions of Cd, not biological processes. I find no evidence that pelagic precipitation of CdS occurred during this interval. More work will be needed in the modern (Chapter 3) to determine whether remineralization could have played a role in modulating sedimentary Cd isotope compositions.

In Chapter 5, I move to Fe, which is an important micronutrient that limits the efficiency of the biological pump in many ocean regions. While Fe concentrations and isotopes can be used to distinguish between sources of Fe to modern seawater, reconstructing Fe sources in the past is more challenging as multiple processes affect to the Fe chemistry of the sediment. To address this, I coupled Fe isotopes and statistical analysis to unmix sources to the hydrogenous fraction of sediments. In order to explore the sources of Fe over the Cenozoic, I first date the pelagic clays using Os chronostratigraphy. Next, I measure Fe isotopes, and finally, I use Q-mode factor analysis on 9 elemental concentrations of the hydrogenous fraction of the sediment. I find that five sources contribute to the hydrogenous sediment: dust, a processed ligand-bound background, two types of hydrothermal, and volcanic ash. Our study suggests that it is important to examine each of these sources to fully understand how Fe is sourced in the South Pacific and the Southern Ocean. When some of our samples were near spreading ridges the majority of the Fe came from hydrothermal sources. Thus, future work should explore how hydrothermal fluids are advected. These studies should, in turn, be used to estimate when and where the hydrothermal fluid may be upwelled into surface waters and used for metabolic processes.

Although most of my dissertation was focused on marine sediments, I had the opportunity to go to sea to collect samples as well. Working with seawater and sediment samples has broadened my understanding of how complex ocean systems are and has underscored the need for the community to connect these two fields. Of course, because of the complexities in the marine and sediment environments, it is easy to see how one could spend a career in one corner of the seafloor or even a cubic meter of seawater. But seawater and sediment *are still interconnected*. We do a disservice to the oceanographic community by not striving to integrate these fields. I look forward to developing my seawater and biological toolbox in my next steps. I hope to use the geochemical

tools and statistics on sediments and seawater I learned here to make inferences about the natural world, past and present, and begin to span the dissolved–particulate divide.

Supplemental Tables and Figures

Supplemental Figure 1 (Chapter 2)

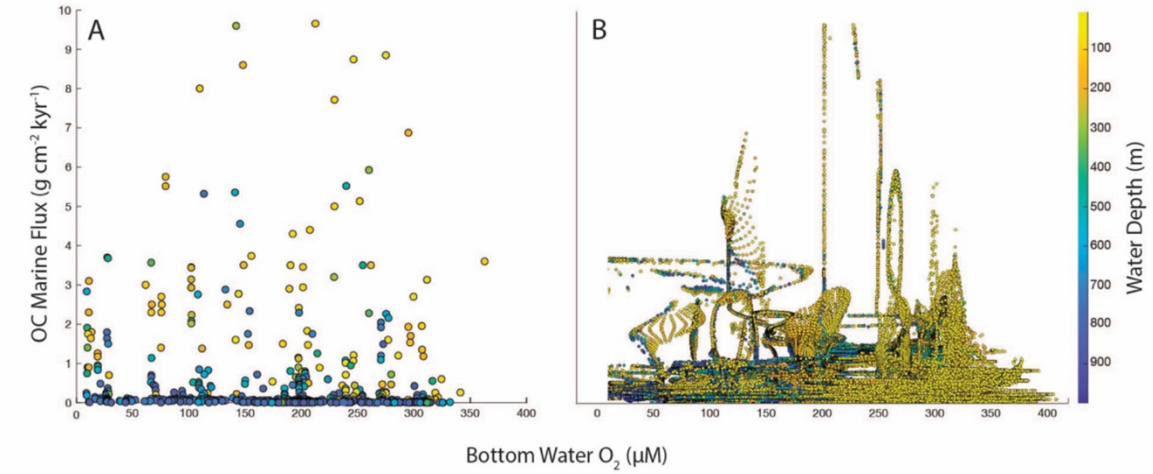

Fig. S1. (A) The raw flux data plotted against the bottom water O_2 concentration extrapolated from the WOA 18 and colored by water depth. (B) the interpolated flux data versus bottom water oxygen concentration and depth

Supplemental Table 1: Chapter 4

Height (m)	δ^{114}Cd (‰)	error	[Cd] µg g^{-1}
111	-0.08	0.03	0.37
113.46	-0.05	0.03	0.38
118.13	-0.13	0.03	0.42
121.39	-0.15	0.03	0.39
125.25	-0.07	0.03	1.15
127.25	-0.15	0.03	0.45
128.17	-0.31	0.03	0.59
130.76	-0.08	0.03	0.45
132.13	-0.24	0.03	1.06
133.97	-0.2	0.03	1.7
135.58	-0.15	0.03	1.35
137.31	-0.1	0.03	2.93
138.38	-0.12	0.03	2.22
138.74	-0.07	0.03	4.28
139.97	-0.16	0.03	4.03
140.95	-0.05	0.03	4.25
141.47	-0.17	0.03	6.3
142.41	-0.13	0.03	4.35
143.45	-0.18	0.03	8.21
144.36	-0.19	0.03	5.39
145.16	-0.07	0.03	3.04
145.61	-0.08	0.03	4.19
146.45	-0.16	0.03	2.97
147.3	-0.08	0.03	2.36
147.64	-0.07	0.03	1.79
148.27	-0.1	0.03	1.72
149.3	-0.14	0.03	2.77
150.24	-0.02	0.03	1.43
152.43	-0.09	0.03	0.82
153.18	-0.1	0.03	0.91
154.43	-0.26	0.03	0.68
170.39	-0.16	0.03	0.27
173.09	-0.14	0.03	0.54
173.5	-0.17	0.03	0.83
173.73	-0.12	0.03	0.49
174.67	-0.11	0.03	0.72
175.51	-0.05	0.03	0.6

eight (m)	δ^{114}Cd (‰)	error	[Cd] µg g^{-1}
177.1	0.03	0.03	2.18
178.61	-0.05	0.03	0.3
179.05	-0.03	0.03	1.03
180.33	0.01	0.03	0.6
182.5	-0.09	0.03	0.63
183.65	-0.05	0.03	0.45
185.43	-0.09	0.03	0.35
187.46	-0.11	0.03	0.52
188.01	-0.09	0.03	0.38
188.87	-0.14	0.03	0.44
189.39	-0.16	0.03	0.41

Chapter 5 Supplemental

Supplemental Table 1: Multi-elemental concentrations used in QFA

Supplemental Table 2: Os and Fe isotope raw data

Exp	Site	Hole	Core	Type	Sect.	Top	Bot	osmium (myr)	C0Age (Ma)	Al	Ti	Fe	Mn	Ca	Mg	P.	Li	Sc	V.	Cr	Co
329	U1366	F	1	H	1	20	22	-2.555	**0**	0.87	0.04	1.22	0.24	0.41	0.55	0.07	6.35	4.46	12.04	2.20	24.80
329	U1366	D	1	H	1	30	40	-0.324	2.47	1.07	0.03	1.39	0.16	0.52	0.61	0.13	9.15		11.16	3.46	27.52
329	U1366	D	1	H	1	130	140	2.868	6.16	0.99	0.02	1.36	0.15	0.54	0.60	0.13	9.00		10.91	3.40	25.85
329	U1366	F	1	H	2	110	112	5.795	7.95	0.60	0.02	0.95	0.12	0.45	0.42	0.11	10.30	4.59	15.51	2.13	18.71
329	U1366	D	1	H	2	80	90	6.326	9.73	0.94	0.02	1.33	0.11	0.58	0.56	0.17	8.77		12.65	3.37	18.99
330	U1366	F	1	H	3	60	70	9.605	12.70	1.01	0.02	1.32	0.10	0.63	0.55	0.19	8.92		12.54	2.97	17.51
329	U1366	D	1	H	3	30	40	9.978	13.05	0.98	0.02	1.36	0.10	0.66	0.58	0.20	9.04		12.33	3.14	19.29
329	U1366	F	1	H	3	100	102	10.948	6.53	0.67	0.02	0.94	0.09	0.39	0.42	0.08	10.70	4.93	10.07	1.71	12.88
329	U1366	D	1	H	3	130	140	13.681	16.32	1.09	0.02	1.21	0.09	0.62	0.56	0.18	8.40		12.12	2.91	18.20
329	U1366	F	1	H	4	55	57	14.805	16.88	0.82	0.02	0.85	0.09	0.50	0.46	0.12	5.58	6.24	13.28	1.52	14.48
329	U1366	F	1	H	4	70	72	15.367	17.44	0.74	0.01	0.83	0.09	0.41	0.40	0.09	9.36	4.85	10.17	1.57	14.89
329	U1366	D	1	H	4	30	40	15.565	18.00	0.86	0.01	0.92	0.06	0.48	0.41	0.12	6.91		9.57	1.85	13.78
329	U1366	F	1	H	4	80	82	15.763	18.01	0.73	0.01	0.83	0.10	0.41	0.37	0.09	9.20	4.95	10.51	1.56	15.85
329	U1366	D	1	H	4	55	57	16.553	18.01	0.72	0.01	0.82	0.08	0.41	0.38	0.09	8.00	4.96	9.80	1.52	13.86
329	U1366	D	1	H	4	78	80	17.51	18.02	1.04	0.02	0.90	0.10	0.54	0.48	0.13	5.54	7.19	14.70	1.48	14.18
329	U1366	D	1	H	4	80	90	17.597	19.72	1.43	0.02	1.28	0.09	0.65	0.55	0.20	7.75		13.86	2.44	17.27
329	U1366	D	1	H	4	95	97	18.245	19.71	1.01	0.02	0.85	0.10	0.52	0.44	0.13	4.84	6.86	14.68	1.23	14.07
329	U1366	D	1	H	4	115	117	19.146	19.70	1.03	0.01	0.91	0.09	0.47	0.41	0.11	7.89	5.94	11.94	1.42	13.32
329	U1366	D	1	H	4	130	140	19.869	21.32	1.39	0.02	1.02	0.06	0.58	0.43	0.15	6.72		12.96	1.66	12.10
329	U1366	D	1	H	5	5	7	20.628	21.32	1.30	0.01	0.87	0.11	0.94	0.54	0.27	7.76	5.80	15.19	2.13	21.19
329	U1366	D	1	H	5	20	22	21.466	21.33	1.01	0.01	0.69	0.10	0.72	0.40	0.19	9.09	4.38	12.19	1.63	17.26
329	U1366	D	1	H	5	35	37	22.278	21.33	1.29	0.01	0.68	0.08	0.83	0.45	0.23	5.38	5.16	13.76	1.48	15.00
329	U1366	D	1	H	5	30	40	22.544	22.99	1.69	0.02	1.24	0.08	0.63	0.52	0.19	6.99		14.44	1.84	15.63
329	U1366	D	1	H	5	80	90	24.88	24.79	1.57	0.02	1.07	0.06	0.56	0.44	0.14	6.47		14.34	1.46	12.17
329	U1366	D	1	H	5	130	140	27.151	26.57	2.34	0.02	1.26	0.07	0.63	0.52	0.18	6.38		17.01	1.52	13.98
329	U1366	F	2	H	1	55	57	28.04	26.58	1.42	0.02	0.90	0.10	0.43	0.38	0.09	7.30	6.29	14.72	1.07	13.83
329	U1366	F	2	H	1	75	77	28.576	26.58	1.84	0.02	1.06	0.10	0.61	0.48	0.14	10.96	7.53	15.98	1.31	16.29
329	U1366	F	2	H	1	95	97	29.066	26.59	1.43	0.01	0.81	0.10	0.50	0.36	0.12	7.67	6.04	12.71	1.11	13.33
329	U1366	D	1	H	6	80	90	29.874	30.62	1.81	0.01	1.10	0.10	1.29	0.58	0.48	8.23		16.04	2.82	23.41
329	U1366	F	2	H	2	5	7	30.235	31.72	0.51	0.01	0.93	0.16	1.03	0.52	0.30	6.66	6.70	19.40	2.64	24.20
329	U1366	D	1	H	7	10	20	31.182	32.81	1.27	0.01	0.77	0.06	0.85	0.41	0.27	6.96		11.34	1.92	15.09
329	U1366	F	2	H	2	50	60	31.513	33.22	0.75	0.01	1.20	0.11	1.31	0.65	0.47	10.28		19.11	3.91	24.61
329	U1366	F	2	H	2	95	97	33.223	34.57	0.48	0.01	0.80	0.13	1.21	0.51	0.37	6.94	6.96	18.21	2.07	23.60
329	U1366	D	2	H	1	15	17	34.418	35.92	0.45	0.01	0.83	0.14	1.16	0.53	0.33	6.81	6.99	17.35	2.04	27.48
329	U1366	D	2	H	1	30	40	35.239	37.27	0.73	0.01	1.19	0.11	1.52	0.64	0.55	10.41		16.24	3.65	31.13
329	U1366	F	2	H	2	135	137	35.512	38.28	0.47	0.01	0.85	0.17	1.42	0.51	0.42	7.34	8.06	20.00	2.18	30.88
329	U1366	D	2	H	1	55	57	36.532	39.29	0.43	0.01	0.90	0.13	1.17	0.48	0.33	12.02	6.54	14.37	2.50	30.81
329	U1366	D	2	H	1	80	90	37.769	40.30	0.58	0.01	0.95	0.09	1.41	0.51	0.48	9.60		13.33	2.77	26.45
329	U1366	D	2	H	1	105	107	38.99	42.02	0.58	0.01	0.94	0.17	1.87	0.59	0.57	7.88	9.85	19.31	2.05	36.48
329	U1366	D	2	H	1	130	140	40.194	43.74	0.82	0.01	1.57	0.11	2.34	0.70	0.84	11.17		19.24	2.86	30.41
329	U1366	D	2	H	2	5	7	41.387	45.80	0.63	0.01	1.51	0.17	1.99	0.63	0.57	9.93	9.95	24.00	2.16	35.16
329	U1366	D	2	H	2	55	57	43.719	47.86	0.50	0.01	1.31	0.12	1.69	0.52	0.44	11.30	8.86	24.78	1.53	22.03
329	U1366	F	2	H	4	15	17	44.156	49.91	0.54	0.01	1.22	0.13	1.89	0.62	0.52	5.58	10.33	35.28	1.22	17.68
329	U1366	D	2	H	2	80	90	45.002	50.25	0.76	0.00	1.84	0.09	2.29	0.71	0.76	7.00		33.79	1.67	17.82
329	U1366	F	2	H	4	50	60	46.094	51.26	0.82	0.00	2.07	0.10	2.42	0.73	0.78	7.02		40.70	1.60	17.47
329	U1366	D	2	H	2	105	107	46.364	51.77	0.50	0.00	1.31	0.11	1.71	0.64	0.44	4.97	8.96	37.85	0.92	15.14
329	U1366	F	2	H	4	75	77	47.318	52.28	0.60	0.00	1.71	0.15	1.75	0.67	0.44	6.16	8.76	45.38	1.06	21.32
329	U1366	D	2	H	2	130	140	47.562	52.79	0.61	0.00	1.78	0.09	1.73	0.62	0.47	5.70		42.17	1.05	15.67
329	U1366	F	2	H	4	95	97	48.292	53.68	0.43	0.00	1.43	0.14	1.30	0.51	0.30	7.22	6.54	38.51	0.81	19.34
329	U1366	D	2	H	3	5	7	48.802	54.57	0.48	0.00	1.39	0.17	1.87	0.61	0.47	4.31	10.05	55.57	0.83	19.31
329	U1366	D	2	H	3	30	40	50.085	55.46	0.74	0.00	2.06	0.12	2.75	0.73	0.87	5.50		62.52	1.18	17.08
329	U1366	F	2	H	4	135	137	50.343	56.81	0.49	0.00	1.37	0.14	2.30	0.64	0.61	4.23	11.74	62.45	0.82	15.68
329	U1366	D	2	H	3	55	57	51.42	58.16	0.51	0.00	1.68	0.17	2.36	0.62	0.64	4.66	11.65	68.27	0.84	21.51
329	U1366	F	2	H	5	45	47	53.094	59.51	0.45	0.00	1.41	0.12	2.69	0.55	0.76	6.22	13.87	63.11	0.79	15.92
329	U1366	D	2	H	3	105	107	53.535	60.86	0.40	0.00	1.38	0.11	2.60	0.54	0.69	5.38	13.12	57.94	0.70	14.07
329	U1366	D	2	H	3	130	140	54.717	62.21	0.75	0.00	1.45	0.09	4.54	0.69	1.85	5.83		62.16	1.46	16.74
329	U1366	F	2	H	5	80	90	54.717	62.21	1.02	0.00	0.34	0.05	4.27	0.45	1.84	7.96		36.70	0.55	8.16
329	U1366	D	2	H	4	28	30	57.081	64.59	1.18	0.00	0.35	0.11	5.10	0.56	2.00	7.05	39.03	47.18	0.55	12.92
331	U1366	F	2	H	6	0	10	57.884	66.97	0.77	0.00	0.34	0.07	3.30	0.46	1.46	7.70		46.54	0.74	8.68
329	U1366	D	2	H	4	80	90	58.968	68.81	1.50	0.00	0.25	0.08	3.40	0.53	1.59	7.28		39.80	0.65	10.57

Exp	Site	Hole	Core	Type	Sect.	Top	Bot	osmium (myr)	C0Age (Ma)	Al	Ti	Fe	Mn	Ca	Mg	P.	Li	Sc	V.	Cr	Co
329	U1366	F	2	H	6	35	37	59.149	69.44	0.51	0.00	0.50	0.13	2.85	0.57	1.01	8.38	24.59	74.36	0.41	10.04
329	U1366	D	2	H	4	105	107	60.171	70.07	0.71	0.00	0.30	0.09	3.28	0.48	1.26	6.07	27.98	45.11	0.55	9.18
329	U1366	F	2	H	6	55	57	60.171	70.70	0.45	0.00	0.60	0.26	2.21	0.62	0.75	9.66	15.29	100.11	0.27	13.89
329	U1366	D	2	H	4	125	127	61.185	71.33	0.52	0.00	0.31	0.08	2.80	0.39	1.03	9.14	24.08	35.44	0.59	9.44
329	U1366	D	2	H	4	130	140	61.5	71.96	0.84	0.00	0.46	0.07	4.11	0.56	1.90	7.72		48.66	0.73	7.51
329	U1366	F	3	H	1	30	40	64.873	74.85	0.31	0.00	0.99	0.05	1.32	0.33	0.41	2.73		31.81	0.58	7.71
329	U1366	F	3	H	1	40	42	65.298	76.29	0.46	0.00	1.37	0.15	1.48	0.55	0.37	8.00	7.37	36.57	1.12	18.75
329	U1366	F	3	H	1	80	90	65.793	77.72	0.64	0.00	1.65	0.10	3.13	0.59	1.08	5.87		62.75	1.13	13.59
329	U1366	F	3	H	1	95	97	65.961	78.27	0.72	0.00	0.45	0.18	2.78	0.54	0.98	6.62	19.79	59.29	0.39	14.84
329	U1366	F	3	H	1	105	107	66.192	78.81	0.59	0.00	0.45	0.13	1.93	0.52	0.64	11.90	10.98	49.21	0.38	12.33
329	U1366	F	3	H	1	130	140	66.324	79.36	0.19	0.00	0.40	0.08	0.54	0.22	0.17	2.01		48.33	0.09	4.25
329	U1366	F	3	H	1	125	127	66.368	79.49	0.15	0.00	0.35	0.14	0.52	0.22	0.14	1.90	2.81	45.57	0.06	5.75
329	U1366	F	3	H	2	20	22	66.517	79.63	0.31	0.00	0.67	0.25	1.19	0.59	0.29	3.12	3.17	149.64	0.05	7.69
329	U1366	F	3	H	2	30	40	66.588	79.76	0.41	0.00	0.75	0.13	1.22	0.59	0.38	4.81		99.11	0.06	7.09
329	U1366	F	3	H	2	45	47	66.653	79.97	0.33	0.00	0.58	0.20	1.29	0.58	0.40	8.79	4.09	49.62	0.15	9.43
329	U1366	F	3	H	2	65	67	66.714	80.18	0.19	0.00	0.51	0.27	0.93	0.34	0.24	2.32	3.32	67.74	0.08	7.64
329	U1366	F	3	H	2	80	90	66.758	80.39	0.41	0.00	0.57	0.12	1.90	0.57	0.74	8.16		54.99	0.17	7.90
329	U1366	F	3	H	2	90	92	66.869	80.84	0.31	0.00	0.56	0.17	1.36	0.52	0.40	7.72	4.64	53.25	0.14	7.96
329	U1366	F	3	H	2	98	100	66.895	81.28	0.28	0.00	0.40	0.23	1.68	0.52	0.58	5.48	6.41	44.86	0.14	9.85
329	U1366	F	3	H	3	30	40	67.373	81.73	0.31	0.00	0.61	0.13	1.16	0.43	0.39	6.40		46.11	0.15	7.89
329	U1366	F	3	H	3	130	140	69.65	82.75	0.28	0.00	1.12	0.13	1.41	0.68	0.25	7.25		62.89	0.06	4.51
329	U1366	F	3	H	4	80	90	71.95	83.39	0.33	0.00	1.26	0.15	0.85	1.02	0.07	0.10		40.28	0.06	4.17
329	U1366	F	3	H	5	30	40	74.26	83.99	0.28	0.00	1.46	0.21	1.31	0.95	0.08	0.06		56.58	0.06	6.91
329	U1366	F	3	H	5	130	140	76.56	84.83	0.27	0.00	1.57	0.21	1.43	0.97	0.09	0.09		24.90	0.09	7.26
329	U1366	F	3	H	6	80	90	78.87	85.95	0.50	0.00	0.86	0.14	1.10	0.78	0.23	0.36		20.40	0.08	29.74
329	U1366	F	3	H	7	20	30	81.17	87.10	0.19	0.00	0.69	0.13	1.59	0.38	0.43	0.06		25.68	0.09	6.24
329	U1366	F	4	H	1	80	90	83.48	88.44	0.20	0.00	0.84	0.18	1.55	0.47	0.37	0.06		42.50	0.18	8.18
329	U1366	F	4	H	2	30	40	85.78	89.49	0.24	0.00	1.18	0.18	1.87	0.75	0.15	0.03		53.61	0.04	6.90
329	U1366	F	4	H	2	120	130	88.09	90.30	0.24	0.00	1.25	0.20	1.58	0.73	0.07	0.03		53.70	0.05	6.93
329	U1366	F	4	H	3	80	90	90.39	91.15	0.25	0.00	1.44	0.27	1.34	0.83	0.04	0.04		66.57	0.04	7.85
329	U1366	F	4	H	4	10	20	92.69	91.78	0.28	0.00	1.19	0.18	0.93	0.56	0.07	0.02		65.40	0.04	15.83

Exp	Site	Hole	Core	Type	Sect.	Top	Bot	osmium (myr)	C0Age (Ma)	Ni	Cu	Zn	Sr	Y.	Mo	Ba	La	Ce	Pr	Nd	Sm
329	U1366	F	1	H	1	20	22	-2.555	0	95.54	133.33	43.74	96.54	58.76	0.00	90.55	36.89	90.92	11.95	48.95	10.62
329	U1366	D	1	H	1	30	40	-0.324	2.47	104.66	156.88	64.47	101.47	59.00	0.15	121.84	33.68	64.02		46.27	11.47
329	U1366	D	1	H	1	130	140	2.868	6.16	113.35	168.63	66.46	101.54	62.28	0.23	84.52	35.97	64.83		49.91	12.40
329	U1366	F	1	H	2	110	112	5.795	7.95	90.96	123.58	40.18	69.05	66.76	0.00	42.19	38.50	65.32	12.57	50.34	11.35
329	U1366	D	1	H	2	80	90	6.326	9.73	85.32	125.68	60.91	97.12	67.29	0.30	66.03	38.49	64.47		54.03	13.57
330	U1366	F	1	H	3	60	70	9.605	12.70	94.05	123.77	61.50	102.85	75.70	0.23	68.17	43.10	63.89		60.15	15.00
329	U1366	D	1	H	3	30	40	9.978	13.05	92.66	123.40	64.28	108.67	80.38	0.25	73.11	47.75	67.99		65.06	16.00
329	U1366	F	1	H	3	100	102	10.948	6.53	58.87	79.85	37.80	68.83	53.23	0.00	47.66	34.76	54.07	10.99	42.52	9.67
329	U1366	D	1	H	3	130	140	13.681	16.32	78.30	100.95	57.25	98.38	65.91	0.24	65.90	39.27	58.77		52.11	12.80
329	U1366	F	1	H	4	55	57	14.805	16.88	55.52	69.35	34.63	87.00	73.39	0.72	65.41	45.46	71.11	14.30	57.95	12.31
329	U1366	F	1	H	4	70	72	15.367	17.44	60.30	67.17	33.41	69.82	54.93	0.00	47.55	35.09	57.61	10.97	42.93	9.85
329	U1366	D	1	H	4	30	40	15.565	18.00	60.25	81.60	41.94	92.31	55.85	0.21	63.46	34.50	51.59		49.13	11.80
329	U1366	F	1	H	4	80	82	15.763	18.01	60.52	67.37	33.72	68.81	55.12	0.00	47.00	34.46	55.24	10.47	41.74	9.57
329	U1366	D	1	H	4	55	57	16.553	18.01	57.74	68.44	33.65	70.49	54.43	0.00	48.65	34.57	56.49	10.25	42.31	9.78
329	U1366	D	1	H	4	78	80	17.51	18.02	53.49	68.24	35.94	94.55	82.54	0.72	75.38	49.96	72.11	15.62	63.28	13.46
329	U1366	D	1	H	4	80	90	17.597	19.72	72.96	98.39	58.50	105.13	70.96	0.32	79.53	41.00	58.11		53.78	13.13
329	U1366	D	1	H	4	95	97	18.245	19.71	54.70	66.06	33.97	88.90	78.89	0.55	72.28	46.51	68.70	14.36	58.20	12.34
329	U1366	D	1	H	4	115	117	19.146	19.70	56.23	66.51	35.58	77.37	64.40	0.00	55.89	37.85	57.18	11.73	45.53	10.50
329	U1366	D	1	H	4	130	140	19.869	21.32	54.57	77.90	43.87	99.43	65.23	0.24	78.67	37.88	51.31		53.68	12.95
329	U1366	D	1	H	5	5	7	20.628	21.32	115.80	91.20	46.79	114.78	77.58	0.00	70.42	46.64	62.37	14.30	58.02	12.61
329	U1366	D	1	H	5	20	22	21.466	21.33	91.86	70.37	36.13	87.31	68.00	0.00	54.25	40.35	60.33	11.74	46.20	10.39
329	U1366	D	1	H	5	35	37	22.278	21.33	78.23	69.70	35.48	106.34	86.31	0.73	79.79	49.58	68.89	14.37	58.37	12.01
329	U1366	D	1	H	5	30	40	22.544	22.99	69.50	89.18	56.22	102.70	70.05	0.25	85.96	39.34	54.13		51.61	12.56
329	U1366	D	1	H	5	80	90	24.88	24.79	60.15	77.85	46.91	104.35	60.83	0.20	85.10	34.61	48.12		47.70	11.41
329	U1366	D	1	H	5	130	140	27.151	26.57	68.86	85.57	55.74	103.05	65.70	0.27	99.44	36.59	48.87		50.15	12.22
329	U1366	F	2	H	1	55	57	28.04	26.58	51.96	55.38	43.87	75.43	59.27	0.00	69.76	36.65	49.96	11.06	45.16	10.43
329	U1366	F	2	H	1	75	77	28.576	26.58	73.28	74.94	41.67	99.17	85.85	0.00	84.06	48.95	66.09	14.25	56.43	12.84
329	U1366	F	2	H	1	95	97	29.066	26.59	60.07	57.82	31.93	75.06	70.25	0.00	61.26	39.86	51.46	12.09	47.33	10.72
329	U1366	D	1	H	6	80	90	29.874	30.62	140.88	123.56	66.87	133.56	121.94	0.40	85.35	65.38	70.15		80.81	19.50
329	U1366	F	2	H	2	5	7	30.235	31.72	97.70	79.05	48.48	120.22	110.06	1.05	66.25	63.74	92.98	17.79	71.86	14.77
329	U1366	D	1	H	7	10	20	31.182	32.81	100.94	91.86	50.66	115.08	70.50	0.32	76.35	41.42	54.90		54.67	12.71
329	U1366	F	2	H	2	50	60	31.513	33.22	130.99	102.47	78.51	133.49	92.56	0.46	73.89	52.89	72.79		63.94	15.30
329	U1366	F	2	H	2	95	97	33.223	34.57	105.77	67.81	48.81	129.17	127.79	0.74	66.65	71.39	97.12	20.99	86.55	17.92
329	U1366	D	2	H	1	15	17	34.418	35.92	114.08	67.66	52.09	133.81	130.88	0.86	70.92	74.92	105.86	21.94	89.92	18.72
329	U1366	D	2	H	1	30	40	35.239	37.27	166.53	94.23	84.16	152.55	119.02	0.37	80.39	64.35	87.38		80.03	19.45
329	U1366	F	2	H	2	135	137	35.512	38.28	137.49	77.03	56.80	147.76	150.13	1.03	78.90	87.18	118.19	24.16	99.67	20.53
329	U1366	D	2	H	1	55	57	36.532	39.29	132.79	65.50	56.21	127.06	113.61	0.00	60.75	67.17	98.53	19.21	80.40	17.04
329	U1366	D	2	H	1	80	90	37.769	40.30	162.18	86.24	76.31	153.16	109.22	0.35	82.19	62.27	87.24		78.39	19.45
329	U1366	D	2	H	1	105	107	38.99	42.02	181.42	80.22	69.90	190.59	201.20	0.77	99.44	112.48	154.38	31.76	130.74	27.54
329	U1366	D	2	H	1	130	140	40.194	43.74	224.58	121.58	105.41	233.72	192.38	0.42	120.36	107.15	137.54		134.46	33.07
329	U1366	D	2	H	2	5	7	41.387	45.80	202.18	99.86	82.29	223.93	185.23	0.00	113.16	114.49	152.60	35.67	145.70	32.27
329	U1366	D	2	H	2	55	57	43.719	47.86	157.25	76.21	68.83	187.25	192.30	0.00	78.68	121.48	165.82	35.79	150.18	31.57
329	U1366	F	2	H	4	15	17	44.156	49.91	129.09	70.25	65.53	219.22	247.42	1.03	126.73	153.74	185.88	46.66	191.24	39.55
329	U1366	D	2	H	2	80	90	45.002	50.25	196.41	101.59	108.56	249.19	244.08	0.37	141.65	148.83	151.11		196.82	47.45
329	U1366	F	2	H	4	50	60	46.094	51.26	205.99	112.83	118.00	261.60	250.99	0.44	150.39	153.38	150.61		200.35	48.10
329	U1366	D	2	H	2	105	107	46.364	51.77	133.62	68.55	72.28	218.56	256.48	0.80	132.15	163.63	176.11	51.01	211.36	44.88
329	U1366	F	2	H	4	75	77	47.318	52.28	183.16	86.79	87.13	222.37	197.86	0.00	123.37	133.00	151.35	43.53	176.91	38.44
329	U1366	D	2	H	2	130	140	47.562	52.79	177.32	92.14	106.64	233.99	192.87	0.49	149.15	124.30	137.01		161.69	39.28
329	U1366	F	2	H	4	95	97	48.292	53.68	142.67	66.78	69.64	171.08	175.01	0.00	94.33	114.37	143.94	33.86	142.94	29.45
329	U1366	D	2	H	3	5	7	48.802	54.57	139.03	69.23	79.00	239.35	287.86	0.88	146.92	182.56	194.63	55.04	223.59	47.56
329	U1366	D	2	H	3	30	40	50.085	55.46	218.81	114.24	141.58	294.60	317.01	0.52	184.76	194.96	158.47		255.22	61.14
329	U1366	F	2	H	4	135	137	50.343	56.81	148.80	76.51	89.04	265.40	357.45	1.01	169.58	226.24	189.69	69.55	285.04	65.22
329	U1366	D	2	H	3	55	57	51.42	58.16	210.08	94.45	110.81	270.98	310.61	0.00	162.30	212.48	171.61	69.66	284.45	63.10
329	U1366	F	2	H	5	45	47	53.094	59.51	185.07	100.23	99.50	259.97	424.00	0.00	119.09	271.75	172.76	85.10	357.26	80.02
329	U1366	D	2	H	3	105	107	53.535	60.86	189.86	99.11	100.41	261.84	412.41	0.00	130.30	265.89	165.77	83.35	351.88	78.61
329	U1366	D	2	H	3	130	140	54.717	62.21	224.77	176.16	140.91	357.62	540.81	0.85	196.45	320.64	189.84		447.27	104.92
329	U1366	F	2	H	5	80	90	54.717	62.21	253.52	182.63	109.03	292.34	523.23	1.15	136.40	338.60	172.51		458.26	106.59
329	U1366	D	2	H	4	28	30	57.081	64.59	203.71	192.30	99.96	320.03	802.75	1.57	167.17	497.69	316.68	159.47	650.49	150.48
331	U1366	F	2	H	6	0	10	57.884	66.97	283.40	267.32	121.64	257.85	575.98	1.42	176.54	376.25	162.91		556.63	131.80
329	U1366	D	2	H	4	80	90	58.968	68.81	252.35	228.47	115.53	231.79	469.34	1.33	155.94	293.70	150.14		415.51	99.11

Exp	Site	Hole	Core	Type	Sect.	Top	Bot	osmium (myr)	C0Age (Ma)	Ni	Cu	Zn	Sr	Y.	Mo	Ba	La	Ce	Pr	Nd	Sm
329	U1366	F	2	H	6	35	37	59.149	69.44	162.52	224.19	93.04	246.18	626.22	1.69	212.69	414.95	189.39	138.43	573.15	133.94
329	U1366	D	2	H	4	105	107	60.171	70.07	166.81	214.39	89.18	247.31	722.90	1.37	161.53	469.06	212.57	158.98	660.79	155.96
329	U1366	F	2	H	6	55	57	60.171	70.70	158.36	211.16	84.24	219.39	413.21	1.46	197.41	281.57	136.04	92.47	383.42	89.00
329	U1366	D	2	H	4	125	127	61.185	71.33	219.29	230.08	80.78	211.99	604.16	1.28	121.81	408.65	186.20	135.32	579.36	132.64
329	U1366	D	2	H	4	130	140	61.5	71.96	263.60	322.36	129.08	293.63	674.54	1.50	168.88	418.30	153.19		608.36	142.96
329	U1366	F	3	H	1	30	40	64.873	74.85	109.07	58.08	69.53	148.55	164.49	0.27	89.59	103.38	75.93		138.27	33.81
329	U1366	F	3	H	1	40	42	65.298	76.29	146.39	70.34	118.54	172.91	195.10	0.00	90.93	127.17	145.25	38.91	164.03	34.12
329	U1366	F	3	H	1	80	90	65.793	77.72	221.62	143.18	141.24	322.24	440.30	0.62	179.31	288.77	164.63		396.57	95.91
329	U1366	F	3	H	1	95	97	65.961	78.27	152.97	163.94	89.55	226.28	508.82	1.33	178.44	327.44	190.28	109.33	447.77	104.47
329	U1366	F	3	H	1	105	107	66.192	78.81	158.67	175.80	98.94	170.50	296.10	0.98	128.98	198.37	114.10	63.46	268.74	61.52
329	U1366	F	3	H	1	130	140	66.324	79.36	31.15	91.20	37.79	104.34	50.52	0.54	226.01	39.63	17.08		54.59	12.19
329	U1366	F	3	H	1	125	127	66.368	79.49	30.72	80.95	44.44	124.86	52.28	0.00	247.45	44.02	18.86	13.69	55.62	11.66
329	U1366	F	3	H	2	20	22	66.517	79.63	53.91	155.15	48.84	187.63	128.65	1.26	212.48	102.67	47.75	31.84	129.01	26.09
329	U1366	F	3	H	2	30	40	66.588	79.76	58.58	188.55	55.17	171.95	98.29	1.29	241.63	78.70	38.31		104.92	24.65
329	U1366	F	3	H	2	45	47	66.653	79.97	49.82	139.75	44.05	128.59	124.94	1.06	119.89	87.77	49.57	26.54	110.83	22.48
329	U1366	F	3	H	2	65	67	66.714	80.18	70.45	167.85	54.27	190.91	96.28	0.63	285.85	75.55	29.99	23.66	96.53	19.46
329	U1366	F	3	H	2	80	90	66.758	80.39	73.99	229.42	75.97	187.89	171.00	1.10	223.19	122.29	68.84		174.80	42.74
329	U1366	F	3	H	2	90	92	66.869	80.84	66.14	176.36	55.51	144.29	136.35	0.98	187.77	98.97	60.13	31.58	133.07	27.64
329	U1366	F	3	H	2	98	100	66.895	81.28	52.39	173.57	52.17	152.43	192.32	0.87	169.55	131.53	93.51	43.74	179.03	37.35
329	U1366	F	3	H	3	30	40	67.373	81.73	46.57	150.42	74.16	177.58	116.19	0.58	479.77	93.15	38.57		134.58	32.54
329	U1366	F	3	H	3	130	140	69.65	82.75	98.86	246.73	143.83	343.33	140.95	0.69	283.60	159.70	17.93		177.23	39.24
329	U1366	F	3	H	4	80	90	71.95	83.39	73.79	170.31	97.31	423.52	69.36	0.36	196.74	80.92	13.99		94.78	20.69
329	U1366	F	3	H	5	30	40	74.26	83.99	130.35	316.67	145.31	702.59	111.27	0.39	299.62	132.11	10.98		149.00	32.00
329	U1366	F	3	H	5	130	140	76.56	84.83	188.06	387.16	188.25	834.07	82.93	0.25	281.22	99.71	7.43		95.72	19.80
329	U1366	F	3	H	6	80	90	78.87	85.95	15.49	277.81	121.39	805.01	85.51	0.12	265.65	66.72	17.64		94.21	23.38
329	U1366	F	3	H	7	20	30	81.17	87.10	6.20	236.59	50.42	809.58	154.09	0.02	435.96	124.03	32.14		176.63	42.85
329	U1366	F	4	H	1	80	90	83.48	88.44	30.36	235.85	63.76	865.27	140.91	0.11	374.51	110.92	21.97		156.09	37.89
329	U1366	F	4	H	2	30	40	85.78	89.49	130.67	143.50	132.15	954.83	130.79	0.23	314.12	174.11	6.46		179.81	38.16
329	U1366	F	4	H	2	120	130	88.09	90.30	155.49	145.06	131.35	1010.87	110.70	0.17	415.30	150.09	8.49		170.27	37.54
329	U1366	F	4	H	3	80	90	90.39	91.15	277.06	198.02	112.85	983.50	95.38	0.20	409.63	113.61	8.93		145.11	32.86
329	U1366	F	4	H	4	10	20	92.69	91.78	47.46	183.07	61.83	1042.72	74.93	0.02	403.38	85.02	11.56		126.99	29.20

Exp	Site	Hole	Core	Type	Sect.	Top	Bot	osmium (myr)	C0Age (Ma)	Eu	Gd	Tb	Dy	Ho	Er	Yb	Pb	Th	U.	Tl	187/188Os	d56/54
329	U1366	F	1	H	1	20	22	-2.555	**0**	2.14	11.98	1.88	10.92	2.27	6.43	5.86	65.34	4.82	0.72	1.28	0.8188	-0.2044
329	U1366	D	1	H	1	30	40	-0.324	2.47		12.31		11.99		7.06	6.08	49.55	4.57	0.76	1.29	0.9500	-0.1714
329	U1366	D	1	H	1	130	140	2.868	6.16		13.26		12.93		7.52	6.59	52.00	4.03	0.81	1.34	0.9500	-0.1862
329	U1366	F	1	H	2	110	112	5.795	7.95	2.29	12.92	0.00	12.42	2.53	7.28	6.46	43.87	3.33	0.72	1.23	0.8809	-0.2340
329	U1366	D	1	H	2	80	90	6.326	9.73		14.32		13.97		8.10	7.00	43.88	4.23	0.83	1.39	0.8800	-0.2171
330	U1366	F	1	H	3	60	70	9.605	12.70		15.73		15.41		8.92	7.75	41.84	3.83	0.88	1.52	0.5100	-0.1804
329	U1366	D	1	H	3	30	40	9.978	13.05		17.17		16.86		9.88	8.65	45.11	4.18	0.99	1.45	0.8200	-0.1607
329	U1366	F	1	H	3	100	102	10.948	6.53	1.95	11.05	0.00	10.50	2.14	6.15	5.50	36.52	2.68	0.68	0.93	0.7231	-0.1303
329	U1366	D	1	H	3	130	140	13.681	16.32		13.73		13.29		7.71	6.65	38.75	3.32	0.90	1.02	0.8300	-0.1743
329	U1366	F	1	H	4	55	57	14.805	16.88	2.46	13.99	2.19	12.95	2.74	7.82	7.09	45.47	3.09	0.83	0.71	0.7800	-0.1555
329	U1366	F	1	H	4	70	72	15.367	17.44	1.98	11.18	0.00	10.56	2.14	6.14	5.47	36.07	2.58	0.69	0.74	0.8480	-0.1653
329	U1366	D	1	H	4	30	40	15.565	18.00		12.48		12.57		7.22	6.25	36.95	3.15	0.88	0.88		-0.1510
329	U1366	F	1	H	4	80	82	15.763	18.01	1.92	10.86	0.00	10.46	2.14	6.20	5.56	36.05	2.41	0.73	0.71	0.6460	-0.1565
329	U1366	D	1	H	4	55	57	16.553	18.01	1.96	10.96	0.00	10.61	2.17	6.25	5.58	37.66	2.59	0.72	0.85	0.8229	-0.1809
329	U1366	D	1	H	4	78	80	17.51	18.02	2.68	15.50	2.43	14.46	3.05	8.76	8.00	47.28	2.74	0.93	0.73	0.7380	-0.1755
329	U1366	D	1	H	4	80	90	17.597	19.72		14.33		14.01		8.24	7.09	40.23	2.81	0.95	0.79	0.7900	-0.1915
329	U1366	D	1	H	4	95	97	18.245	19.71	2.48	14.42	2.25	13.54	2.89	8.31	7.59	47.51	2.51	0.87	0.85	0.7703	-0.1291
329	U1366	D	1	H	4	115	117	19.146	19.70	2.14	12.18	0.00	11.77	2.40	6.96	6.21	37.73	2.22	0.78	0.73	0.7862	-0.2038
329	U1366	D	1	H	4	130	140	19.869	21.32		13.90		14.04		8.26	7.12	36.82	3.00	0.94	0.79		-0.1552
329	U1366	D	1	H	5	5	7	20.628	21.32	2.36	14.05	2.16	14.05	3.01	8.74	7.72	28.66	1.74	0.96	1.35	0.7200	-0.2243
329	U1366	D	1	H	5	20	22	21.466	21.33	2.09	12.10	0.00	11.75	2.48	7.26	6.54	25.97	1.62	0.86	1.21	0.7766	-0.1798
329	U1366	D	1	H	5	35	37	22.278	21.33	2.41	14.17	2.25	13.74	3.01	8.78	8.05	32.13	1.59	1.02	1.31	0.5793	-0.2061
329	U1366	D	1	H	5	30	40	22.544	22.99		13.85		13.74		8.16	7.06	40.06	2.37	0.93	0.88	0.7400	-0.1542
329	U1366	D	1	H	5	80	90	24.88	24.79		12.52		12.65		7.42	6.33	35.30	2.07	0.88	1.00		-0.1336
329	U1366	D	1	H	5	130	140	27.151	26.57		13.37		13.11		7.64	6.61	34.30	1.98	0.91	1.29	0.4300	-0.1265
329	U1366	F	2	H	1	55	57	28.04	26.58	2.14	12.17	0.00	11.67	2.37	6.83	5.99	34.44	1.78	0.75	0.93	0.6235	-0.1257
329	U1366	F	2	H	1	75	77	28.576	26.58	2.65	15.43	0.00	14.86	3.11	9.07	8.05	44.17	1.96	0.93	1.39	0.6523	-0.1445
329	U1366	F	2	H	1	95	97	29.066	26.59	2.21	12.85	0.00	12.40	2.59	7.55	6.69	33.15	1.66	0.73	1.14	0.4835	-0.1829
329	U1366	D	1	H	6	80	90	29.874	30.62		21.77		21.98		13.56	11.93	32.34	2.59	1.28	2.20		-0.1134
329	U1366	F	2	H	2	5	7	30.235	31.72	2.93	17.58	2.74	17.35	3.70	10.88	10.14	38.00	3.37	1.24	1.67	0.6833	-0.0520
329	U1366	D	1	H	7	10	20	31.182	32.81		14.02		14.35		8.72	7.49	26.57	1.76	1.07	1.49		-0.1163
329	U1366	F	2	H	2	50	60	31.513	33.22		17.07		16.75		10.20	8.65	30.12	3.21	1.30	1.59	0.5300	-0.1223
329	U1366	F	2	H	2	95	97	33.223	34.57	3.62	21.16	3.31	22.60	4.32	12.47	10.86	34.90	2.52	1.35	1.87	0.6218	-0.1275
329	U1366	D	2	H	1	15	17	34.418	35.92	3.78	22.27	3.44	23.57	4.59	13.07	11.08	37.90	2.65	1.30	1.91	0.3861	-0.1538
329	U1366	D	2	H	1	30	40	35.239	37.27		21.67		21.01		12.79	10.62	33.68	2.89	1.44	2.83	0.7700	-0.1122
329	U1366	F	2	H	2	135	137	35.512	38.28	4.17	24.88	3.84	26.52	5.25	15.29	12.95	41.42	2.75	1.58	2.74	0.5708	-0.1063
329	U1366	D	2	H	1	55	57	36.532	39.29	3.47	20.09	0.00	19.13	4.00	11.58	9.86	35.66	2.42	1.24	2.32	0.5419	-0.1358
329	U1366	D	2	H	1	80	90	37.769	40.30		21.15		20.77		12.39	10.18	31.17	2.50	1.45	2.51		-0.0849
329	U1366	D	2	H	1	105	107	38.99	42.02	5.60	37.92	5.15	35.29	7.68	21.98	16.51	45.60	2.58	1.91	3.32	0.4906	-0.0866
329	U1366	D	2	H	1	130	140	40.194	43.74		36.82		35.63		21.25	17.20	46.80	3.34	2.29	4.26	0.7000	-0.1367
329	U1366	D	2	H	2	5	7	41.387	45.80	6.19	36.65	5.53	37.64	7.99	22.55	17.02	52.02	3.00	2.14	3.11	0.4854	-0.0913
329	U1366	D	2	H	2	55	57	43.719	47.86	6.46	36.17	0.00	36.74	7.61	21.62	16.07	35.98	2.36	1.88	2.70	0.3494	-0.2093
329	U1366	F	2	H	4	15	17	44.156	49.91	8.12	51.47	7.90	46.23	9.79	27.55	20.16	38.14	2.58	2.32	2.56	0.4262	-0.2866
329	U1366	D	2	H	2	80	90	45.002	50.25		50.44		46.33		26.37	20.68	35.50	2.99	2.59	3.18	0.6500	-0.2718
329	U1366	F	2	H	4	50	60	46.094	51.26		50.52		46.71		26.47	20.90	35.92	2.72	2.83	3.40	0.4700	-0.2952
329	U1366	D	2	H	2	105	107	46.364	51.77	8.72	55.57	8.53	49.08	10.31	28.99	21.98	39.90	2.50	2.40	2.73	0.5337	-0.2478
329	U1366	F	2	H	4	75	77	47.318	52.28	7.23	43.38	6.26	40.82	8.44	23.65	17.25	36.91	2.19	2.33	2.61	0.5015	-0.3857
329	U1366	D	2	H	2	130	140	47.562	52.79		40.77		39.12		22.36	17.56	38.22	2.46	2.74	3.31		-0.3057
329	U1366	F	2	H	4	95	97	48.292	53.68	5.92	33.99	0.00	32.77	6.52	18.13	14.22	35.57	1.87	2.01	1.95	0.5434	-0.3753
329	U1366	D	2	H	3	5	7	48.802	54.57	9.54	58.84	9.00	52.43	11.06	31.01	25.84	42.78	2.56	2.65	2.19	0.5187	-0.3397
329	U1366	D	2	H	3	30	40	50.085	55.46		63.55		58.00		32.83	25.82	37.76	2.93	3.30	2.82	0.5200	-0.2736
329	U1366	F	2	H	4	135	137	50.343	56.81	13.15	74.62	11.42	65.87	14.01	39.34	31.63	41.73	2.69	3.08	2.45	0.4953	-0.2743
329	U1366	D	2	H	3	55	57	51.42	58.16	11.74	69.65	10.34	64.00	13.37	37.35	27.30	42.08	2.88	3.16	2.94	0.4611	-0.2881
329	U1366	F	2	H	5	45	47	53.094	59.51	16.29	90.02	0.00	79.50	16.29	45.89	35.60	32.29	3.00	3.11	2.93	0.4628	-0.2806
329	U1366	D	2	H	3	105	107	53.535	60.86	16.10	87.10	0.00	78.34	15.90	44.66	35.19	34.78	3.02	3.08	3.29	0.4853	-0.2033
329	U1366	D	2	H	3	130	140	54.717	62.21		111.03		99.44		56.15	43.14	21.16	4.76	3.28	3.18	0.7000	-0.1577
329	U1366	F	2	H	5	80	90	54.717	62.21		110.53		104.13		58.04	44.67	9.99	2.27	3.20	3.13	0.3400	0.0818
329	U1366	D	2	H	4	28	30	57.081	64.59	30.23	167.11	25.20	145.35	30.11	83.43	68.17	11.72	2.73	3.15	2.83	0.3306	0.0543
331	U1366	F	2	H	6	0	10	57.884	66.97		138.04		126.10		66.06	50.78	8.36	1.94	2.45	3.33	0.4200	0.0856
329	U1366	D	2	H	4	80	90	58.968	68.81		104.94		93.39		50.25	39.16	10.99	1.26	2.05	3.69	0.6100	0.1085

Exp	Site	Hole	Core	Type	Sect.	Top	Bot	osmium (myr)	C0Age (Ma)	Eu	Gd	Tb	Dy	Ho	Er	Yb	Pb	Th	U.	Tl	187/188Os	d56/54
329	U1366	F	2	H	6	35	37	59.149	69.44	27.52	151.90	23.08	132.17	26.87	73.33	60.22	7.87	1.63	2.36	3.08	0.4583	-0.0278
329	U1366	D	2	H	4	105	107	60.171	70.07	31.57	173.45	26.18	147.86	29.82	80.17	64.64	10.18	1.92	2.18	3.32	0.3376	0.0621
329	U1366	F	2	H	6	55	57	60.171	70.70	18.41	100.38	15.25	86.39	17.68	48.59	40.19	6.28	1.07	1.98	3.56	0.5064	-0.1498
329	U1366	D	2	H	4	125	127	61.185	71.33	27.47	149.63	0.00	129.25	25.33	68.99	55.16	6.97	1.91	1.98	2.99	0.4906	0.0399
329	U1366	D	2	H	4	130	140	61.5	71.96		152.24		136.60		73.64	57.84	6.97	1.89	2.54	3.37	0.4800	0.0706
329	U1366	F	3	H	1	30	40	64.873	74.85		33.64		31.50		17.73	14.14	19.21	1.54	1.82	1.54	0.3800	-0.3068
329	U1366	F	3	H	1	40	42	65.298	76.29	6.86	41.96	0.00	37.71	7.69	21.69	15.84	32.08	1.92	2.00	2.18	0.2850	-0.3990
329	U1366	F	3	H	1	80	90	65.793	77.72		95.32		89.04		50.08	39.33	32.22	3.85	3.91	3.41	0.4000	-0.2941
329	U1366	F	3	H	1	95	97	65.961	78.27	21.28	116.70	17.68	101.59	20.87	57.13	47.18	12.30	1.54	2.25	2.37	0.3861	-0.1297
329	U1366	F	3	H	1	105	107	66.192	78.81	12.11	68.18	0.00	59.51	11.73	32.35	25.23	6.76	0.85	1.47	2.82	0.3586	-0.1122
329	U1366	F	3	H	1	130	140	66.324	79.36		12.42		11.49		6.36	5.35	2.62	0.15	0.79	1.91	0.4400	-0.2737
329	U1366	F	3	H	1	125	127	66.368	79.49	2.27	12.26	1.81	11.15	2.29	6.40	5.51	4.52	0.23	0.83	2.47	0.5375	-0.2338
329	U1366	F	3	H	2	20	22	66.517	79.63	5.31	28.66	4.31	27.76	5.47	14.00	11.98	2.89	0.20	1.63	1.81	0.5477	
329	U1366	F	3	H	2	30	40	66.588	79.76		24.76		22.82		12.67	10.23	2.20	0.18	1.35	1.68	0.6300	-0.34
329	U1366	F	3	H	2	45	47	66.653	79.97	4.67	25.21	0.00	23.00	4.69	13.47	11.65	2.41	0.28	1.02	1.29	0.5148	
329	U1366	F	3	H	2	65	67	66.714	80.18	3.97	20.85	3.12	17.88	3.63	10.05	8.92	4.33	0.15	1.13	5.46	0.5335	-0.22
329	U1366	F	3	H	2	80	90	66.758	80.39		42.64		39.52		22.28	18.84	2.70	0.37	1.60	1.47	0.4500	-0.18
329	U1366	F	3	H	2	90	92	66.869	80.84	5.73	29.60	0.00	26.88	5.38	15.27	13.31	2.94	0.30	1.23	1.27	0.4696	
329	U1366	F	3	H	2	98	100	66.895	81.28	7.69	45.36	6.93	39.17	8.11	22.78	17.91	2.08	0.41	1.28	1.12	0.4910	-0.16
329	U1366	F	3	H	3	30	40	67.373	81.73		31.48		28.45		14.97	12.26	1.80	0.24	1.27	1.14	0.3200	-0.20
329	U1366	F	3	H	3	130	140	69.65	82.75		39.06		35.16		18.72	15.04	7.35	0.09	2.35	1.88	0.4300	-0.17
329	U1366	F	3	H	4	80	90	71.95	83.39		19.26		16.59		8.48	6.52	7.82	0.34	1.22	0.93		-0.18
329	U1366	F	3	H	5	30	40	74.26	83.99		30.59		26.86		14.11	11.10	8.23	0.07	2.91	1.07		-0.17
329	U1366	F	3	H	5	130	140	76.56	84.83		19.64		17.87		10.24	8.52	2.93	0.32	2.49	1.22		-0.31
329	U1366	F	3	H	6	80	90	78.87	85.95		23.56		21.57		11.27	8.75	4.81	0.60	1.89	0.34		-0.24
329	U1366	F	3	H	7	20	30	81.17	87.10		42.50		38.29		19.60	14.48	1.93	0.07	1.83	2.30		-0.01
329	U1366	F	4	H	1	80	90	83.48	88.44		37.96		34.22		17.88	13.44	1.23	0.10	2.57	2.28		-0.11
329	U1366	F	4	H	2	30	40	85.78	89.49		37.23		33.26		17.94	13.97	7.81	0.03	3.64	1.74		-0.02
329	U1366	F	4	H	2	120	130	88.09	90.30		34.97		30.14		15.47	11.85	9.68	0.04	3.64	1.52		-0.02
329	U1366	F	4	H	3	80	90	90.39	91.15		30.19		25.43		12.60	9.38	6.62	0.04	3.32	0.90		-0.13
329	U1366	F	4	H	4	10	20	92.69	91.78		26.04		21.62		10.45	7.78	1.28	0.07	3.01	0.05		-0.30

Exp	Site	Hole	Core	Type	Sect.	Top	Bot	osmium myr	C0Age (Ma)	Al	Ti	Fe	Mn	Ca	Mg	P.	Li	V.	Cr	Co	Ni	Cu	Zn	Sr
329	U1369	C	1	H	1	5	15	4.3	0.14	1.125	0.011	0.859	0.176	0.214	0.547	0.025	9.8	17.5	2.2	28.3	78.1	137.3	48.8	
329	U1369	C	1	H	1	40	50	7.92	0.66	1.300	0.009	0.746	0.100	0.204	0.546	0.025	10.1	13.4	1.8	17.8	70.6	132.9	39.0	81.7
329	U1369	C	1	H	1	140	150	15.66	2.64	1.733	0.009	0.728	0.090	0.255	0.544	0.040	10.3	11.3	1.4	17.5	84.2	157.0	42.4	82.7
329	U1369	C	1	H	2	90	100	18.21	5.08	2.177	0.008	0.683	0.085	0.305	0.528	0.065	9.7	16.3	1.6	15.4	81.1	149.6	40.4	96.1
329	U1369	C	1	H	2	140	150	19.24	6.22	2.389	0.008	0.640	0.079	0.360	0.517	0.085	9.5	13.5	1.4	14.3	64.8	107.8	35.7	93.8
329	U1369	C	1	H	3	40	50	20.22	7.12	2.063	0.006	0.584	0.067	0.335	0.571	0.077	12.6	16.5	1.4	11.2	84.1	111.4	39.5	102.7
329	U1369	C	1	H	3	90	100	21.19	7.96	1.013	0.004	0.527	0.085	0.399	0.644	0.100	12.8	19.9	1.7	12.5	94.3	83.8	43.2	89.0
329	U1369	C	1	H	3	140	150	21.79	8.92	1.121	0.004	0.458	0.086	0.400	0.596	0.103	13.1	20.7	1.5	12.7	103.6	80.6	43.9	94.7
329	U1369	C	1	H	4	122	132	22.87	12.06	2.984	0.008	0.612	0.061	0.622	0.463	0.210	8.7	15.0	1.2	10.4	83.3	126.2	38.9	91.5
329	U1369	C	2	H	1	140	150	24.14	18.48	2.413	0.007	0.618	0.068	0.821	0.427	0.277	6.9	12.6	1.6	14.9	106.1	109.6	37.0	117.3
329	U1369	C	2	H	2	140	150	25.28	25.59	2.037	0.007	0.734	0.069	1.004	0.469	0.353	8.2	16.9	2.4	14.5	98.0	104.8	43.1	149.7
329	U1369	C	2	H	3	140	150	26.52	31.26	2.743	0.005	0.572	0.061	0.939	0.397	0.339	6.9	15.6	1.9	10.7	68.1	86.3	34.6	165.0
329	U1369	C	2	H	4	140	150	27.88	36.27	3.441	0.005	0.528	0.074	1.018	0.406	0.368	6.6	17.0	1.4	11.2	117.2	109.6	39.0	140.2
329	U1369	C	2	H	5	90	100	28.51	39.83	3.339	0.005	0.499	0.074	1.386	0.452	0.520	7.4	20.5	1.5	10.9	111.2	115.1	41.2	163.2
329	U1369	C	2	H	6	40	50	29.09	44.01	4.088	0.006	0.498	0.062	1.528	0.390	0.581	6.0	23.6	1.2	10.9	104.4	107.2	39.8	182.9
329	U1369	C	2	H	6	140	150	29.67	50.29	4.065	0.006	0.518	0.063	2.030	0.368	0.810	6.5	25.4	1.1	12.0	145.2	117.7	57.8	191.6
329	U1369	C	2	H	7	35	45	29.98	53.67	4.073	0.006	0.542	0.064	2.025	0.392	0.798	7.1	25.3	1.3	11.9	162.2	130.6	59.7	238.3
329	U1369	C	2	H	7	69	79	30.23	56.14	3.961	0.006	0.524	0.064	1.693	0.381	0.660	6.7	24.5	1.2	12.0	142.1	124.6	54.1	239.0
																								213.4

Exp	Site	Hole	Core	Type	Sect.	Top	Bot	osmium myr	C0Age (Ma)	Y.	Mo	Ba	La	Ce	Nd	Sm	Gd	Dy	Er	Yb	Pb	Th	U.	Tl
329	U1369	C	1	H	1	5	15	4.3	0.14	13.4	0.2	227.3	12.1	78.5	15.1	3.8	3.6	3.3	1.8	1.6	24.1	3.4	0.4	1.0
329	U1369	C	1	H	1	40	50	7.92	0.66	14.9	0.2	316.8	12.4	77.5	15.8	4.0	3.9	3.6	1.9	1.8	23.6	6.1	0.4	0.8
329	U1369	C	1	H	1	140	150	15.66	2.64	27.7	0.2	350.7	20.3	83.0	28.9	7.5	7.2	6.6	3.5	3.0	30.5	5.2	0.4	0.8
329	U1369	C	1	H	2	90	100	18.21	5.08	36.1	0.3	266.7	23.8	72.4	32.9	8.5	8.3	7.9	4.4	3.8	26.8	3.8	0.5	0.7
329	U1369	C	1	H	2	140	150	19.24	6.22	47.8	0.3	339.5	28.8	68.8	40.7	10.4	10.4	10.1	5.7	5.0	25.8	3.3	0.5	0.7
329	U1369	C	1	H	3	40	50	20.22	7.12	40.7	0.3	290.1	24.5	66.8	36.1	9.3	9.1	8.7	4.9	4.4	19.7	3.5	0.4	0.7
329	U1369	C	1	H	3	90	100	21.19	7.96	48.9	0.6	342.0	30.2	63.0	40.0	10.1	10.0	9.7	5.5	4.9	18.6	3.4	0.5	0.8
329	U1369	C	1	H	3	140	150	21.79	8.92	44.4	0.6	339.5	27.2	64.9	37.8	9.7	9.6	9.2	5.2	4.7	18.4	3.1	0.5	1.1
329	U1369	C	1	H	4	122	132	22.87	12.06	78.2	0.3	385.1	45.8	59.8	64.9	16.5	16.6	15.8	8.8	7.6	19.0	2.7	0.8	0.7
329	U1369	C	2	H	1	140	150	24.14	18.48	99.6	0.2	195.4	59.0	77.0	80.0	19.9	19.8	18.9	10.9	9.5	19.0	2.4	0.9	1.0
329	U1369	C	2	H	2	140	150	25.28	25.59	105.8	0.3	170.3	59.1	77.6	76.2	18.5	19.2	18.7	11.3	9.8	18.9	2.5	1.1	0.7
329	U1369	C	2	H	3	140	150	26.52	31.26	79.6	0.3	290.8	44.2	62.2	56.5	13.7	14.0	13.8	8.4	7.5	13.3	2.1	1.0	0.4
329	U1369	C	2	H	4	140	150	27.88	36.27	94.8	0.3	270.5	53.7	60.1	68.9	16.8	17.3	16.8	10.3	9.1	16.5	1.5	1.1	1.2
329	U1369	C	2	H	5	90	100	28.51	39.83	114.3	0.5	271.9	63.3	62.3	80.8	19.7	20.3	19.9	12.1	10.4	14.9	1.6	1.4	0.7
329	U1369	C	2	H	6	40	50	29.09	44.01	136.3	0.4	202.9	71.6	66.9	92.1	22.3	23.3	22.8	14.0	12.0	14.3	1.7	1.5	0.6
329	U1369	C	2	H	6	140	150	29.67	50.29	194.6	0.5	185.8	105.3	87.4	132.6	32.7	34.1	33.2	19.7	16.3	16.6	2.1	1.8	1.2
329	U1369	C	2	H	7	35	45	29.98	53.67	190.0	0.4	188.2	100.7	84.6	126.1	31.5	32.8	31.7	19.1	15.8	17.2	1.8	1.8	1.2
329	U1369	C	2	H	7	69	79	30.23	56.14	154.7	0.5	151.4	83.1	77.5	104.7	26.0	26.9	26.1	15.7	13.1	17.6	1.7	1.6	0.8

Exp	Site	Hole	Core	Type	Sect.	Top	Bot	osmium myr	C0Age (Ma)	187/188Os	d56/54
329	U1369	C	1	H	1	5	15	4.3	0.14	0.9025	-0.24
329	U1369	C	1	H	1	40	50	7.92	0.66	0.817	-0.20
329	U1369	C	1	H	1	140	150	15.66	2.64	0.7078	-0.14
329	U1369	C	1	H	2	90	100	18.21	5.08	0.7219	-0.21
329	U1369	C	1	H	2	140	150	19.24	6.22	0.7219	-0.18
329	U1369	C	1	H	3	40	50	20.22	7.12	0.7057	-0.06
329	U1369	C	1	H	3	90	100	21.19	7.96	0.7027	-0.06
329	U1369	C	1	H	3	140	150	21.79	8.92	0.6623	-0.02
329	U1369	C	1	H	4	122	132	22.87	12.06	0.7527	-0.10
329	U1369	C	2	H	1	140	150	24.14	18.48	0.7594	-0.16
329	U1369	C	2	H	2	140	150	25.28	25.59	0.7047	-0.15
329	U1369	C	2	H	3	140	150	26.52	31.26	0.7706	-0.10
329	U1369	C	2	H	4	140	150	27.88	36.27	0.5877	-0.21
329	U1369	C	2	H	5	90	100	28.51	39.83	0.7968	-0.10
329	U1369	C	2	H	6	40	50	29.09	44.01	0.7859	-0.06
329	U1369	C	2	H	6	140	150	29.67	50.29	0.5946	-0.07
329	U1369	C	2	H	7	35	45	29.98	53.67	0.6582	-0.03
329	U1369	C	2	H	7	69	79	30.23	56.14	0.6658	-0.09

Exp	Site	Hole	Core	Type	Sect.	Top	Bot	osmium (myr)	C0Age (Ma)	Al	Ti	Fe	Mn	Ca	Mg	P.	Li	V.	Cr	Co	Ni	Cu	Zn	Sr
329	U1370	E	1	H	1	5	15	0.798	0.05	0.72849	0.01469	1.02533	0.32030	0.20957	0.48332	0.02409	9.8	19.3	3.1	37.8	80.9	115.0	54.4	55.0
329	U1370	E	1	H	1	42.5	52.5	1.152	0.24	0.68164	0.01203	0.90139	0.23698	0.18960	0.46305	0.02054	10.1	15.3	2.6	27.3	63.2	101.6	48.0	50.1
329	U1370	E	1	H	1	140	150	1.989	0.71	0.67982	0.01062	0.69995	0.13035	0.17723	0.48616	0.01543	10.2	10.5	2.0	16.4	56.4	81.4	42.1	49.2
329	U1370	E	1	H	3	40	50	3.612	1.73	0.63236	0.00844	0.67794	0.09356	0.16140	0.48237	0.01386	10.6	11.0	2.1	16.0	48.7	92.6	42.2	44.4
329	U1370	E	2	H	1	140	150	7.493	3.75	0.42660	0.00331	0.48050	0.05511	0.18110	0.46642	0.02724	9.5	16.2	2.0	9.1	35.6	45.3	32.9	37.6
329	U1370	E	2	H	2	140	150	8.815	4.28	0.42714	0.00389	0.54106	0.06114	0.19945	0.51187	0.03446	10.1	19.1	2.3	10.7	45.3	44.6	37.7	40.2
329	U1370	E	2	H	4	140	150	11.462	5.82	0.76478	0.00353	0.46185	0.04806	0.30515	0.38938	0.08337	7.7	18.5	1.6	8.3	31.6	45.5	30.7	50.1
329	U1370	E	2	H	6	113	123	13.854	7.70	1.07379	0.00382	0.49154	0.04701	0.33870	0.36888	0.10078	7.3	17.4	1.7	8.6	32.4	56.7	34.7	56.5
329	U1370	E	3	H	1	140	150	15.815	9.16	0.50128	0.00289	0.52985	0.07190	0.53427	0.48942	0.17560	8.9	25.9	2.9	8.3	44.3	47.6	46.8	71.0
329	U1370	E	3	H	2	140	150	17.108	9.87	0.46813	0.00413	0.50198	0.07973	0.56996	0.51223	0.19075	8.9	24.7	3.0	9.6	48.1	45.8	45.9	71.0
329	U1370	E	3	H	3	140	150	18.308	10.63	0.71807	0.00648	0.62825	0.11858	0.62250	0.52138	0.19591	9.2	32.0	3.3	14.5	47.5	53.9	47.6	76.9
329	U1370	E	3	H	4	140	150	19.419	11.29	0.60035	0.00389	0.51582	0.08005	0.50747	0.49724	0.14971	7.9	27.5	2.6	10.0	37.2	37.7	39.3	68.5
329	U1370	E	3	H	5	140	150	20.52	11.87	0.51703	0.00302	0.48247	0.07183	0.46471	0.48815	0.13988	8.1	24.5	2.5	8.5	46.0	35.4	39.3	63.8
329	U1370	E	4	H	1	140	150	22.611	13.19	0.47863	0.00329	0.48997	0.07402	0.45662	0.46660	0.13701	7.4	27.7	2.5	9.1	34.0	34.0	37.9	62.9
329	U1370	E	4	H	5	140	150	25.671	16.82	0.47042	0.00253	0.45261	0.06032	0.39747	0.41286	0.11973	7.4	21.5	2.2	9.4	26.3	36.4	35.1	55.8
329	U1370	E	5	H	1	140	150	27.156	19.64	0.63787	0.00334	0.57918	0.07177	0.63028	0.44078	0.20881	8.2	22.9	2.7	10.4	27.0	45.5	39.8	71.2
329	U1370	F	5	H	3	140	150	28.551	22.61	0.58689	0.00280	0.54113	0.06682	0.51992	0.40754	0.17033	8.3	22.3	2.4	9.8	33.9	51.3	41.2	66.3
329	U1370	E	5	H	6	60	70	29.861	25.50	0.45780	0.00286	0.50647	0.07016	0.48116	0.39116	0.14349	7.4	20.1	2.8	9.9	38.3	42.0	40.1	61.8
329	U1370	E	6	H	2	134	144	32.035	30.16	0.45785	0.00227	0.50729	0.07651	0.48388	0.43560	0.12969	7.2	23.4	2.0	10.9	73.0	46.1	45.2	68.5
329	U1370	F	7	H	1	140	150	40.039	43.82	1.02516	0.00178	0.31076	0.06562	0.98239	0.40729	0.34080	6.1	29.8	1.0	9.7	108.9	57.5	63.1	100.9
329	U1370	F	7	H	2	140	150	41.921	47.23	0.91066	0.00214	0.35744	0.07540	1.11599	0.47197	0.39437	6.0	35.8	0.9	11.6	127.5	72.2	79.9	117.0
329	U1370	F	7	H	3	140	150	43.8	51.61	1.28056	0.00286	0.32894	0.06635	2.26535	0.41049	0.95843	6.0	30.6	1.0	10.4	147.2	114.7	84.2	163.2
329	U1370	F	7	H	4	140	150	45.671	56.87	3.36221	0.00325	0.19043	0.05476	2.45432	0.25749	1.04110	4.1	21.1	0.4	8.7	147.5	102.7	74.1	170.8
329	U1370	F	7	H	5	140	150	47.429	62.23	4.12178	0.00444	0.22873	0.06558	2.29475	0.30058	0.96912	4.1	22.9	0.5	10.5	179.6	127.3	89.9	162.0
329	U1370	F	7	H	6	140	150	48.985	63.00	1.36823	0.00380	0.37317	0.07536	2.26151	0.39347	0.39588	5.0	36.8	1.3	9.8	181.4	144.0	114.4	162.9
329	U1370	E	9	H	1	140	150	49.389	64.00	0.67468	0.00632	2.26180	0.07638	2.79420	0.78079	0.88285	8.0	52.9	1.4	1.9	89.7	167.0	137.1	261.2

Exp	Site	Hole	Core	Type	Sect.	Top	Bot	osmium (myr)	C0Age (Ma)	Y.	Mo	Ba	La	Ce	Nd	Sm	Gd	Dy	Er	Yb	Pb	Th	U.	Tl
329	U1370	E	1	H	1	5	15	0.798	0.05	9.3	0.2	188.3	10.0	51.0	13.0	3.2	3.1	2.7	1.4	1.2	33.6	2.4	0.4	0.6
329	U1370	E	1	H	1	42.5	52.5	1.152	0.24	9.8	0.2	134.1	10.1	53.1	13.1	3.2	3.1	2.8	1.5	1.3	32.4	4.4	0.4	0.5
329	U1370	E	1	H	1	140	150	1.989	0.71	8.9	0.1	209.2	9.3	54.1	12.0	2.9	2.8	2.6	1.4	1.3	31.2	7.2	0.4	0.3
329	U1370	E	1	H	3	40	50	3.612	1.73	8.0	0.2	193.6	9.6	60.2	12.3	2.9	2.8	2.5	1.3	1.2	31.9	7.7	0.4	0.3
329	U1370	E	2	H	1	140	150	7.493	3.75	15.3	0.4	150.7	13.1	52.9	18.8	4.6	4.5	4.2	2.3	2.0	19.1	6.1	0.5	0.3
329	U1370	E	2	H	2	140	150	8.815	4.28	17.7	0.6	241.8	14.5	57.9	21.3	5.3	5.1	4.8	2.5	2.3	19.0	7.4	0.6	0.3
329	U1370	E	2	H	4	140	150	11.462	5.82	42.7	0.4	253.0	28.9	54.9	43.9	10.8	11.1	10.5	5.8	5.0	18.9	6.1	0.7	0.3
329	U1370	E	2	H	6	113	123	13.854	7.70	44.6	0.3	140.1	31.4	56.7	48.3	11.8	11.6	10.8	5.9	5.0	16.9	5.3	0.7	0.3
329	U1370	E	3	H	1	140	150	15.815	9.16	46.2	0.7	168.1	28.9	46.3	40.1	9.4	9.6	9.5	5.6	5.0	14.4	3.9	1.0	0.4
329	U1370	E	3	H	2	140	150	17.108	9.87	49.6	0.7	228.3	31.6	47.8	43.8	10.5	10.7	10.5	6.1	5.2	14.6	4.8	1.0	0.4
329	U1370	E	3	H	3	140	150	18.308	10.63	49.1	0.8	328.0	33.4	50.0	42.6	10.0	10.3	10.0	5.9	5.1	16.0	5.6	1.0	0.5
329	U1370	E	3	H	4	140	150	19.419	11.29	37.7	0.4	176.1	24.7	40.0	34.0	8.1	8.2	7.8	4.5	3.8	13.1	3.6	0.8	0.4
329	U1370	E	3	H	5	140	150	20.52	11.87	40.9	0.4	151.3	26.7	39.1	38.3	9.0	9.1	8.8	4.9	4.1	12.8	3.8	0.7	0.5
329	U1370	E	4	H	1	140	150	22.611	13.19	41.2	0.3	122.4	27.2	40.4	37.3	8.7	8.9	8.5	4.9	4.1	14.0	4.2	0.8	0.4
329	U1370	E	4	H	5	140	150	25.671	16.82	38.7	0.2	101.8	26.0	41.4	36.5	8.4	8.6	8.3	4.6	3.8	13.8	4.7	0.7	0.3
329	U1370	E	5	H	1	140	150	27.156	19.64	62.8	0.2	136.3	39.8	48.7	54.7	12.8	13.3	12.8	7.4	6.1	17.1	5.6	0.9	0.2
329	U1370	F	5	H	3	140	150	28.551	22.61	56.2	0.3	153.3	36.9	50.4	50.8	12.0	12.5	11.9	6.8	5.7	14.2	5.1	0.8	0.2
329	U1370	E	5	H	6	60	70	29.861	25.50	45.5	0.2	116.6	29.4	42.8	40.5	9.5	9.6	9.2	5.2	4.3	15.6	4.1	0.6	0.3
329	U1370	E	6	H	2	134	144	32.035	30.16	42.2	0.3	90.9	27.5	47.1	40.2	9.7	9.6	9.1	5.0	4.0	14.1	3.0	0.6	0.8
329	U1370	F	7	H	1	140	150	40.039	43.82	71.1	0.4	117.1	46.9	100.4	64.0	15.1	15.4	14.8	8.6	7.1	11.4	2.6	0.9	1.1
329	U1370	F	7	H	2	140	150	41.921	47.23	88.1	0.4	139.5	57.5	116.4	80.7	19.8	19.5	18.4	10.5	8.6	11.1	3.3	0.9	1.3
329	U1370	F	7	H	3	140	150	43.8	51.61	253.3	0.5	148.6	158.3	196.6	253.1	64.3	60.1	53.3	29.2	22.8	11.3	7.7	1.3	1.0
329	U1370	F	7	H	4	140	150	45.671	56.87	251.0	0.5	154.6	178.4	122.6	242.3	59.9	58.3	51.9	28.2	22.3	9.3	1.8	1.2	1.3
329	U1370	F	7	H	5	140	150	47.429	62.23	230.7	0.4	179.7	163.4	114.9	235.1	59.3	56.1	48.2	26.1	20.0	11.0	1.7	1.0	1.3
329	U1370	F	7	H	6	140	150	48.985	63.00	155.2	0.4	224.6	123.8	80.8	174.3	43.3	42.2	37.5	19.3	14.8	13.8	0.9	0.8	1.8
329	U1370	E	9	H	1	140	150	49.389	64.00	62.2	0.5	211.3	67.9	6.0	67.1	14.0	15.3	15.2	9.1	8.4	6.5	0.3	1.4	1.3

Exp	Site	Hole	Core	Type	Sect.	Top	Bot	osmium (myr)	C0Age (Ma)	187/188Os	δ56Fe
329	U1370	E	1	H	1	5	15	0.798	0.05	0.9677	-0.26
329	U1370	E	1	H	1	42.5	52.5	1.152	0.24	0.9303	
329	U1370	E	1	H	1	140	150	1.989	0.71	0.9173	
329	U1370	E	1	H	3	40	50	3.612	1.73	0.9271	-0.21
329	U1370	E	2	H	1	140	150	7.493	3.75	0.7522	-0.09
329	U1370	E	2	H	2	140	150	8.815	4.28	0.8151	-0.16
329	U1370	E	2	H	4	140	150	11.462	5.82	0.7861	-0.11
329	U1370	E	2	H	6	113	123	13.854	7.70	0.7525	-0.21
329	U1370	E	3	H	1	140	150	15.815	9.16	0.311	-0.10
329	U1370	E	3	H	2	140	150	17.108	9.87	0.6813	-0.07
329	U1370	E	3	H	3	140	150	18.308	10.63	0.6958	-0.13
329	U1370	E	3	H	4	140	150	19.419	11.29	0.5587	-0.12
329	U1370	E	3	H	5	140	150	20.52	11.87	0.6247	-0.16
329	U1370	E	4	H	1	140	150	22.611	13.19	0.665	-0.14
329	U1370	E	4	H	5	140	150	25.671	16.82	0.6666	-0.16
329	U1370	E	5	H	1	140	150	27.156	19.64	0.6681	-0.13
329	U1370	F	5	H	3	140	150	28.551	22.61	0.6252	-0.17
329	U1370	E	5	H	6	60	70	29.861	25.50	0.6324	-0.15
329	U1370	E	6	H	2	134	144	32.035	30.16	0.5841	-0.13
329	U1370	F	7	H	1	140	150	40.039	43.82	0.5565	0.01
329	U1370	F	7	H	2	140	150	41.921	47.23	0.5083	0.00
329	U1370	F	7	H	3	140	150	43.8	51.61	0.423	0.13
329	U1370	F	7	H	4	140	150	45.671	56.87	0.3142	0.08
329	U1370	F	7	H	5	140	150	47.429	62.23	0.3801	0.18
329	U1370	F	7	H	6	140	150	48.985	63.00	0.1973	0.03
329	U1370	E	9	H	1	140	150	49.389	64.00	0.7041	-0.17

Supplemental Table 2: $\delta^{56}Fe$ and $^{187}Os/^{188}Os$

Combined: Lab Code - Site - Date Leached	Lab Code	Exp	Site	Hole	Core	Core Type	Sect.	Interval Top	Interval Bot	Depth	Modified Depth	187Os/188Os	2SE	n	WHOI 56Fe	2SD	n	ASU 56Fe	2SD	n	Rutgers 56Fe	2SD	n	WHOI 56Fe (BULK)	Final 56Fe	2SD
"R" Samples																										
01R-U1366-2017.06.17	01R	329	U1366	D	1	H	1	30	40	0.35	0.75	0.95						-0.17	0.04						-0.17	0.04
02R-U1366-2017.06.17	02R	329	U1366	D	1	H	1	130	140	1.35	1.75	0.95						-0.19	0.03						-0.19	0.03
03R-U1366-2017.06.17	03R	329	U1366	D	1	H	2	80	90	2.35	2.75	0.88						-0.22	0.03						-0.22	0.03
17R-U1366-2017.10.17	17R	329	U1366	F	1	H	3	60	70	3.65	3.65	0.82						-0.18	0.03						-0.18	0.03
04R-U1366-2017.06.17	04R	329	U1366	D	1	H	3	30	40	3.35	3.75	0.83						-0.16	0.04						-0.16	0.04
05R-U1366-2017.06.17	05R	329	U1366	D	1	H	3	130	140	4.35	4.75	0.79						-0.17	0.04						-0.17	0.04
41R-U1366-2017.10.29	41R	329	U1366	D	1	H	4	30	40	4.85	5.25	0.74						-0.15	0.03						-0.15	0.03
06R-U1366-2017.06.17	06R	329	U1366	D	1	H	4	80	90	5.35	5.75	0.43						-0.19	0.04						-0.19	0.04
42R-U1366-2017.10.30	42R	329	U1366	D	1	H	4	130	140	5.85	6.25							-0.16	0.03						-0.16	0.03
07R-U1366-2017.06.17	07R	329	U1366	D	1	H	5	30	40	6.35	6.75	0.77						-0.15	0.03						-0.15	0.03
43R-U1366-2017.10.31	43R	329	U1366	D	1	H	5	80	90	6.85	7.25	0.7						-0.13	0.04						-0.13	0.04
08R-U1366-2017.06.17	08R	329	U1366	D	1	H	5	130	140	7.35	7.75	0.65						-0.13	0.04						-0.13	0.04
09R-U1366-2017.06.17	09R	329	U1366	D	1	H	6	80	90	8.35	8.75	0.52						-0.11	0.03						-0.11	0.03
44R-U1366-2017.10.32	44R	329	U1366	D	1	H	7	10	20	8.85	9.25	0.7						-0.12	0.03						-0.12	0.03
18R-U1366-2017.10.18	18R	329	U1366	F	2	H	2	50	60	7.55	9.35	0.61						-0.12	0.04						-0.12	0.04
10R-U1366-2017.06.17	10R	329	U1366	D	2	H	1	30	40	9.75	10.15	0.48						-0.11	0.03						-0.11	0.03
45R-U1366-2017.10.33	45R	329	U1366	D	2	H	1	80	90	10.25	10.65	0.51						-0.08	0.03						-0.08	0.03
11R-U1366-2017.06.17	11R	329	U1366	D	2	H	1	130	140	10.75	11.15	0.53						-0.14	0.04						-0.14	0.04
12R-U1366-2017.06.17	12R	329	U1366	D	2	H	2	80	90	11.75	12.15	0.47						-0.27	0.04						-0.27	0.04
19R-U1366-2017.10.19	19R	329	U1366	F	2	H	4	50	60	10.55	12.35	0.34						-0.30	0.05						-0.30	0.05
46R-U1366-2017.10.34	46R	329	U1366	D	2	H	2	130	140	12.25	12.65	0.42						-0.31	0.04						-0.31	0.04
13R-U1366-2017.06.17	13R	329	U1366	D	2	H	3	30	40	12.75	13.15	0.38						-0.27	0.05						-0.27	0.05
14R-U1366-2017.06.17	14R	329	U1366	D	2	H	3	130	140	13.75	14.15	0.4						-0.16	0.05						-0.16	0.05
20R-U1366-2017.10.20	20R	329	U1366	F	2	H	5	80	90	12.35	14.15	0.44						0.08	0.04						0.08	0.04
21R-U1366-2017.10.21	21R	329	U1366	F	2	H	6	0	10	13.05	14.85	0.63						0.09	0.04						0.09	0.04
15R-U1366-2017.06.17	15R	329	U1366	D	2	H	4	80	90	14.75	15.15	0.45						0.11	0.05						0.11	0.05
16R-U1366-2017.06.17	16R	329	U1366	D	2	H	4	130	140	15.25	15.65	0.32						0.07	0.04						0.07	0.04
22R-U1366-2017.10.22	22R	329	U1366	F	3	H	1	30	40	14.35	16.15	0.43						-0.31	0.05						-0.31	0.05

Combined: Lab Code - Site - Date Leached	Lab Code	Exp	Site	Hole	Core	Core Type	Sect.	Interval Top	Interval Bot	Depth	Modified Depth	187Os/188Os	2SE	n	WHOI 56Fe	2SD	n	ASU 56Fe	2SD	n	Rutgers 56Fe	2SD	n	WHOI 56Fe (BULK)	Final 56Fe	2SD
23R-U1366-2017.10.23	23R	329	U1366	F	3	H	1	80	90	14.85	16.65							-0.29	0.03						-0.29	0.03
24R-U1366-2017.10.24	24R	329	U1366	F	3	H	1	130	140	15.35	17.15	0.52						-0.27	0.04						-0.27	0.04
25R-U1366-2017.10.25	25R	329	U1366	F	3	H	2	30	40	15.85	17.65	0.47						-0.34	0.04						-0.34	0.04
26R-U1366-2017.10.26	26R	329	U1366	F	3	H	2	80	90	16.35	18.15	0.52						-0.18	0.04						-0.18	0.04
27R-U1366-2017.10.27	27R	329	U1366	F	3	H	3	30	40	17.35	19.15	0.48						-0.20	0.04						-0.20	0.04
28R-U1366-2017.10.28	28R	329	U1366	F	3	H	3	130	140	18.35	20.15	0.51						-0.17	0.04						-0.17	0.04
29R-U1366-2017.07.31	29R	329	U1366	F	3	H	4	80	90	19.35	21.15							-0.18	0.04						-0.18	0.04
30R-U1366-2017.07.31	30R	329	U1366	F	3	H	5	30	40	20.35	22.15							-0.17	0.03						-0.17	0.03
31R-U1366-2017.07.31	31R	329	U1366	F	3	H	5	130	140	21.35	23.15							-0.31	0.03						-0.31	0.03
32R-U1366-2017.07.31	32R	329	U1366	F	3	H	6	80	90	22.35	24.15							-0.24	0.04						-0.24	0.04
33R-U1366-2017.07.31	33R	329	U1366	F	3	H	7	20	30	23.25	25.05							-0.01	0.04						-0.01	0.04
34R-U1366-2017.07.31	34R	329	U1366	F	4	H	1	80	90	24.35	26.15							-0.11	0.03						-0.11	0.03
35R-U1366-2017.07.31	35R	329	U1366	F	4	H	2	30	40	25.35	27.15							-0.02	0.03						-0.02	0.03
36R-U1366-2017.07.31	36R	329	U1366	F	4	H	2	120	130	26.25	28.05							-0.02	0.03						-0.02	0.03
37R-U1366-2017.07.31	37R	329	U1366	F	4	H	3	80	90	27.35	29.15							-0.13	0.03						-0.13	0.03
38R-U1366-2017.07.31	38R	329	U1366	F	4	H	4	10	20	28.15	29.95							-0.30	0.04						-0.30	0.04
39R-U1366-2017.07.31	39R	329	U1366	F	4	H	5	40	50	29.36	31.16							0.10	0.05						0.10	0.05
45R-U1366-2017.07.11	45R	329	U1366	D	2	H	1	80	90	10.25	10.65															
46R-U1366-2017.07.11	46R	329	U1366	D	2	H	2	130	140	12.25	12.65															
47R-U1370-2017.07.11	47R	329	U1370	E	1	H	1	5	15	0.1		0.9859	0.0306	5.00	-0.28	0.06	5.00				-0.22	0.08	2.00		-0.26	0.05
50R-U1370-2017.07.11	50R	329	U1370	E	1	H	3	40	50	3.45		0.9545	0.034	5.00	-0.23	0.06	5.00				-0.17	0.08	2.00		-0.21	0.05
51R-U1370-2017.07.11	51R	329	U1370	E	2	H	1	140	150	7.65		0.7731	0.0304	5.00	-0.09	0.06	5.00				-0.08	0.08	2.00		-0.09	0.05
52R-U1370-2017.07.11	52R	329	U1370	E	2	H	2	140	150	9.15		0.8381	0.0223	5.00	-0.16	0.06	5.00								-0.16	
53R-U1370-2017.07.11	53R	329	U1370	E	2	H	4	140	150	12.15		0.8116	0.0336	2.00							-0.11	0.08	2.00		-0.11	0.08
54R-U1370-2017.07.19	54R	329	U1370	E	2	H	6	113	123	14.88		0.7756	0.0364	5.00	-0.20	0.06	5.00				-0.24	0.08	2.00		-0.21	0.05
55R-U1370-2017.07.19	55R	329	U1370	E	3	H	1	140	150	17.15		0.3328	0.0068	5.00	-0.12	0.06	5.00				-0.04	0.08	2.00	0.01	-0.10	0.05
56R-U1370-2017.07.19	56R	329	U1370	E	3	H	2	140	150	18.65		0.6998	0.0222	5.00	-0.08	0.06	5.00				-0.03	0.08	2.00		-0.07	0.05
57R-U1370-2017.07.19	57R	329	U1370	E	3	H	3	140	150	20.15		0.7106	0.0203	5.00	-0.13	0.06	5.00				-0.13	0.08	2.00		-0.13	0.05
58R-U1370-2017.07.19	58R	329	U1370	E	3	H	4	140	150	21.65		0.5696	0.0097	5.00	-0.12	0.06	5.00				-0.11	0.08	2.00		-0.12	0.05
59R-U1370-2017.07.19	59R	329	U1370	E	3	H	5	140	150	23.15		0.6449	0.0188	5.00	-0.17	0.06	5.00				-0.12	0.08	2.00		-0.16	0.05

Combined: Lab Code - Site - Date Leached	Lab Code	Exp	Site	Hole	Core	Core Type	Sect.	Interval Top	Interval Bot	Depth	Modified Depth	187Os/188Os	2SE	n	WHOI 56Fe	2SD	n	ASU 56Fe	2SD	n	Rutgers 56Fe	2SD	n	WHOI 56Fe (BULK)	Final 56Fe	2SD
60R-U1370-2017.07.19	60R	329	U1370	E	4	H	1	140	150	26.65		0.6852	0.0219	5.00	-0.14	0.06	5.00				-0.13	0.08	2.00		-0.14	0.05
61R-U1370-2017.07.19	61R	329	U1370	E	4	H	5	140	150	32.65		0.6909	0.0181	6.00	-0.16	0.06	6.00				-0.13	0.13	1.00		-0.16	0.06
62R-U1370-2017.07.19	62R	329	U1370	E	5	H	1	140	150	36.15		0.6816	0.0171	6.00	-0.12	0.06	6.00				-0.19	0.13	1.00		-0.13	0.06
63R-U1370-2017.07.19	63R	329	U1370	F	5	H	3	140	150	39.65		0.6552	0.0169	6.00	-0.16	0.06	6.00				-0.24	0.13	1.00		-0.17	0.06
64R-U1370-2017.07.19	64R	329	U1370	E	5	H	6	60	70	42.79		0.6569	0.0244	6.00	-0.13	0.06	6.00				-0.24	0.13	1.00		-0.15	0.06
65R-U1370-2017.07.19	65R	329	U1370	E	6	H	2	134	144	47.09		0.6141	0.012	6.00	-0.14	0.06	6.00				-0.08	0.13	1.00		-0.13	0.06
66R-U1370-2017.07.19	66R	329	U1370	F	7	H	1	140	150	55.65		0.5609	0.0096	6.00	0.00	0.06	6.00				0.08	0.13	1.00		0.01	0.06
67R-U1370-2017.07.19	67R	329	U1370	F	7	H	2	140	150	57.15		0.514	0.0126	6.00	-0.01	0.06	6.00				0.03	0.13	1.00	-0.06	0.00	0.06
68R-U1370-2017.07.19	68R	329	U1370	F	7	H	3	140	150	58.65		0.4361	0.007	6.00	0.12	0.06	6.00				0.18	0.13	1.00		0.13	0.06
69R-U1370-2017.07.19	69R	329	U1370	F	7	H	4	140	150	60.15		0.3383	0.0167	6.00	0.05	0.06	6.00				0.20	0.13	1.00		0.08	0.06
70R-U1370-2017.07.19	70R	329	U1370	F	7	H	5	140	150	61.65		0.3959	0.0115	6.00	0.16	0.06	6.00				0.32	0.13	1.00		0.18	0.06
71R-U1370-2017.07.19	71R	329	U1370	F	7	H	6	140	150	63.15		0.2012	0.002	6.00	0.04	0.06	6.00				-0.03	0.13	1.00		0.03	0.06
72R-U1370-2017.07.19	72R	329	U1370	E	9	H	1	140	150	63.55		0.7097	0.0132	6.00	-0.18	0.06	6.00				-0.12	0.13	1.00		-0.17	0.06
73R-U1369-2017.07.29	73R	329	U1369	C	1	H	1	5	15	0.1		0.9025	0.0191	5.00	-0.25	0.06	5				-0.22	0.13	1.00		-0.24	0.05
74R-U1369-2017.07.29	74R	329	U1369	C	1	H	1	40	50	0.45		0.817	0.0209	5.00	-0.19	0.06	5				-0.24	0.13	2.00		-0.20	0.05
75R-U1369-2017.07.29	75R	329	U1369	C	1	H	1	140	150	1.45		0.7078	0.015	5.00	-0.16	0.06	5				-0.10	0.13	2.00		-0.14	0.05
76R-U1369-2017.07.29	76R	329	U1369	C	1	H	2	90	100	2.45		0.7219	0.0133	5.00	-0.21	0.06	5				-0.20	0.13	2.00		-0.21	0.05
77R-U1369-2017.07.29	77R	329	U1369	C	1	H	2	140	150	2.95		0.7219	0.0133	5.00	-0.18	0.06	5				-0.16	0.13	2.00		-0.18	0.05
78R-U1369-2017.07.29	78R	329	U1369	C	1	H	3	40	50	3.45		0.7057	0.0177	5.00	-0.06	0.06	5				-0.04	0.13	2.00		-0.06	0.05
79R-U1369-2017.07.29	79R	329	U1369	C	1	H	3	90	100	3.95		0.7027	0.0247	5.00	-0.07	0.06	5				-0.05	0.13	2.00		-0.06	0.05
80R-U1369-2017.07.29	80R	329	U1369	C	1	H	3	140	150	4.45		0.6623	0.0242	5.00	-0.06	0.06	5				0.07	0.13	2.00		-0.02	0.05
81R-U1369-2017.07.29	81R	329	U1369	C	1	H	4	122	132	5.77		0.7527	0.0256	5.00	-0.14	0.06	5				0.00	0.13	2.00		-0.10	0.05
82R-U1369-2017.07.29	82R	329	U1369	C	2	H	1	140	150	7.45		0.7594	0.0115	5.00	-0.19	0.06	5				-0.08	0.13	2.00		-0.16	0.05
83R-U1369-2017.07.29	83R	329	U1369	C	2	H	2	140	150	8.95		0.7047	0.015	5.00	-0.17	0.06	5				-0.11	0.13	2.00		-0.15	0.05
84R-U1369-2017.07.29	84R	329	U1369	C	2	H	3	140	150	10.45		0.7706	0.0215	5.00	-0.14	0.07	5				0.00	0.13	2.00		-0.10	0.06
85R-U1369-2017.07.29	85R	329	U1369	C	2	H	4	140	150	11.95		0.5877	0.0164	5.00	-0.22	0.07	5				-0.17	0.13	2.00		-0.21	0.06
86R-U1369-2017.07.29	86R	329	U1369	C	2	H	5	90	100	12.95		0.7968	0.0182	5.00	-0.08	0.07	5				-0.14	0.13	2.00		-0.10	0.06
87R-U1369-2017.07.29	87R	329	U1369	C	2	H	6	40	50	13.95		0.7859	0.015	5.00	-0.08	0.07	5				-0.02	0.13	2.00	0.00	-0.06	0.06
88R-U1369-2017.07.29	88R	329	U1369	C	2	H	6	140	150	14.95		0.5946	0.0063	5.00	-0.09	0.07	5				-0.01	0.13	2.00		-0.07	0.06
89R-U1369-2017.07.29	89R	329	U1369	C	2	H	7	35	45	15.4		0.6582	0.009	5.00	-0.03	0.07	5				-0.01	0.13	2.00		-0.03	0.06

Combined: Lab Code - Site - Date Leached	Lab Code	Exp	Site	Hole	Core	Core Type	Sect.	Interval Top	Interval Bot	Depth	Modified Depth	187Os/188Os	2SE	n	WHOI 56Fe	2SD	n	ASU 56Fe	2SD	n	Rutgers 56Fe	2SD	n	WHOI 56Fe (BULK)	Final 56Fe	2SD
90R-U1369-2017.07.29	90R	329	U1369	C	2	H	7	69	79	15.74		0.6658	0.0125	5.00	-0.09	0.07	5				-0.07	0.13	2.00		-0.09	0.06
												"J Samples"														
23J-U1366-2021.04.04	23J	329	U1366	F	1	H	1	20	22	0.2	0.2	0.82	0.01	6.00	-0.22	0.06	6.0				-0.2	0.1	2		-0.20	0.05
24J-U1366-2020.10.10	24J	329	U1366	F	1	H	2	110	112	2.6	2.6	0.88	0.02	5.00	-0.23	0.07	5.0				-0.2	0.1	2		-0.23	0.05
25J-U1366-2020.10.10	25J	329	U1366	F	1	H	3	100	102	4	4	0.72	0.01	5.00	-0.13	0.07	5.0				-0.1	0.1	2		-0.13	0.05
26J-U1366-2021.04.04	26J	329	U1366	F	1	H	4	55	57	5.05	5.05	0.78	0.01	6.00	-0.15	0.06	6.0				-0.2	0.1	2		-0.16	0.05
27J-U1366-2020.10.10	27J	329	U1366	F	1	H	4	70	72	5.2	5.2	0.85	0.04	5.00	-0.18	0.07	5.0				-0.1	0.1	2		-0.17	0.05
28J-U1366-2020.10.10	28J	329	U1366	F	1	H	4	80	82	5.3	5.3	0.65	0.01	5.00	-0.17	0.07	5.0				-0.1	0.1	2		-0.16	0.05
01J-U1366-2020.10.10	01J	329	U1366	D	1	H	4	55	57	5.1	5.5	0.82	0.02	5.00							-0.18	0.05	5		-0.18	0.05
02J-U1366-2021.04.04	02J	329	U1366	D	1	H	4	78	80	5.33	5.73	0.74	0.01	3.00							-0.18	0.07	3		-0.18	0.07
03J-U1366-2021.04.04	03J	329	U1366	D	1	H	4	95	97	5.5	5.9	0.77	0.01	3.00							-0.13	0.07	3		-0.13	0.07
04J-U1366-2020.10.10	04J	329	U1366	D	1	H	4	115	117	5.7	6.1	0.79	0.01	5.00	-0.20	0.07	5.00				-0.21	0.08	2		-0.20	0.05
05J-U1366-2020.10.03	05J	329	U1366	D	1	H	5	5	7	6	6.4	0.72	0.01	3.00							-0.22	0.07	3		-0.22	0.07
06J-U1366-2020.10.10	06J	329	U1366	D	1	H	5	15	17	6.1	6.5	0.82	0.02	3.00							-0.18	0.07	3		-0.18	0.07
07J-U1366-2020.10.10	07J	329	U1366	D	1	H	5	20	22	6.15	6.55	0.78	0.02	3.00							-0.21	0.07	3		-0.21	0.07
08J-U1366-2021.04.04	08J	329	U1366	D	1	H	5	35	37	6.3	6.7	0.58	0.01	3.00							-0.16	0.07	3		-0.16	0.07
29J-U1366-2020.10.10	29J	329	U1366	F	2	H	1	55	57	6.2	8	0.62	0.01	5.00	-0.14	0.07	5.0				-0.1	0.1	2		-0.13	0.05
30J-U1366-2020.10.10	30J	329	U1366	F	2	H	1	75	77	6.4	8.2	0.65	0.01	5.00	-0.14	0.07	5.0				-0.2	0.1	2		-0.14	0.05
31J-U1366-2020.10.10	31J	329	U1366	F	2	H	1	95	97	6.6	8.4	0.48	0.03	5.00	-0.21	0.07	5.0				-0.1	0.1	2		-0.18	0.05
32J-U1366-2021.04.04	32J	329	U1366	F	2	H	2	5	7	7.1	8.9	0.68	0.01	6.00	-0.01	0.06	6.0				-0.2	0.1	2		-0.05	0.05
33J-U1366-2021.04.04	33J	329	U1366	F	2	H	2	95	97	8	9.8	0.62	0.01	6.00	-0.13	0.06	6.0				-0.1	0.1	2		-0.13	0.05
09J-U1366-2021.04.04	09J	329	U1366	D	2	H	1	15	17	9.6	10	0.39	0.00	3.00							-0.15	0.07	3		-0.15	0.07
34J-U1366-2021.04.04	34J	329	U1366	F	2	H	2	135	137	8.4	10.2	0.57	0.01	6.00	-0.08	0.06	6.0				-0.2	0.1	2		-0.11	0.05
10J-U1366-2020.10.10	10J	329	U1366	D	2	H	1	55	57	10	10.4	0.54	0.01	3.00							-0.14	0.07	3		-0.14	0.07
11J-U1366-2021.04.04	11J	329	U1366	D	2	H	1	105	107	10.5	10.9	0.49	0.00	3.00							-0.09	0.07	3		-0.09	0.07
12J-U1366-2020.10.03	12J	329	U1366	D	2	H	2	5	7	11	11.4	0.49	0.00	3.00							-0.09	0.07	3		-0.09	0.07
13J-U1366-2020.10.10	13J	329	U1366	D	2	H	2	55	57	11.5	11.9	0.35	0.00	3.00							-0.21	0.07	3		-0.21	0.07
35J-U1366-2021.04.04	35J	329	U1366	F	2	H	4	15	17	10.2	12	0.43	0.00	6.00	-0.29	0.06	6.0				-0.3	0.1	1		-0.29	0.06
14J-U1366-2021.04.04	14J	329	U1366	D	2	H	2	105	107	12	12.4	0.53	0.01	3.00							-0.25	0.07	3		-0.25	0.07
36J-U1366-2020.10.03	36J	329	U1366	F	2	H	4	75	77	10.8	12.6	0.50	0.00	5.00	-0.40	0.07	5.0				-0.3	0.1	1	-0.38	-0.39	0.06

Combined: Lab Code - Site - Date Leached	Lab Code	Exp	Site	Hole	Core	Core Type	Sect.	Interval Top	Interval Bot	Depth	Modified Depth	187Os/188Os	2SE	n	WHOI 56Fe	2SD	n	ASU 56Fe	2SD	n	Rutgers 56Fe	2SD	n	WHOI 56Fe (BULK)	Final 56Fe	2SD
37J-U1366-2020.10.10	37J	329	U1366	F	2	H	4	95	97	11	12.8	0.54	0.01	5.00	-0.37	0.07	5.0				-0.4	0.1	1		-0.38	0.06
15J-U1366-2021.04.04	15J	329	U1366	D	2	H	3	5	7	12.5	12.9	0.52	0.01	3.00							-0.34	0.07	3		-0.34	0.07
38J-U1366-2021.04.04	38J	329	U1366	F	2	H	4	135	137	11.4	13.2	0.50	0.01	6.00	-0.26	0.05	6.0				-0.4	0.1	1		-0.27	0.05
16J-U1366-2020.10.03	16J	329	U1366	D	2	H	3	55	57	13	13.4	0.46	0.01	3.00							-0.29	0.07	3		-0.29	0.07
39J-U1366-2020.10.10	39J	329	U1366	F	2	H	5	45	47	12	13.8	0.46	0.01	5.00	-0.27	0.07	5.0				-0.3	0.1	1		-0.28	0.06
17J-U1366-2020.10.10	17J	329	U1366	D	2	H	3	105	107	13.5	13.9	0.49	0.01	3.00							-0.20	0.07	3		-0.20	0.07
18J-U1366-2020.10.10	18J	329	U1366	D	2	H	4	3	5	13.98	14.38	0.30	0.00	3.00							-0.11	0.07	3		-0.11	0.07
40J-U1366-2021.04.04	40J	329	U1366	F	2	H	5	125	127	12.8	14.6	0.27	0.01	6.00	-0.28	0.05	6.0				-0.4	0.1	1		-0.29	0.05
19J-U1366-2021.04.04	19J	329	U1366	D	2	H	4	28	30	14.23	14.63	0.33	0.00	5.00							0.05	0.05	5		0.05	0.05
41J-U1366-2021.04.04	41J	329	U1366	F	2	H	6	35	37	13.4	15.2	0.46	0.01	6.00	-0.02	0.05	6.0				-0.1	0.1	1		-0.03	0.05
20J-U1366-2021.04.04	20J	329	U1366	D	2	H	4	105	107	15	15.4	0.34	0.00	6.00	0.06	0.06	6.0				0.1	0.1	2	-0.13	0.06	0.05
42J-U1366-2021.04.04	42J	329	U1366	F	2	H	6	55	57	13.6	15.4	0.51	0.01	6.00	-0.14	0.05	6.0				-0.2	0.1	1		-0.15	0.05
21J-U1366-2020.10.10	21J	329	U1366	D	2	H	4	125	127	15.2	15.6	0.49	0.02	5.00	0.06	0.07	5.0				0.0	0.1	2		0.04	0.05
43J-U1366-2020.10.10	43J	329	U1366	F	3	H	1	5	7	14.1	15.9	0.49	0.00	5.00	-0.35	0.07	5.0				-0.3	0.1	1		-0.34	0.06
22J-U1366-2020.10.10	22J	329	U1366	D	2	H	5	15	17	15.6	16	0.52	0.01	5.00	0.08	0.07	5.0				0.0	0.1	2		0.05	0.05
44J-U1366-2020.10.10	44J	329	U1366	F	3	H	1	20	22	14.25	16.05	0.44	0.00	5.00	-0.29	0.07	5.0				-0.3	0.1	1		-0.29	0.06
45J-U1366-2020.10.10	45J	329	U1366	F	3	H	1	40	42	14.45	16.25	0.29	0.00	6.00	-0.40	0.06	6.0				-0.4	0.1	1		-0.40	0.06
46J-U1366-2021.04.04	46J	329	U1366	F	3	H	1	95	97	15	16.8	0.39	0.01	6.00	-0.11	0.05	6.0				-0.2	0.1	1		-0.13	0.05
47J-U1366-2020.10.10	47J	329	U1366	F	3	H	1	105	107	15.2	17	0.36	0.00	6.00	-0.11	0.06	6.0				-0.2	0.1	1		-0.11	0.06
48J-U1366-2020.10.03	48J	329	U1366	F	3	H	1	125	127	15.4	17.2	0.54	0.02	6.00	-0.22	0.06	6.0				-0.3	0.1	1		-0.23	0.06
49J-U1366-2021.04.04	49J	329	U1366	F	3	H	2	20	22	15.75	17.55	0.55	0.00													
50J-U1366-2020.10.10	50J	329	U1366	F	3	H	2	45	47	16	17.8	0.51	0.01													
51J-U1366-2021.04.04	51J	329	U1366	F	3	H	2	65	67	16.2	18	0.53	0.01	6.00	-0.22	0.05	6								-0.22	
52J-U1366-2020.10.10	52J	329	U1366	F	3	H	2	90	92	16.72	18.52	0.47	0.01													
53J-U1366-2021.04.04	53J	329	U1366	F	3	H	2	98	100	16.8	18.6	0.49	0.01	6.00	-0.16	0.05	6								-0.16	
Replicates																										
4R-U1366-2020.10.10	04R	329	U1366	D	1	H	3	30	40	3.35	3.75			2.00				-0.16	0.04		-0.16	0.08	2		-0.16	
6R-U1366-2020.10.03	06R	329	U1366	D	1	H	4	80	90	5.35	5.75			2.00				-0.19	0.04		-0.13	0.08	2		-0.13	
12R-U1366-2020.10.03	12R	329	U1366	D	2	H	2	80	90	11.75	12.15			2.00				-0.27	0.04		-0.40	0.08	2		-0.40	
17R-U1366-2020.10.10	17R	329	U1366	F	1	H	3	60	70	3.65	3.65			2.00				-0.18	0.03		-0.11	0.08	2		-0.11	

Combined: Lab Code - Site - Date Leached	Lab Code	Exp	Site	Hole	Core	Core Type	Sect.	Interval Top	Interval Bot	Depth	Modified Depth	187Os/188Os	2SE	n	WHOI 56Fe	2SD	n	ASU 56Fe	2SD	n	Rutgers 56Fe	2SD	n	WHOI 56Fe (BULK)	Final 56Fe	2SD
19R-U1366-2020.10.03	19R	329	U1366	F	2	H	4	50	60	10.55	12.35			2.00				-0.30	0.05		-0.34	0.08	2		-0.34	
Additional Os Samples(Not analyzed for Fe)																										
01K-2021.12.06	01K	329	U1369	C	1	H	1	90	100	0.95		0.6731	0.0191													
02K-2021.12.06	02K	329	U1369	C	1	H	2	40	50	1.95		0.7786	0.046													
03K-2021.12.06	03K	329	U1369	C	2	H	5	40	50	12.45		0.7469	0.0168													
04K-2021.12.06	04K	329	U1369	C	2	H	5	140	150	13.45		0.7916	0.0099													
05K-2021.12.06	05K	329	U1369	C	2	H	6	90	100	14.45		0.8134	0.0062													
06K-2021.12.06	06K	329	U1369	C	2	H	7	69	79	15.74		0.5930	0.0084													
07K-2021.12.06	07K	329	U1370	D	3	H	1	118	119	19.49		0.6461	0.0268													
08K-2021.12.06	08K	329	U1370	D	7	H	6	70	71	61.73		0.41														
09K-2021.12.06	09K	329	U1370	D	7	H	6	130	131	62.33		0.4356	0.0176													
10K-2021.12.06	10K	329	U1370	D	7	H	7	46	47	62.99		0.4596	0.047													
11K-2021.12.06	11K	329	U1370	D	8	H	2	94	95	65.45		0.5194	0.0077													
12K-2021.12.06	12K	329	U1370	E	1	H	2	40	50	1.95		0.8935	0.03													
13K-2021.12.06	13K	329	U1370	E	1	H	2	140	150	2.95		0.9544	0.0263													
14K-2021.12.06	14K	329	U1370	E	1	H	3	90	100	3.95		0.9046	0.0227													
15K-2021.12.06	15K	329	U1370	E	1	H	3	140	150	4.45		0.8893	0.0212													
16K-2021.12.06	16K	329	U1370	E	1	H	4	142	152	5.97		0.7557	0.0355													
17K-2021.12.06	17K	329	U1370	E	2	H	3	140	150	10.65		0.764	0.0216													
18K-2021.12.06	18K	329	U1370	E	3	H	6	58	68	23.83		0.6124	0.0244													
19K-2021.12.06	19K	329	U1370	E	4	H	2	140	150	28.15		0.7239	0.017													
20K-2021.12.06	20K	329	U1370	E	4	H	4	140	150	31.15		0.6437	0.02													
21K-2021.12.06	21K	329	U1370	E	5	H	2	134	144	37.59		0.6764	0.0177													
22K-2021.12.06	22K	329	U1370	E	5	H	3	140	150	39.09		0.7108	0.0167													
23K-2021.12.06	23K	329	U1370	E	5	H	4	140	150	40.59		0.6571	0.0182													
24K-2021.12.06	24K	329	U1370	E	5	H	5	140	150	42.09		0.6702	0.019													
25K-2021.12.06	25K	329	U1370	E	6	H	1	140	150	45.65		0.5667	0.0101													
26K-2021.12.06	26K	329	U1370	E	6	H	3	140	150	48.58		0.6205	0.0236													
27K-2021.12.06	27K	329	U1370	E	6	H	4	140	150	50.08		0.5962	0.0074													
28K-2021.12.06	28K	329	U1370	F	5	H	4	140	150	41.15		0.693	0.0157													

Combined: Lab Code - Site - Date Leached	Lab Code	Exp	Site	Hole	Core	Core Type	Sect.	Interval Top	Interval Bot	Depth	Modified Depth	187Os/188Os	2SE	n	WHOI 56Fe	2SD	n	ASU 56Fe	2SD	n	Rutgers 56Fe	2SD	n	WHOI 56Fe (BULK)	Final 56Fe	2SD
29K-2021.12.06	29K	329	U1370	F	5	H	5	140	150	42.65		0.6809	0.0211													
30K-2021.12.06	30K	329	U1370	F	6	H	2	140	150	47.65		0.5506	0.0107													
31K-2021.12.06	31K	329	U1370	F	6	H	3	140	150	49.15		0.6195	0.0106													
32K-2021.12.06	32K	329	U1370	F	6	H	4	140	150	50.65		0.6157	0.0101													
33K-2021.12.06	33K	329	U1370	F	6	H	5	140	150	52.15		0.617	0.0229													